人の巧みさに関する軟組織の力学の解明

研究課題番号 20246049

平成20年度～平成22年度 科学研究費補助金
(基盤研究(A)(2)) 研究成果報告書

平成23年3月

研究代表者　　平井　慎一

(立命館大学 理工学部 教授)

Soft Tissue Mechanics in Human Dexterity

Project Number 20246049

From April 2008 to March 2011
Report for the Research Project
Grant in Aid for Scientific Research (A)(2)
by the Ministry of Education, Culture, Sports,
Science and Technology of Japan

March 2011

Head investigator Shinichi Hirai

(Professor, Faculty of Science and Engineering,

Ritsumeikan University)

平成 20 年度～平成 22 年度 科学研究費補助金
(基盤研究 (A)(2)) 研究成果報告書

課題番号　20246049
研究課題　人の巧みさに関する軟組織の力学の解明

研究組織
研究代表者: 平井 慎一 (立命館大学 理工学部 教授)
研究分担者: 田中 弘美 (立命館大学 情報理工学部 教授)
研究分担者: 犬伏 俊郎 (滋賀医科大学 MR 医学総合研究センター 教授)
研究分担者: 森川 茂廣 (滋賀医科大学 医学部 教授)
研究分担者: 井上 貴浩 (岡山県立大学 情報工学部 准教授)

交付決定額 (金額単位: 千円)

	直接経費	間接経費	合計
平成 20 年度	14,000	4,200	18,200
平成 21 年度	11,500	3,450	14,950
平成 22 年度	10,000	3,000	13,000
総計	35,500	10,650	46,150

まえがき

本提案の目的は，人の皮膚や軟骨などの軟組織が，人の運動の巧みさにどのように貢献しているかを力学的に解明することである．人は，意識することなく様々な物体を把持し，様々な道具を巧みに操ることができる．運動生理学やロボティクスの分野では，このような人の巧みさを解明する試みが成されてきた．運動生理学では，物体によって異なる把持形態の記述や手指の運動に関する脳神経系の活動部位の同定が進められている．一方，ロボティクスの分野では，柔軟な組織が触覚に与える影響の力学的解析や柔軟指による物体把持の力学解析が成され，柔らかい組織が触覚のフィルターの役割を果たすことやポテンシャルエネルギーの形成を通して安定な把持と操作に寄与していることが明らかになりつつある．しかしながら，人が物体を操作するときに，どのような力学で巧みな操作が可能になっているかは不明のままである．そこで本研究では，内部イメージング技術に基づき人の軟組織の変形を計測し，力学モデリングを通して人の巧みな操作における軟組織の力学を解明することを目的とする．

第 1 章では，軟組織の変形をモデリングする手法について述べる．軟組織は，弾性変形と塑性変形の両方を示し，非線形や非一様など複雑な変形特性を有する．このような変形特性を表わすために，動的なレオロジー変形を有限要素近似により定式化するとともに，変形過程の計測結果から変形モデルのパラメータを推定する手法を確立した (成果 論文 [1]，論文 [7]，国際会議 [7]，口頭発表 [10]，口頭発表 [11]，口頭発表 [16]，口頭発表 [19]，口頭発表 [21])．有限要素近似による定式化においては，直列モデルと並列モデルを解析し，それぞれの限界を明らかにするとともに，その限界を克服するために多重粘性要素を提案した．レオロジー変形のモデリングにおいては，コーシー歪みとグリーン歪みを用いて変形を定式化し，回転を含む変形のシミュレーションを示した．さらに，制約安定化法を用いて，非一様な層状物体をモデリングする手法を提案した．特に，変形モデルのパラメータ推定においては，変形形状と変形により生じる力を同時に再生するように，モデルを選択しパラメータを推定する手法を提案した (成果 国際会議 [6]，国際会議 [11]，国際会議 [14]，国際会議 [16]，口頭発表 [6])．

第 2 章では，人指の内部変位の計測と変形シミュレーションについて述べる．第

3 章で述べる手法を基に，人指の MR 画像から人指の内部変形を計測する．さらに，前章で確立したモデリング手法を基に，人指の変形モデルを構成し，人指の変形をシミュレーションした結果を述べる．指先の変形計測を進めるとともに，軟組織が硬い物体と接触し転がりや滑りを生じる状態のモデリングを進めた (成果　論文 [2]，国際会議 [3]，国際会議 [13]，国際会議 [18]，口頭発表 [1]，口頭発表 [12]，口頭発表 [13])．軟組織の転がりのモデリングでは，軟組織を梁の集まりで表わし，転がりに起因する制約を課している．軟組織の滑りのモデリングでは，梁と梁の間に弾性要素を配置することにより，局所滑りを表わしている．

第 3 章では，軟組織の MR 画像から内部変形を計算する手法を述べる．変形前と変形後の MR 画像を撮影し，これらを比較することにより内部変形を計算する．変形場の計算においては，画像のアフィン変換に加えて画像の変形に対処する必要がある．また，軟組織の MR 画像は，解像度が少なく輪郭が明瞭でない場合が多い．このような MR 画像に対して，ロバストに画像間の対応点を求め，変形場を計算するアルゴリズムが求められる．本研究では，局所不変特徴量を用いた変形場の計算手法と，SAC と TPS を用いた変形場の計算手法について述べる．前者は，局所的に不変な特徴量を用いて画像間の対応点を計算する (成果　国際会議 [9])．後者は，Spatial Association Correspondence (SAC) と Thin Plate Spline (TPS) を用いて，局所的な対応点探索と大域的なモデル更新を交互に実行することで，変形場を計算する手法である (成果　国際会議 [10]，口頭発表 [7])．また，MR 画像の解像度と画質の向上を試みた (成果　論文 [4]，論文 [6]，論文 [11]，論文 [12]，国際会議 [20]，口頭発表 [8]，口頭発表 [9]，口頭発表 [15]，口頭発表 [23])．

第 4 章では，柔軟指操作の力学と制御について述べる．平行分布モデルにより柔軟指のポテンシャルエネルギーを定式化し，柔軟指操作の三次元力学モデルを構成するとともに，柔軟指による把持物体の姿勢と位置を制御する二段階制御を提案した (成果　書籍 [1]，論文 [5]，国際会議 [15]，国際会議 [19]，国際会議 [22]，口頭発表 [5]，口頭発表 [17]，口頭発表 [18])．さらに提案した制御則を，二自由度二指による把持物体の姿勢と位置の制御 (成果　国際会議 [1]，国際会議 [17]，口頭発表 [22])，一自由度三指による把持物体の三次元空間内における姿勢制御 (成果　口頭発表 [2]，口頭発表 [4])，連動関節を有する指による物体操作 (成果　国際会議 [8]，口頭発表 [3]，口頭発表 [14]) に拡張した．

第 5 章では，視覚情報遅れ下における物体操作について述べる．人の視覚や神経系には，数ミリ秒ないしは数十ミリ秒に至る情報伝達の遅れがある．このような遅れに関わらず，人は巧みに物体を操作することができる．なぜこのような操作が可能であるかを探究することが目的である．第 4 章の成果を基にして，二段階制御法では情報伝達の遅れに対してロバストに物体を操作できることを示し，それが柔軟

指のポテンシャルエネルギーの性質に帰することを示した (成果 論文 [8]，論文 [10]，国際会議 [4])．

本研究課題の成果は，手術のシミュレーション等に応用できる (成果 国際会議 [21]，国際会議 [24]，口頭発表 [20])．さらに，本研究の発展として，柔軟指の内部にセンサを埋め込み，滑り覚を得ることを試みた (成果 論文 [3]，国際会議 [2]，国際会議 [23])．滑り覚のセンシングにおいては，柔軟指が対象の表面を滑ることが重要な役割を果たす．本研究で進めた柔軟指のモデリング，特に人指のモデリングが，滑り覚のセンシングの解析において基礎となると考える．また，滑りを用いた布地のハンドリングに関する研究を進めた (成果 論文 [9]，国際会議 [5]，国際会議 [12])．滑りを用いることで，摘みハンドによる布地の展開が可能になった．滑りの解析には，本研究で進めた柔軟指のモデリングが基礎になると考える．

本研究では，軟組織の変形モデリングを進めた．軟組織単体のモデリングに関しては多くの成果が得られたが，軟組織と軟組織との接触に伴うトライボロジーに関しては未開拓の部分が多い．上記のように軟組織の滑りや転がりは，触覚や物体の操作において重要な役割りを演じる．このような軟組織のトライボロジーに関しては今後の課題としたい．

著書

[1] Takahiro Inoue and Shinichi Hirai, *Mechanics and Control of Soft-fingered Manipulation*, Springer–Verlag, ISBN 978–1–84800–980–6, Jan., 2009.

論文

[1] Zhongkui Wang and Shinichi Hirai, *Modeling and Estimation of Rheological Properties of Food Products for Manufacturing Simulations*, Journal of Food Engineering, Vol.102, pp.136–144, 2011.

[2] Van Ho and Shinichi Hirai, *Modeling and Analysis of a Frictional Sliding Soft Fingertip, and Experimental Validations*, Advanced Robotics, Vol.25, No.3, pp. 291–311, 2011.

[3] Van Ho, Viet Dzung Dao, Susumu Sugiyama, Shinichi Hirai, *Development and Analysis of a Sliding Tactile Soft Fingertip Embedded with a Micro Force/Moment Sensor*, IEEE Transaction on Robotics, accepted for publication

[4] 森川 茂廣, 村山 浩之, 藤本 栄, 椎野 顯彦, 犬伏 俊郎, 栗林 秀人, パラレルイメージング用アレイコイルを利用した13C スペクトロスコピックイメージングの試み, 日磁医誌, Vol.31, pp.65–69, 2011.

[5] 平井 慎一, 物理世界と情報世界をつなぐソフトインターフェース, 日本ロボット学会誌, ロボティック・サイエンス論文特集号, Vol.28, No.4, pp.503–511, May, 2010.

[6] Amatsubo, T., Yanagisawa, D., Morikawa, S., Taguchi, H., and Tooyama, I., *Amyloid imaging using high-field magnetic resonance*, Magn Reson Med Sci, Vol.9, pp.95–99, 2010.

[7] Zhongkui Wang, Kazuki Namima, and Shinichi Hirai, *Physical Parameter Identification of Uniform Rheological Deformation Based on FE Simulation*, 生体医工学, Vol.47, No.1, pp.1–6, 2009.

[8] 井上 貴浩, 平井 慎一, 柔軟指による把持物体の姿勢制御, 日本機械学会論文集C編, Vol.75, No.757, pp.2537–2546, Sept., 2009.

[9] 柴田 瑞穂, 太田 剛士, 平井 慎一, 摘み滑り動作を利用した布地の展開動作, 日本ロボット学会誌, Vol.27, No.9, pp.1029–1036, 2009.

[10] 井上 貴浩, 松井 俊樹, 平井 慎一, 視覚情報遅れを考慮した2指1自由度対ロボットハンドによる対向操り動作, 計測自動制御学会論文集, Vol.45, No.12, pp.678–687, Dec., 2009.

[11] Takahashi, S., Saruhashi, Y., Odate, S., Matsusue, Y., and Morikawa, S., *Percutaneous aspiration of spinal ventricle cysts using real-time magnetic resonance imaging and navigation*, Spine Vol.34, pp.629–634, 2009.

[12] Tokuda J., Morikawa S., Haque H.-A., Tsukamoto T., Matsumiya K., Liao H., Masamune K., and Dohi T., *Adaptive 4D MR Imaging for MRI-guided Therapy Using Navigator-Based Respiratory Signal*, Magn Reson Med Vol.59, pp.1051-1061, 2008.

国際会議

[1] Yujiro Yamazaki, Takahiro Inoue, and Shinichi Hirai, *Two-Phased Controller for a Pair of 2-DOF Soft Fingertips Based on the Qualitative Relationship between Joint Angles and Object Location*, Proc. IEEE Int. Conf. on Robotics and Automation, pp. 4294–4301, Anchorage, May 3–8, 2010.

[2] Van Ho, Viet Dzung Dao, Susumu Sugiyama, and Shinichi Hirai, *Design of a Small-Scale Tactile Sensor with Three Sensing Points for Using in Robotic Fingertips*, Proc. IEEE Int. Conf. on Robotics and Automation, pp. 4855-4860, Anchorage, May 3–8, 2010.

[3] Van Ho and Shinichi Hirai, *Two-Dimensional Dynamic Modeling of a Sliding Motion of a Soft Fingertip Focusing on Stick-To-Slip Transition*, Proc. IEEE Int. Conf. on Robotics and Automation, pp. 4315-4321, Anchorage, May 3–8, 2010.

[4] Takahiro Inoue and Shinichi Hirai, *Robotic Manipulation with Large Time Delay on Visual Feedback Systems*, IEEE/ASME Int. Conf. on Advanced Intelligent Mechatronics (AIM2010), Montreal, Canada, July 7–9, 2010.

[5] Mizuho Shibata, Tsuyoshi Ota, and Shinichi Hirai, *Robotic Unfolding of Hemmed Fabric using Pinching Slip Motion*, Int. Conf. on Advanced Mechatronics (ICAM2010), Suita, Japan, Oct. 4–6, 2010.

[6] Zhongkui Wang and Shinichi Hirai, *Modeling and Parameter Estimation of Rheological Objects for Simultaneous Reproduction of Force and Deformation*, 1st

Int. Conf. on Applied Bionics and Biomechanics (ICABB–2010), Venice, Italy, Oct. 14–16, 2010.

[7] Zhongkui Wang, Shinichi Hirai, *Modeling and Property Estimation of Japanese Sweets for Their Manufacturing Simulation*, IEEE/RSJ Int. Conf. on Intelligent Robots and Systems (IROS 2010), Taipei, Oct. 18–22, 2010.

[8] Takahiro Inoue, Shinichi Hirai, Daisuke Takizawa, *Modelless and Grasping-Forceless Control by Robotic Fingers Capable of Mechanically Coupled Movement*, IEEE/RSJ Int. Conf. on Intelligent Robots and Systems (IROS 2010), Taipei, Oct. 18–22, 2010.

[9] Penglin Zhang and Hirai Shinichi, *A Local Geometric Preserving Approach For Interior Deformation Fields Measurement From MR Volumetric Images of Human Tissues*, IEEE Int. Conf. on Robotics and Biomimetics (Robio 2010), pp.437–441, Tianjin, China, Dec. 14–18, 2010.

[10] Xubing Zhang, Shinichi Hirai and Penglin Zhang, *SURF and Spatial Association Correspondence for the Extraction and Matching of Feature Points from MR Images of Deformed Tissues*, IEEE Int. Conf. on Robotics and Biomimetics (Robio 2010), pp.448–453, Tianjin, China, Dec. 14–18, 2010.

[11] Zhongkui Wang and Shinichi Hirai, *Contact Modeling and Parameter Switching for Simultaneous Reproduction of Rheological Force and Deformation*, IEEE Int. Conf. on Robotics and Biomimetics (Robio 2010), pp.726–731, Tianjin, China, Dec. 14–18, 2010.

[12] Mizuho Shibata, Tsuyoshi Ota, and Shinichi Hirai, *Wiping Motion for Deformable Object Handling*, Proc. IEEE Int. Conf. on Robotics and Automation, pp.134–139, Kobe, May 12–17, 2009.

[13] Van Ho Anh, Viet Dzung Dao, Susumu Sugiyama, and Shinichi Hirai, *Analysis of Sliding of a Soft Fingertip Embedded with a Novel Micro Force/Moment Sensor: Simulation, Experiment, and Application*, Proc. IEEE Int. Conf. on Robotics and Automation, pp.889–894, Kobe, May 12–17, 2009.

[14] Zhongkui Wang, Kazuki Namima, and Shinichi Hirai, *Physical Parameter Identification of Rheological Object Based on Measurement of Deformation and Force*, Proc. IEEE Int. Conf. on Robotics and Automation, pp.1238–1243, Kobe, May 12–17, 2009.

[15] Takahiro Inoue and Shinichi Hirai, *Parallel–distributed Model in Three–dimensional Soft–fingered Grasping and Manipulation*, Proc. IEEE Int. Conf. on Robotics and Automation, pp.2092–2097, Kobe, May 12–17, 2009.

[16] Zhongkui Wang and Shinichi Hirai, *Modeling and Parameter Identification of Rheological Object Based on FE Method and Nonlinear Optimization*, IEEE/RSJ Int. Conf. on Intelligent Robots and Systems (IROS 2009), St. Louis, U.S.A., Oct. 11–15, 2009.

[17] Yujiro Yamazaki, Takaihro Inoue, and Shinichi Hirai, *Two–Phased Force and Coordinates Controller for a Pair of 2–DOF Soft Fingers*, IEEE Int. Conf. on Robotics and Biomimetics (Robio 2009), pp.931–937, Guilin, China, Dec. 19–23, 2009.

[18] Kazuki Namima, Zhongkui Wang, and Shinichi Hirai, *Simulation of Soft Fingertip Deformation under Contact and Rolling Constraints using FEM and CSM*, IEEE Int. Conf. on Robotics and Biomimetics (Robio 2009), pp.1585–1590, Guilin, China, Dec. 19–23, 2009.

[19] Shinichi Hirai, *Simulation of Deformation in Robotics* (Keynote Speech), Asia Simulation Conference 2009, Oct. 7, 2009.

[20] Morikawa, S., Haque, H.-A., Naka, S., Murakami, K., Kurumi, Y., Tani, T, and Inubushi, T., *An Optical and Electromagnetic Hybrid Tracking System for MR Image Guided Interventional Procedures*, ISMRM 17th Scientific Meeting and Exhibition, Honolulu, U.S.A., April 18–24, 2009.

[21] Yamaguchi, S., Satake, K., Shirai, Y., Tanaka, H. T., and Morikawa, S., *3-dimensional finite element method based needle insertion simulation considering needle tip shape*, 23rd Int. Cong. and Exh. Computer Assisted Radiology and Surgery (CARS) 2009, Berlin, Germany, June 23–27, 2009.

[22] Takahiro Inoue and Shinichi Hirai, *Task-selection Control by Thumb and Forefinger Based on Softfinger Contact*, Third Asia International Symposium on Mechatronics (AISM2008), Sapporo, August 27–31, 2008.

[23] Van Ho Anh, Viet Dzung Dao, Susumu Sugiyama, and Shinichi Hirai, *Force/Moment Sensing During Sliding Motion using a Micro Sensor Embedded in a Soft Fingertip*, Proc. 10th Int. Conf. on Control, Automation, Robotics and Vision (ICARCV 2008), Dec. 17-20, Hanoi, Vietnam, 2008.

[24] Yamaguchi, S., Morikawa, S., Shirai, Y., and Tanaka, H. T., *Modeling of Needle Insertion for Percutaneous Minimally Invasive Therapy*, 22nd Int. Cong. and Exh. Computer Assisted Radiology and Surgery (CARS 2008), Barcelona, Spain, June 25–28, 2008.

口頭発表

[1] Van Ho and Shinich Hirai, *Toward a Platform for Modeling and Simulating Dynamic Stick-Slip Transitions of Soft Fingertips*, 第 16 回ロボティクスシンポジア予稿集, pp.275–282, 指宿, March 14–15, 2011.

[2] 上本 宏明, 平井 慎一, 柔軟 3 指による把持対象物の姿勢制御, ロボティクス・メカトロニクス'10 講演会予稿集 CD–ROM, 旭川, June 15–16, 2010.

[3] 井上 貴浩, 滝澤 大祐, 平井 慎一, 指関節連動運動を備えた 2 指多自由度ロボットハンドによる物体姿勢非ヤコビ制御, ロボティクス・メカトロニクス'10 講演会予稿集 CD–ROM, 旭川, June 15–16, 2010.

[4] 上本 宏明, 平井 慎一, 柔軟 3 指の配置が把持対象物の姿勢角制御に与える影響, 日本ロボット学会, 名古屋, Sept. 22–24, 2010.

[5] 平井 慎一, ソフトインターフェースによる機構と制御の単純化, 日本ロボット学会, 名古屋, Sept. 22–24, 2010.

[6] Zhongkui Wang and Shinichi Hirai, *Finite Element Modeling of Rheological Objects for Simultaneously Reproducing their Deformation and Force Behaviors*, 6th Joint Workshop on Machine Perception and Robotics (MPR2010), Fukuoka, Oct. 8–9, 2010.

[7] Xubing Zhang, Shinichi Hirai, and Penglin Zhang, *The Feature Points Matching of Non-rigid Tissues Based on SURF, Spatial Association Correspondence and Clustering: Application to MR 2-D Slice Deformation Measurement*, 6th Joint Workshop on Machine Perception and Robotics (MPR2010), Fukuoka, Oct. 8–9, 2010.

[8] 森川 茂廣, 村山 浩之, 藤本 栄, 椎野 顯彦, 犬伏 俊郎, 栗林 秀人, 実験動物での肝臓 T1 強調画像撮像のための一工夫, 第 38 回日本磁気共鳴医学会大会, つくば市, 9/30–10/2, 2010.

[9] 森川 茂廣, 村山 浩之, 藤本 栄, 椎野 顯彦, 犬伏 俊郎, 栗林 秀人, パラレルイメージング用アレイコイルを利用した 13C スペクトロスコピックイメージングの試み, 第 38 回日本磁気共鳴医学会大会, つくば市, 9/30–10/2, 2010.

[10] 中川 智史, 山口 哲, 平井 慎一, 田中 弘美, 連続体力学に基づくオンラインリメッシュ型変形シミュレーション, 情報処理学会 第 71 回全国大会, Kusatsu, March 10–12, 2009.

[11] Zhongkui Wang and Shinichi Hirai, *Parameter Estimation of Rheological Object Based on FE Simulation and Nonlinear Optimization*, 5th Joint Workshop on Machine Perception and Robotics (MPR2009), Kyoto, Oct. 4–5, 2009.

[12] Yoshiyuki Abe, Zhongkui Wang, Kazuki Namima, Shigehiro Morikawa, and Shinichi Hirai, *Inner Displacement Measurement of Grasping by Robotic Hand*, 5th Joint Workshop on Machine Perception and Robotics (MPR2009), Kyoto, Oct. 4–5, 2009.

[13] 阿部 慶之, 平井 慎一, ロボットハンドによる把持の内部変位計測, 計測自動制御学会システムインテグレーション部門学術講演会, pp.625–628, 豊洲, Dec. 24–26, 2009.

[14] 井上 貴浩, 滝澤 大佑, 谷川 弘典, 平井 慎一, 指節骨連動運動を実現する腱駆動 2 指ハンドの設計, 計測自動制御学会システムインテグレーション部門学術講演会, pp.1371–1373, 豊洲, Dec. 24–26, 2009.

[15] 土井 健人, 常俊 顕三, 菊田 健一郎, 森川 茂廣, 犬伏 俊郎, 超高磁場 MRI によるマウス脳血管評価, 第 34 回日本脳卒中学会総会, 松江, 3/20-22, 2009.

[16] Zhongkui Wang and Shinichi Hirai, *Physical Parameter Identification of Uniform Rheological Deformation through FE Model Simulation*, ロボティクス・メカトロニクス'08 講演会予稿集 CD–ROM, Nagano, June, 2008.

[17] 井上 貴浩, 平井 慎一, 摘みタスクにおける非ヤコビ制御, 精密工学会　知能メカトロニクスワークショップ, 高松, Sept., 2008.

[18] 平井 慎一, 井上 貴浩, 柔軟指による三次元把持と操作, 第 26 回日本ロボット学会学術講演会予稿集 CD-ROM, 神戸, Sept., 2008.

[19] Zhongkui Wang, Kazuki Namima, Shinichi Hirai, *Physical Parameter Identification of Isotropic Uniform Deformation Based on FE Simulation*, 生体医工学シンポジウム 2008 (BMES2008), Toyonaka, Sept., 2008.

[20] 浪間 一希, 王 忠奎, 平井 慎一, アクティブ虚血ダイナミクスのシミュレーション, 生体医工学シンポジウム 2008 (BMES2008), Toyonaka, Sept., 2008.

[21] Zhongkui Wang and Shinichi Hirai, *Physical Parameter Identification of Rheological Object Based on FE Dynamic Model*, 4th Joint Workshop on Machine Perception and Robotics (MPR2008), Beijing, China, November, 2008.

[22] 山崎 雄二郎, 平井 慎一, 拡張二段階法による把持物体の位置姿勢制御, 計測自動制御学会システムインテグレーション部門学術講演会, pp.319–320, 2008.

[23] 森川 茂廣, 腹部外科領域の術中 MR 画像 (特別講演), 第 8 回日本脳神経外科術中画像研究会, 大阪, 7/26, 2008.

目 次

第1章　軟組織の変形モデリングと力学パラメータ推定

1.1　緒言

1.1.1　柔軟物のモデリング

There are many deformable objects in our daily life, such as human organs and tissues, pottery, clay, and various food products. Modeling and simulation of such deformable objects has been studied for over 20 years and many applications have been involved, including computer aided surgery, food automation, and robot manipulation. In our definition, deformable objects were roughly divided into three categories (Fig. 1.1): elastic object, in which the deformation is completely reversible; plastic object, in which the deformation is completely maintained; and rheological object, in which the deformation is partially reversible.

Early work on the modeling of deformable objects can date back to [1] and [2]. They have shown the advantages of physically-based models over kinematic models for computer animation and have proposed several physically-based models for simulating inelastic deformation. Generally, a physically-based model consists of a finite numbers of elastic and viscous elements connected in a certain configuration. Some famous physically-based models, such as the Maxwell model[1], the Kelvin-Voigt model[2], the Lethersich model[3], and the Burgers model[4] (Fig. 1.2), were often used to describe the behaviors of deformable materials. In conventional material tests, *e.g.*, force relaxation and creep recovery tests, one-dimensional (1D) models were used to describe the behaviors of materials. However, along with the developments of computer, we are able to reconstruct an object with two-dimensional (2D) and

[1]It was introduced by J. C. Maxwell in 1867.
[2]It was firstly introduced by L. Kelvin in 1875 and later by W. Voigt in 1889.
[3]It was firstly introduced by W. Lethersich in 1942.
[4]It was firstly introduced by J. M. Burgers in 1935.

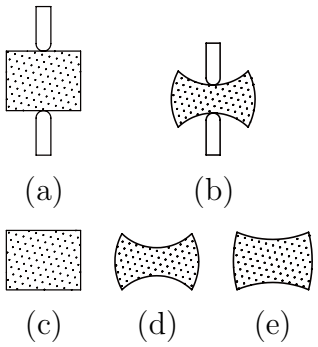

図 1.1: Categories of deformable objects. (a) Original shape before pushing. (b) Deformed shape during manipulation. (c), (d), and (e) Deformed shape after releasing. (c) Elastic object. (d) Plastic object. (e) Rheological object.

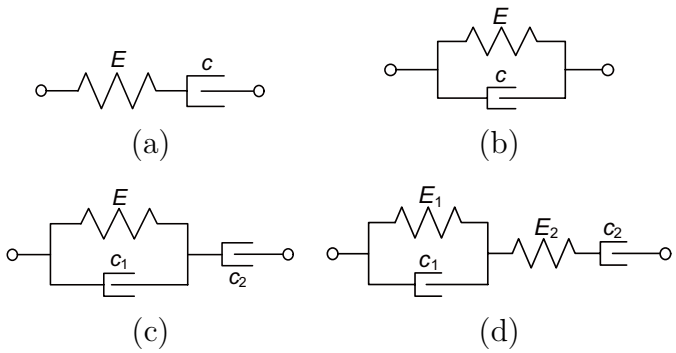

図 1.2: Widely used physically-based models: (a) the Maxwell model, (b) the Kelvin-Voigt model, (c) the Lethersich model, and (d) the Burgers model.

three-dimensional (3D) geometry to achieve more realistic simulation behaviors of deformable objects.

The most popular methods for 2D and 3D modeling of deformable objects are the mass-spring-damper (MSD) method [3] and the finite element method (FEM) [4]. The MSD method has been used to simulate cloth animation [5], facial expressions [6], and the deformation of a myoma (pathology) [7], respectively. The MSD method has the advantage of conceptual simplicity and relatively low computation costs. However, the formulation of MSD method was not based on continuum mechanics and the simulation accuracy is quite limited. Therefore, a finite element (FE) model has been used as a reference to calibrate MSD model based on genetic algorithm optimization [8] and analytical expression [7], respectively.

The FE method has proven to be a powerful tool for simulating complex behaviors

of deformable objects. In FE formulation, an object is described by a set of elements (*e.g.*, triangles in 2D case and tetrahedrons in 3D case). The dynamic behaviors of the object are then determined by analyzing the behaviors of individual elements. In recent years, many commercial FE softwares are available and more and more researchers have been using FE method in their applications. The FE method has been widely used in computer-aided surgery to simulate the deformation behaviors of biological organs and tissues, such as porcine liver [9], human skin [10], liver [11], and uterus [12]. It currently also was employed to model some surgical operations, such as needle insertion [13] and soft tissue cutting [14]. FE method is based on continuum mechanics and does not suffer from geometry problems. But, it is quite time-consuming. In order to speed up FE simulation, matrix condensation technology [15] and fast FEM [16] have been proposed. Current parallel calculation architecture, such as graphics processing unit (GPU), also has been investigated by [17]. In addition, to achieve real-time simulation of soft tissue, other modeling methods were also presented, such as the radial elements method [18] and the point collocation-based method of finite spheres [19]. The FEM also has been used in food industry to model food products. For example, FE analysis has been used to model and simulate the indentation of bread crumbs [20]; FE simulation has been used to evaluate the dependence of temperature and water content on process time during meat cooking [21]; and FE method also has been employed to calculate food quality and safety losses during processing, storage and distribution [22].

To date, the modeling of soft organs and tissues mostly supposed that the organs and tissues are completely recoverable and the deformation behaviors after unloading operations are not considered in most applications. Some organs and tissues, however, may fail to totally recover from the deformation after loading-unloading operations. [23] found that porcine brain tissue did not recover completely after a loading-unloading cycle. In vivo experimental results showed that residual deformation may also present in human liver [11]. In addition, residual deformation may also exist when biological organs and tissues suffer from some diseases or undergoing a significant external forces. Such residual deformations could be handled by rheological models. On the other hand, modeling and property estimation of food materials were studied so far mainly on the chemical and ingredient composition point of view for improving the cooking ability, product quality, and nutrition. As an "engineering material", however, it was not well developed. [24] stated that the most critical barrier against the application of robotics and automation in food industry is a lack of

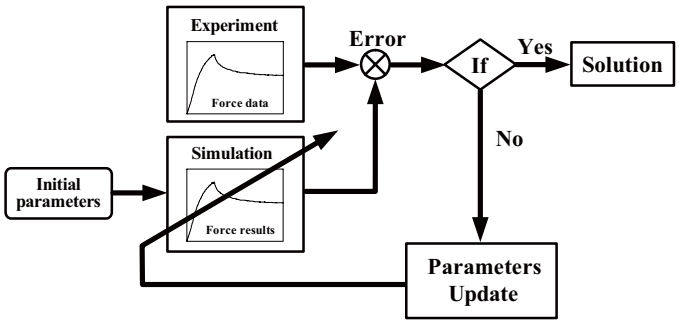

図 1.3: Optimization process for parameter estimation.

understanding of the food product properties as an "engineering" material for handling operations. We have therefore turn our attention on the modeling, simulation, and parameter estimation of rheological objects, especially considering the residual deformations which has not been studied intensively.

1.1.2 柔軟物の力学パラメータの推定

Before simulating any real objects, some physical parameters of the model have to be available in advance. In conventional material science, material properties were usually estimated by direct calculation or curve fitting based on the measurements of experimental tests, such as compressive, tensile, force relaxation, and creep recovery tests [25]. However, these calculations and tests were mostly under an assumption of 1D deformation (pure uniaxial or pure shear deformation). Deformable objects, on the other hand, have more complex deformation behaviors and sometimes include several different material properties. Therefore, they have to be simulated as a 2D/3D continuum and complex deformation behaviors have to be considered during parameter estimation. It is a quite challenging work to estimate physical parameters for accurately reproducing the behaviors of deformable objects.

So far, the most popular method used in estimating physical parameters of deformable objects is simulation-based optimization, *i.e.*, the simulation is iterated with updated physical parameters until the difference between the simulation and experiment becomes minimal, as shown in Fig. 1.3. Using this method, many work has been done. For example, [12] characterized human uteri in vivo through an aspiration experiment; [13] investigated the force behaviors during the insertion of a needle into a porcine liver; [26] developed a robotic indenter for minimally invasive

measurements and characterized the material properties of pig liver; [9] characterized a porcine liver by indentation experiments with various indentation depths and two different tip shapes; [27] performed a compression test inside a magnetic resonance imaging (MRI) system and estimated the material properties of a layered soft tissue; [28] investigated the physical parameters of pig heart based on cyclical inflation experiments and MRI tagged images with simultaneous pressure recordings; and [29] calibrated a food dough which was simulated by a hierarchical MSD model. In order to accomplish the optimization problem of the estimation method, many optimization algorithms have been used, such as Levenberg-Marquardt method [12], sequential quadratic programming (SQP) [28], genetic algorithm (GA) [29] and extended Kalman filter [30]. The optimization-based estimation method is quite robust and works well with different models. However, this method is time-consuming since it is based on iterative simulations.

Direct calculation and curve fitting methods have also been used to estimate physical parameters of deformable objects. [31] have performed a series of compressive and shear tests on pig kidney and estimated its physical parameters by using curve fitting. [32] formulated a "Norimaki-sushi" by a 2-layered Maxwell model and directly calculated its physical parameters by using least squares method based on the measurements of force and displacements. In order to well capture the force response during the grasping of the "Norimaki-sushi", [33] used a Fung's viscoelastic model to describe the force behaviors of the sushi and employed curve fitting method to determine the physical parameters. Direct calculation or curve fitting method for estimating parameters are efficient since no simulation was involved. However, this method needs the analytical expressions of force or displacement, which are not always available. Therefore, such method is not always applicable. In this dissertation, both simulation-based and calculation-based methods will be discussed and mixed together to achieve better reproductions of both force and deformation simultaneously.

1.1.3 レオロジー物体のモデリングとパラメータ推定

Rheological object has both elastic and plastic properties. Generally, it is more difficult to model a rheological object than model an elastic object due to the presence of residual deformation. Early work on the modeling of rheological objects was started by [2], who have employed a Burgers model to describe rheological be-

haviors. However, it is only a conceptual description and no simulation results and information of parameter determination were given. A plenty of work on modeling and parameter estimation of rheological objects has been done by [34], who have employed a Lethersich model and MSD method to construct a food dough, a typical rheological object [35]. They investigated three different mesh configurations: the lattice [36], the truss [37], and the hierarchical [29] structures, with decreased MSD elements connected between nodal points to reduce the computation cost. Two optimization methods, modified randomized algorithm [34] and genetic algorithm [29], were used to estimate the physical parameters. As we mentioned above, the MSD model has an advantage of low computation cost but the simulation accuracy is quite limited and the physical parameters are dependent on mesh configuration and resolution. A two-layered Maxwell model [32] and a Fung's viscoelastic model [33] have been used respectively to reproduce the force response of a sushi when grasped by a robot hand. Good approximations of force behaviors were obtained. However, both models are still 1D models. In addition, the ISU exoskeleton technique has been used in modeling clay to simulate an interaction between virtual clay and a human finger [38].

Interestingly, most above-mentioned work of rheological objects modeling has focused on either reproduction of deformation alone [34], [37], [35], [36], [29] or reproduction of force alone [32], [33]. Reproduction of both force and deformed shapes of a food dough has been studied by [39] with a MSD model. Experimental results suggested that shape calibration (parameter estimation by minimizing the difference of deformed shape) could only yield good shape reproduction and force calibration only resulted in good force reproduction. It is impossible to reproduce both force and deformed shape simultaneously by using one set of parameters. However, they did not mention the reason of this impossibility and how to solve it. This will be the main concern of this dissertation.

On the other hand, rheological properties of food materials were frequently studied in food engineering. Many instruments have been developed to measure rheological properties, such as rheometer, farinograph, and dynamic oscillator, as reviewed by [40]. [41] have used a farinograph and a rheometer to assess the rheological properties of various types of rice dough to determine their suitability for making rice bread. [42] have investigated the use of extrusion cooking on pastes by estimating the dynamic rheological properties of extruded flaxseed-maize pastes through dynamic oscillation and creep-recovery tests. However, properties tests and behavior models on food

materials are usually carried out in 1D condition and mainly focusing on chemical and ingredient composition. Our work has been motivated from an engineering point of view for grasping and manipulating of rheological objects. Therefore, the object or material investigated in this dissertation basically has a 2D or 3D shape and the deformed shapes are always of concern.

1.1.4 まとめ

As discussed above, the modeling of rheological objects has not been well developed and mostly is based on MSD modeling method or with a 1D assumption. An effective approach for estimating physical parameters of rheological objects has also not been well established. To our knowledge, the residual (permanent) deformation after loading-unloading operation has not been taken into consideration during the modeling and parameter estimation of rheological objects so far. The residual deformation might be important in some situations where the desired shape is needed without any damage. The aim of this dissertation is the determination of appropriate models for simulating rheological objects and of their physical parameters in order to reproduce both rheological force and deformation behaviors simultaneously. In other words, we hope that our present work is able to help us to understand rheological behaviors and to choose an appropriate model and parameters for accurately capturing those behaviors, such as force response, deformed shapes, and final recovered shapes. Possible application fields of our present work may include surgical simulation, food engineering, and robot manipulation.

1.2 力学モデル

Physically-based models are often employed to describe deformable materials and objects, *e.g.*, an elastic element (Fig. 1.4a) and a viscous element (Fig. 1.4b) represent ideal elastic and viscous material, respectively. Note that the deformation generated in an elastic element is completely recoverable while the deformation generated in a viscous element will be totally maintained after loading-unloading operations. An elastic and a viscous elements connected in series is called a Maxwell element (Fig. 1.4c), which denotes a simplest rheological material. An elastic and a viscous elements connected in parallel is called a Kelvin (or Kelvin-Voigt) element

(Fig. 1.4d), which denotes a visco-elastic material. We shall call the above four elements as basic elements (Fig. 1.4). By connecting several basic elements in different configurations, many physically-based models can be obtained for simulating rheological behaviors. We categorized such models into two groups: serial and parallel models, as shown in Fig. 1.5.

1.2.1 一般直列モデル

A serial rheological model consists of numbers of Kelvin elements and a viscous or a Maxwell element connected in series. Note that the deformation generated in an elastic or a Kelvin element is completely recoverable. Therefore, a serial rheological model must include a viscous element connected in series, which causes the residual (permanent) deformation. According to the presence of elastic element, serial models can be further divided into two types, as shown in Fig. 1.6. Let us take the serial model of type 1 (Fig. 1.6(a)) as an example to show the derivation procedure of the constitutive law.

Note that the constitutive law of four basic elements can be formulated as:

$$\begin{aligned} \text{Elastic element}: &\quad \sigma = E\epsilon, \\ \text{Viscous element}: &\quad \sigma = c\dot{\epsilon}, \\ \text{Maxwell element}: &\quad \dot{\sigma} + \frac{E}{c}\sigma = E\dot{\epsilon}, \\ \text{Kelvin element}: &\quad \sigma = E\epsilon + c\dot{\epsilon}, \end{aligned} \tag{1.1}$$

Let ϵ_i and ϵ_{n+1} be the strain at the i-th Kelvin element and the $(n+1)$-th viscous element, respectively, in type 1 serial model. Let E_i and c_i be the Young's modulus

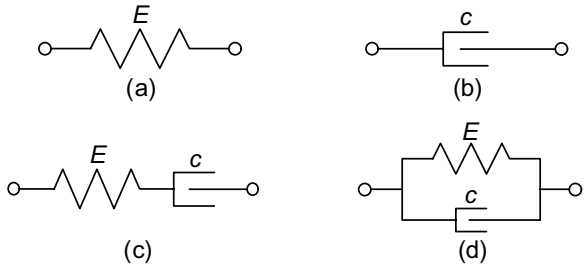

図 1.4: The basic elements for describing deformable materials: (a) the elastic; (b) the viscous; (c) the Maxwell; and (d) the Kelvin elements.

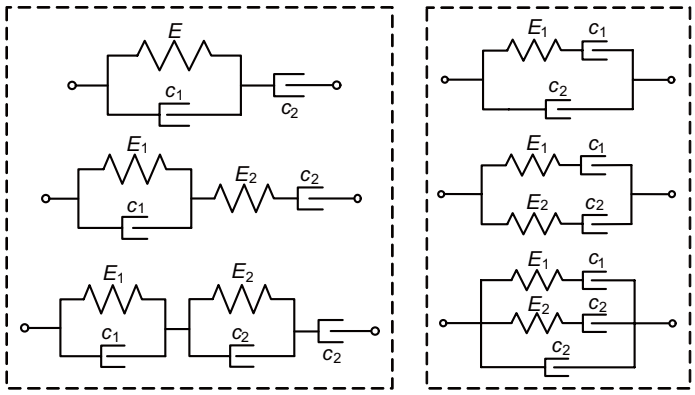

図 1.5: Two groups of rheological physically-based models: (a) serial models, and (b) parallel models.

and viscous modulus of the i-th elastic and viscous elements, respectively. Due to the serial connections among these basic elements, the total stress at the serial model is equal to the stress at each basic element and the total strain at the serial model is equal to the summation of the strain at each basic element. That is,

$$\begin{aligned} \sigma &= E_i \epsilon_i + c_i \dot{\epsilon}_i, \quad 1 \leq i \leq n, \\ \sigma &= c_{n+1} \dot{\epsilon}_{n+1}, \\ \epsilon &= \sum_{i=1}^{n+1} \epsilon_i. \end{aligned} \tag{1.2}$$

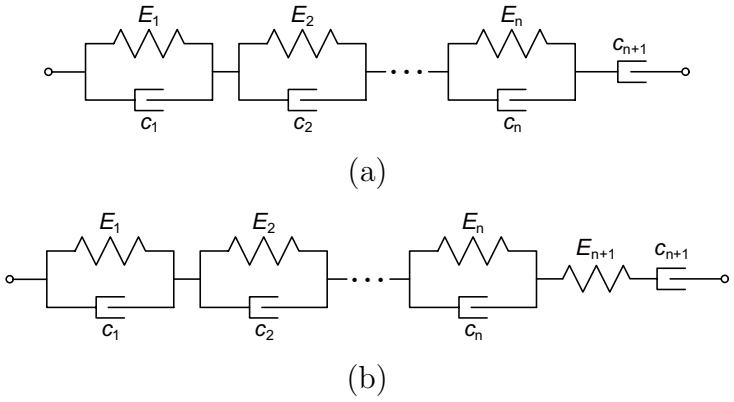

図 1.6: Generalized serial models: (a) type 1, and (b) type 2.

Taking Laplace transform of the above equations, we have

$$\begin{aligned}
\sigma(s) &= E_i\epsilon_i(s) + c_i s\epsilon_i(s), \quad 1 \le i \le n, \\
\sigma(s) &= c_{n+1} s\epsilon_{n+1}(s), \\
\epsilon(s) &= \sum_{i=1}^{n+1} \epsilon_i(s).
\end{aligned} \tag{1.3}$$

Eliminating $\epsilon_i(s)$ from the above equations, we then have

$$\epsilon(s) = \Big[\big(\sum_{i=1}^{n} \frac{1}{s+r_i}\frac{1}{c_i}\big) + \big(\frac{1}{s}\frac{1}{c_{n+1}}\big)\Big]\sigma(s), \tag{1.4}$$

where $r_i = E_i/c_i$. Let us define a polynomial as below:

$$\prod_{i=1}^{n}(s+r_i) = A_n s^n + A_{n-1}s^{n-1} + \cdots + A_1 s + A_0. \tag{1.5}$$

The coefficients of the above polynomial have the forms of:

$$\begin{aligned}
A_n &= 1, \\
A_{n-1} &= \sum_{i=1}^{n} r_i, \\
A_{n-2} &= \sum_{i=1}^{n}\sum_{\substack{j=1 \\ j\neq i}}^{n} r_i r_j, \\
A_{n-3} &= \sum_{i=1}^{n}\sum_{\substack{j=1 \\ j\neq i}}^{n}\sum_{\substack{k=1 \\ k\neq i \\ k\neq j}}^{n} r_i r_j r_k, \\
&\cdots \\
A_0 &= \prod_{i=1}^{n} r_i.
\end{aligned} \tag{1.6}$$

Multiplying Eq. 1.4 by Eq. 1.5, we have

$$\begin{aligned}
\prod_{i=1}^{n}(s+r_i)\epsilon(s) &= \prod_{i=1}^{n}(s+r_i)\Big[\big(\sum_{i=1}^{n} \frac{1}{s+r_i}\frac{1}{c_i}\big) + \big(\frac{1}{s}\frac{1}{c_{n+1}}\big)\Big]\sigma(s) \\
&= \Big[\sum_{i=1}^{n}\prod_{\substack{j=1 \\ j\neq i}}^{n}\frac{(s+r_j)}{c_i} + \prod_{j=1}^{n}\frac{s+r_j}{s}\frac{1}{c_{n+1}}\Big]\sigma(s).
\end{aligned} \tag{1.7}$$

We then find the following equation:

$$\begin{aligned}\prod_{\substack{j=1\\j\neq i}}^{n}(s+r_j) &= (s+r_1)\cdots(s+r_{i-1})(s+r_{i+1})\cdots(s+r_n)\\ &= s^{n-1}+B_{i,1}s^{n-2}+\cdots+B_{i,n-2}s+B_{i,n-1},\end{aligned} \tag{1.8}$$

where

$$\begin{aligned}B_{i,1} &= \sum_{\substack{j=1\\j\neq i}}^{n} r_j,\\ B_{i,2} &= \sum_{\substack{j=1\\j\neq i}}^{n}\sum_{\substack{k=1\\k\neq i\\k\neq j}}^{n} r_j r_k,\\ B_{i,3} &= \sum_{\substack{j=1\\j\neq i}}^{n}\sum_{\substack{k=1\\k\neq i\\k\neq j}}^{n}\sum_{\substack{l=1\\l\neq i\\l\neq j\\l\neq k}}^{n} r_j r_k r_l,\\ &\cdots\\ B_{i,n-1} &= \prod_{\substack{j=1\\j\neq i}}^{n} r_j.\end{aligned} \tag{1.9}$$

Substituting Eqs. 1.5 and 1.8 into Eq. 1.7, we have the following Laplace transform equation:

$$\begin{aligned}&(A_n s^{n+1}+A_{n-1}s^n+\cdots+A_0 s)\epsilon(s)\\ &\qquad = (B_n^{s1}s^n+B_{n-1}^{s1}s^{n-1}+\cdots+B_1^{s1}s+B_0^{s1})\sigma(s),\end{aligned} \tag{1.10}$$

where

$$\begin{aligned} B_n^{s1} &= \sum_{i=1}^{n} \frac{1}{c_i} + \frac{A_n}{c_{n+1}}, \\ B_{n-1}^{s1} &= \sum_{i=1}^{n} \frac{B_{i,1}}{c_i} + \frac{A_{n-1}}{c_{n+1}}, \\ &\cdots \\ B_1^{s1} &= \sum_{i=1}^{n} \frac{B_{i,n-1}}{c_i} + \frac{A_1}{C_{n+1}}, \\ B_0^{s1} &= \frac{A_0}{c_{n+1}}. \end{aligned} \tag{1.11}$$

Applying the inverse Laplace transform to Eq. 1.10 yields the constitutive law of serial model of type 1 as follows:

$$\sum_{i=1}^{n+1} A_{i-1} \frac{\partial^i \epsilon}{\partial t^i} = \sum_{j=0}^{n} B_j^{s1} \frac{\partial^j \sigma}{\partial t^j}. \tag{1.12}$$

Note that the highest-order derivative of strain ϵ is one order larger than the highest-order of stress σ. In addition, there is no constant term in the coefficients of strain polynomial (the subscript i starts from 1 in the left side of Eq. 1.12).

Following the same derivation procedure, we can obtain the constitutive law of serial model of type 2 as follows:

$$\sum_{i=1}^{n+1} A_{i-1} \frac{\partial^i \epsilon}{\partial t^i} = \sum_{j=0}^{n+1} B_j^{s2} \frac{\partial^j \sigma}{\partial t^j}, \tag{1.13}$$

where

$$\begin{aligned} B_{n+1}^{s2} &= \frac{1}{E_{n+1}}, \\ B_n^{s2} &= \sum_{i=1}^{n} \frac{1}{c_i} + \frac{A_n}{c_{n+1}} + \frac{A_{n-1}}{E_{n+1}}, \\ B_{n-1}^{s2} &= \sum_{i=1}^{n} \frac{B_{i,1}}{c_i} + \frac{A_{n-1}}{c_{n+1}} + \frac{A_{n-2}}{E_{n+1}}, \\ &\cdots \\ B_0^{s2} &= \frac{A_0}{c_{n+1}}. \end{aligned} \tag{1.14}$$

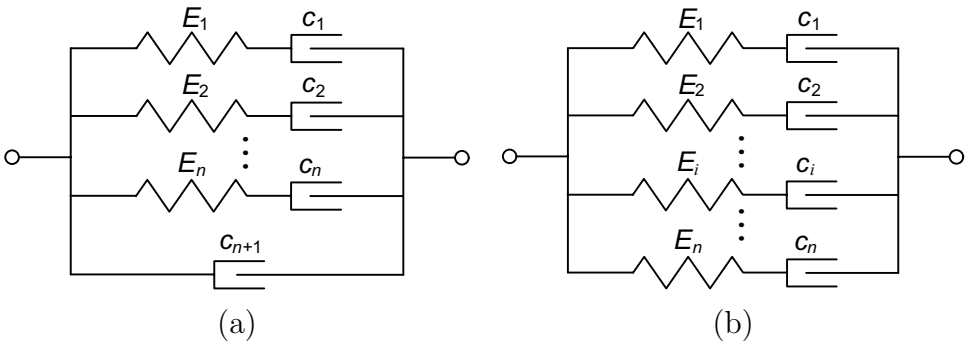

図 1.7: Generalized parallel models: (a) type 1; and (b) type 2.

Equation 1.13 indicates that the highest-order derivative of strain ϵ is equal to the highest-order of stress σ. Note that the left side of Eq. 1.13 has the same form with the left side of Eq. 1.12.

1.2.2 一般並列モデル

Two kinds of parallel rheological models were shown in Fig. 1.7. Due to the parallel connections among basic elements, the total strain at the parallel model is equal to the strain at each basic element and the total stress at the parallel model is equal to the summation of the stress at each basic element. For parallel model of

表 1.1: The constitutive laws of generalized serial and parallel models

Models	Type	The constitutive law
Serial	1	$\sum_{j=0}^{n} B_j^{s1} \frac{\partial^j \sigma}{\partial t^j} = \sum_{i=1}^{n+1} A_{i-1} \frac{\partial^i \epsilon}{\partial t^i}$
	2	$\sum_{j=0}^{n+1} B_j^{s2} \frac{\partial^j \sigma}{\partial t^j} = \sum_{i=1}^{n+1} A_{i-1} \frac{\partial^i \epsilon}{\partial t^i}$
Parallel	1	$\sum_{i=0}^{n} A_i \frac{\partial^i \sigma}{\partial t^i} = \sum_{j=1}^{n+1} B_j^{p1} \frac{\partial^j \epsilon}{\partial t^j}$
	2	$\sum_{i=0}^{n} A_i \frac{\partial^i \sigma}{\partial t^i} = \sum_{j=1}^{n} B_j^{p2} \frac{\partial^j \epsilon}{\partial t^j}$

type 1, we therefore have

$$\begin{aligned} \dot{\sigma}_i + \frac{E_i}{c_i}\sigma_i &= E_i\dot{\epsilon}, \quad 1 \le i \le n, \\ \sigma_{n+1} &= c_{n+1}\dot{\epsilon}, \\ \sigma &= \sum_{i=1}^{n+1} \sigma_i. \end{aligned} \tag{1.15}$$

Following the same derivation with serial models, we can end up with the constitutive law of parallel model of type 1 (Fig. 1.7a) as follows:

$$\sum_{i=0}^{n} A_i \frac{\partial^i \sigma}{\partial t^i} = \sum_{j=1}^{n+1} B_j^{p1} \frac{\partial^j \epsilon}{\partial t^j}, \tag{1.16}$$

where

$$\begin{aligned} B_{n+1}^{p1} &= c_{n+1}, \\ B_n^{p1} &= \sum_{i=1}^{n} E_i + A_{n-1}c_{n+1}, \\ B_{n-1}^{p1} &= \sum_{i=1}^{n} B_{i,1}E_i + A_{n-2}c_{n+1}, \\ &\cdots \\ B_1^{p1} &= \sum_{i=1}^{n} B_{i,n-1}E_i + A_0 c_{n+1}. \end{aligned} \tag{1.17}$$

Correspondingly, the constitutive law of parallel model of type 2 (Fig. 1.7b) can be formulated as:

$$\sum_{i=0}^{n} A_i \frac{\partial^i \sigma}{\partial t^i} = \sum_{j=1}^{n} B_j^{p2} \frac{\partial^j \epsilon}{\partial t^j}, \tag{1.18}$$

where

$$\begin{aligned} B_n^{p2} &= \sum_{i=1}^{n} E_i, \\ B_{n-1}^{p2} &= \sum_{i=1}^{n} B_{i,1}E_i, \\ &\cdots \\ B_1^{p2} &= \sum_{i=1}^{n} B_{i,n-1}E_i. \end{aligned} \tag{1.19}$$

We summarize the constitutive laws of generalized serial and parallel models in Table 1.1, where Eqs. 1.12 and 1.13 are rearranged for convenient comparisons. We found that the constitutive law of serial model of type 1 has the identical form with the parallel model of type 1 except some coefficients having different formulations. Correspondingly, the constitutive laws of serial model of type 2 also has the same form with the parallel model of type 2 by replacing the summation limit $n+1$ by n. Note that same constitutive laws yield same deformation behaviors. Therefore, for simulating a certain behavior, we can use either a serial model or a parallel model. Actually, for any type of physically-based model, which consists of any numbers of basic elements connected in any configuration, we are always able to find one pair of serial and parallel models which are corresponding to each other and yield the same behaviors. This allows us to investigate only one kind of model instead of both for simulating a certain behaviors of deformable objects. In this dissertation, we mainly investigate the parallel models. In addition, according to Eq. 1.2, if the total stress at the serial model is available, we can easily obtain the strain at each basic element by solving a series of ordinary differential equations and therefore have the total strain by summing up the individual strain at each element. On the other hand, equation 1.15 indicates that the convenient calculation of rheological stress can be achieved by using the parallel models. This tells us how to choose a model between serial and parallel models. If you are interested in the calculation of deformation, you should use a serial model. On the contrary, you should go with parallel models if you have more concern with force behaviors. In this dissertation, we choose parallel models because the experimental measurements including continuous force responses and static images of deformed shapes. We suppose that the continuous deformation measurements are not available.

1.2.3 並列モデルの解析

レオロジー変形の特性

Typical rheological behaviors (force and deformed shapes) of commercial available clay and Japanese sweets material are shown in Figs. 1.8 and 1.9. Clays were bought from supermarket and were supposed to be played by children above 3 years old. The sweets materials were provided by OIMATU, a sweets company in Kyoto. Detailed experimental setup and results will be presented in Section 1.6. Our target is to find an appropriate model to simulate the rheological behaviors of these objects.

Normally, physical parameters of an object should keep the same even though its size may change or it may be deformed in different ways. This feature allows us to use a regular shaped object with simple tests to estimate the properties of the object. Such tests include the uniaxial compressive and tensile tests as used in material engineering. In our study, we conducted a compressive test with a pushing-holding-releasing procedure. We fashioned a 2D rheological object with a flat-squared shape. We firstly pushed the entire top surface of the object with a constant velocity to reach a desired displacement during time 0 to t_p, which was called pushing phase (Figs. 1.8(a) and 1.9(a)). During this phase, force was increasing with the deformation increasing. Before releasing, the deformed shape was maintained from time t_p to $t_p + t_h$. This time period was called holding phase and the deformed shape during this phase was called held-shape (Figs. 1.8(b) and 1.9(b)). In the holding phase, rheological force was decreasing (called force relaxation) in a nonlinear manner. After unloading, however, rheological force went to zero and the deformed shape were partially recovered. Figures 1.8 and 1.9 also indicate that rheological behaviors of different materials are quite different. Comparing with clay, the force relaxation behavior of sweets material is slower and the residual deformation is larger. Let us now investigate the ability of physically-based models for reproducing the above-mentioned rheological behaviors.

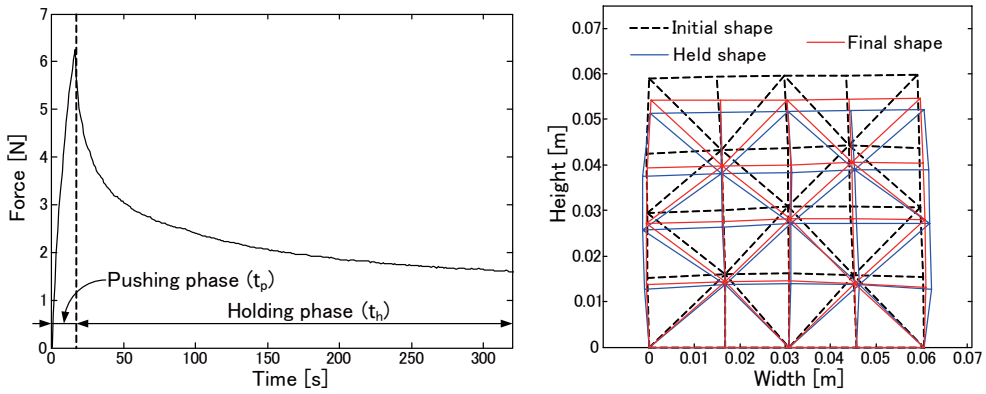

(a) (b)

図 1.8: Experimental measurements of commercial available clay: (a) force response, and (b) deformed shapes.

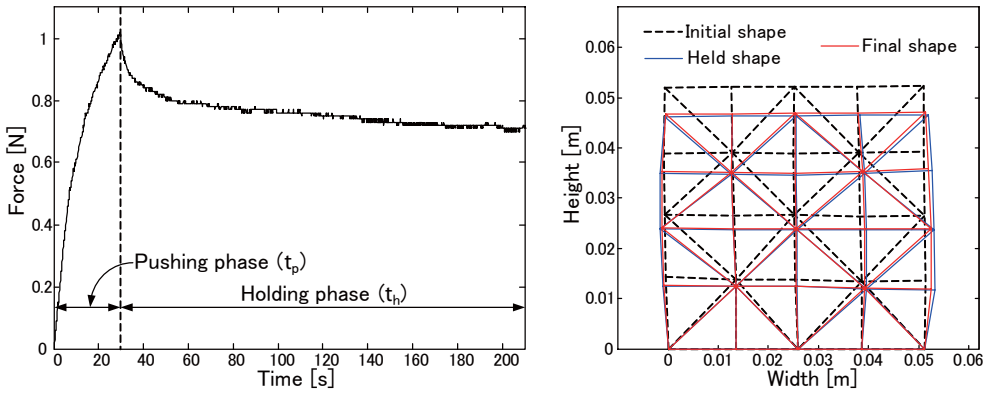

(a) (b)

図 1.9: Experimental measurements of Japanese sweets material: (a) force response, and (b) deformed shapes.

レオロジー変形における応力

We take the parallel model of type 1 as an example to show the derivations of analytical expressions of rheological stresses. During the pushing phase, the strain rate is constant, *i.e.*, $\dot{\epsilon} = p$. By solving Eq. 1.15, we have the analytical stress expression in the pushing phase as below:

$$\sigma(t) = \sum_{i=1}^{n} c_i p\big(1 - e^{-\frac{E_i}{c_i}t}\big) + c_{n+1}p, \quad (0 \leq t \leq t_p). \tag{1.20}$$

In the holding phase, solving Eq. (1.15) with $\dot{\epsilon} = 0$ and initial condition of $\sigma_i(t_p)$, we can formulate the analytical stress expression in this phase as:

$$\sigma(t) = \sum_{i=1}^{n} c_i p\big(1 - e^{-\frac{E_i}{c_i}t_p}\big)e^{-\frac{E_i}{c_i}(t-t_p)}, \quad (t_p \leq t \leq t_p + t_h). \tag{1.21}$$

レオロジー変形における残留歪み

After unloading, we intuitively consider to solve the constitutive law Eq. 1.16 with $\sigma = 0$ to formulate the strain recovering profile over time. Unfortunately, when the order of time derivative of strain ϵ exceeds two, it becomes impossible to solve Eq. 1.16 because we have no information about the initial condition of strain derivatives. Therefore, we turn our attention to focus on each viscous element. Let $\epsilon_i^{ela}(t)$ and $\epsilon_i^{vis}(t)$ be the strain at each elastic and viscous element, respectively. Note that the

stress at a Maxwell element is equal to the stress at the elastic element and the viscous element as well. Thus, total stress after unloading can be formulated as:

$$\sigma(t) = \sum_{i=1}^{n+1} \sigma_i(t) = \sum_{i=1}^{n} c_i \dot{\epsilon}_i^{vis}(t) + c_{n+1}\dot{\epsilon}(t) = 0. \tag{1.22}$$

Integrating the above equation from time $t_p + t_h$ to time infinite, we have

$$\sum_{i=1}^{n} c_i \int_{t_p+t_h}^{\infty} \dot{\epsilon}_i^{vis}(t)\mathrm{d}t + c_{n+1} \int_{t_p+t_h}^{\infty} \dot{\epsilon}(t)\mathrm{d}t = 0, \tag{1.23}$$

and thus

$$\sum_{i=1}^{n} c_i \big[\epsilon_i^{vis}(\infty) - \epsilon_i^{vis}(t_p + t_h)\big] + c_{n+1}\big[\epsilon(\infty) - \epsilon(t_p + t_h)\big] = 0. \tag{1.24}$$

It is important to note that the residual strain at every viscous element in a parallel model should be the same and equal to the total residual strain when time goes to infinite, *i.e.,* $\epsilon_1^{vis}(\infty)$=$\epsilon_2^{vis}(\infty)$=$\cdots$=$\epsilon_n^{vis}(\infty)$=$\epsilon(\infty)$, because all elastic elements completely recovered from the deformation. Thus, equation 1.24 yields

$$\epsilon(\infty) = \sum_{i=1}^{n} \frac{c_i \epsilon_i^{vis}(t_p + t_h)}{\sum_{j=1}^{n+1} c_j} + \frac{c_{n+1}\epsilon(t_p + t_h)}{\sum_{j=1}^{n+1} c_j}. \tag{1.25}$$

In addition, each viscous element has its own constitutive law as σ_i=$c_i\dot{\epsilon}_i^{vis}$. Integrating it through time 0 to time $t_p + t_h$ and rearranging it, we have

$$\epsilon_i^{vis}(t_p + t_h) = \frac{1}{c_i} \int_0^{t_p+t_h} \sigma_i(t)\mathrm{d}t. \tag{1.26}$$

Substituting Eq. 1.26 into Eq. 1.25 and considering $\sigma(t) = \sum_{i=1}^{n+1} \sigma_i(t)$, we finally end up with the expression of total residual strain as:

$$\epsilon(\infty) = \frac{1}{\sum_{i=1}^{n+1} c_i} \int_0^{t_p+t_h} \sigma(t)\mathrm{d}t. \tag{1.27}$$

This equation indicates that the final residual strain in a parallel model is dominated by the summation of viscous moduli and the integration of force through the pushing and holding phase.

For the parallel model of type 2, we can obtain the same formulation of stress expression in the holding phase and the same formulation of final residual strain

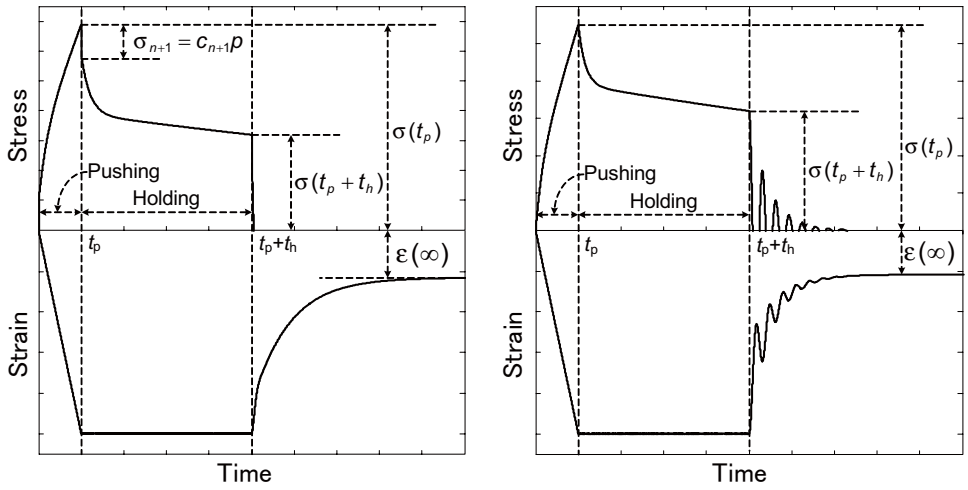

図 1.10: Typical simulation results of rheological behaviors by using: (a) 5-element model, and (b) 2-layered Maxwell model.

with the summation limit $n+1$ replaced by n in Eq. 1.27. The only difference of the parallel model of type 2 is the stress expression in the pushing phase, which is

$$\sigma(t) = \sum_{i=1}^{n} c_i p\big(1 - e^{-\frac{E_i}{c_i}t}\big), \quad (0 \le t \le t_p). \tag{1.28}$$

Typical simulation results of rheological stress and strain were shown in Fig. 1.10 by using a five-element model (the last row of Fig. 1.5(b)) and a two-layered Maxwell model (the middle row of Fig. 1.5(b)). According to Eqs. 1.20, 1.21, and 1.28, we find that the stress curve can be determined by viscous moduli c_i and time coefficients E_i/c_i of exponential functions. The coefficients E_i/c_i dominate the stress relaxation behavior during the holding phase, as formulated in Eq. 1.21 and shown in Fig. 1.10. In order to obtain similar force relaxation curves with real materials as shown in Figs. 1.8 and 1.9, at least two exponential terms are needed [[43]], one with large value of E_i/c_i and another one with small E_i/c_i. The large E_i/c_i describes the rapid relaxation in force and the small one denotes the slow decreasing. For example, figure 1.11 shows the curve fitting results of force relaxation behaviors of commercial clay material by using a force expression with one and two exponential terms, respectively. We can see that two exponential terms are enough to achieve a good reproduction of force relaxation behavior. The values of E_i/c_i used in Fig 1.11(b) were $E_1/c_1 = 0.2514$ and $E_2/c_2 = 0.00213$. After determining E_i/c_i and substituting

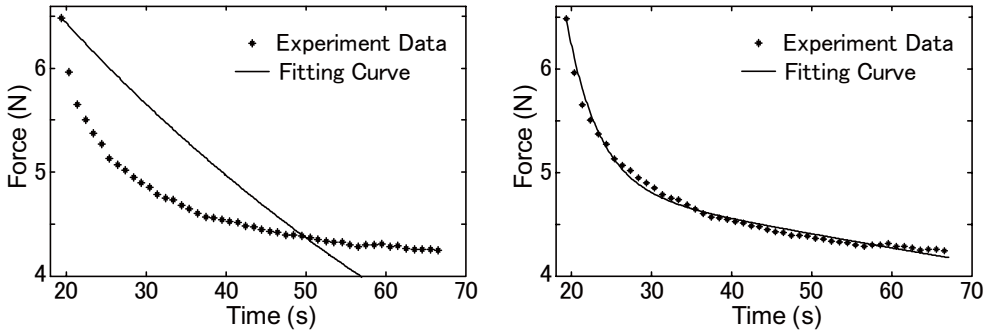

図 1.11: Curve fitting of force relaxation behaviors by using expressions with: (a) one exponential term, and (b) two exponential terms.

into Eq. 1.20, we find that the viscous moduli c_i will dominate peak stress at time t_p. Note that there is a sudden drop in stress (Fig. 1.10(a)) at the end of pushing phase for five-element model (parallel type 1). This sudden drop is denoted by $\sigma = c_{n+1}p$. Figure 1.10(b) showed that the two-layered Maxwell model(parallel type 2) results in attenuated vibrations in both stress and strain curves after unloading. Based on the above discussions, we can say that the physically-based models with at least two exponential terms in force expressions have the ability to accurately reproduce rheological force behaviors. Our work [[43]] has shown good reproductions of rheological forces for commercial clay. However, we failed to reproduce the final recovered shape at the same time. Let us now discuss the reason of this failure.

According to Eq. 1.27, the residual strain is dominated by the summation $\sum_{i=1}^{n+1} c_i$. On the other hand, parameters c_i also strongly affect stress amplitude as formulated in Eqs. 1.20, 1.21, and 1.28. This causes a contradiction between the reproductions of stress and residual strain. For example, if we determine the parameters c_i from stress, the summation of c_i will therefore yields a certain residual strain. We are unable to change this residual strain to another desired one. On the contrary, if we firstly calculate the summation of c_i based on Eq. 1.27, we have an upper limit $(\sum_{i=1}^{n+1} c_i)$ for each modulus c_i and we have to keep each c_i under this limit during the reproduction of stress. For some materials, we may be able to achieve a good reproduction of stress with c_i under this limit, as will be presented in Section 1.6. For most materials, however, this limit always will be broken in order to well capture the stress. The above discussions suggest that the physically-based models have some difficulties to reproduce both rheological force and deformation, especially residual

deformation, simultaneously. The reason of this difficulty is the linearity of the physically-based models, especially, the linear viscous elements, which dominated both residual strain and stress behaviors.

To solve this problem, the first idea come to our mind is to change the physically-based models. We can add more elements to the physical model or change the configurations of the basic elements. However, this will not work well. Actually, we are able to find a corresponding parallel model for any physical model no matter how many elements are involved and how these elements are connected. We have already discussed that a contradiction phenomenon always exist for arbitrary parallel model. Therefore, we are unable to solve this problem by adding more elements or changing the elements connections in physically-based models. The second idea for solving this problem is to introduce some nonlinear physical models. From textbooks or literatures, we can find some nonlinear physical models, such as the followings:

$$\begin{aligned}
\text{Wertheim (1847)} \quad & \epsilon^2 = a\sigma^2 + b\sigma, \\
\text{Morgan (1960)} \quad & \epsilon = a\sigma^n, \\
\text{Kenedi et al. (1964)} \quad & \sigma = k\epsilon^d, \quad \text{and} \quad \sigma = B\left[e^{ms} - 1\right], \\
\text{Ridge and Wright (1964)} \quad & \epsilon = C + k\sigma^b, \quad \text{and} \quad \epsilon = x + y\log\sigma.
\end{aligned} \tag{1.29}$$

Unfortunately, most of these nonlinear models cannot be extended to 2D/3D FE models. Even some of them may be able to be extended to 2D/3D models, the FE simulation will be very time consuming and it may be impossible to estimate all the parameters. We have tried to introduce some nonlinear models into our FE simulation, but we did not obtain any good result for reproducing both rheological force and residual deformation simultaneously so far. We have therefore turn to another idea which will be introduced in the next section.

1.2.4 多重粘性要素

According to the above discussions, we found that the summation $\sum_{i=1}^{n} c_i$ dominates both rheological forces and residual deformation simultaneously. Therefore, it is difficult to use one set of c_i to capture both force and residual deformation simultaneously. In addition, we found that one set of c_i is enough to capture both force and deformation behaviors during operations, such as pushing and holding phase. However, this set of parameter c_i cannot guarantee good reproduction of residual deformation. It is also clear that the force response goes to zero immediately after

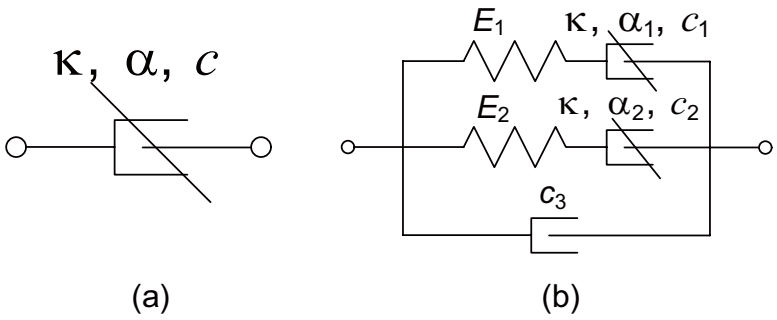

図 1.12: (a) the dual-moduli viscous element and (b) parallel 5-element model with two dual-moduli viscous elements.

releasing. During deformation recovery, we do not concern about force any more. Therefore, we are able to use another set of c_i to capture residual deformation. We can switch these two sets of parameters during simulation when the deformation starts to recover. We have therefore introduced a dual-moduli viscous element, as shown in Fig. 1.12a into our physically-based model in order to reproduce both rheological force and deformation, especially residual deformation simultaneously. The governing equation for the dual-moduli viscous element can be formulated as

$$\sigma(t) = (\kappa\alpha + c)\dot{\epsilon}(t), \tag{1.30}$$

where scalars α and c were parameters to be determined. Switch function κ takes the following values:

$$\kappa = \begin{cases} 1 & \text{Criterion is satisfied,} \\ -1 & \text{Otherwise.} \end{cases} \tag{1.31}$$

This dual-moduli viscous element has an ability to switch the parameters from one to the other during simulation. The physical meaning of this element can be explained as the property changing of a material during operation and recovery. For example, some elastic materials experience a hysteresis phenomenon during loading and unloading operations. The material properties are slightly changed during hysteresis. In addition, some metal materials also demonstrate strain hardening behavior when they are strained beyond the yield point. In this case, the properties of the materials are also changed during the operation. For rheological materials, both hysteresis and strain hardening may also happen and may be in more stronger way. This causes the material properties changing significantly during loading and the materials therefore

behave in another way after unloading. In other words, the physical parameters of rheological objects may be continuously changing during operations and reach another set of values when operations are finished. Unfortunately, continuous change of parameters during operation brings troubles in implement of parameter estimation. In our work, therefore, we suppose that the parameters are kept constants during operation and change to another set when the operation is finished.

The criterion used in Eq. 1.31 has different options depending on different applications. If the operation time is available before simulation, the simulation time can be a perfect criterion to trigger the parameter switching. In some applications such as surgical training and virtual reality, the simulation time may be not available in advance. Fortunately in such cases, an interaction often happens between the object and external instruments. This interaction can provide a good criterion for the parameter switching since the deformation recovery normally happens after the interaction was finished. This will be further investigated in Section 1.4. By introducing two dual-moduli viscous elements into a parallel five-element model, we can formulate an effective model (Fig. 1.12b) for capturing both rheological forces and deformation behaviors.

1.2.5 まとめ

In this section, the physically-based models for simulating rheological behaviors were summarized. We categorized such models into two groups: serial and parallel models. The constitutive laws for both generalized serial and parallel models were derived. We surprisingly found that the serial and parallel models are corresponding to each other and can be replaced by each other. This allowed us to focus on one group only and save us much time to go over various kinds of physically-based models. We also found that the serial models yield easy calculation of strain while the parallel models result in convenient calculation of stress. This suggested us how to choose the models between both groups depending on our applications. Analytical expressions of rheological stress and residual strain were derived and compared with rheological behaviors of real material. We found that at least two exponential terms in stress expressions are required to accurately reproduce the rheological stress behaviors. We also found the value of summation $\sum_{i=1}^{n} c_i$ dominates the residual strain and strongly affect the force amplitude as well. There is a contradiction between the reproductions of rheological forces and residual deformation. The linear

physically-based models have troubles to capture both rheological forces and deformation behaviors simultaneously. We have therefore introduced a dual-moduli viscous element into our physically-based model to cope with this problem. This model has an ability to switch parameters from one to the other during simulation and each set of parameters was responsible for capturing rheological forces and residual deformation respectively. The physical meaning of this element can be explained as hysteresis and strain hardening behaviors of rheological objects. In the following sections, the FE dynamic models, parameter estimation methods, and experimental results will be addressed.

1.3 動的 2D/3D 有限要素モデル

FEM is the most successful method for numerical computation of object deformation. In FE modeling, an object is described by a set of elements (*e.g.*, triangles in 2D case or tetrahedra in 3D case). Dynamic behaviors of the object are then determined by analyzing the behaviors of individual element. In this section, we formulate the 2D/3D dynamic model of deformable objects based on the linear Cauchy and nonlinear Green strain tensors, respectively. We firstly derive the FE model of elastic material and then extended to rheological material.

1.3.1 コーシー歪みを用いた有限要素モデル

二次元弾性モデル

Linear elastic material (*e.g.*, a linear spring) in 1D deformation satisfies the following equation:

$$\sigma = E\epsilon, \tag{1.32}$$

where σ and ϵ are stress and strain. Constant E denotes Young's modulus. According to the Hooke's law, the above 1D relationship can be extended to 2D deformation for an isotropic material as

$$\sigma = (\lambda \mathbf{I}_\lambda + \mu \mathbf{I}_\mu)\epsilon, \tag{1.33}$$

where $\sigma = [\sigma_{xx}, \sigma_{yy}, \sigma_{xy}]^{\mathrm{T}}$ and $\epsilon = [\epsilon_{xx}, \epsilon_{yy}, \epsilon_{xy}]^{\mathrm{T}}$ are 2D stress and linear Cauchy strain tensors. Scalars λ and μ denote Lamé's constants, which can be calculated by

Young's modulus E and Poisson's ratio γ as follows:

$$\lambda = \frac{\gamma E}{(1+\gamma)(1-2\gamma)}, \qquad \mu = \frac{E}{2(1+\gamma)}. \tag{1.34}$$

Constant matrices $\mathbf{I}_\lambda$ and $\mathbf{I}_\mu$ have the forms of

$$\mathbf{I}_\lambda = \begin{bmatrix} 1 & 1 & 0 \\ 1 & 1 & 0 \\ 0 & 0 & 0 \end{bmatrix}, \qquad \mathbf{I}_\mu = \begin{bmatrix} 2 & 0 & 0 \\ 0 & 2 & 0 \\ 0 & 0 & 1 \end{bmatrix}. \tag{1.35}$$

Let S be a region of a 2D elastic object. Assuming that the object is composed of linear elastic material, strain energy of the object is formulated as follows:

$$U = \int_S \frac{1}{2} \epsilon^{\mathrm{T}} \left(\lambda \mathbf{I}_\lambda + \mu \mathbf{I}_\mu\right) \epsilon h \, \mathrm{d}S.$$

Partitioning region S into a set of triangles, strain energy is described as

$$U = \sum_{\triangle \mathrm{P}_i \mathrm{P}_j \mathrm{P}_k} U_{i,j,k},$$

where

$$U_{i,j,k} = \int_{\triangle \mathrm{P}_i \mathrm{P}_j \mathrm{P}_k} \frac{1}{2} \epsilon^{\mathrm{T}} \left(\lambda \mathbf{I}_\lambda + \mu \mathbf{I}_\mu\right) \epsilon h \, \mathrm{d}S. \tag{1.36}$$

In the region of $\triangle \mathrm{P}_i \mathrm{P}_j \mathrm{P}_k$, displacement vector $\mathbf{u}_\mathrm{P} = [u, v]^{\mathrm{T}}$ at arbitrary point P inside $\triangle \mathrm{P}_i \mathrm{P}_j \mathrm{P}_k$ can be approximated by a linear combination of nodal displacements $\mathbf{u}_i = [u_i, v_i]^{\mathrm{T}}$, $\mathbf{u}_j = [u_j, v_j]^{\mathrm{T}}$, and $\mathbf{u}_k = [u_k, v_k]^{\mathrm{T}}$ as follows:

$$\begin{aligned} u &= u_i N_{i,j,k} + u_j N_{j,k,i} + u_k N_{k,i,j}, \\ v &= v_i N_{i,j,k} + v_j N_{j,k,i} + v_k N_{k,i,j}, \end{aligned} \tag{1.37}$$

where $N_{i,j,k}$, $N_{j,k,i}$, and $N_{k,i,j}$ are the interpolating shape functions. Each of them has a value of 1 at each nodal point P_i, P_j, or P_k, respectively and zeros at all other nodal points. Taking partial derivatives of u and v relative to x and y respectively, we have

$$\begin{aligned} \frac{\partial u}{\partial x} &= u_i \frac{\partial N_{i,j,k}}{\partial x} + u_j \frac{\partial N_{j,k,i}}{\partial x} + u_k \frac{\partial N_{k,i,j}}{\partial x}, \\ \frac{\partial u}{\partial y} &= u_i \frac{\partial N_{i,j,k}}{\partial y} + u_j \frac{\partial N_{j,k,i}}{\partial y} + u_k \frac{\partial N_{k,i,j}}{\partial y}, \\ \frac{\partial v}{\partial x} &= v_i \frac{\partial N_{i,j,k}}{\partial x} + v_j \frac{\partial N_{j,k,i}}{\partial x} + v_k \frac{\partial N_{k,i,j}}{\partial x}, \\ \frac{\partial v}{\partial y} &= v_i \frac{\partial N_{i,j,k}}{\partial y} + v_j \frac{\partial N_{j,k,i}}{\partial y} + v_k \frac{\partial N_{k,i,j}}{\partial y}. \end{aligned} \tag{1.38}$$

Let $[\xi_i, \eta_i]^{\mathrm{T}}$, $[\xi_j, \eta_j]^{\mathrm{T}}$, and $[\xi_k, \eta_k]^{\mathrm{T}}$ be initial coordinates of nodal points P_i, P_j, and P_k, respectively. Partial derivatives of shape functions in Eq. 1.38 can be calculated as:

$$\begin{aligned} N_{ix} &= \frac{\partial N_{i,j,k}}{\partial x} = \frac{\eta_j - \eta_k}{2\triangle}, \quad N_{iy} = \frac{\partial N_{i,j,k}}{\partial y} = -\frac{\xi_j - \xi_k}{2\triangle}, \\ N_{jx} &= \frac{\partial N_{j,k,i}}{\partial x} = \frac{\eta_k - \eta_i}{2\triangle}, \quad N_{jy} = \frac{\partial N_{j,k,i}}{\partial y} = -\frac{\xi_k - \xi_i}{2\triangle}, \\ N_{kx} &= \frac{\partial N_{k,i,j}}{\partial x} = \frac{\eta_i - \eta_j}{2\triangle}, \quad N_{ky} = \frac{\partial N_{k,i,j}}{\partial y} = -\frac{\xi_i - \xi_j}{2\triangle}, \end{aligned} \tag{1.39}$$

where $\triangle$ denotes the signed area of triangle $\triangle \mathrm{P}_i\mathrm{P}_j\mathrm{P}_k$ and was given by

$$\triangle \mathrm{P}_i\mathrm{P}_j\mathrm{P}_k = \frac{1}{2} \begin{bmatrix} \xi_i & \xi_j & \xi_k \end{bmatrix} \begin{bmatrix} \eta_j - \eta_k \\ \eta_k - \eta_i \\ \eta_i - \eta_j \end{bmatrix}.$$

Note that the Cauchy strain tensor $\epsilon = [\epsilon_{xx}, \epsilon_{yy}, \epsilon_{xy}]^{\mathrm{T}}$ was formulated as

$$\begin{aligned} \epsilon_{xx} &= \frac{\partial u}{\partial x}, \\ \epsilon_{yy} &= \frac{\partial v}{\partial y}, \\ 2\epsilon_{xy} &= \frac{\partial u}{\partial y} + \frac{\partial v}{\partial x}. \end{aligned} \tag{1.40}$$

Substituting Eqs. 1.38 and 1.39 into Eq. 1.40 and then substituting the consequential Cauchy strain tensor into Eq. 1.36, we have

$$U_{i,j,k} = \frac{1}{2} \begin{bmatrix} \mathbf{u}_i^{\mathrm{T}} & \mathbf{u}_j^{\mathrm{T}} & \mathbf{u}_k^{\mathrm{T}} \end{bmatrix} \mathbf{K}_{i,j,k} \begin{bmatrix} \mathbf{u}_i \\ \mathbf{u}_j \\ \mathbf{u}_k \end{bmatrix}, \tag{1.41}$$

where stiffness matrix $\mathbf{K}_{i,j,k}$ can be decomposed into two as follows:

$$\mathbf{K}_{i,j,k} = \lambda \mathbf{J}_{\lambda}^{i,j,k} + \mu \mathbf{J}_{\mu}^{i,j,k}. \tag{1.42}$$

Matrices $\mathbf{J}_{\lambda}^{i,j,k}$ and $\mathbf{J}_{\mu}^{i,j,k}$ have the following forms:

$$\mathbf{J}_{\lambda}^{i,j,k} = \frac{h}{4\triangle \mathrm{P}_i\mathrm{P}_j\mathrm{P}_k}\begin{bmatrix} \mathbf{A}_{j,k;\,j,k} & \mathbf{A}_{j,k;\,k,i} & \mathbf{A}_{j,k;\,i,j} \\ \mathbf{A}_{k,i;\,j,k} & \mathbf{A}_{k,i;\,k,i} & \mathbf{A}_{k,i;\,i,j} \\ \mathbf{A}_{i,j;\,j,k} & \mathbf{A}_{i,j;\,k,i} & \mathbf{A}_{i,j;\,i,j} \end{bmatrix},$$

$$\mathbf{J}_{\mu}^{i,j,k} = \frac{h}{4\triangle \mathrm{P}_i\mathrm{P}_j\mathrm{P}_k}\begin{bmatrix} 2\mathbf{B}_{j,k;\,j,k}+\mathbf{C}_{j,k;\,j,k} & 2\mathbf{B}_{j,k;\,k,i}+\mathbf{C}_{j,k;\,k,i} & 2\mathbf{B}_{j,k;\,i,j}+\mathbf{C}_{j,k;\,i,j} \\ 2\mathbf{B}_{k,i;\,j,k}+\mathbf{C}_{k,i;\,j,k} & 2\mathbf{B}_{k,i;\,k,i}+\mathbf{C}_{k,i;\,k,i} & 2\mathbf{B}_{k,i;\,i,j}+\mathbf{C}_{k,i;\,i,j} \\ 2\mathbf{B}_{i,j;\,j,k}+\mathbf{C}_{i,j;\,j,k} & 2\mathbf{B}_{i,j;\,k,i}+\mathbf{C}_{i,j;\,k,i} & 2\mathbf{B}_{i,j;\,i,j}+\mathbf{C}_{i,j;\,i,j} \end{bmatrix}, \tag{1.43}$$

where

$$\begin{aligned} \mathbf{A}_{i,j;\,l,m} &\triangleq \begin{bmatrix} (\eta_i-\eta_j)(\eta_l-\eta_m) & -(\eta_i-\eta_j)(\xi_l-\xi_m) \\ -(\xi_i-\xi_j)(\eta_l-\eta_m) & (\xi_i-\xi_j)(\xi_l-\xi_m) \end{bmatrix}, \\ \mathbf{B}_{i,j;\,l,m} &\triangleq \begin{bmatrix} (\eta_i-\eta_j)(\eta_l-\eta_m) & 0 \\ 0 & (\xi_i-\xi_j)(\xi_l-\xi_m) \end{bmatrix}, \\ \mathbf{C}_{i,j;\,l,m} &\triangleq \begin{bmatrix} (\xi_i-\xi_j)(\xi_l-\xi_m) & -(\xi_i-\xi_j)(\eta_l-\eta_m) \\ -(\eta_i-\eta_j)(\xi_l-\xi_m) & (\eta_i-\eta_j)(\eta_l-\eta_m) \end{bmatrix}. \end{aligned} \tag{1.44}$$

Note that matrices $\mathbf{J}_{\lambda}^{i,j,k}$ and $\mathbf{J}_{\mu}^{i,j,k}$ depend on geometric quantities, say, coordinates of nodal points alone. As a result, the global stiffness matrix $\mathbf{K}$ also can be decomposed into two terms as follows:

$$\mathbf{K} = \lambda\mathbf{J}_{\lambda} + \mu\mathbf{J}_{\mu}, \tag{1.45}$$

where $\mathbf{J}_{\lambda}$ and $\mathbf{J}_{\mu}$ are referred to as connection matrices. Both matrices also depend on geometric quantities alone and can be calculated by incorporating matrices $\mathbf{J}_{\lambda}^{i,j,k}$ and $\mathbf{J}_{\mu}^{i,j,k}$ of each triangles based on the contribution of each triangle to the whole triangle mesh. Let N be the number of nodal points in an FE triangle mesh. The dimensions of both connection matrices are $2N \times 2N$.

After having the global stiffness matrix $\mathbf{K}$, strain energy of the object was formulated by

$$U = \frac{1}{2}\mathbf{u}_N^{\mathrm{T}}\mathbf{K}\mathbf{u}_N, \tag{1.46}$$

where $\mathbf{u}_N$ represents the nodal displacement vector. Taking the derivative of the above strain energy relative to vector $\mathbf{u}_N$, we have the formulation of a set of elastic forces generated on all nodal points as

$$\mathbf{F}_{2D}^{ela} = \mathbf{K}\mathbf{u}_N = (\lambda\mathbf{J}_{\lambda} + \mu\mathbf{J}_{\mu})\mathbf{u}_N. \tag{1.47}$$

Comparing Eqs. 1.32, 1.33, and 1.47, we found that the 2D stress-strain relation Eq. 1.33 can be obtained from 1D relation Eq. 1.32 by replacing Young's modulus E by a matrix with two Lamé's constants λ and μ. Furthermore, the 2D FE force-displacement relationship Eq. 1.47 can be obtained from 2D stress-strain relation Eq. 1.33 by replacing σ by $\mathbf{F}_{2D}^{ela}$, ϵ by $\mathbf{u}_N$, $\mathbf{I}_\lambda$ by $\mathbf{J}_\lambda$, and $\mathbf{I}_\mu$ by $\mathbf{J}_\mu$, respectively. In the next section, we extend the 2D elastic formulation to a 2D rheological formulation.

二次元レオロジーモデル

A Maxwell model, as shown in Fig. 1.4(c), is a simplest physical model for simulating rheological behaviors. The Maxwell model consists of an elastic and a viscous elements connected in serial. The 1D stress-strain relationship of the Maxwell model can be formulated as

$$\dot{\sigma} = -\frac{E}{c}\sigma + E\dot{\epsilon}, \tag{1.48}$$

Solving the above ordinary differential equation yields:

$$\sigma(t) = \int_0^t R(t-t')\dot{\epsilon}(t')\mathrm{d}t', \tag{1.49}$$

where $R(t-t') = Ee^{-\frac{E}{c}(t-t')}$ is referred as a relaxation function, which determines the nature of rheological deformation. Replacing two elastic constants λ and μ in Eq. 1.33 by two relaxation functions yields a relaxation matrix in 2D isotropic deformation of the Maxwell model:

$$\mathbf{R}(t-t') = r_\lambda(t-t')\mathbf{I}_\lambda + r_\mu(t-t')\mathbf{I}_\mu, \tag{1.50}$$

where

$$r_\lambda(t-t') = \lambda e^{-\frac{E}{c}(t-t')}, \qquad r_\mu(t-t') = \mu e^{-\frac{E}{c}(t-t')}. \tag{1.51}$$

Replacing $R(t-t')$ in Eq. 1.49 by Eq. 1.50, we have the 2D stress-strain relationship of the Maxwell model as

$$\sigma(t) = \int_0^t \left[r_\lambda(t-t')\mathbf{I}_\lambda + r_\mu(t-t')\mathbf{I}_\mu\right]\dot{\epsilon}(t')\mathrm{d}t'. \tag{1.52}$$

From the above equation, replacing $\sigma(t)$ by $\mathbf{F}_{2D}^{Max}(t)$, ϵ by $\mathbf{u}_N$, $\mathbf{I}_\lambda$ by $\mathbf{J}_\lambda$, $\mathbf{I}_\mu$ by $\mathbf{J}_\mu$, we have the 2D force-displacement relationship of the Maxwell model as

$$\mathbf{F}_{2D}^{Max}(t) = \int_0^t \left[\lambda e^{-\frac{E}{c}(t-t')}\mathbf{J}_\lambda + \mu e^{-\frac{E}{c}(t-t')}\mathbf{J}_\mu\right]\dot{\mathbf{u}}_N(t')\mathrm{d}t'. \tag{1.53}$$

Differentiating the above equation, we finally have

$$\dot{\mathbf{F}}_{2D}^{Max} = -\frac{E}{c}\mathbf{F}_{2D}^{Max} + (\lambda \mathbf{J}_\lambda + \mu \mathbf{J}_\mu)\dot{\mathbf{u}}_N, \tag{1.54}$$

Comparing Eq. 1.48 and Eq. 1.54, we find that the 1D constitutive law of Maxwell model can be easily extended to 2D case by simple replacements as performed above.

Then, let us investigate the formulation of a parallel five-element model, as shown in the last row of Fig. 1.5(b). The parallel five-element model consists of two Maxwell models and one viscous element connected in parallel. Let σ_1, σ_2, and σ_3 be the stress at the first, the second Maxwell models, and the third viscous element, respectively. Let σ and ϵ be the stress and strain at the five-element model. Due to the parallel configuration, the 1D stress-strain relationship can be formulated as:

$$\begin{aligned} \dot{\sigma}_1 + \frac{E_1}{c_1}\sigma_1 &= E_1\dot{\epsilon}, \\ \dot{\sigma}_2 + \frac{E_2}{c_2}\sigma_2 &= E_2\dot{\epsilon}, \\ \sigma_3 &= c_3\dot{\epsilon}, \\ \sigma &= \sigma_1 + \sigma_2 + \sigma_3. \end{aligned} \tag{1.55}$$

Following the same replacing procedures presented above, we can easily extend the 1D stress-strain relation Eq. 1.55 to 2D force-displacement relation as:

$$\begin{aligned} \dot{\mathbf{F}}_1 + \frac{E_1}{c_1}\mathbf{F}_1 &= (\lambda_1^{ela}\mathbf{J}_\lambda + \mu_1^{ela}\mathbf{J}_\mu)\dot{\mathbf{u}}_N, \\ \dot{\mathbf{F}}_2 + \frac{E_2}{c_2}\mathbf{F}_2 &= (\lambda_2^{ela}\mathbf{J}_\lambda + \mu_2^{ela}\mathbf{J}_\mu)\dot{\mathbf{u}}_N, \\ \mathbf{F}_3 &= (\lambda_3^{vis}\mathbf{J}_\lambda + \mu_3^{vis}\mathbf{J}_\mu)\dot{\mathbf{u}}_N, \\ \mathbf{F}_{2D}^{rheo} &= \mathbf{F}_1 + \mathbf{F}_2 + \mathbf{F}_3, \end{aligned} \tag{1.56}$$

where $\mathbf{F}_1$, $\mathbf{F}_2$, $\mathbf{F}_3$, and $\mathbf{F}_{2D}^{rheo}$ are force vectors corresponding to stress vectors σ_1, σ_2, σ_3, and σ, respectively. Parameters λ_1^{ela}, μ_1^{ela}, λ_2^{ela}, and μ_2^{ela} are Lamé constants corresponding to E_1 and E_2 and can be calculated by Eq. 1.34. Parameters λ_3^{vis} and μ_3^{vis} described the model's viscosity and are defined as

$$\lambda_3^{vis} = \frac{c_3\gamma}{(1+\gamma)(1-2\gamma)}, \qquad \mu_3^{vis} = \frac{c_3}{2(1+\gamma)}. \tag{1.57}$$

Supposing that a 2D object is fixed on the ground and the top surface of the object is pushed downward with a displacement function of $\mathbf{d}(t)$. These two constraints can

be formulated as follows by using constraint stabilization method (CSM) [[44]].

$$\begin{aligned} \mathbf{A}^T\ddot{\mathbf{u}}_N + \mathbf{A}^T(2\omega\dot{\mathbf{u}}_N + \omega^2\mathbf{u}_N) = 0, \\ \mathbf{B}^T(\ddot{\mathbf{u}}_N - \ddot{\mathbf{d}}) + \mathbf{B}^T[2\omega(\dot{\mathbf{u}}_N - \dot{\mathbf{d}}) + \omega^2(\mathbf{u}_N - \mathbf{d})] = 0, \end{aligned} \tag{1.58}$$

where matrices $\mathbf{A}$ and $\mathbf{B}$ denote which nodal points should be constrained on the bottom and top surface, respectively. Scalar ω is a predetermined angular frequency and is set to 2000 for both constraints.

Let $\mathbf{M}$ be an inertia matrix and $\ell_\mathbf{1}$ and $\ell_\mathbf{2}$ be the Lagrange multipliers which denote a set of constraint forces corresponding to both geometric constraints. Using the Lagrange dynamic method, dynamic equations of the nodal points are given by

$$-\mathbf{F}_{2D}^{rheo} + \mathbf{A}\ell_\mathbf{1} + \mathbf{B}\ell_\mathbf{2} - \mathbf{M}\ddot{\mathbf{u}}_N = 0. \tag{1.59}$$

Combining Eqs. 1.56, 1.58, 1.59, and considering $\mathbf{v}_N = \dot{\mathbf{u}}_N$, we have a set of differential equations for simulating the 2D FE dynamic behaviors of a rheological object under a pushing or pulling operations. In the next section, the 2D FE model will be extended to 3D model by changing the triangle mesh to tetrahedral mesh and adding the z-axis components in all the matrices and vectors. Figure 1.13 demonstrates 2D simulation results of rheological behaviors. The center part of the top surface of a 2D rheological object was pushed downward from 0 s to 20 s with a constant velocity. The deformation was then maintained for 20 seconds. From 40 s, the deformation started to recover. Figure 1.13f shows the force responses on the bottom surface of the object.

三次元レオロジーモデル

In our 3D FE formulation, an object is constructed by a set of tetrahedra. Let P_i be a nodal point of a tetrahedron and $[\xi_i, \eta_i, \zeta_i]^{\mathrm{T}}$ be coordinates of point P_i. Let $\Diamond \mathrm{P}_i\mathrm{P}_j\mathrm{P}_k\mathrm{P}_l$ be a tetrahedron consisting of nodal points P_i, P_j, P_k, and P_l. Note that linear isotropic elastic material satisfies

$$\sigma = \mathbf{D}\epsilon, \tag{1.60}$$

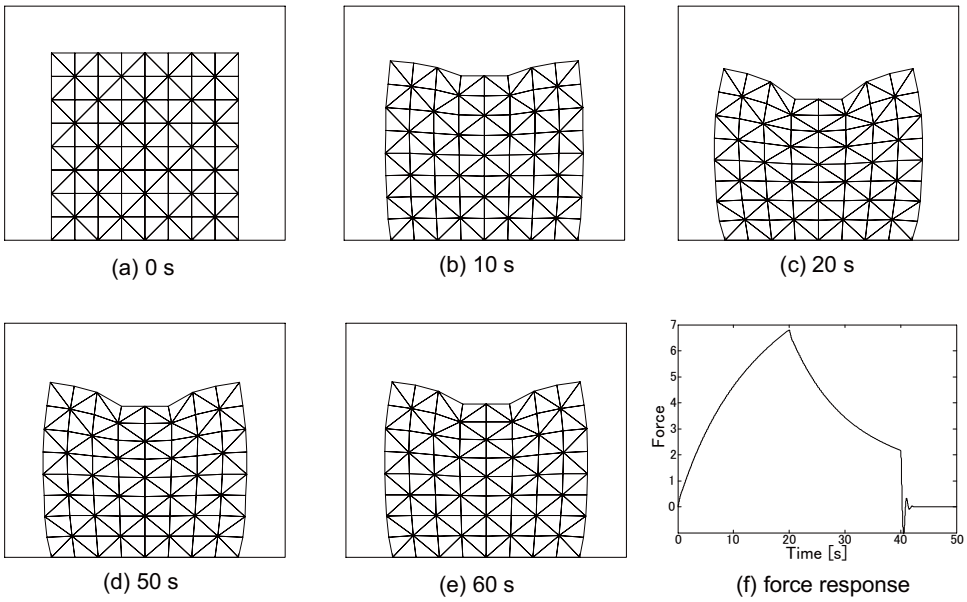

図 1.13: Simulation behaviors of a 2D rheological object: initial shape (a), deformed shape (b) at time 10 s, (c) at 20 s, (d) at 50 s, (e) at 60 s, and (f) force response on the bottom surface.

where

$$\mathbf{D} = \begin{bmatrix} \lambda+2\mu & \lambda & \lambda & 0 & 0 & 0 \\ \lambda & \lambda+2\mu & \lambda & 0 & 0 & 0 \\ \lambda & \lambda & \lambda+2\mu & 0 & 0 & 0 \\ 0 & 0 & 0 & \mu & 0 & 0 \\ 0 & 0 & 0 & 0 & \mu & 0 \\ 0 & 0 & 0 & 0 & 0 & \mu \end{bmatrix}.$$

Stress vector σ and linear strain vector ϵ in 3D case are defined as

$$\sigma = [\sigma_{\xi\xi}, \sigma_{\eta\eta}, \sigma_{\zeta\zeta}, \sigma_{\eta\zeta}, \sigma_{\zeta\xi}, \sigma_{\xi\eta}]^{\mathrm{T}},$$
$$\epsilon = [\epsilon_{\xi\xi}, \epsilon_{\eta\eta}, \epsilon_{\zeta\zeta}, 2\epsilon_{\eta\zeta}, 2\epsilon_{\zeta\xi}, 2\epsilon_{\xi\eta}]^{\mathrm{T}}.$$

Performing similar derivation as presented in 2D elastic deformation, we can obtain a stiffness matrix $\mathbf{K}_{i,j,k,l}$ for a tetrahedron $\Diamond \mathrm{P}_i\mathrm{P}_j\mathrm{P}_k\mathrm{P}_l$ as follows:

$$\mathbf{K}_{i,j,k,l} = \lambda \mathbf{J}_{\lambda}^{i,j,k,l} + \mu \mathbf{J}_{\mu}^{i,j,k,l}, \tag{1.61}$$

where

$$\mathbf{J}_{\lambda}^{i,j,k,l} = \frac{1}{36\Diamond}\begin{bmatrix} \mathbf{A}_{j,k,l;j,k,l} & -\mathbf{A}_{j,k,l;k,l,i} & \mathbf{A}_{j,k,l;l,i,j} & -\mathbf{A}_{j,k,l;i,j,k} \\ -\mathbf{A}_{k,l,i;j,k,l} & \mathbf{A}_{k,l,i;k,l,i} & -\mathbf{A}_{k,l,i;l,i,j} & \mathbf{A}_{k,l,i;i,j,k} \\ \mathbf{A}_{l,i,j;j,k,l} & -\mathbf{A}_{l,i,j;k,l,i} & \mathbf{A}_{l,i,j;l,i,j} & -\mathbf{A}_{l,i,j;i,j,k} \\ -\mathbf{A}_{i,j,k;j,k,l} & \mathbf{A}_{i,j,k;k,l,i} & -\mathbf{A}_{i,j,k;l,i,j} & \mathbf{A}_{i,j,k;i,j,k} \end{bmatrix},$$

$$\begin{aligned} \mathbf{J}_{\mu}^{i,j,k,l} = & \frac{1}{36\Diamond}\begin{bmatrix} 2\mathbf{B}_{j,k,l;j,k,l} & -2\mathbf{B}_{j,k,l;k,l,i} & 2\mathbf{B}_{j,k,l;l,i,j} & -2\mathbf{B}_{j,k,l;i,j,k} \\ -2\mathbf{B}_{k,l,i;j,k,l} & 2\mathbf{B}_{k,l,i;k,l,i} & -2\mathbf{B}_{k,l,i;l,i,j} & 2\mathbf{B}_{k,l,i;i,j,k} \\ 2\mathbf{B}_{l,i,j;j,k,l} & -2\mathbf{B}_{l,i,j;k,l,i} & 2\mathbf{B}_{l,i,j;l,i,j} & -2\mathbf{B}_{l,i,j;i,j,k} \\ -2\mathbf{B}_{i,j,k;j,k,l} & 2\mathbf{B}_{i,j,k;k,l,i} & -2\mathbf{B}_{i,j,k;l,i,j} & 2\mathbf{B}_{i,j,k;i,j,k} \end{bmatrix} \\ & + \frac{1}{36\Diamond}\begin{bmatrix} \mathbf{C}_{j,k,l;j,k,l} & -\mathbf{C}_{j,k,l;k,l,i} & \mathbf{C}_{j,k,l;l,i,j} & -\mathbf{C}_{j,k,l;i,j,k} \\ -\mathbf{C}_{k,l,i;j,k,l} & \mathbf{C}_{k,l,i;k,l,i} & -\mathbf{C}_{k,l,i;l,i,j} & \mathbf{C}_{k,l,i;i,j,k} \\ \mathbf{C}_{l,i,j;j,k,l} & -\mathbf{C}_{l,i,j;k,l,i} & \mathbf{C}_{l,i,j;l,i,j} & -\mathbf{C}_{l,i,j;i,j,k} \\ -\mathbf{C}_{i,j,k;j,k,l} & \mathbf{C}_{i,j,k;k,l,i} & -\mathbf{C}_{i,j,k;l,i,j} & \mathbf{C}_{i,j,k;i,j,k} \end{bmatrix}. \end{aligned} \tag{1.62}$$

The signed volume of tetrahedron $\Diamond = \Diamond \mathrm{P}_i\mathrm{P}_j\mathrm{P}_k\mathrm{P}_l$ is given by

$$\begin{aligned} \Diamond \mathrm{P}_i\mathrm{P}_j\mathrm{P}_k\mathrm{P}_l &= \Diamond \mathrm{O}\mathrm{P}_j\mathrm{P}_k\mathrm{P}_l + \Diamond \mathrm{P}_i\mathrm{O}\mathrm{P}_k\mathrm{P}_l + \Diamond \mathrm{P}_i\mathrm{P}_j\mathrm{O}\mathrm{P}_l + \Diamond \mathrm{P}_i\mathrm{P}_j\mathrm{P}_k\mathrm{O} \\ &= \Diamond \mathrm{O}\mathrm{P}_j\mathrm{P}_k\mathrm{P}_l + \Diamond \mathrm{O}\mathrm{P}_k\mathrm{P}_l\mathrm{P}_i + \Diamond \mathrm{O}\mathrm{P}_l\mathrm{P}_i\mathrm{P}_j + \Diamond \mathrm{O}\mathrm{P}_i\mathrm{P}_j\mathrm{P}_k, \end{aligned} \tag{1.63}$$

where the signed volume of tetrahedron $\Diamond \mathrm{O}\mathrm{P}_i\mathrm{P}_j\mathrm{P}_k$ is defined as follows:

$$\Diamond \mathrm{O}\mathrm{P}_i\mathrm{P}_j\mathrm{P}_k = \frac{1}{2}\frac{1}{3}\begin{vmatrix} \xi_i & \xi_j & \xi_k \\ \eta_i & \eta_j & \eta_k \\ \zeta_i & \zeta_j & \zeta_k \end{vmatrix}. \tag{1.64}$$

The matrices $\mathbf{A}_{i,j,k;l,m,n}$, $\mathbf{B}_{i,j,k;l,m,n}$, and $\mathbf{C}_{i,j,k;l,m,n}$ in Eq. 1.62 are defined as:

$$\begin{aligned} \mathbf{A}_{i,j,k;l,m,n} &\triangleq \begin{bmatrix} a_{i,j,k}a_{l,m,n} & a_{i,j,k}b_{l,m,n} & a_{i,j,k}c_{l,m,n} \\ b_{i,j,k}a_{l,m,n} & b_{i,j,k}b_{l,m,n} & b_{i,j,k}c_{l,m,n} \\ c_{i,j,k}a_{l,m,n} & c_{i,j,k}b_{l,m,n} & c_{i,j,k}c_{l,m,n} \end{bmatrix}, \\ \mathbf{B}_{i,j,k;l,m,n} &\triangleq \begin{bmatrix} a_{i,j,k}a_{l,m,n} & 0 & 0 \\ 0 & b_{i,j,k}b_{l,m,n} & 0 \\ 0 & 0 & c_{i,j,k}c_{l,m,n} \end{bmatrix}, \\ \mathbf{C}_{i,j,k;l,m,n} &\triangleq \\ & \begin{bmatrix} b_{i,j,k}b_{l,m,n} + c_{i,j,k}c_{l,m,n} & b_{i,j,k}a_{l,m,n} & c_{i,j,k}a_{l,m,n} \\ a_{i,j,k}b_{l,m,n} & c_{i,j,k}c_{l,m,n} + a_{i,j,k}a_{l,m,n} & c_{i,j,k}b_{l,m,n} \\ a_{i,j,k}c_{l,m,n} & b_{i,j,k}c_{l,m,n} & a_{i,j,k}a_{l,m,n} + b_{i,j,k}b_{l,m,n} \end{bmatrix}, \end{aligned} \tag{1.65}$$

where

$$
\begin{aligned}
a_{i,j,k} &= \begin{vmatrix} \eta_i & \eta_j \\ \zeta_i & \zeta_j \end{vmatrix} + \begin{vmatrix} \eta_j & \eta_k \\ \zeta_j & \zeta_k \end{vmatrix} + \begin{vmatrix} \eta_k & \eta_i \\ \zeta_k & \zeta_i \end{vmatrix}, \\
b_{i,j,k} &= \begin{vmatrix} \zeta_i & \zeta_j \\ \xi_i & \xi_j \end{vmatrix} + \begin{vmatrix} \zeta_j & \zeta_k \\ \xi_j & \xi_k \end{vmatrix} + \begin{vmatrix} \zeta_k & \zeta_i \\ \xi_k & \xi_i \end{vmatrix}, \\
c_{i,j,k} &= \begin{vmatrix} \xi_i & \xi_j \\ \eta_i & \eta_j \end{vmatrix} + \begin{vmatrix} \xi_j & \xi_k \\ \eta_j & \eta_k \end{vmatrix} + \begin{vmatrix} \xi_k & \xi_i \\ \eta_k & \eta_i \end{vmatrix}.
\end{aligned} \tag{1.66}
$$

After having stiffness matrix on each tetrahedron as given in Eq. 1.61, we can calculate the global stiffness matrix as follows by incorporating the contribution of each tetrahedron:

$$\mathbf{K}^{3D} = \lambda \mathbf{J}_{\lambda}^{3D} + \mu \mathbf{J}_{\mu}^{3D}, \tag{1.67}$$

The dimensions of connection matrices $\mathbf{J}_{\lambda}^{3D}$ and $\mathbf{J}_{\mu}^{3D}$ are $3N \times 3N$. Therefore, a set of elastic forces $\mathbf{F}_{3D}^{ela}$ can be formulated as:

$$\mathbf{F}_{3D}^{ela} = \mathbf{K}^{3D}\mathbf{u}_N^{3D} = \left(\lambda \mathbf{J}_{\lambda}^{3D} + \mu \mathbf{J}_{\mu}^{3D}\right) \mathbf{u}_N^{3D}, \tag{1.68}$$

where vectors $\mathbf{F}_{3D}^{ela}$ and $\mathbf{u}_N^{3D}$ consist of x-, y-, and z-axis components of all nodal points and the dimensions of both vectors are $3N \times 1$. Comparing the above equation and Eq. 1.47, the difference between 2D and 3D FE formulation is the calculation of connection matrices and the configuration of force and displacement vectors. In 3D deformation, the object is constructed with a set of tetrahedra and all the matrices and vectors include the z-axis components in their formulations.

Similarly, we can extend 2D rheological FE formulation to 3D case. Replacing the 2D matrices and vectors in Eqs. 1.56, 1.58, 1.59 and considering $\mathbf{v}_N^{3D} = \dot{\mathbf{u}}_N^{3D}$, we have

3D FE formulation of rheological deformation as follows:

$$
\begin{aligned}
\dot{\mathbf{u}}_N^{3D} &= \mathbf{v}_N^{3D}, \\
\mathbf{M}_{3D}\dot{\mathbf{v}}_N^{3D} &= \mathbf{A}_{3D}\ell_1^{3D} + \mathbf{B}_{3D}\ell_2^{3D} - \mathbf{F}_{3D}^{rheo} + \mathbf{F}_{3D}^{ext}, \\
-\mathbf{A}_{3D}^T\dot{\mathbf{v}}_N^{3D} &= \mathbf{A}_{3D}^T\left(2\omega\mathbf{v}_N^{3D} + \omega^2\mathbf{u}_N^{3D}\right), \\
-\mathbf{B}_{3D}^T\dot{\mathbf{v}}_N^{3D} &= \mathbf{B}_{3D}^T\left[2\omega\left(\mathbf{v}_N^{3D} - \dot{\mathbf{d}}^{3D}\right) + \omega^2\left(\mathbf{u}_N^{3D} - \mathbf{d}^{3D}\right)\right] - \ddot{\mathbf{d}}^{3D}, \\
\dot{\mathbf{F}}_1^{3D} &= -\frac{E_1}{c_1}\mathbf{F}_1^{3D} + \left(\lambda_1^{ela}\mathbf{J}_\lambda^{3D} + \mu_1^{ela}\mathbf{J}_\mu^{3D}\right)\dot{\mathbf{u}}_N^{3D}, \\
\dot{\mathbf{F}}_2^{3D} &= -\frac{E_2}{c_2}\mathbf{F}_2^{3D} + \left(\lambda_2^{ela}\mathbf{J}_\lambda^{3D} + \mu_2^{ela}\mathbf{J}_\mu^{3D}\right)\dot{\mathbf{u}}_N^{3D}, \\
\mathbf{F}_3^{3D} &= \left(\lambda_3^{vis}\mathbf{J}_\lambda^{3D} + \mu_3^{vis}\mathbf{J}_\mu^{3D}\right)\mathbf{v}_N^{3D}, \\
\mathbf{F}_{3D}^{rheo} &= \mathbf{F}_1^{3D} + \mathbf{F}_2^{3D} + \mathbf{F}_3^{3D}.
\end{aligned}
\tag{1.69}
$$

Note that the above linear equations are solvable since the coefficient matrix is regular, implying that we can compute $\dot{\mathbf{u}}_N^{3D}$, $\dot{\mathbf{v}}_N^{3D}$, $\dot{\mathbf{F}}_1^{3D}$, and $\dot{\mathbf{F}}_2^{3D}$. Thus, we can obtain the integrals of these variables using the Runge-Kutta method and finally compute 3D rheological deformation and force behaviors. For example, Fig. 1.14 demonstrates simulated behaviors of a 3D cube. The entire top surface of the cube was compressed downward with a constant velocity from time 0 s to 20 s. Before releasing, the deformed object was maintained for 20 seconds. Then, the deformation was partially recovered until time 50 s. The rheological force behavior is also given in Fig. 1.14d. In addition, our FE model is not limited to regular-shaped objects. It can be used to simulate objects with arbitrary shape as long as tetrahedra mesh is available. For example, the deformation of a 3D index finger pushed by an external cube was performed as shown in Fig. 1.15. Both 2D and 3D views are given for the convenience of comparison. The contact modeling used in this example will be discussed in Section 1.4.

The FE models presented so far are based on linear Cauchy strain tensor. Linear FE formulation has an advantage of constant connection matrices $\mathbf{J}_\lambda$ and $\mathbf{J}_\mu$, which can be prepared before performing simulation. This results in more efficient simulation comparing with nonlinear FE formulation. However, linear FE models cannot cover large deformation and cannot simulate deformation with rotation motion, which may frequently happen in many applications, such as surgical simulation and food products manipulation. We will therefore introduce the nonlinear Green strain tensor into our FE model in the next section to deal with this problem.

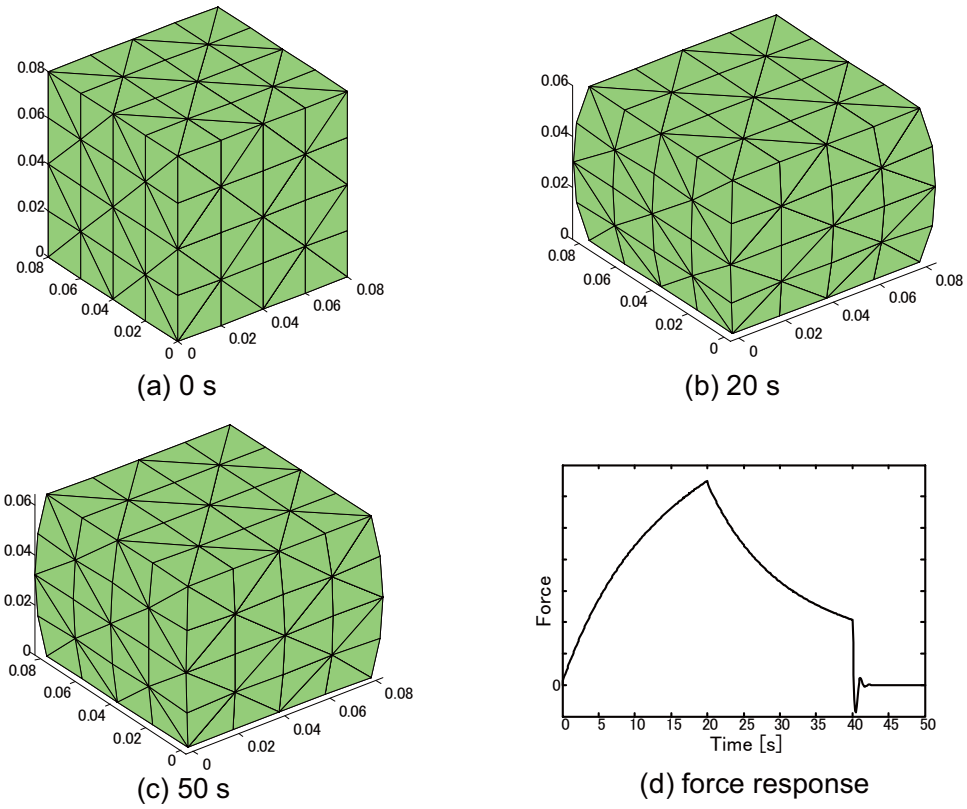

図 1.14: Simulation behaviors of a 3D rheological object: initial shape (a), deformed shape (b) at time 20 s, (c) at 50 s, and (d) force response on the bottom surface.

1.3.2 グリーン歪みを用いた有限要素モデル

二次元弾性モデル

The Green strain tensor is a nonlinear strain measure which can handle large deformation and rotation. For 2D elastic material, the components of Green strain tensor ϵ^g are formulated as:

$$\begin{aligned}
\epsilon^g_{xx} &= \frac{\partial u}{\partial x} + \frac{1}{2}\left[\left(\frac{\partial u}{\partial x}\right)^2 + \left(\frac{\partial v}{\partial x}\right)^2\right], \\
\epsilon^g_{yy} &= \frac{\partial v}{\partial y} + \frac{1}{2}\left[\left(\frac{\partial u}{\partial y}\right)^2 + \left(\frac{\partial v}{\partial y}\right)^2\right], \\
2\epsilon^g_{xy} &= \left(\frac{\partial u}{\partial y} + \frac{\partial v}{\partial x}\right) + \left(\frac{\partial u}{\partial x}\frac{\partial u}{\partial y} + \frac{\partial v}{\partial x}\frac{\partial v}{\partial y}\right),
\end{aligned} \tag{1.70}$$

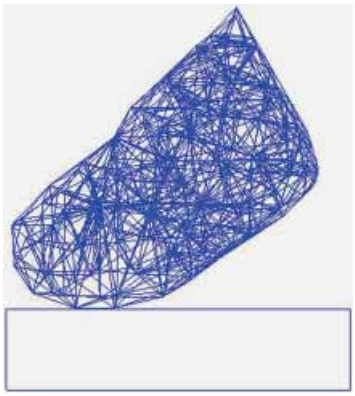

Snapshot at time 0s in 2D view
(a)

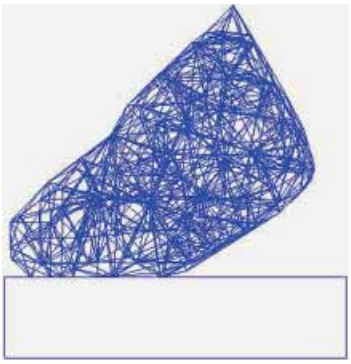

Snapshot at time 0.3s in 2D view
(b)

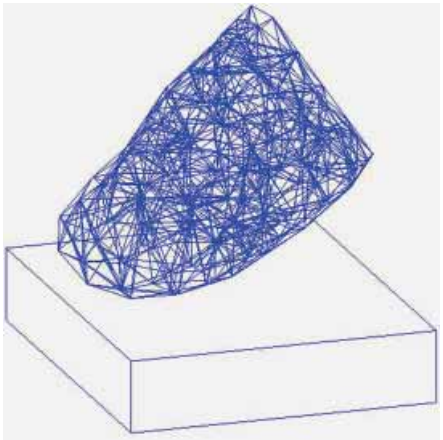

Snapshot at time 0s in 3D view
(c)

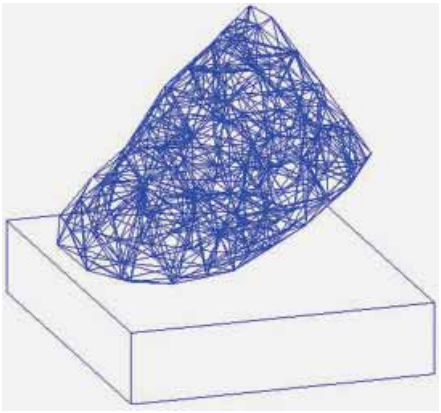

Snapshot at time 0.3s in 3D view
(d)

図 1.15: Simulation behaviors of a 3D finger pushed by an external cube: (a) initial shape in 2D view, (b) deformed shape at 0.3 s in 2D view, (c) initial shape in 3D view, and (d) deformed shape at 0.3 s in 3D view.

where $u(x, y)$ and $v(x, y)$ denote the displacement of arbitrary point $\mathrm{P}(x, y)$ along x-axis and y-axis respectively. Note that neglecting the quadratic part from the right side of the above equation yields the linear Cauchy strain tensor. Again assuming a 2D object composed of elastic material and constructed by a set of triangles, the

strain energy of arbitrary triangle $\triangle \mathrm{P}_i\mathrm{P}_j\mathrm{P}_k$ can be formulated as

$$U_{i,j,k} = \int_{\triangle \mathrm{P}_i\mathrm{P}_j\mathrm{P}_k} \frac{1}{2} \left(\epsilon^g\right)^{\mathrm{T}} \left(\lambda \mathbf{I}_\lambda + \mu \mathbf{I}_\mu\right) \epsilon^g h \, \mathrm{d}S. \tag{1.71}$$

Substituting Eq. 1.35 into the above equation and considering $\epsilon^g = \left[\epsilon^g_{xx}, \epsilon^g_{yy}, 2\epsilon^g_{xy}\right]^{\mathrm{T}}$, we have

$$U_{i,j,k} = U^\lambda_{i,j,k} + U^\mu_{i,j,k}, \tag{1.72}$$

where

$$\begin{aligned} U^\lambda_{i,j,k} &= \int_{\triangle \mathrm{P}_i\mathrm{P}_j\mathrm{P}_k} \frac{1}{2}\lambda \left(\epsilon^g_{xx} + \epsilon^g_{yy}\right)^2 h \, \mathrm{d}S, \\ U^\mu_{i,j,k} &= \int_{\triangle \mathrm{P}_i\mathrm{P}_j\mathrm{P}_k} \frac{1}{2}\mu \left[2\left(\epsilon^g_{xx}\right)^2 + 2\left(\epsilon^g_{yy}\right)^2 + \left(2\epsilon^g_{xy}\right)^2\right] h \, \mathrm{d}S. \end{aligned} \tag{1.73}$$

In the region of $\triangle \mathrm{P}_i\mathrm{P}_j\mathrm{P}_k$, displacement vector $\mathbf{u}_{\mathrm{P}} = [u, v]^{\mathrm{T}}$ at arbitrary point P inside $\triangle \mathrm{P}_i\mathrm{P}_j\mathrm{P}_k$ can be approximated by a linear combination of nodal displacements $\mathbf{u}_i = [u_i, v_i]^{\mathrm{T}}$, $\mathbf{u}_j = [u_j, v_j]^{\mathrm{T}}$, and $\mathbf{u}_k = [u_k, v_k]^{\mathrm{T}}$ as follows:

$$\begin{aligned} u &= u_i N_{i,j,k} + u_j N_{j,k,i} + u_k N_{k,i,j}, \\ v &= v_i N_{i,j,k} + v_j N_{j,k,i} + v_k N_{k,i,j}, \end{aligned} \tag{1.74}$$

where $N_{i,j,k}$, $N_{j,k,i}$, and $N_{k,i,j}$ are the interpolating shape functions. Each of them has a value of 1 at each nodal point P_i, P_j, or P_k, respectively and zeros at all other nodal points. Taking partial derivatives of u and v relative to x and y respectively, we have

$$\begin{aligned} \frac{\partial u}{\partial x} &= u_i \frac{\partial N_{i,j,k}}{\partial x} + u_j \frac{\partial N_{j,k,i}}{\partial x} + u_k \frac{\partial N_{k,i,j}}{\partial x}, \\ \frac{\partial u}{\partial y} &= u_i \frac{\partial N_{i,j,k}}{\partial y} + u_j \frac{\partial N_{j,k,i}}{\partial y} + u_k \frac{\partial N_{k,i,j}}{\partial y}, \\ \frac{\partial v}{\partial x} &= v_i \frac{\partial N_{i,j,k}}{\partial x} + v_j \frac{\partial N_{j,k,i}}{\partial x} + v_k \frac{\partial N_{k,i,j}}{\partial x}, \\ \frac{\partial v}{\partial y} &= v_i \frac{\partial N_{i,j,k}}{\partial y} + v_j \frac{\partial N_{j,k,i}}{\partial y} + v_k \frac{\partial N_{k,i,j}}{\partial y}. \end{aligned} \tag{1.75}$$

Let $[\xi_i, \eta_i]^{\mathrm{T}}$, $[\xi_j, \eta_j]^{\mathrm{T}}$, and $[\xi_k, \eta_k]^{\mathrm{T}}$ be initial coordinates of nodal points P_i, P_j, and P_k, respectively. Partial derivatives of shape functions in Eq. 1.75 can be calculated

as:

$$
\begin{aligned}
N_{ix} &= \frac{\partial N_{i,j,k}}{\partial x} = \frac{\eta_j - \eta_k}{2\triangle}, \quad N_{iy} = \frac{\partial N_{i,j,k}}{\partial y} = -\frac{\xi_j - \xi_k}{2\triangle}, \\
N_{jx} &= \frac{\partial N_{j,k,i}}{\partial x} = \frac{\eta_k - \eta_i}{2\triangle}, \quad N_{jy} = \frac{\partial N_{j,k,i}}{\partial y} = -\frac{\xi_k - \xi_i}{2\triangle}, \\
N_{kx} &= \frac{\partial N_{k,i,j}}{\partial x} = \frac{\eta_i - \eta_j}{2\triangle}, \quad N_{ky} = \frac{\partial N_{k,i,j}}{\partial y} = -\frac{\xi_i - \xi_j}{2\triangle},
\end{aligned} \tag{1.76}
$$

where $\triangle$ denotes the area of triangle $\triangle \mathrm{P}_i\mathrm{P}_j\mathrm{P}_k$. Substituting Eqs. 1.75 and 1.76 into Eq. 1.70, we have

$$
\begin{aligned}
\epsilon^g_{xx} &= \alpha^{\mathrm{T}}\mathbf{q}, \\
\epsilon^g_{yy} &= \beta^{\mathrm{T}}\mathbf{q}, \\
2\epsilon^g_{xy} &= \zeta^{\mathrm{T}}\mathbf{q},
\end{aligned} \tag{1.77}
$$

where

$$
\alpha = \begin{bmatrix}
N_{ix} \\ 0 \\ N_{jx} \\ 0 \\ N_{kx} \\ 0 \\ \frac{1}{2}(N_{ix})^2 \\ \frac{1}{2}(N_{ix})^2 \\ \frac{1}{2}(N_{jx})^2 \\ \frac{1}{2}(N_{jx})^2 \\ \frac{1}{2}(N_{kx})^2 \\ \frac{1}{2}(N_{kx})^2 \\ N_{jx}N_{kx} \\ N_{jx}N_{kx} \\ N_{kx}N_{ix} \\ N_{kx}N_{ix} \\ N_{ix}N_{jx} \\ N_{ix}N_{jx}
\end{bmatrix}, \beta = \begin{bmatrix}
0 \\ N_{iy} \\ 0 \\ N_{jy} \\ 0 \\ N_{ky} \\ \frac{1}{2}(N_{iy})^2 \\ \frac{1}{2}(N_{iy})^2 \\ \frac{1}{2}(N_{jy})^2 \\ \frac{1}{2}(N_{jy})^2 \\ \frac{1}{2}(N_{ky})^2 \\ \frac{1}{2}(N_{ky})^2 \\ N_{jy}N_{ky} \\ N_{jy}N_{ky} \\ N_{ky}N_{iy} \\ N_{ky}N_{iy} \\ N_{iy}N_{jy} \\ N_{iy}N_{jy}
\end{bmatrix}, \zeta = \begin{bmatrix}
N_{iy} \\ N_{ix} \\ N_{jy} \\ N_{jx} \\ N_{ky} \\ N_{kx} \\ N_{ix}N_{iy} \\ N_{ix}N_{iy} \\ N_{jx}N_{jy} \\ N_{jx}N_{jy} \\ N_{kx}N_{ky} \\ N_{kx}N_{ky} \\ N_{jx}N_{ky} + N_{kx}N_{jy} \\ N_{jx}N_{ky} + N_{kx}N_{jy} \\ N_{kx}N_{iy} + N_{ix}N_{ky} \\ N_{kx}N_{iy} + N_{ix}N_{ky} \\ N_{ix}N_{jy} + N_{jx}N_{iy} \\ N_{ix}N_{jy} + N_{jx}N_{iy}
\end{bmatrix}, \mathbf{q} = \begin{bmatrix}
u_i \\ v_i \\ u_j \\ v_j \\ u_k \\ v_k \\ (u_i)^2 \\ (v_i)^2 \\ (u_j)^2 \\ (v_j)^2 \\ (u_k)^2 \\ (v_k)^2 \\ u_j u_k \\ v_j v_k \\ u_k u_i \\ v_k v_i \\ u_i u_j \\ v_i v_j
\end{bmatrix}. \tag{1.78}
$$

Substituting Eq. 1.77 into Eq. 1.73 and taking the partial derivative of Eq. 1.72 relative to displacement vector $\mathbf{u}_{i,j,k} = [u_i, v_i, u_j, v_j, u_k, v_k]^{\mathrm{T}}$, we have the elastic force

formulation with Green strain tensor as:

$$\mathbf{F}_{ela(g)}^{i,j,k} = \mathbf{F}_{\lambda(g)}^{i,j,k} + \mathbf{F}_{\mu(g)}^{i,j,k}, \tag{1.79}$$

where

$$\begin{aligned}
\mathbf{F}_{\lambda(g)}^{i,j,k} &= \lambda h \triangle \left(\alpha^{\mathrm{T}}\mathbf{q} + \beta^{\mathrm{T}}\mathbf{q}\right) \begin{bmatrix} \alpha^{\mathrm{T}}\frac{\partial \mathbf{q}}{\partial u_i} + \beta^{\mathrm{T}}\frac{\partial \mathbf{q}}{\partial u_i} \\ \alpha^{\mathrm{T}}\frac{\partial \mathbf{q}}{\partial v_i} + \beta^{\mathrm{T}}\frac{\partial \mathbf{q}}{\partial v_i} \\ \alpha^{\mathrm{T}}\frac{\partial \mathbf{q}}{\partial u_j} + \beta^{\mathrm{T}}\frac{\partial \mathbf{q}}{\partial u_j} \\ \alpha^{\mathrm{T}}\frac{\partial \mathbf{q}}{\partial v_j} + \beta^{\mathrm{T}}\frac{\partial \mathbf{q}}{\partial v_j} \\ \alpha^{\mathrm{T}}\frac{\partial \mathbf{q}}{\partial u_k} + \beta^{\mathrm{T}}\frac{\partial \mathbf{q}}{\partial u_k} \\ \alpha^{\mathrm{T}}\frac{\partial \mathbf{q}}{\partial v_k} + \beta^{\mathrm{T}}\frac{\partial \mathbf{q}}{\partial v_k} \end{bmatrix}, \\
\mathbf{F}_{\mu(g)}^{i,j,k} &= \mu h \triangle \begin{bmatrix} 2\left(\alpha^{\mathrm{T}}\mathbf{q}\right)\left(\alpha^{\mathrm{T}}\frac{\partial \mathbf{q}}{\partial u_i}\right) + 2\left(\beta^{\mathrm{T}}\mathbf{q}\right)\left(\beta^{\mathrm{T}}\frac{\partial \mathbf{q}}{\partial u_i}\right) + \left(\zeta^{\mathrm{T}}\mathbf{q}\right)\left(\zeta^{\mathrm{T}}\frac{\partial \mathbf{q}}{\partial u_i}\right) \\ 2\left(\alpha^{\mathrm{T}}\mathbf{q}\right)\left(\alpha^{\mathrm{T}}\frac{\partial \mathbf{q}}{\partial v_i}\right) + 2\left(\beta^{\mathrm{T}}\mathbf{q}\right)\left(\beta^{\mathrm{T}}\frac{\partial \mathbf{q}}{\partial v_i}\right) + \left(\zeta^{\mathrm{T}}\mathbf{q}\right)\left(\zeta^{\mathrm{T}}\frac{\partial \mathbf{q}}{\partial v_i}\right) \\ 2\left(\alpha^{\mathrm{T}}\mathbf{q}\right)\left(\alpha^{\mathrm{T}}\frac{\partial \mathbf{q}}{\partial u_j}\right) + 2\left(\beta^{\mathrm{T}}\mathbf{q}\right)\left(\beta^{\mathrm{T}}\frac{\partial \mathbf{q}}{\partial u_j}\right) + \left(\zeta^{\mathrm{T}}\mathbf{q}\right)\left(\zeta^{\mathrm{T}}\frac{\partial \mathbf{q}}{\partial u_j}\right) \\ 2\left(\alpha^{\mathrm{T}}\mathbf{q}\right)\left(\alpha^{\mathrm{T}}\frac{\partial \mathbf{q}}{\partial v_j}\right) + 2\left(\beta^{\mathrm{T}}\mathbf{q}\right)\left(\beta^{\mathrm{T}}\frac{\partial \mathbf{q}}{\partial v_j}\right) + \left(\zeta^{\mathrm{T}}\mathbf{q}\right)\left(\zeta^{\mathrm{T}}\frac{\partial \mathbf{q}}{\partial v_j}\right) \\ 2\left(\alpha^{\mathrm{T}}\mathbf{q}\right)\left(\alpha^{\mathrm{T}}\frac{\partial \mathbf{q}}{\partial u_k}\right) + 2\left(\beta^{\mathrm{T}}\mathbf{q}\right)\left(\beta^{\mathrm{T}}\frac{\partial \mathbf{q}}{\partial u_k}\right) + \left(\zeta^{\mathrm{T}}\mathbf{q}\right)\left(\zeta^{\mathrm{T}}\frac{\partial \mathbf{q}}{\partial u_k}\right) \\ 2\left(\alpha^{\mathrm{T}}\mathbf{q}\right)\left(\alpha^{\mathrm{T}}\frac{\partial \mathbf{q}}{\partial v_k}\right) + 2\left(\beta^{\mathrm{T}}\mathbf{q}\right)\left(\beta^{\mathrm{T}}\frac{\partial \mathbf{q}}{\partial v_k}\right) + \left(\zeta^{\mathrm{T}}\mathbf{q}\right)\left(\zeta^{\mathrm{T}}\frac{\partial \mathbf{q}}{\partial v_k}\right) \end{bmatrix}.
\end{aligned} \tag{1.80}$$

Substituting vectors α, β, ζ, and $\mathbf{q}$ of Eq. 1.78 into the above equation and performing a series of transformations, we can end up with a formulation of elastic forces with green strain as follows, which has a similar form with Eq. 1.47:

$$\mathbf{F}_{ela(g)}^{i,j,k} = \left(\lambda \mathbf{J}_{\lambda(g)}^{i,j,k} + \mu \mathbf{J}_{\mu(g)}^{i,j,k}\right) \mathbf{u}_{i,j,k}, \tag{1.81}$$

where

$$\begin{aligned}
\mathbf{J}_{\lambda(g)}^{i,j,k} &= \mathbf{J}_{\lambda}^{cons} + \mathbf{J}_{\lambda}^{var1} + \mathbf{J}_{\lambda}^{var2}, \\
\mathbf{J}_{\mu(g)}^{i,j,k} &= \mathbf{J}_{\mu}^{cons} + \mathbf{J}_{\mu}^{var1} + \mathbf{J}_{\mu}^{var2},
\end{aligned} \tag{1.82}$$

with constant matrices $\mathbf{J}_\lambda^{cons}$ and $\mathbf{J}_\mu^{cons}$ given by:

$$\mathbf{J}_\lambda^{cons} = h\triangle \begin{bmatrix} N_{ix}^2 & N_{ix}N_{iy} & N_{ix}N_{jx} & N_{ix}N_{jy} & N_{ix}N_{kx} & N_{ix}N_{ky} \\ N_{iy}N_{ix} & N_{iy}^2 & N_{iy}N_{jx} & N_{iy}N_{jy} & N_{iy}N_{kx} & N_{iy}N_{ky} \\ N_{jx}N_{ix} & N_{jx}N_{iy} & N_{jx}^2 & N_{jx}N_{jy} & N_{jx}N_{kx} & N_{jx}N_{ky} \\ N_{jy}N_{ix} & N_{jy}N_{iy} & N_{jy}N_{jx} & N_{jy}^2 & N_{jy}N_{kx} & N_{jy}N_{ky} \\ N_{kx}N_{ix} & N_{kx}N_{iy} & N_{kx}N_{jx} & N_{kx}N_{jy} & N_{kx}^2 & N_{kx}N_{ky} \\ N_{ky}N_{ix} & N_{ky}N_{iy} & N_{ky}N_{jx} & N_{ky}N_{jy} & N_{ky}N_{kx} & N_{ky}^2 \end{bmatrix},$$

$$\mathbf{J}_\mu^{cons} = h\triangle \begin{bmatrix} 2N_{ix}^2 + N_{iy}^2 & N_{iy}N_{ix} & 2N_{ix}N_{jx} + N_{iy}N_{jy} \\ N_{ix}N_{iy} & 2N_{iy}^2 + N_{ix}^2 & N_{ix}N_{jy} \\ 2N_{jx}N_{ix} + N_{jy}N_{iy} & N_{jy}N_{ix} & 2N_{jx}^2 + N_{jy}^2 \\ N_{jx}N_{iy} & 2N_{jy}N_{iy} + N_{jx}N_{ix} & N_{jx}N_{jy} \\ 2N_{kx}N_{ix} + N_{ky}N_{iy} & N_{ky}N_{ix} & 2N_{kx}N_{jx} + N_{ky}N_{jy} \\ N_{kx}N_{iy} & 2N_{ky}N_{iy} + N_{kx}N_{ix} & N_{kx}N_{jy} \end{bmatrix} \tag{1.83}$$

$$\begin{bmatrix} N_{iy}N_{jx} & 2N_{ix}N_{kx} + N_{iy}N_{ky} & N_{iy}N_{kx} \\ 2N_{iy}N_{jy} + N_{ix}N_{jx} & N_{ix}N_{ky} & 2N_{iy}N_{ky} + N_{ix}N_{kx} \\ N_{jy}N_{jx} & 2N_{jx}N_{kx} + N_{jy}N_{ky} & N_{jy}N_{kx} \\ 2N_{jy}^2 + N_{jx}^2 & N_{jx}N_{ky} & 2N_{jy}N_{ky} + N_{jx}N_{kx} \\ N_{ky}N_{jx} & 2N_{kx}^2 + N_{ky}^2 & N_{ky}N_{kx} \\ 2N_{ky}N_{jy} + N_{kx}N_{jx} & N_{kx}N_{ky} & 2N_{ky}^2 + N_{kx}^2 \end{bmatrix}.$$

Time-varying matrices $\mathbf{J}_{\lambda}^{var1}$ and $\mathbf{J}_{\mu}^{var1}$ have the following symmetrical forms:

$$\mathbf{J}_{\lambda}^{var1} = h\triangle\left(\alpha^{\mathrm{T}}\mathbf{q}+\beta^{\mathrm{T}}\mathbf{q}\right)\left[\begin{array}{ccc} N_{ix}^2+N_{iy}^2 & 0 & 2N_{ix}N_{jx}+N_{iy}N_{jy} \\ 0 & N_{iy}^2+N_{ix}^2 & 0 \\ N_{jx}N_{ix}+N_{jy}N_{iy} & 0 & N_{jx}^2+N_{jy}^2 \\ 0 & N_{jy}N_{iy}+N_{jx}N_{ix} & 0 \\ N_{kx}N_{ix}+N_{ky}N_{iy} & 0 & N_{kx}N_{jx}+N_{ky}N_{jy} \\ 0 & N_{ky}N_{iy}+N_{kx}N_{ix} & 0 \end{array}\right.$$
$$\left.\begin{array}{ccc} 0 & N_{ix}N_{kx}+N_{iy}N_{ky} & 0 \\ N_{iy}N_{jy}+N_{ix}N_{jx} & 0 & N_{iy}N_{ky}+N_{ix}N_{kx} \\ 0 & N_{jx}N_{kx}+N_{jy}N_{ky} & 0 \\ N_{jy}^2+N_{jx}^2 & 0 & N_{jy}N_{ky}+N_{jx}N_{kx} \\ 0 & N_{kx}^2+N_{ky}^2 & 0 \\ N_{ky}N_{jy}+N_{kx}N_{jx} & 0 & N_{ky}^2+N_{kx}^2 \end{array}\right].$$

$$\mathbf{J}_{\mu}^{var1} = 2h\triangle\left(\alpha^{\mathrm{T}}\mathbf{q}\right)\left[\begin{array}{cccccc} N_{ix}^2 & 0 & N_{ix}N_{jx} & 0 & N_{ix}N_{kx} & 0 \\ 0 & N_{ix}^2 & 0 & N_{ix}N_{jx} & 0 & N_{ix}N_{kx} \\ N_{jx}N_{ix} & 0 & N_{jx}^2 & 0 & N_{jx}N_{kx} & 0 \\ 0 & N_{jx}N_{ix} & 0 & N_{jx}^2 & 0 & N_{jx}N_{kx} \\ N_{kx}N_{ix} & 0 & N_{kx}N_{jx} & 0 & N_{kx}^2 & 0 \\ 0 & N_{kx}N_{ix} & 0 & N_{kx}N_{jx} & 0 & N_{kx}^2 \end{array}\right]$$
$$+2h\triangle\left(\beta^{\mathrm{T}}\mathbf{q}\right)\left[\begin{array}{cccccc} N_{iy}^2 & 0 & N_{iy}N_{jy} & 0 & N_{iy}N_{ky} & 0 \\ 0 & N_{iy}^2 & 0 & N_{iy}N_{jy} & 0 & N_{iy}N_{ky} \\ N_{jy}N_{iy} & 0 & N_{jy}^2 & 0 & N_{jy}N_{ky} & 0 \\ 0 & N_{jy}N_{iy} & 0 & N_{jy}^2 & 0 & N_{jy}N_{ky} \\ N_{ky}N_{iy} & 0 & N_{ky}N_{jy} & 0 & N_{ky}^2 & 0 \\ 0 & N_{ky}N_{iy} & 0 & N_{ky}N_{jy} & 0 & N_{ky}^2 \end{array}\right]$$
$$+h\triangle\left(\gamma^{\mathrm{T}}\mathbf{q}\right)\left[\begin{array}{ccc} 2N_{ix}N_{iy} & 0 & N_{ix}N_{jy}+N_{jx}N_{iy} \\ 0 & 2N_{ix}N_{iy} & 0 \\ N_{jx}N_{iy}+N_{ix}N_{jy} & 0 & 2N_{jx}N_{jy} \\ 0 & N_{jx}N_{iy}+N_{ix}N_{jy} & 0 \\ N_{kx}N_{iy}+N_{ix}N_{ky} & 0 & N_{kx}N_{jy}+N_{jx}N_{ky} \\ 0 & N_{kx}N_{iy}+N_{ix}N_{ky} & 0 \end{array}\right.$$
$$\left.\begin{array}{ccc} 0 & N_{ix}N_{ky}+N_{kx}N_{iy} & 0 \\ N_{ix}N_{jy}+N_{jx}N_{iy} & 0 & N_{ix}N_{ky}+N_{kx}N_{iy} \\ 0 & N_{jx}N_{ky}+N_{kx}N_{jy} & 0 \\ 2N_{jy}N_{jx} & 0 & N_{jx}N_{ky}+N_{kx}N_{jy} \\ 0 & 2N_{kx}N_{ky} & 0 \\ N_{kx}N_{jy}+N_{jx}N_{ky} & 0 & 2N_{kx}N_{ky} \end{array}\right]. \tag{1.84}$$

Time-varying matrices $\mathbf{J}_{\lambda}^{var2}$ and $\mathbf{J}_{\mu}^{var2}$ have the following unsymmetrical forms:

$$\mathbf{J}_{\lambda}^{var2}=\frac{h\triangle}{2}\left[\begin{array}{ccc}
N_{ix}(\mathbf{H}_1^{\alpha}+\mathbf{H}_1^{\beta})^{\mathrm{T}}\mathbf{u}_{i,j,k} & N_{ix}(\mathbf{H}_2^{\alpha}+\mathbf{H}_2^{\beta})^{\mathrm{T}}\mathbf{u}_{i,j,k} & N_{ix}(\mathbf{H}_3^{\alpha}+\mathbf{H}_3^{\beta})^{\mathrm{T}}\mathbf{u}_{i,j,k}\\
N_{iy}(\mathbf{H}_1^{\alpha}+\mathbf{H}_1^{\beta})^{\mathrm{T}}\mathbf{u}_{i,j,k} & N_{iy}(\mathbf{H}_2^{\alpha}+\mathbf{H}_2^{\beta})^{\mathrm{T}}\mathbf{u}_{i,j,k} & N_{iy}(\mathbf{H}_3^{\alpha}+\mathbf{H}_3^{\beta})^{\mathrm{T}}\mathbf{u}_{i,j,k}\\
N_{jx}(\mathbf{H}_1^{\alpha}+\mathbf{H}_1^{\beta})^{\mathrm{T}}\mathbf{u}_{i,j,k} & N_{jx}(\mathbf{H}_2^{\alpha}+\mathbf{H}_2^{\beta})^{\mathrm{T}}\mathbf{u}_{i,j,k} & N_{jx}(\mathbf{H}_3^{\alpha}+\mathbf{H}_3^{\beta})^{\mathrm{T}}\mathbf{u}_{i,j,k}\\
N_{jy}(\mathbf{H}_1^{\alpha}+\mathbf{H}_1^{\beta})^{\mathrm{T}}\mathbf{u}_{i,j,k} & N_{jy}(\mathbf{H}_2^{\alpha}+\mathbf{H}_2^{\beta})^{\mathrm{T}}\mathbf{u}_{i,j,k} & N_{jy}(\mathbf{H}_3^{\alpha}+\mathbf{H}_3^{\beta})^{\mathrm{T}}\mathbf{u}_{i,j,k}\\
N_{kx}(\mathbf{H}_1^{\alpha}+\mathbf{H}_1^{\beta})^{\mathrm{T}}\mathbf{u}_{i,j,k} & N_{kx}(\mathbf{H}_2^{\alpha}+\mathbf{H}_2^{\beta})^{\mathrm{T}}\mathbf{u}_{i,j,k} & N_{kx}(\mathbf{H}_3^{\alpha}+\mathbf{H}_3^{\beta})^{\mathrm{T}}\mathbf{u}_{i,j,k}\\
N_{ky}(\mathbf{H}_1^{\alpha}+\mathbf{H}_1^{\beta})^{\mathrm{T}}\mathbf{u}_{i,j,k} & N_{ky}(\mathbf{H}_2^{\alpha}+\mathbf{H}_2^{\beta})^{\mathrm{T}}\mathbf{u}_{i,j,k} & N_{ky}(\mathbf{H}_3^{\alpha}+\mathbf{H}_3^{\beta})^{\mathrm{T}}\mathbf{u}_{i,j,k}
\end{array}\right.$$

$$\left.\begin{array}{ccc}
N_{ix}(\mathbf{H}_4^{\alpha}+\mathbf{H}_4^{\beta})^{\mathrm{T}}\mathbf{u}_{i,j,k} & N_{ix}(\mathbf{H}_5^{\alpha}+\mathbf{H}_5^{\beta})^{\mathrm{T}}\mathbf{u}_{i,j,k} & N_{ix}(\mathbf{H}_6^{\alpha}+\mathbf{H}_6^{\beta})^{\mathrm{T}}\mathbf{u}_{i,j,k}\\
N_{iy}(\mathbf{H}_4^{\alpha}+\mathbf{H}_4^{\beta})^{\mathrm{T}}\mathbf{u}_{i,j,k} & N_{iy}(\mathbf{H}_5^{\alpha}+\mathbf{H}_5^{\beta})^{\mathrm{T}}\mathbf{u}_{i,j,k} & N_{iy}(\mathbf{H}_6^{\alpha}+\mathbf{H}_6^{\beta})^{\mathrm{T}}\mathbf{u}_{i,j,k}\\
N_{jx}(\mathbf{H}_4^{\alpha}+\mathbf{H}_4^{\beta})^{\mathrm{T}}\mathbf{u}_{i,j,k} & N_{jx}(\mathbf{H}_5^{\alpha}+\mathbf{H}_5^{\beta})^{\mathrm{T}}\mathbf{u}_{i,j,k} & N_{jx}(\mathbf{H}_6^{\alpha}+\mathbf{H}_6^{\beta})^{\mathrm{T}}\mathbf{u}_{i,j,k}\\
N_{jy}(\mathbf{H}_4^{\alpha}+\mathbf{H}_4^{\beta})^{\mathrm{T}}\mathbf{u}_{i,j,k} & N_{jy}(\mathbf{H}_5^{\alpha}+\mathbf{H}_5^{\beta})^{\mathrm{T}}\mathbf{u}_{i,j,k} & N_{jy}(\mathbf{H}_6^{\alpha}+\mathbf{H}_6^{\beta})^{\mathrm{T}}\mathbf{u}_{i,j,k}\\
N_{kx}(\mathbf{H}_4^{\alpha}+\mathbf{H}_4^{\beta})^{\mathrm{T}}\mathbf{u}_{i,j,k} & N_{kx}(\mathbf{H}_5^{\alpha}+\mathbf{H}_5^{\beta})^{\mathrm{T}}\mathbf{u}_{i,j,k} & N_{kx}(\mathbf{H}_6^{\alpha}+\mathbf{H}_6^{\beta})^{\mathrm{T}}\mathbf{u}_{i,j,k}\\
N_{ky}(\mathbf{H}_4^{\alpha}+\mathbf{H}_4^{\beta})^{\mathrm{T}}\mathbf{u}_{i,j,k} & N_{ky}(\mathbf{H}_5^{\alpha}+\mathbf{H}_5^{\beta})^{\mathrm{T}}\mathbf{u}_{i,j,k} & N_{ky}(\mathbf{H}_6^{\alpha}+\mathbf{H}_6^{\beta})^{\mathrm{T}}\mathbf{u}_{i,j,k}
\end{array}\right],$$

$$\mathbf{J}_{\mu}^{var2}=\frac{h\triangle}{2}\left[\begin{array}{ccc}
2N_{ix}(\mathbf{H}_1^{\alpha})^{\mathrm{T}}\mathbf{u}_{i,j,k}+N_{iy}(\mathbf{H}_1^{\zeta})^{\mathrm{T}}\mathbf{u}_{i,j,k} & 2N_{ix}(\mathbf{H}_2^{\alpha})^{\mathrm{T}}\mathbf{u}_{i,j,k}+N_{iy}(\mathbf{H}_2^{\zeta})^{\mathrm{T}}\mathbf{u}_{i,j,k}\\
2N_{iy}(\mathbf{H}_1^{\beta})^{\mathrm{T}}\mathbf{u}_{i,j,k}+N_{ix}(\mathbf{H}_1^{\zeta})^{\mathrm{T}}\mathbf{u}_{i,j,k} & 2N_{iy}(\mathbf{H}_2^{\beta})^{\mathrm{T}}\mathbf{u}_{i,j,k}+N_{ix}(\mathbf{H}_2^{\zeta})^{\mathrm{T}}\mathbf{u}_{i,j,k}\\
2N_{jx}(\mathbf{H}_1^{\alpha})^{\mathrm{T}}\mathbf{u}_{i,j,k}+N_{jy}(\mathbf{H}_1^{\zeta})^{\mathrm{T}}\mathbf{u}_{i,j,k} & 2N_{jx}(\mathbf{H}_2^{\alpha})^{\mathrm{T}}\mathbf{u}_{i,j,k}+N_{jy}(\mathbf{H}_2^{\zeta})^{\mathrm{T}}\mathbf{u}_{i,j,k}\\
2N_{jy}(\mathbf{H}_1^{\beta})^{\mathrm{T}}\mathbf{u}_{i,j,k}+N_{jx}(\mathbf{H}_1^{\zeta})^{\mathrm{T}}\mathbf{u}_{i,j,k} & 2N_{jy}(\mathbf{H}_2^{\beta})^{\mathrm{T}}\mathbf{u}_{i,j,k}+N_{jx}(\mathbf{H}_2^{\zeta})^{\mathrm{T}}\mathbf{u}_{i,j,k}\\
2N_{kx}(\mathbf{H}_1^{\alpha})^{\mathrm{T}}\mathbf{u}_{i,j,k}+N_{ky}(\mathbf{H}_1^{\zeta})^{\mathrm{T}}\mathbf{u}_{i,j,k} & 2N_{kx}(\mathbf{H}_2^{\alpha})^{\mathrm{T}}\mathbf{u}_{i,j,k}+N_{ky}(\mathbf{H}_2^{\zeta})^{\mathrm{T}}\mathbf{u}_{i,j,k}\\
2N_{ky}(\mathbf{H}_1^{\beta})^{\mathrm{T}}\mathbf{u}_{i,j,k}+N_{kx}(\mathbf{H}_1^{\zeta})^{\mathrm{T}}\mathbf{u}_{i,j,k} & 2N_{ky}(\mathbf{H}_2^{\beta})^{\mathrm{T}}\mathbf{u}_{i,j,k}+N_{kx}(\mathbf{H}_2^{\zeta})^{\mathrm{T}}\mathbf{u}_{i,j,k}
\end{array}\right.$$

$$\left.\begin{array}{ccc}
2N_{ix}(\mathbf{H}_3^{\alpha})^{\mathrm{T}}\mathbf{u}_{i,j,k}+N_{iy}(\mathbf{H}_3^{\zeta})^{\mathrm{T}}\mathbf{u}_{i,j,k} & 2N_{ix}(\mathbf{H}_4^{\alpha})^{\mathrm{T}}\mathbf{u}_{i,j,k}+N_{iy}(\mathbf{H}_4^{\zeta})^{\mathrm{T}}\mathbf{u}_{i,j,k}\\
2N_{iy}(\mathbf{H}_3^{\beta})^{\mathrm{T}}\mathbf{u}_{i,j,k}+N_{ix}(\mathbf{H}_3^{\zeta})^{\mathrm{T}}\mathbf{u}_{i,j,k} & 2N_{iy}(\mathbf{H}_4^{\beta})^{\mathrm{T}}\mathbf{u}_{i,j,k}+N_{ix}(\mathbf{H}_4^{\zeta})^{\mathrm{T}}\mathbf{u}_{i,j,k}\\
2N_{jx}(\mathbf{H}_3^{\alpha})^{\mathrm{T}}\mathbf{u}_{i,j,k}+N_{jy}(\mathbf{H}_3^{\zeta})^{\mathrm{T}}\mathbf{u}_{i,j,k} & 2N_{jx}(\mathbf{H}_4^{\alpha})^{\mathrm{T}}\mathbf{u}_{i,j,k}+N_{jy}(\mathbf{H}_4^{\zeta})^{\mathrm{T}}\mathbf{u}_{i,j,k}\\
2N_{jy}(\mathbf{H}_3^{\beta})^{\mathrm{T}}\mathbf{u}_{i,j,k}+N_{jx}(\mathbf{H}_3^{\zeta})^{\mathrm{T}}\mathbf{u}_{i,j,k} & 2N_{jy}(\mathbf{H}_4^{\beta})^{\mathrm{T}}\mathbf{u}_{i,j,k}+N_{jx}(\mathbf{H}_4^{\zeta})^{\mathrm{T}}\mathbf{u}_{i,j,k}\\
2N_{kx}(\mathbf{H}_3^{\alpha})^{\mathrm{T}}\mathbf{u}_{i,j,k}+N_{ky}(\mathbf{H}_3^{\zeta})^{\mathrm{T}}\mathbf{u}_{i,j,k} & 2N_{kx}(\mathbf{H}_4^{\alpha})^{\mathrm{T}}\mathbf{u}_{i,j,k}+N_{ky}(\mathbf{H}_4^{\zeta})^{\mathrm{T}}\mathbf{u}_{i,j,k}\\
2N_{ky}(\mathbf{H}_3^{\beta})^{\mathrm{T}}\mathbf{u}_{i,j,k}+N_{kx}(\mathbf{H}_3^{\zeta})^{\mathrm{T}}\mathbf{u}_{i,j,k} & 2N_{ky}(\mathbf{H}_4^{\beta})^{\mathrm{T}}\mathbf{u}_{i,j,k}+N_{kx}(\mathbf{H}_4^{\zeta})^{\mathrm{T}}\mathbf{u}_{i,j,k}
\end{array}\right.$$

$$\left.\begin{array}{ccc}
2N_{ix}(\mathbf{H}_5^{\alpha})^{\mathrm{T}}\mathbf{u}_{i,j,k}+N_{iy}(\mathbf{H}_5^{\zeta})^{\mathrm{T}}\mathbf{u}_{i,j,k} & 2N_{ix}(\mathbf{H}_6^{\alpha})^{\mathrm{T}}\mathbf{u}_{i,j,k}+N_{iy}(\mathbf{H}_6^{\zeta})^{\mathrm{T}}\mathbf{u}_{i,j,k}\\
2N_{iy}(\mathbf{H}_5^{\beta})^{\mathrm{T}}\mathbf{u}_{i,j,k}+N_{ix}(\mathbf{H}_5^{\zeta})^{\mathrm{T}}\mathbf{u}_{i,j,k} & 2N_{iy}(\mathbf{H}_6^{\beta})^{\mathrm{T}}\mathbf{u}_{i,j,k}+N_{ix}(\mathbf{H}_6^{\zeta})^{\mathrm{T}}\mathbf{u}_{i,j,k}\\
2N_{jx}(\mathbf{H}_5^{\alpha})^{\mathrm{T}}\mathbf{u}_{i,j,k}+N_{jy}(\mathbf{H}_5^{\zeta})^{\mathrm{T}}\mathbf{u}_{i,j,k} & 2N_{jx}(\mathbf{H}_6^{\alpha})^{\mathrm{T}}\mathbf{u}_{i,j,k}+N_{jy}(\mathbf{H}_6^{\zeta})^{\mathrm{T}}\mathbf{u}_{i,j,k}\\
2N_{jy}(\mathbf{H}_5^{\beta})^{\mathrm{T}}\mathbf{u}_{i,j,k}+N_{jx}(\mathbf{H}_5^{\zeta})^{\mathrm{T}}\mathbf{u}_{i,j,k} & 2N_{jy}(\mathbf{H}_6^{\beta})^{\mathrm{T}}\mathbf{u}_{i,j,k}+N_{jx}(\mathbf{H}_6^{\zeta})^{\mathrm{T}}\mathbf{u}_{i,j,k}\\
2N_{kx}(\mathbf{H}_5^{\alpha})^{\mathrm{T}}\mathbf{u}_{i,j,k}+N_{ky}(\mathbf{H}_5^{\zeta})^{\mathrm{T}}\mathbf{u}_{i,j,k} & 2N_{kx}(\mathbf{H}_6^{\alpha})^{\mathrm{T}}\mathbf{u}_{i,j,k}+N_{ky}(\mathbf{H}_6^{\zeta})^{\mathrm{T}}\mathbf{u}_{i,j,k}\\
2N_{ky}(\mathbf{H}_5^{\beta})^{\mathrm{T}}\mathbf{u}_{i,j,k}+N_{kx}(\mathbf{H}_5^{\zeta})^{\mathrm{T}}\mathbf{u}_{i,j,k} & 2N_{ky}(\mathbf{H}_6^{\beta})^{\mathrm{T}}\mathbf{u}_{i,j,k}+N_{kx}(\mathbf{H}_6^{\zeta})^{\mathrm{T}}\mathbf{u}_{i,j,k}
\end{array}\right],\tag{1.85}$$

where

$$\mathbf{H}_1^{\alpha} = \begin{bmatrix} N_{ix}^2 \\ 0 \\ N_{ix}N_{jx} \\ 0 \\ N_{ix}N_{kx} \\ 0 \end{bmatrix}, \quad \mathbf{H}_2^{\alpha} = \begin{bmatrix} 0 \\ N_{ix}^2 \\ 0 \\ N_{ix}N_{jx} \\ 0 \\ N_{ix}N_{kx} \end{bmatrix}, \quad \mathbf{H}_3^{\alpha} = \begin{bmatrix} N_{jx}N_{ix} \\ 0 \\ N_{jx}^2 \\ 0 \\ N_{jx}N_{kx} \\ 0 \end{bmatrix},$$

$$\mathbf{H}_4^{\alpha} = \begin{bmatrix} 0 \\ N_{jx}N_{ix} \\ 0 \\ Njx^2 \\ 0 \\ N_{jx}N_{kx} \end{bmatrix}, \quad \mathbf{H}_5^{\alpha} = \begin{bmatrix} N_{kx}N_{ix} \\ 0 \\ N_{kx}N_{jx} \\ 0 \\ N_{kx}^2 \\ 0 \end{bmatrix}, \quad \mathbf{H}_6^{\alpha} = \begin{bmatrix} 0 \\ N_{kx}N_{ix} \\ 0 \\ N_{kx}N_{jx} \\ 0 \\ N_{kx}^2 \end{bmatrix},$$

$$\mathbf{H}_1^{\beta} = \begin{bmatrix} N_{iy}^2 \\ 0 \\ N_{iy}N_{jy} \\ 0 \\ N_{iy}N_{ky} \\ 0 \end{bmatrix}, \quad \mathbf{H}_2^{\beta} = \begin{bmatrix} 0 \\ N_{iy}^2 \\ 0 \\ N_{iy}N_{jy} \\ 0 \\ N_{iy}N_{ky} \end{bmatrix}, \quad \mathbf{H}_3^{\beta} = \begin{bmatrix} N_{jy}N_{iy} \\ 0 \\ N_{jy}^2 \\ 0 \\ N_{jy}N_{ky} \\ 0 \end{bmatrix},$$

$$\mathbf{H}_4^{\beta} = \begin{bmatrix} 0 \\ N_{jy}N_{iy} \\ 0 \\ Njy^2 \\ 0 \\ N_{jy}N_{ky} \end{bmatrix}, \quad \mathbf{H}_5^{\beta} = \begin{bmatrix} N_{ky}N_{iy} \\ 0 \\ N_{ky}N_{jy} \\ 0 \\ N_{ky}^2 \\ 0 \end{bmatrix}, \quad \mathbf{H}_6^{\beta} = \begin{bmatrix} 0 \\ N_{ky}N_{iy} \\ 0 \\ N_{ky}N_{jy} \\ 0 \\ N_{ky}^2 \end{bmatrix},$$

$$\mathbf{H}_1^{\zeta} = \begin{bmatrix} 2N_{ix}N_{iy} \\ 0 \\ N_{ix}N_{jy} + N_{jx}N_{iy} \\ 0 \\ N_{ix}N_{ky} + N_{kx}N_{iy} \\ 0 \end{bmatrix}, \mathbf{H}_2^{\zeta} = \begin{bmatrix} 0 \\ 2N_{ix}N_{iy} \\ 0 \\ N_{ix}N_{jy} + N_{jx}N_{iy} \\ 0 \\ N_{ix}N_{ky} + N_{kx}N_{iy} \end{bmatrix}, \mathbf{H}_3^{\zeta} = \begin{bmatrix} N_{ix}N_{jy} + N_{jx}N_{iy} \\ 0 \\ 2N_{jx}N_{jy} \\ 0 \\ N_{jx}N_{ky} + N_{kx}N_{jy} \\ 0 \end{bmatrix},$$

$$\mathbf{H}_4^{\zeta} = \begin{bmatrix} 0 \\ N_{ix}N_{jy} + N_{jx}N_{iy} \\ 0 \\ 2N_{jx}N_{jy} \\ 0 \\ N_{jx}N_{ky} + N_{kx}N_{jy} \end{bmatrix}, \mathbf{H}_5^{\zeta} = \begin{bmatrix} N_{ix}N_{ky} + N_{kx}N_{iy} \\ 0 \\ N_{jx}N_{ky} + N_{kx}N_{jy} \\ 0 \\ 2N_{kx}N_{ky} \\ 0 \end{bmatrix}, \mathbf{H}_6^{\zeta} = \begin{bmatrix} 0 \\ N_{ix}N_{ky} + N_{kx}N_{iy} \\ 0 \\ N_{jx}N_{ky} + N_{kx}N_{jy} \\ 02N_{kx}N_{ky} \end{bmatrix}. \tag{1.86}$$

From the above derivations we found that the connection matrices $\mathbf{J}_{\lambda(g)}^{i,j,k}$ and $\mathbf{J}_{\mu(g)}^{i,j,k}$ are no longer constant and depend on the time-varying displacement vector $\mathbf{u}_{i,j,k}$. We were not able to prepare those two matrices before simulation and we have to calculate them at every time step.

二次元レオロジーモデル

Following the same replacement procedure presented in the previous section, we can extend the above elastic model to a rheological model. Performing a series of replacements to Eq. 1.56, we have

$$\begin{aligned}
\dot{\mathbf{F}}_1^g + \frac{E_1}{c_1}\mathbf{F}_1^g &= (\lambda_1^{ela}\mathbf{J}_\lambda^g + \mu_1^{ela}\mathbf{J}_\mu^g)\dot{\mathbf{u}}_N, \\
\dot{\mathbf{F}}_2^g + \frac{E_2}{c_2}\mathbf{F}_2^g &= (\lambda_2^{ela}\mathbf{J}_\lambda^g + \mu_2^{ela}\mathbf{J}_\mu^g)\dot{\mathbf{u}}_N, \\
\mathbf{F}_3^g &= (\lambda_3^{vis}\mathbf{J}_\lambda^g + \mu_3^{vis}\mathbf{J}_\mu^g)\dot{\mathbf{u}}_N, \\
\mathbf{F}_{2D(g)}^{rheo} &= \mathbf{F}_1^g + \mathbf{F}_2^g + \mathbf{F}_3^g,
\end{aligned} \tag{1.87}$$

where superscript g denotes the variables with a formulation of Green strain tensor. Total connection matrices $\mathbf{J}_\lambda^g$ and $\mathbf{J}_\mu^g$ were calculated by incorporating the matrices $\mathbf{J}_{\lambda(g)}^{i,j,k}$ and $\mathbf{J}_{\mu(g)}^{i,j,k}$ of each triangles based on the contribution of each triangle to the whole triangle mesh. Vector $\mathbf{F}_{2D(g)}^{rheo}$ is the rheological forces generated on each nodal point.

For performing an operation on a virtual object, boundary constraints need to be formulated. For example, we suppose a 2D object was fixed on the ground and the top edge or some nodal points were pushed down or pulled up with a displacement function of $\mathbf{d}(t)$. Two boundary constraints on both top and bottom edges can be formulated as given in Eq. 1.58:

Let $\mathbf{M}$ be the inertia matrix of the object and ℓ_1 and ℓ_2 be the Lagrange multipliers which denote a set of constraint forces corresponding to both boundary constraints. Using the Lagrange dynamic method, a set of dynamic equations of all nodal points is formulated as

$$-\mathbf{F}_{2D(g)}^{rheo} + \mathbf{A}\boldsymbol{\ell_1} + \mathbf{B}\boldsymbol{\ell_2} - \mathbf{M}\ddot{\mathbf{u}}_N = 0. \tag{1.88}$$

Combining Eqs. 1.87, 1.58, 1.88, and considering $\mathbf{v}_N = \dot{\mathbf{u}}_N$, we can end up with a set of differential equations which describe the 2D dynamic behaviors of a rheological object formulated with nonlinear Green strain tensor. By numerically solving these equations, we can calculate the deformation and forces at each nodal points of the object.

コーシー歪みとグリーン歪みの比較

In order to show the difference between the linear Cauchy strain and nonlinear Green strain, several FE simulations were performed with formulations of both strain

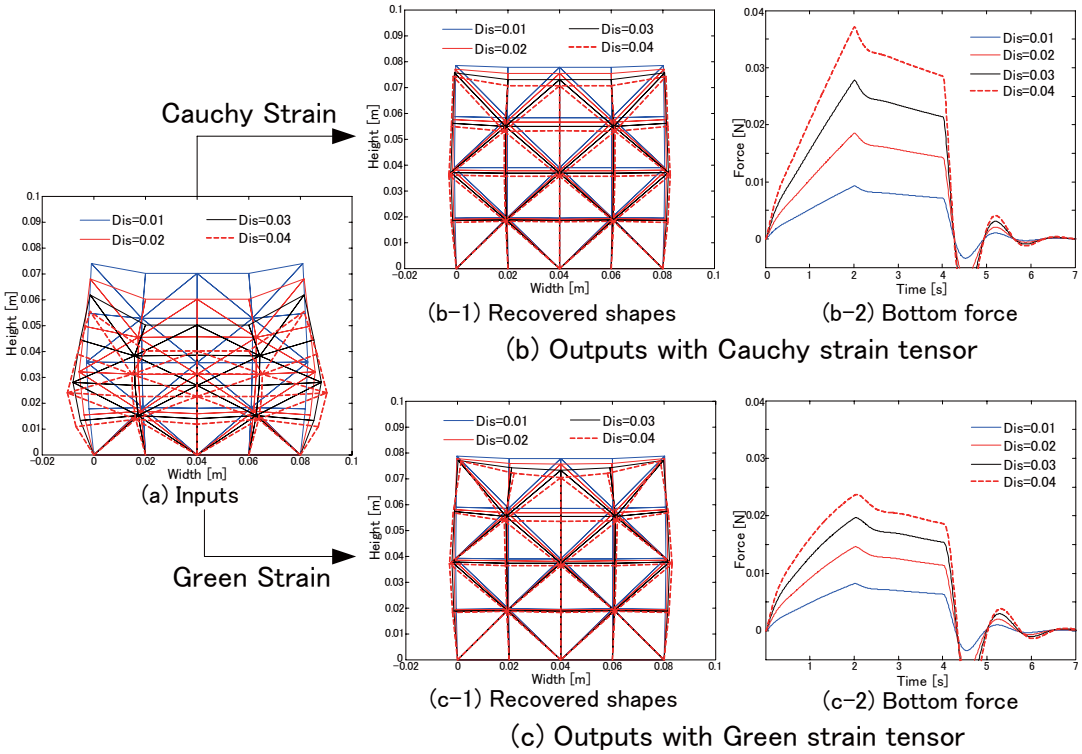

図 1.16: FE simulations of rheological behaviors under an input of different displacements, where the FE models were formulated with (b) Cauchy and (c) Green strain tensors.

tensors. The first simulation is under an input of constant velocities. Within the first 2 seconds, 3 nodal points on the top surface of the objects were pushed downward to a desired displacement of 0.01 m, 0.02 m, 0.03 m, and 0.04 m respectively, as shown in Fig. 1.16a. The deformed shapes were then held unchange for 2 seconds before releasing. The final recovered shapes and force responses from FE models with both strain tensors were shown in Fig. 1.16b and 1.16c. The second simulation was performed with different force inputs acting on the top right corner of the object, as shown in Fig. 1.17a. The force input can be easily incorporated with the above-mentioned FE model by adding an external force vector $\mathbf{F}^{ext}$ into Eq. 1.88. In this simulation, the top right corners of the objects were pulled upward with constant forces for 2 seconds. The deformed objects were then released with 2 seconds for recovery. The deformed and recovered shapes for both strain tensors were shown in Fig. 1.17b and 1.17c respectively.

From Figs. 1.16b and 1.17b we find that linear model with Cauchy strain tensor

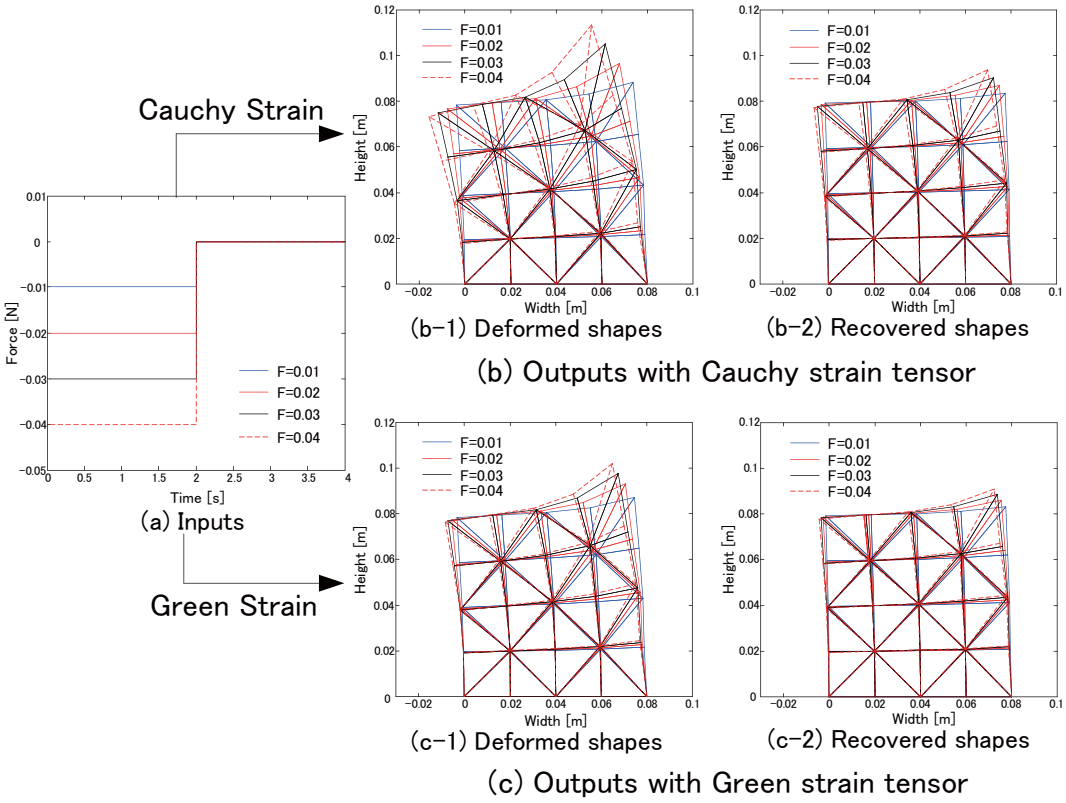

図 1.17: FE simulations of rheological behaviors under an input of different forces, where the FE models were formulated with (b) Cauchy and (c) Green strain tensors.

always yields linear behaviors, *i.e.,* the output is always proportional to the input and no matter the input is force or displacement. However, such behaviors will not happen in real rheological objects when the deformation is getting large. This is the limitation of the linear model. The nonlinear modeling is therefore necessary to cover such large deformation. Figures 1.16c and 1.17c show that output behaviors simulated with Green strain tensor do not have the proportional relationship with the inputs of both forces and displacements. When the inputs take small values (*e.g.,* Dis=0.01 m in Fig. 1.16 and F=0.01 N in Fig. 1.17), the outputs behaviors simulated by Cauchy and Green strain tensors have small differences. However, the differences increased with the increase of input values as shown in Fig. 1.16 and 1.17. Apparently, the simulation results with nonlinear Green strain tensor demonstrate more natural behaviors when the deformation becomes large.

In order to further compare the ability of both models for handling deformation

with rotation motion, pushing and rolling simulations with both models were performed. An object with circular shape is pushed downward by an external instrument for 5 seconds with a constant velocity of 0.01 m/s and then the instrument starts to move left for another 5 seconds with the same velocity. The instrument is then moved upward and let the deformation to recover. The total simulation time is 15 seconds. The material properties of the object are represented by a parallel five-element physical model with parameters: $E_1 = 200\,\text{Pa}$, $E_2 = 500\,\text{Pa}$, $c_1 = 8000\,\text{Pa·s}$, $c_2 = 5000\,\text{Pa·s}$, and $c_3 = 100\,\text{Pa·s}$. Several simulation snapshots using both models are given in Figs. 1.18 and 1.19, respectively. From Fig. 1.18, we find that linear Cauchy strain tensor results in some strange behaviors when simulating deformation with rotation motion. The triangular mesh of the object is expanded during rolling motion which should not happen in a real world object. After recovery, the object become much bigger (Fig. 1.18d) comparing with the initial shape (Fig. 1.18a). On the other hand, the object simulated with nonlinear Green strain does not show such strange behaviors, as shown in Fig. 1.19. We therefore conclude that the nonlinear Green strain tensor provide more natural deformation behaviors comparing with linear Cauchy strain tensor for dealing with large deformation and rotation. The modeling of contact between a rheological object and an external instrument shown in Figs. 1.18 and 1.19 will be introduced in the next section.

1.3.3 多重粘性要素を用いた有限要素モデル

As presented in Section 1.2, a five-element physically-based model with two dual-moduli viscous elements can yield simultaneous reproductions of both rheological forces and deformation behaviors. Now, let us extend the 1D physically-based model to a 2D FE dynamic model.

Recall that a stress-strain relationship in a Maxwell model is described by Eq. 1.48. Thus, replacing viscous coefficient c by dual-moduli viscous coefficient $\kappa\alpha + c$, we have the stress-strain relationship in a Maxwell model with a dual-moduli viscous element as:

$$\dot{\sigma} = -\frac{E}{\kappa\alpha + c}\sigma + E\dot{\epsilon}. \tag{1.89}$$

Then, by performing the same replacements for deriving 2D FE model (Eq. 1.56), we have a 2D FE formulation with a physically-based model including two dual-moduli

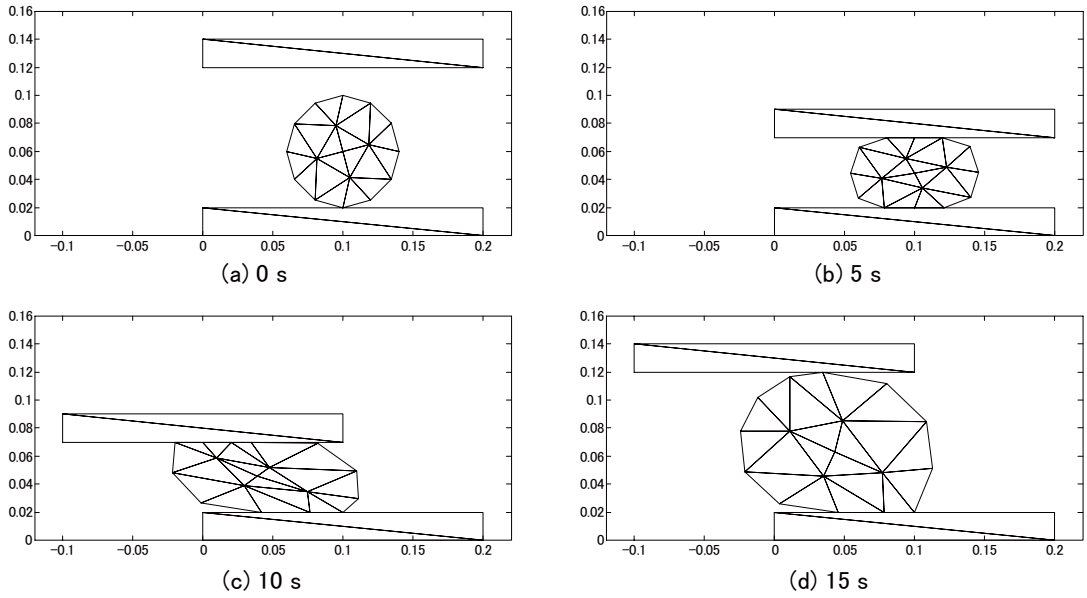

図 1.18: Simulation snapshots of a rheological object pushed and rolled by an external instrument, where the model of the object was formulated by linear Cauchy strain tensor.

viscous elements shown in Fig. 1.12b as:

$$\begin{aligned}
\dot{\mathbf{F}}_1 + \frac{E_1}{\kappa\alpha_1 + c_1}\mathbf{F}_1 &= (\lambda_1^{ela}\mathbf{J}_\lambda + \mu_1^{ela}\mathbf{J}_\mu)\dot{\mathbf{u}}_N, \\
\dot{\mathbf{F}}_2 + \frac{E_2}{\kappa\alpha_2 + c_2}\mathbf{F}_2 &= (\lambda_2^{ela}\mathbf{J}_\lambda + \mu_2^{ela}\mathbf{J}_\mu)\dot{\mathbf{u}}_N, \\
\mathbf{F}_3 &= (\lambda_3^{vis}\mathbf{J}_\lambda + \mu_3^{vis}\mathbf{J}_\mu)\dot{\mathbf{u}}_N, \\
\mathbf{F}_{2D}^{rheo} &= \mathbf{F}_1 + \mathbf{F}_2 + \mathbf{F}_3,
\end{aligned} \tag{1.90}$$

This formulation also can be easily extended to 3D cases and models with the Green strain tensor as well by performing similar replacements as we did here.

1.3.4 まとめ

In this section, the formulations of FE dynamic models for simulating rheological behaviors were presented. We started from a 2D formulation of elastic model based on generalized Hooke's law and linear Cauchy strain tensor. The FE formulation of elastic deformation was then extended to 2D rheological model and further extended

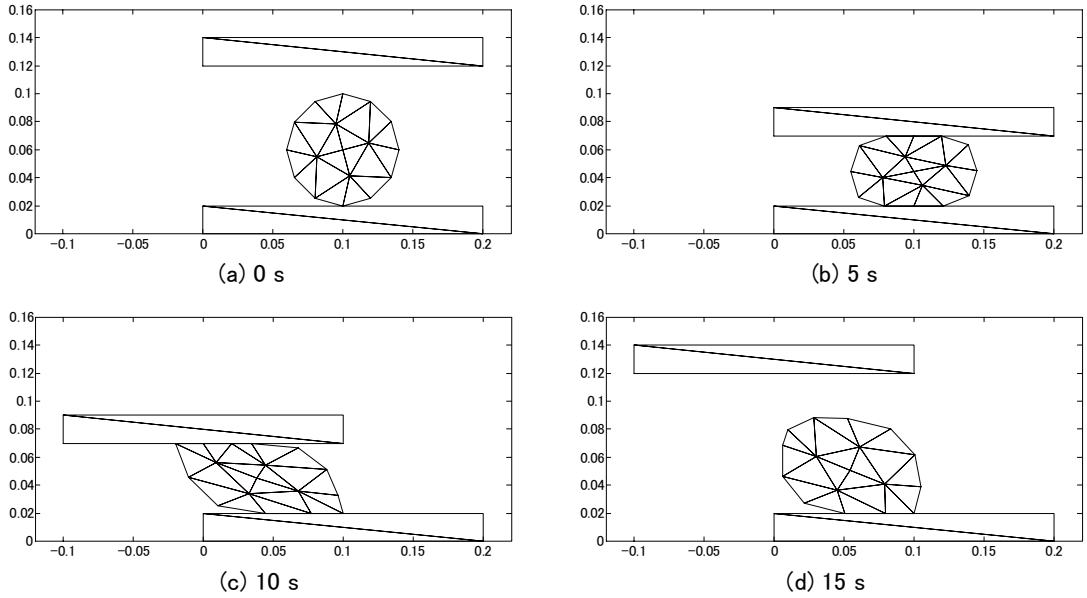

図 1.19: Simulation snapshots of a rheological object pushed and rolled by an external instrument, where the model of the object was formulated by nonlinear Green strain tensor.

to handle 3D rheological deformation. Simulation results were given. In FE model with linear Cauchy strain tensor, the connection matrices are constant and can be prepared in advance which can yield more efficient calculations comparing with nonlinear models. However, FE model with linear Cauchy strain tensor is not suitable for simulating large deformation and rotation. We have therefore introduced nonlinear Green strain tensor to model large deformation and rotation. The derivation of FE model with Green strain tensor was presented. It also starts from the formulation of elastic deformation and further extended to rheological deformation by performing a series of replacements. Simulation results using FE models with Cauchy and Green strain tensors were then given to compare the differences between both models. We found that the FE model with nonlinear Green strain tensor yields more natural behaviors when dealing with large deformation and rotation. However, since the connection matrices are no longer constant, we are not able to prepare these matrices in advance and have to calculate them in every time step. This makes the FE simulation with nonlinear Green strain tensor very time-consuming. At last, we also presented FE model with a five-element physical model which includes two dual-moduli viscous elements.

1.4 非一様物体と接触のモデリング

The FE dynamic models presented in the last chapter are basically used to simulate uniform and isotropic objects. However most objects in the real world are not uniform and may include several different layers with different material properties. In addition, a contact interaction between an object and an external instrument may often happen during handling or manipulation. We therefore investigate the modeling of non-uniform layered objects and contact interaction between a rheological object and external instruments in this chapter.

1.4.1 非一様層状物体の有限要素モデリング

When we started to model non-uniform objects, the first idea came to our mind is to set different parameters to each triangle. However, this idea does not work well. If we look at the dynamic equations presented in the last chapter, for instance, Eq. 1.56, we find that all the parameters are associated with nodal points rather than triangles. In other words, the physical parameters in our FE models are point-wise instead of triangle-wise, which makes the difficulty of choosing appropriate parameters for the boundary nodal points between two layers when dealing with layered objects. We have therefore proposed the following idea for modeling non-uniform layered objects.

Considering a two-layered object with different material properties in each layer, we artificially separate this non-uniform layered object into two uniform objects with their own properties during simulation, as shown in Fig. 1.20. Note that the boundary nodal points on both layers (*i.e.*, the hollow nodes on the top layer and the solid nodes on the bottom layer) always have the same displacements (as they are in fact the same points), *i.e.*:

$$\mathbf{u}^{bott} = \mathbf{u}^{top}. \tag{1.91}$$

The modeling of this layered object can therefore be divided into the modeling of two uniform objects with a displacement constraint on the boundary nodal points. As shown in Fig. 1.20, we imposed the displacements of the top boundary points onto the bottom boundary points during simulation by applying a displacement constraint of Eq. 1.91. Using the CSM, this constraint can be formulated as:

$$(\ddot{\mathbf{u}}^{bott} - \ddot{\mathbf{u}}^{top}) + 2\omega(\dot{\mathbf{u}}^{bott} - \dot{\mathbf{u}}^{top}) + \omega^2(\mathbf{u}^{bott} - \mathbf{u}^{top}) = 0. \tag{1.92}$$

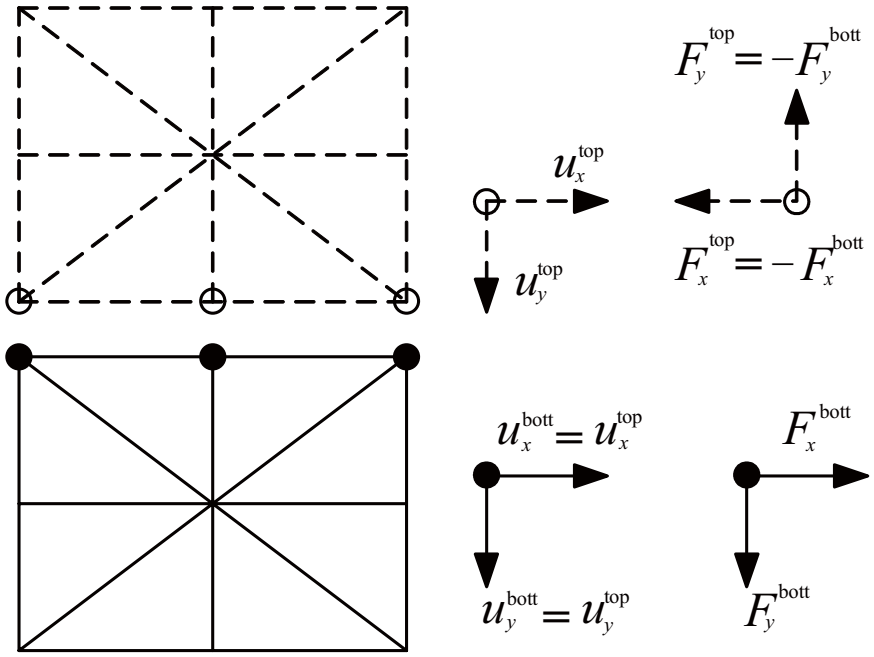

図 1.20: Modeling strategy for non-uniformed layered object.

Accordingly, the constraint forces generated on the bottom boundary points are reacted back to the top boundary points, *i.e.*, $\mathbf{F}^{top} = -\mathbf{F}^{bott}$. By integrating Eq. 1.92 into the dynamic equations of the object on the bottom layer and substituting $\mathbf{F}^{top}$ as an external force into the dynamic equations of the object on the top layer, we can derive an FE model for simulating rheological behaviors of a non-uniform layered object. A typical deformation behavior of a two-layered object is shown in Fig. 1.21, where the top layer is three times softer (all parameters are three times smaller) than the bottom layer. Another example, as shown in Fig. 1.22, is a semi-spherical object made of two types of materials (denoted by solid and dash line, respectively) grasped by a robot hand. We can see that our modeling method demonstrated natural behaviors of non-uniform layered objects. In addition, this 2D FE model can be easily extended to a 3D case by changing the triangular meshes to tetrahedral meshes and adding z-axis components to all the vectors and matrices.

1.4.2 接触のモデリング

The contact modeling is always required when dealing with interactions between a deformable object and an external instrument and is important for many applica-

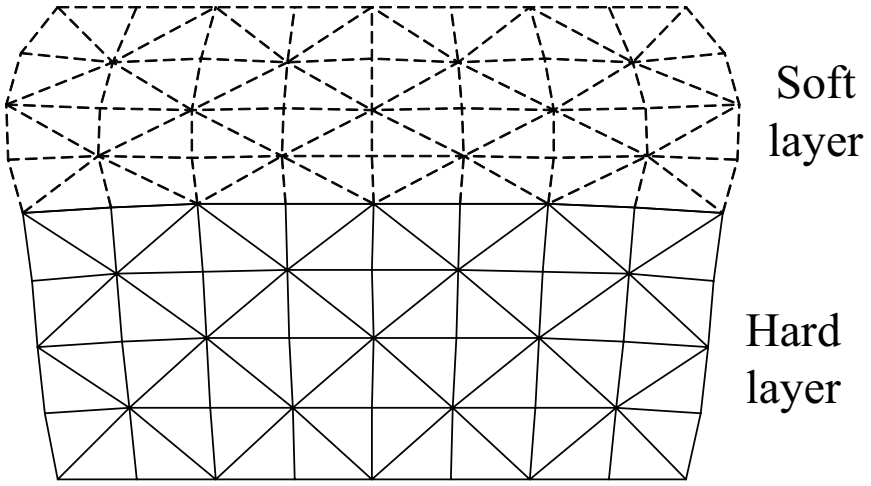

図 1.21: Deformed shape of a two-layered object with soft material in the top layer.

tions, such as food manufacturing simulation and surgical operation. Depending on the contact area between the object and the external instrument, we roughly divide contact models into two categories, as shown in Fig. 1.23. The modeling of these two kinds of contacts, however, is quite different. In wide area contact (Fig. 1.23a), contact modeling only requires a detection of contact moment and a constraint condition between the instrument and the object can then be imposed. On the other hand, in small area contact (Fig. 1.23b), the object needs a remeshing or at least a local remeshing to ensure that the contact nodes on the instrument are coincided with some nodes on the object. Otherwise, the instrument and the object may penetrate each other in some regions. In the following subsections, we will investigate the contact modeling of both categories.

広域接触

In the modeling of wide area contact, we should keep the object mesh unchange and only focus on the detection of contact moment, losing contact moment, and imposing constraints on the contact nodes.

Contact Moment Detection As shown in Fig. 1.23a, the object and the instrument are constructed by triangular meshes. Since the instrument is assumed to be rigid, we can use a simplest mesh (only two triangles) for its modeling. During simulation, the instrument is moving downward with a constant velocity to compress

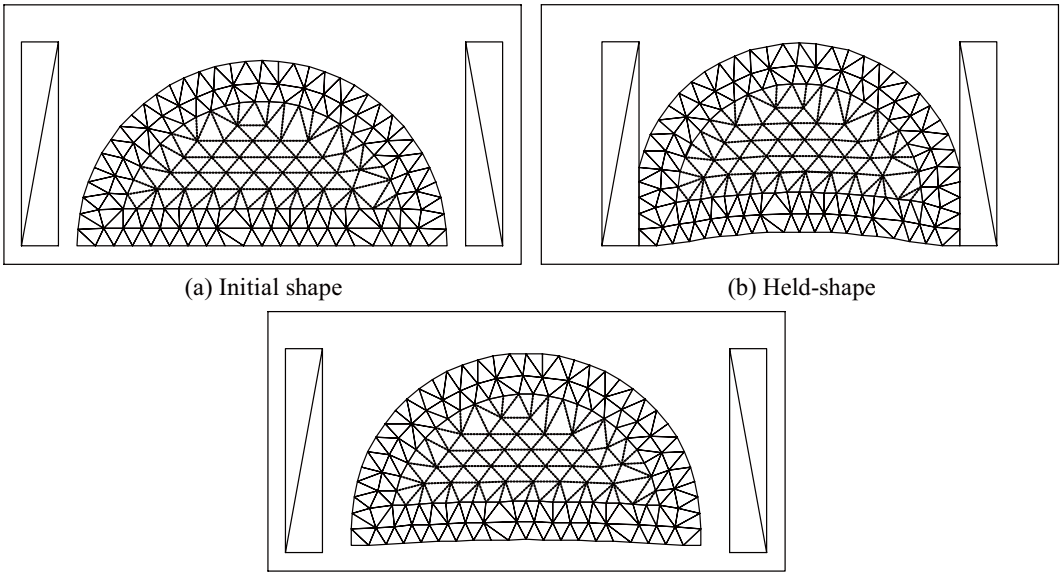

図 1.22: Deformation behaviors of a semi-spherical object made of two types of materials grasped by a robot hand.

the object with a specific displacement. We virtually connect one node P on the object with three nodes of a triangle (△ABC) on the instrument to construct three triangles: △PAB, △PBC, and △PCA. Let $\triangle \mathrm{P}_i\mathrm{P}_j\mathrm{P}_k$ be an arbitrary triangle with three vertices: P_i, P_j, and P_k. Coordinates of these vertices are $[x_i, y_i]$, $[x_j, y_j]$, and $[x_k, y_k]$, respectively. We define a signed area of a triangle as:

$$\triangle \mathrm{P}_i\mathrm{P}_j\mathrm{P}_k = \frac{1}{2}[x_i, x_j, x_k] \begin{bmatrix} y_j - y_k \\ y_k - y_i \\ y_i - y_j \end{bmatrix}. \tag{1.93}$$

This signed area is positive if the triangular loop (the order of the three vertices of a triangle) is counter clockwise while is negative if the loop is clockwise. Now, let us check the signed areas of the triangles △PAB, △PBC, and △PCA shown in Fig. 1.23a, we find that the area of △PAB is negative. However, once the nodal point P is located on any edge or inside of the triangle △ABC, each signed area of above three triangles will became zero or positive. This can serve as a criterion to detect the contact moment and start the contact constraint. In every time step, we check all the nodal points on the object to see if any of them is in contact with the instrument or not. The algorithm can be roughly described as follows:

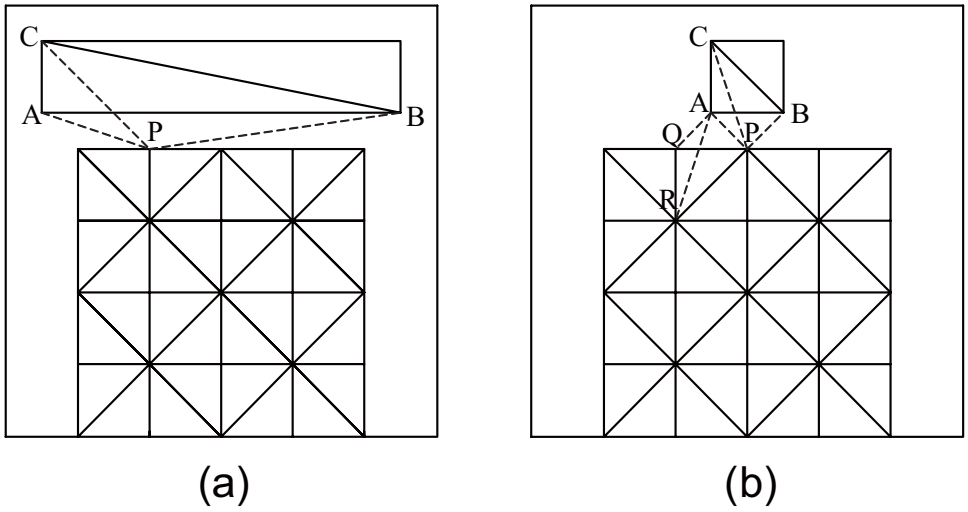

図 1.23: Two kinds of contact models: (a) wide area contact, and (b) narrow area contact.

In each time step

for loop: each nodal point on the object (node P for instance)

for loop: each triangle on the instrument (△ABC *for instance)*

if $\triangle PAB \geq 0$ *and* $\triangle PBC \geq 0$ *and* $\triangle PCA \geq 0$

Start contact;

end if, for.

接触ノードにおける制約

Once the instrument was in contact with the object, the contact points on both instrument and object would have the same displacement and velocity. Let $\mathbf{v}_c^{ins}$, $\mathbf{v}_c^{obj}$, $\mathbf{u}_c^{ins}$, and $\mathbf{u}_c^{obj}$ be the velocity and displacement vectors of the contact points on the instrument and object respectively after contact moment. Using CSM, a set of constraint equations are formulated as:

$$\mathbf{C}^T(\dot{\mathbf{v}}_c^{obj} - \dot{\mathbf{v}}_c^{ins}) + \mathbf{C}^T[2\omega(\mathbf{v}_c^{obj} - \mathbf{v}_c^{ins}) + \omega^2(\mathbf{u}_c^{obj} - \mathbf{u}_c^{ins})] = 0, \tag{1.94}$$

where constant matrix $\mathbf{C}$ denotes which nodal points on the object are in contact. Note that vectors $\mathbf{v}_c^{ins}$ and $\mathbf{u}_c^{ins}$ of arbitrary point on edge AB (Fig. 1.23a) can be

obtained from velocities and displacements of vertices A and B by using interpolation. Combining Eq. 1.94 with the FE model presented in Chapter 3, we are able to simulate the contact interaction between a rheological object and an external instrument.

Losing Contact and Switching Parameters Once the instrument started to move back after pushing and holding operations, we at first thought that it is necessary to determine the losing contact moment and then release the constraint accordingly. However, we found out that we do not have to do that and our contact model has an ability to automatically lose the contact as long as the instrument started to leave the object. Let us recall the idea of our contact model and dig a little bit deeper. During each time step in simulation, if any nodal point on the object is located inside the instrument, it will be pushed down to coincide with the instrument boundary after this time step due to the CSM constraint. Note that this pushing down action will happen in next time step but not in the current time step. In other word, the CSM constraints for the points in contact are always performed one time step later than the time step where the contact happens. Now, let us consider the losing contact situation. When the instrument started to move back, the object will also start to recover. If the recovery rate of the object is faster than the rate of instrument moving back, the contact is still in effect. However, the recovery rate of the object is always decreasing with time. In a certain time step, once the recovery rate of the object is slower than the moving back rate of the instrument, the nodal points in contact will be located outside the instrument boundary. This separation will happen because the CSM constraints are always one time step later than the detection of contact as we just discussed above. Once the separation happens, the contact constraint therefore will be automatically released. This made our contact model much simple and natural.

According to the above discussion, the moment of in contact and losing contact can be determined without explicitly using of simulation time. This can also serve as a good criterion for dual-moduli viscous element to switch parameters, as discussed in Section 1.2.4. We therefore use a flag to memorize the contact points and to serve as the criterion. The algorithm for contact modeling now becomes:

In each time step

for loop: each nodal point on the object (node P for instance)

Initialize: flag(p)=0;

for loop: each triangle on the instrument ($\triangle$ABC *for instance)*

if $\triangle PAB \geq 0$ *and* $\triangle PBC \geq 0$ *and* $\triangle PCA \geq 0$

flag(p)=1;

Start contact;

end if, for

We will switch the parameters when all contacting points lose their contacts. The switch function κ now becomes:

$$\kappa = \begin{cases} -1 & \text{flag(p)} = 0 \qquad \forall \text{p} \in \text{object}, \\ 1 & \text{otherwise.} \end{cases} \tag{1.95}$$

Now, we are able to perform the contact simulation with the parameter switching strategy to reproduce both rheological force and deformation behaviors. The next subsection will demonstrate some simulation results to show the ability of our contact model.

Contact Simulation Using the proposed FE contact model, we are able to simulate deformation behaviors of the rheological objects undergoing a compressing, holding, and releasing procedures. The first example is a semi-circular shaped object deformed by a flat squared instrument. Total simulation time is 16 seconds. The instrument moves down 25 mm in first 4 seconds with a constant velocity. Then, the instrument stops pushing and maintains the deformed object for another 4 seconds. The instrument then moves back to the original position within 4 seconds. After the instrument moves back to the original position, the object still has 4 seconds to recover. Some snapshots of simulation results are shown in Fig. 1.24, where the FE model with dual-moduli viscous elements is employed. All the parameters used here are estimated from real Japanese sweets materials and how to estimate these parameters will be discussed in the next chapter. To compare the different performance, simulation snapshots of FE model without dual-moduli viscous elements are also given in Fig. 1.25. We can easily see the differences between Figs. 1.24 and 1.25. At simulation time 8.2 s, the instrument and object has lost contact in Fig. 1.24d but still in contact in Fig. 1.25a. The final recovered shapes of both cases are

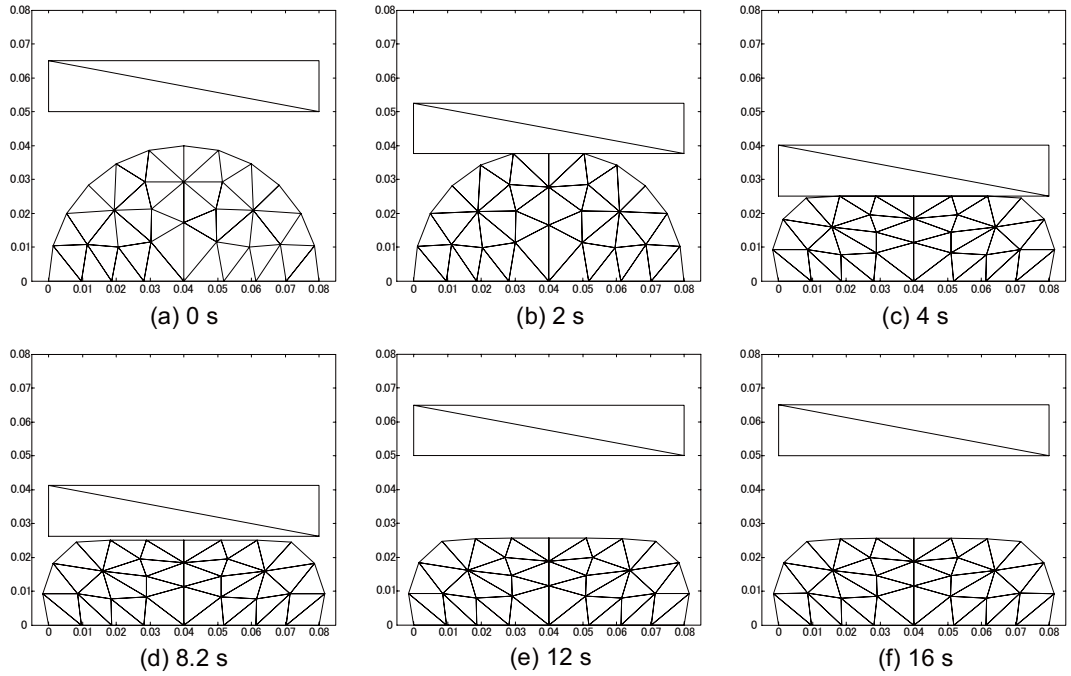

図 1.24: Simulation snapshots of a semi-circular object pushed down by a flat squared instrument with parameter switching strategy.

also quite different. The deformation recovery takes longer time if we do not use the dual-moduli viscous elements.

The second example is a circular object operated by two external instruments with one from the top and another one from the bottom, as shown in Fig. 1.26. The bottom instrument is static and the top instrument is moving down to push the object. Figure 1.26b showed that the object have already deformed and contacted with the bottom instrument due to gravity before the top instrument touches the object. The final recovered shape is also not symmetrical relative to the horizontal axis due to the gravity. Figure 1.26 shows the simulation results of FE model with dual-moduli viscous elements. Some snapshots of simulation results without dual-moduli viscous elements are also given in Fig. 1.27 to show the differences. In addition, simulation results of contact model also can be found in Figs. 1.17 and 1.18 in the last chapter.

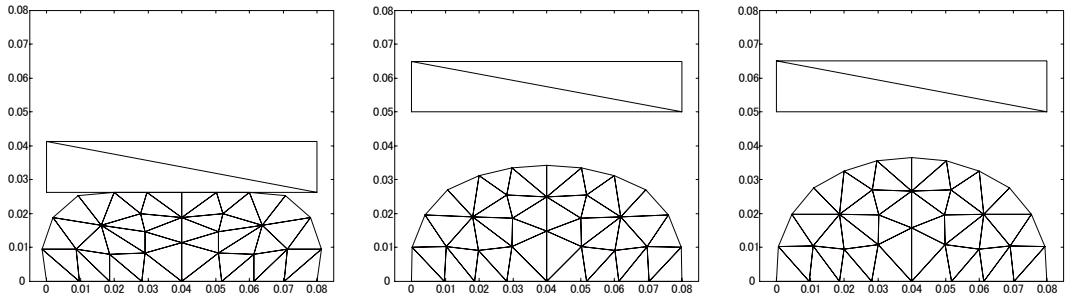

図 1.25: Simulation snapshots of a semi-circular object pushed down by a flat squared instrument without parameter switching strategy.

局所接触

Different with wide area contact, the modeling of narrow area contact requires either a global remeshing or a local remeshing because the contact area of the instrument is smaller than the area of the object as shown in Fig. 1.23b. Moreover,same with wide area contact, narrow area contact also needs a detection of contact moment, which will serve as a trigger to start the performance of remeshing.

Object Remeshing In order to generate triangular mesh automatically, we have employed a MATLAB toolbox of 2D meshing routines named MESH2D, which allows automatic generation of unstructured triangular meshes for general 2D geometry. For using MESH2D, one all need to do is to provide some boundary points which can best describe the object shape (piecewise linear geometry input). By setting some parameters, we also can control the mesh resolution or specify some special nodal points and some special connections between some nodal points. In our application, we only use the basic function and input several boundary points into MESH2D. In every time step during integration, we perform the following processes:

1. Perform the contact detection to see if the instrument and the object are in contact or not. If it is not in contact, jump to step 2. If it is in contact, jump to step 3 and perform the steps followed.

2. Using the initial triangular meshes for both object and the instrument to calculate all the variables and finish the calculation for this time step.

3. Remember the current coordinates of the contact points on the instrument. These

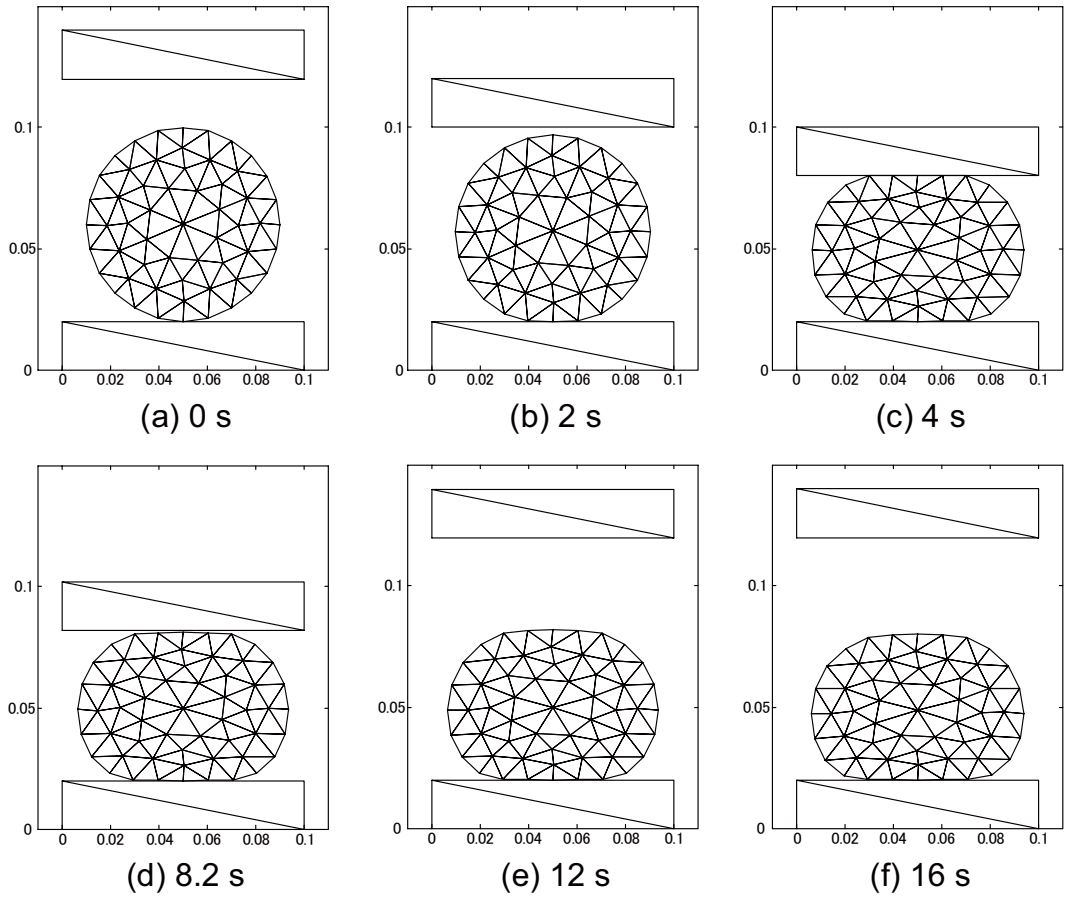

図 1.26: Simulation snapshots of a circular object operated by two instruments with parameter switching strategy.

points and the initial boundary points will serve as a set of new boundary points to generate the new mesh.

4. Perform the remeshing using MESH2D and recalculate all the required matrices, such as the inertial matrix and connection matrices.

5. Use the new mesh and new matrices to calculate all the variables needed to be integrated and finish the calculation of the current time step.

Note that since the remeshing and calculations of connection matrices, which are usually quite large, must be performed inside the time integration, this contact simulation with remeshing is quite time-consuming.

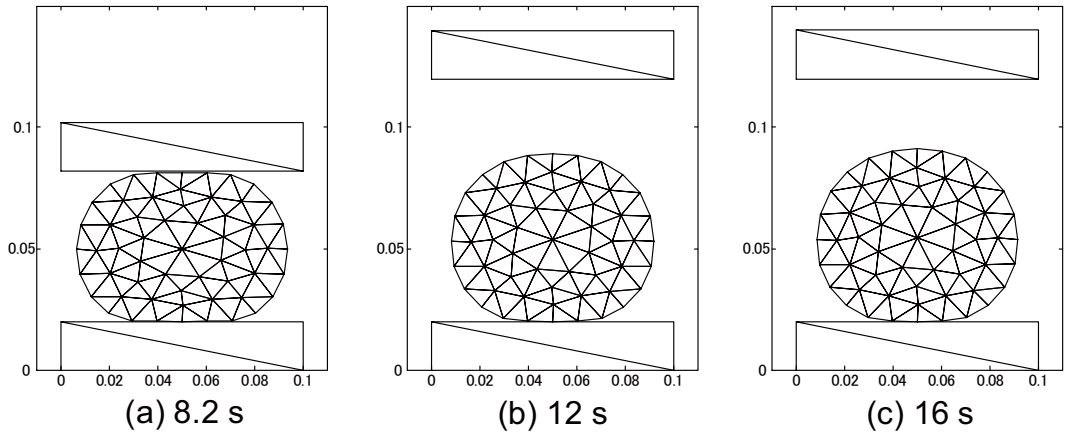

図 1.27: Simulation snapshots of a circular object operated by two instruments without parameter switching strategy.

Contact Simulation with Remeshing A simulation was conducted to show the performance of narrow area contact model with remeshing. A 2D squared object was deformed by a instrument whose contact area is a quarter of the contact area of the object. The instrument and the object have an initial distance of 0.2 m. The instrument was moved down 0.4 m from the initial position in 2 seconds with a constant velocity. Before releasing, the deformed object was maintained for 2 seconds. Then, the instrument was moved back to its initial position in 2 seconds with a constant velocity. After this, the deformed object still had another 2 seconds to recover. The total simulation time is therefore 8 seconds. Several simulation snapshots are given in Fig. 1.28. We can see that the instrument starts to contact with the object at the moment of 1 s and the two contact points in the instrument are not coincide with any nodal point on the object. In the next time step, the object is remeshed and now two new points on the object are generated and are coincided with the corresponding nodes on the instrument. The constraints are then imposed on these contact points to perform the contact simulation.

1.4.3 まとめ

In this chapter, the modeling of non-uniform layered objects and contact interaction between rheological object and external instrument were formulated. We artificially separated a non-uniform layered object into several uniform ones and performed the uniform simulation independently. The non-uniform behaviors were

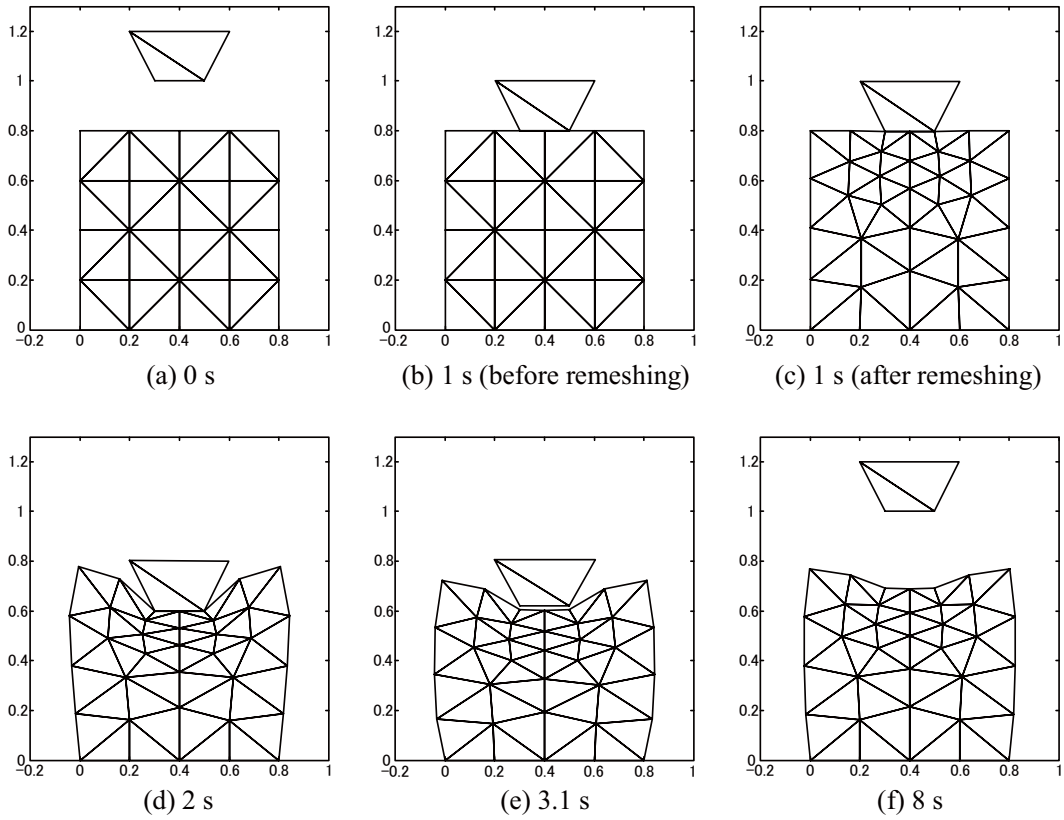

図 1.28: Simulation results of narrow area contact with remeshing.

then obtained by imposing a constraint on the nodal points of the boundary between both layers. This idea works very well for different shaped objects. For modeling of contact interaction, we roughly divided the contact models into two categories depending on the contact areas of the object and the instrument. For wide area contact, the only thing we need to do is to detect the contact moment and then impose constraints on the contacting points. However for narrow area contact, we have to perform object remeshing or at least local remeshing during the simulation. To conduct the remeshing, we need an automatic mesh generation during simulation. This can be done by using a MATLAB toolbox named MESH2D. In each time step, the detection of contact moment is also performed. Once the contact starts, the remeshing is performed and then the constraints are also imposed on the contact nodal points. Simulation results were performed to demonstrate the performance of both contact models.

1.5 力学パラメータの推定

In order to accurately simulate the behaviors of real objects, the properties (physical parameters) have to be determined in advance. However, the estimation of those parameters is a challenging work, especially for rheological objects which always yield residual deformation after a loading-unloading operation. These estimated parameters have to be able to regenerate the rheological force, deformed shape (*e.g.*, the held-shape) during the operation and the final deformed shape (the final-shape) after recovery as well. This section introduce the methods used in our work to estimate physical parameters for simultaneous reproductions of both rheological forces and deformation, especially the residual deformation behaviors. At first, let us investigate the contributions of mesh resolution and each parameter to the rheological behaviors based on 2D FE simulation.

1.5.1 有限要素シミュレーションの解析

Let us take the FE model presented in Section 1.3 as an example to perform the simulation analysis. This 2D FE model includes 6 unknown physical parameters, *i.e.*, Young's moduli E_1, E_2, viscous moduli c_1, c_2, c_3, and Poisson's ratio γ. We suppose that a 2D flat-squared object with a size of $0.08\,\mathrm{m}\times0.08\,\mathrm{m}$ was fixed on the ground and the entire top surface was pushed down with a constant velocity of $0.002\,\mathrm{m/s}$ during time 0 to 10 seconds. This time period is referred to as pushing phase. The deformation was then held for 10 seconds before releasing. Similarly, this time period is referred to as holding phase. The deformed shape in this phase is called held-shape accordingly. After releasing the constraint, the deformed object still has 20 seconds to recover from the deformation. The deformed shape in the end of simulation is referred as final-shape accordingly. Therefore, the total simulation time is set to 40 seconds. Such pushing and holding procedures are used throughout our simulation analysis and similar ones are also employed in our experimental validations. One may ask why we use this simple simulation or experimental setups. We believe that firstly the material properties (physical parameters) will not differ even though the object may have different sizes or shapes or may be subjected to different operations. Secondly, if we could estimate all the parameters by using a simple setup, there would be no problem to estimate them using more complicated setups. Now, let us see how the mesh resolution and physical parameters will affect the simulation behaviors.

メッシュの解像度の影響

As we all known, mesh resolution in FE simulation significantly affects the simulation cost and the simulation accuracy as well. In a certain application, we therefore have to compromise between time cost and simulation accuracy. Since the objects with flat-squared shape are used in most of our simulations and experimental tests, it is necessary to investigate the influence of mesh resolution on our applications. Simulation results with different mesh resolutions are given in Fig. 1.29, where mesh resolution 2×2 means the width and height sides are both divided into two segments. From Fig. 1.29, we can see that the mesh resolution of 4×4 is fine enough to simulate the behaviors for this simple setup. Finer mesh resolutions do not yield significant difference in both force and deformation behaviors. We have therefore employed 4×4 mesh resolution throughout our simulations and parameter estimation processes.

ヤング率の影響

Figures 1.30 and 1.31 show simulation behaviors using different Young's moduli E_1 and E_2, respectively. We can see that both elastic moduli have similar influences on the rheological behaviors. Larger values of those moduli yield larger force amplitudes in the pushing phase and faster decay in the holding phase. This can be explained by Eqs. 1.20 and 1.21, where the value of E_i/c_i determines the increasing and decreasing speed of force amplitude during pushing and holding phases respectively. Note that the held-shapes with different Young's moduli are exactly the same. On the other hand, the final-shapes are dependent on these moduli. Larger values resulted in larger residual (permanent) deformation. Considering the five-element physical model (the last row of Fig. 1.5b), during pushing phase, all elastic elements (denoted

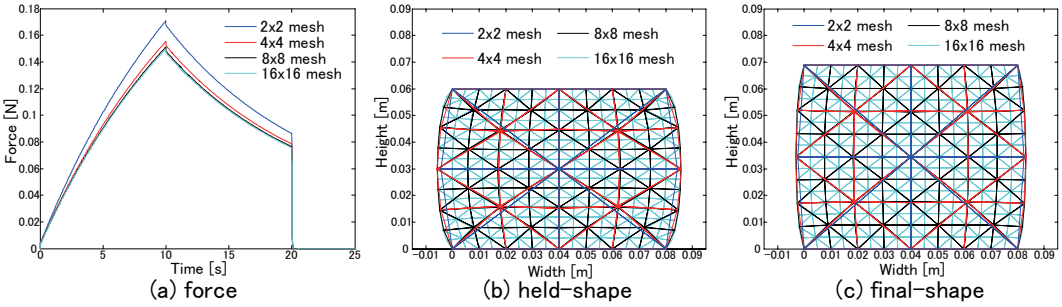

図 1.29: Simulation results with different mesh resolutions.

by E_1 and E_2) and viscous elements (denoted by c_1, c_2, and c_3) are compressed with some deformation. During holding phase, the total deformation of the object is kept unchange. However, the deformation generated in the elastic elements will change to the deformation of viscous elements, which also yields the force relaxation (reduction) behavior in holding phase. Larger elastic moduli (E_1 or E_2) therefore produce bigger deformation changing rate and finally yield larger residual deformation in a certain time period.

粘性率の影響

Figures 1.32 and 1.33 show different simulation behaviors using different viscous moduli c_1 and c_2, respectively. We can see that parameters c_1 and c_2 also have similar influences on the rheological behaviors. Larger values of c_1 and c_2 yield larger force amplitudes in pushing phase and slower decay in holding phase. Explanations also can be obtained by looking at Eqs. 1.20 and 1.21. Similarly, both parameters c_1 and c_2 do not affect deformed shapes during holding phase. However, larger values of c_1 and c_2 yield smaller residual (permanent) deformation. During the holding phase, larger viscous moduli c_1 and c_2 actually will slow down the deformation changing rate. Therefore, less deformation will be changed to viscous element and more deformation will be recovered after releasing, which results in less residual deformation.

Figure 1.34 shows different simulation results with different values of viscous modulus c_3. If we compare Eqs. 1.20 and 1.21 at time t_p (10 s in this case), we find that c_{n+1} (c_3 in this case) is responsible for the sudden drop in force at time t_p. The force behaviors in the holding phase are the same with different parameter c_3, as shown in Fig. 1.34a. Once again, the held-shape is not dependent on parameter c_3. However, c_3 has a little effect on the final-shapes but not in a significant way, as shown in

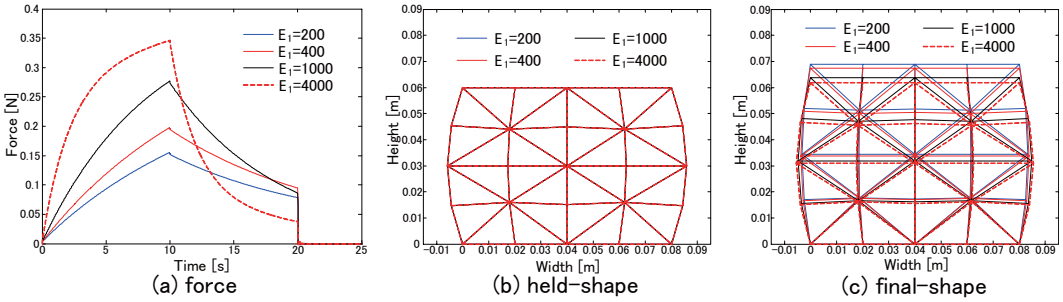

図 1.30: Simulation results with different Young's modulus E_1.

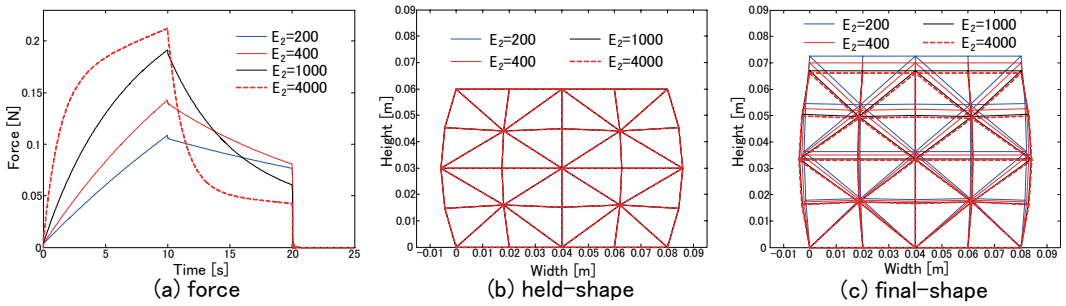

図 1.31: Simulation results with different Young's modulus E_2.

Fig. 1.34c. Since parameter c_3 does not affect simulated behaviors in a significant way, one may ask why we have to include this viscous element in our FE model. Actually, without using parameter c_3, we are still able to reproduce rheological force and deformation. However without using c_3, vibration always happens in both force and displacement curve after releasing, as shown in Fig. 1.10b. A small value of parameter c_3 can remove this vibration and without changing the simulated behaviors significantly.

ポワソン比の影響

Figure 1.35 shows different simulated behaviors using different values of Poisson's ratios γ. We can see that parameter γ affects all the rheological behaviors: force, held-shape, and final-shape. Larger parameter γ results in larger force responses and larger transverse deformation behaviors but does not affect the normal deformation in both held-shape and final-shape. This coincides with the definition of Poisson's ratio, *i.e.*, a ratio between the transverse strain and axial strain. We summarize the

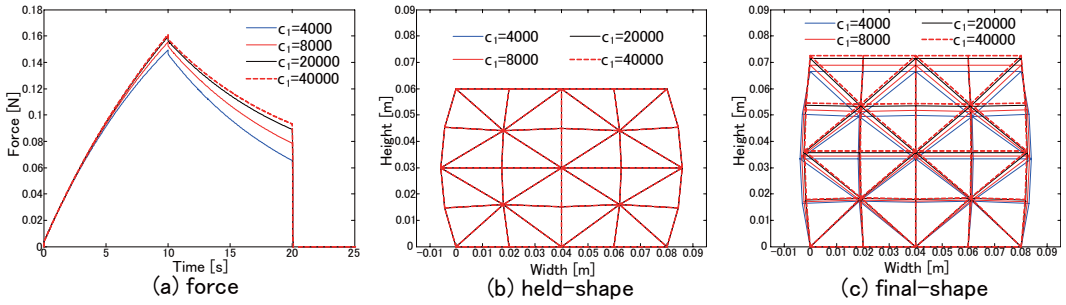

図 1.32: Simulation results with different viscous modulus c_1.

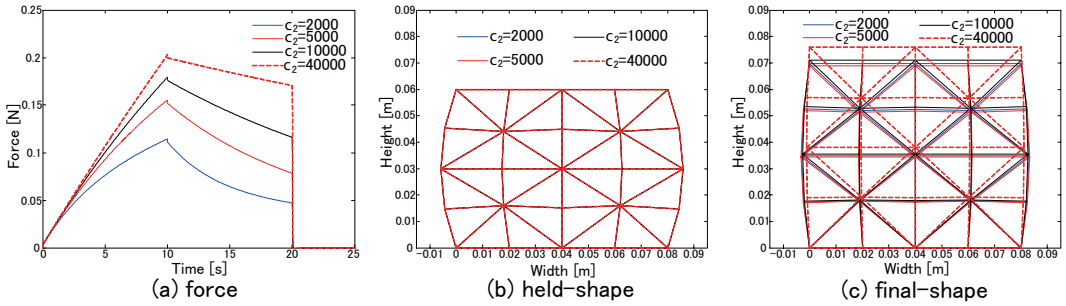

図 1.33: Simulation results with different viscous modulus c_2.

influences of all physical parameters (five-element physical model for instance) on rheological behaviors in Table 1.2. Interestingly, we find that only Poisson's ratio γ affect the held-shape and all the other parameters do not affect this shape at all. This feature allows us to estimate Poisson's ratio γ separately.

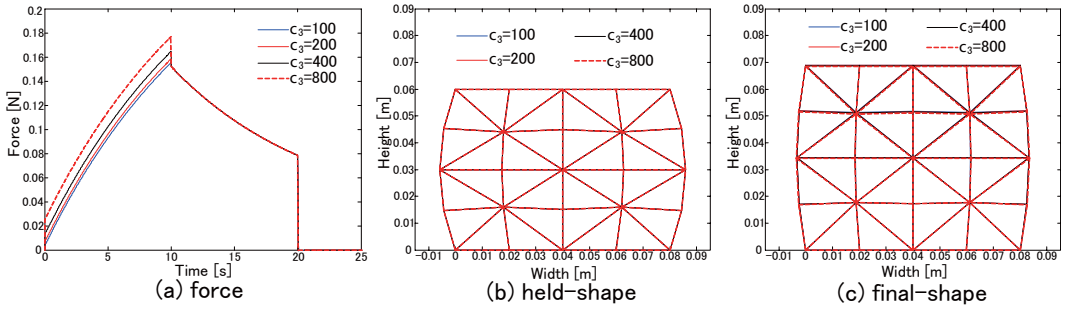

図 1.34: Simulation results with different viscous modulus c_3.

表 1.2: Influences of physical parameters on rheological behaviors

Parameter	Force in pushing	Force relaxation	Held-shape	Final-shape
E_1	○	○	×	○
E_2	○	○	×	○
c_1	○	○	×	○
c_2	○	○	×	○
c_3	○	×	×	○
γ	○	○	○	○

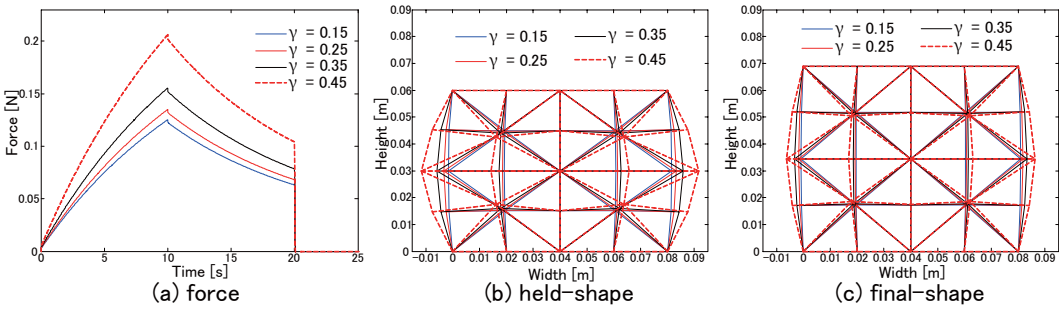

図 1.35: Simulation results with different Poisson's ratio γ.

1.5.2 最適化に基づくパラメータ推定

Parameter estimation of deformable objects has been studied intensively, as presented in Introduction. One popular and robust method is based on optimization, which aims at minimizing the difference between simulation or calculation results and experimental measurements. When the simulation or calculation is performed by using FE model, this optimization process is usually called inverse FE optimization (Fig. 1.3), *i.e.*, the FE simulation or calculation is iterated with updated physical parameters until the differences between the simulation and experiment becomes minimal. In our work, this method was also used to determine the physical parameters of rheological objects. However, due to the presence of residual deformation, accurately reproductions of both rheological forces and residual deformation are quite challenging and parameter estimation for capturing both force and residual deformation is also quite difficult. In order to deal with this problem, we firstly proposed a parameter estimation method with the following three steps:

1. Minimize the held-shape to estimate Poisson's ratio γ;
2. Calculate the summation $\sum_{i=1}^{n} c_i$ to approximate the final-shape;
3. Minimize the force differences to estimate the remaining parameters with a constraint of summation $\sum_{i=1}^{n} c_i$ from the second step.

The details about each step will be presented in the following subsections.

ポワソン比の推定

As we discussed in the last section, only Poisson's ratio γ affects the held-shape and other parameters do not affect this shape at all. We can therefore estimate

γ separately by minimizing the difference of held-shapes between simulation and experiments. The objective function used for this optimization is given by:

$$E(\gamma) = \sum_{i=1}^{m} \|\mathbf{x}_i^{sim}(\gamma) - \mathbf{x}_i^{exp}\|^2, \tag{1.96}$$

where $\mathbf{x}_i^{sim}(\gamma)$ and $\mathbf{x}_i^{exp}$ are the displacement vectors from simulation and experiment, respectively. Scalar $m = 2N$ with N be the total number of nodal points calculated in this optimization problem. The optimization is terminated when the tolerance on the function value $E(\gamma)$ is less than 1×10^{-12} or the tolerance on parameter γ is less than 1×10^{-6}. Optimization results will be presented in the next section and we can find a global minimum for this optimization problem actually.

粘性率の総和の計算

As we discussed in Section 1.2, we can calculate the residual strain by using the integration of stress history and the summation of viscous moduli, as given in Eq. 1.27. By extending this 1D equation to 2D case, we have

$$\mathbf{M}_\gamma \mathbf{u}_N(\infty) = \frac{1}{\sum_{i=1}^{n+1} c_i} \int_0^{t_p+t_h} \mathbf{F}(t)\mathrm{d}t. \tag{1.97}$$

where

$$\mathbf{M}_\gamma = \gamma_\lambda \mathbf{J}_\lambda + \gamma_\mu \mathbf{J}_\mu = \frac{\gamma}{(1+\gamma)(1-2\gamma)}\mathbf{J}_\lambda + \frac{1}{2(1+\gamma)}\mathbf{J}_\mu.$$

Note that the residual displacements $\mathbf{u}_N(\infty)$ and force history $\mathbf{F}(t)$ can be obtained from experimental measurements. Matrix $\mathbf{M}_\gamma$ can be prepared in advance and it only depends on the initial geometrical coordinates and Poisson's ratio γ. Therefore, Eq. 1.97 allows us to calculate the summation of viscous moduli $\sum_{i=1}^{n+1} c_i$ and this summation can be used as a constraint during the estimation of other parameters. Since the residual displacements $\mathbf{u}_N(\infty)$ was included in this calculation, the calculated value of $\sum_{i=1}^{n+1} c_i$ would guarantee a good reproduction of final-shape. Validation results will be presented in the next section.

力誤差を基準とする最適化

After the first two steps as presented in the above, we have estimated one parameter γ and one constraint of $\sum_{i=1}^{n+1} c_i$. Considering the FE model with the parallel

five-element model as an example which totally includes 6 physical parameters, we still have 4 independent parameters to be determined. This can be accomplished by minimizing the difference in rheological forces between simulation results and experimental measurements. The objective function of this optimization problem can be formulated as:

$$E(\mathbf{\Theta}) = \sum_{i=1}^{n} \|\mathbf{f}_i^{sim}(\mathbf{\Theta}) - \mathbf{f}_i^{exp}\|^2, \tag{1.98}$$

where vector $\mathbf{\Theta}$ consists of the parameters to be determined. Vector $\mathbf{f}_i^{exp}$ is the force measurements from experiments at the i-th sampling time and vector $\mathbf{f}_i^{sim}(\mathbf{\Theta})$ is the force response during simulation with parameter $\mathbf{\Theta}$. The threshold used to terminate the optimization is the tolerance on $E(\mathbf{\Theta})$ or the tolerance on $\mathbf{\Theta}$ less than 1×10^{-6}. In both optimizations presented in the first and third steps, the optimization toolbox of MATLAB and "Nonlinear Least Squares" method were employed to minimize the objective functions.

From Eq. 1.98, we can see that this optimization process involves iterative FE simulations, which is usually time consuming. Based on our experiences, this optimization process takes hours or days depending on the initial setting of the parameters. However, this simulation-based optimization is quite robust. As long as the simulation can be done, this optimization process can be performed as well and it does not require any special treatments of the physical models. We have tested this method with different physical models and it works well.

解析的計算による力誤差の最適化

As presented in Section 1.2, the analytical expressions of stress in pushing and holding phases can be formulated as given in Eqs. 1.20 and 1.21. Extending these two equations from 1D to 2D case, we have

$$\mathbf{F}(t) = \sum_{i=1}^{n} c_i\big(1 - e^{-\frac{E_i}{c_i}t}\big)\mathbf{M}_\gamma \mathbf{v}_N^{Push},\ (0 \le t \le t_p), \tag{1.99}$$

$$\mathbf{F}(t) = \sum_{i=1}^{n} c_i\big(1 - e^{-\frac{E_i}{c_i}t_p}\big)e^{-\frac{E_i}{c_i}(t-t_p)}\mathbf{M}_\gamma \mathbf{v}_N^{Push},\ (t_p \le t \le t_p + t_h), \tag{1.100}$$

where vector $\mathbf{v}_N^{Push}$ consists of velocities of all nodal points during pushing phase. We assume that this is a constant vector which corresponding to the constant velocity p used in Eqs. 1.20 and 1.21. During the pushing phase, if we push the top surface

of the object with a constant velocity and if this pushing velocity is not significantly big, this assumption can be satisfied. After we estimated the Poisson's ratio γ, vector $\mathbf{v}_N^{Push}$ can be easily obtained by performing the simulation in the pushing phase with all the other parameters taking arbitrary values since these parameters do not affect the deformation behaviors during pushing phase. Based on Eqs. 1.99 and 1.100, we are able to calculate the force responses during both pushing and holding phases and these calculated forces can be then used in Eq. 1.98 (instead of the simulated forces) to perform the force optimization. Since now there is no iterative FE simulations involved in this optimization process, we can obtain a optimal solution within only several seconds depending on the initial setting of parameters. However, this method only can be used in parallel physical models in which force expressions can be analytically derived. For other physical models, such as serial models, this method cannot be used and we have to perform simulation-based optimization instead, as proposed in the last subsection.

In some applications, if we only focus on reproducing force behaviors, the second step proposed in Section 1.5 can be ignored and all parameters except Poisson's ratio γ should be included in the force optimization (the third step). This will yield the best performance of force reproduction. But at the same time, we have to sacrifice some accuracy of the reproduction of final-shape. Detailed validation and discussions will be presented in the next section accompanying with various experimental results and comparisons.

多重粘性要素を用いた有限要素モデルにおけるパラメータ推定

In the above discussions, we supposed that only one set of parameters was used in the FE model. However, due to the linearity of the physically based models (*e.g.*, the parallel five-element model), it is difficult to reproduce both rheological forces and residual deformation simultaneously for most rheological objects. We have therefore introduced a dual-moduli viscous element into our FE formulation, as presented in Section 1.3. This dual-moduli viscous element has an ability to switch two parameters from one to the other during simulation. It can successfully capture both rheological deformation and force behaviors simultaneously. We have also proposed that the simulation time and losing contact moment can serve as a criterion to start the parameter switching.

Note that we usually switch the parameters at the moment when the operation is finished and the external instrument start to leave the object. During the operations

(*e.g.*, pushing and holding), the deformation only depends on the Poisson's ratio γ. This suggests that we can use the estimated parameters by force optimization to reproduce both rheological force and deformation during operations. However, this set of parameters cannot guarantee accurate reproduction of residual deformation at the same time. We have therefore employed the dual-moduli viscous element to switch parameters when contact was lost. Since parameters c_i dominate the residual deformation as shown in Eq. 1.97, we only need to switch parameters c_i for capturing residual deformation. For example, we suppose the viscous moduli estimated by force optimization as c_i^{load} which will be used during operation (loading). We named another set of viscous moduli as c_i^{unload}, which will be used after operation (unloading). Our idea is to use those c_i^{unload} as unknown parameters to optimize the difference of final-shapes between experiments and simulation. Note that during this optimization the parameter c_i^{load} will be switched to c_i^{unload} automatically when the deformation starts to recover. The objective function of this optimization problem can be formulated as:

$$E(c_i^{unload}) = \sum_{i=1}^{m} \|\mathbf{x}_i^{sim}(c_i^{unload}) - \mathbf{x}_i^{exp}\|^2. \tag{1.101}$$

After having c_i^{unload}, we can easily determine the parameters used in the dual-moduli viscous elements by using the following equations:

$$\begin{aligned} c_i + \alpha_i &= c_i^{load}, \\ c_i - \alpha_i &= c_i^{unload}. \end{aligned} \tag{1.102}$$

Estimation results of FE model with dual-moduli viscous elements for objects made of Japanese sweets materials will be presented in the next section.

1.5.3 まとめ

In this section, the parameter estimation methods were presented for capturing both rheological forces and deformation behaviors simultaneously. At first, FE simulations were performed with different mesh resolutions and physical parameters to investigate the influence of these factors on the simulation behaviors. We found that a 4×4 triangular mesh is fine enough for the simple setup used in our parameter estimation procedures. We also found that only Poisson's ratio γ affect the held-shape and all the other parameters do not affect this shape at all. This allows us to

estimated Poisson's ratio γ separately by minimizing the difference of held-shapes between simulation results and experimental measurements. We have therefore proposed a three-steps estimation method. Except estimating γ (the first step), we also calculate the summation of viscous coefficients $\sum_{i=1}^{n} c_i$ (the second step) by using the measured data of force and final-shape. This summation was then served as a constraint during estimating the other parameters (the third step) by minimizing the force differences. Depending on the force results obtained from FE simulation or straightforward calculation, the third step can be perform in two different ways. The simulation-based force optimization is robust and can be used in any model, but it is time-consuming since iterative FE simulations are involved. On the other hand, the calculation-based force optimization method is very efficient but only can be used in parallel physical models. In some applications, these two methods can be mixed to achieve the best estimation results. At last, the parameter estimation method for FE model with dual-moduli viscous elements was also presented based on the above-mentioned methods.

1.6 実験的検証

In the previous chapters, we have presented the FE models and parameter estimation methods for simulating rheological objects, especially focusing on the simultaneous reproductions of both rheological forces and deformation behaviors. In this chapter, we will demonstrate a series of experimental results and comparisons with simulation results for validating proposed FE models and parameter estimation methods.

1.6.1 実験システム

As we mentioned before, a pushing-holding-releasing operation has been employed through out our discussions. Such kind of operation is frequently encountered in real applications and provides enough information to estimate the physical parameters included in the FE model. We have therefore performed a series of experiments on two different materials using this pushing-holding-releasing procedure. In order to perform such procedure, a testing device is necessary. At the same time, the force measurements should be recorded for the follow-up parameter estimation. Experimental setup used in our experiments is shown in Fig. 1.36. A motorized stage (KX1250C-L,

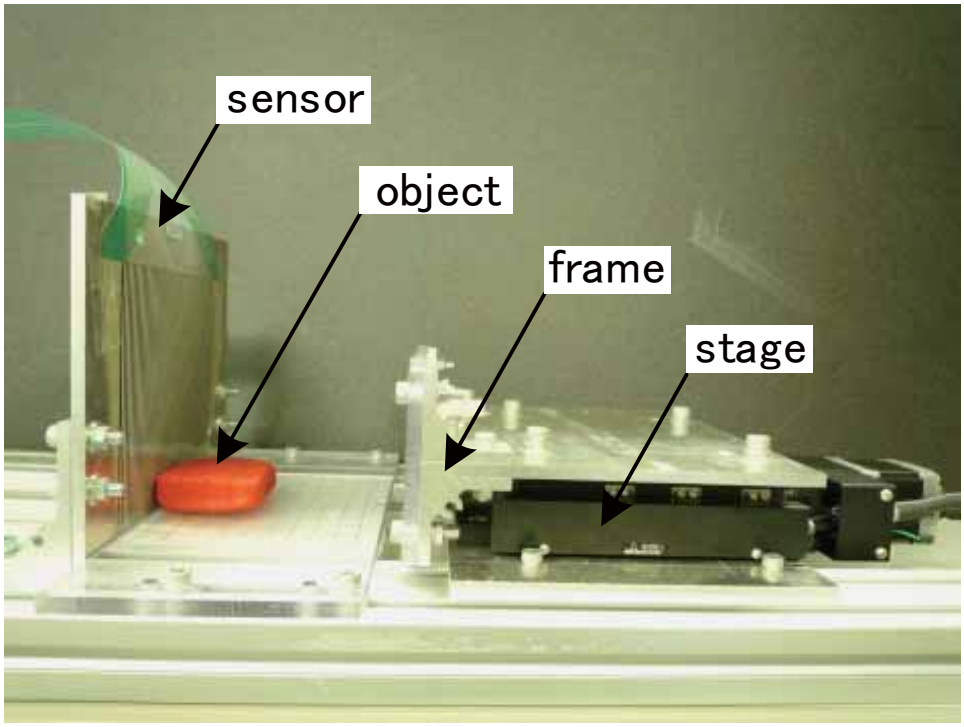

図 1.36: Experimental setup used for compressive tests.

SURUGA SEIKI Co.) was used to perform the pushing-holding-releasing operation. Force responses on the bottom surface of the object were measured by a tactile sensor (I-SCAN100L, NITTA Co.). In addition, several static images including the initial, deformed, and recovered shapes, were recorded by a camera (Canon Eos Kiss X2). These measurements were used to estimate the rheological properties of the object.

1.6.2 圧縮試験

Two kinds of rheological materials were tested in our experiments, which are commercial available clay and Japanese sweets materials. These two materials show typical rheological behaviors under a loading-unloading operation.

粘土

The commercial clay is available in supermarket and is supposed to be played by kids (the one we used is supposed to be play by children over 3 years old, as shown

(a)

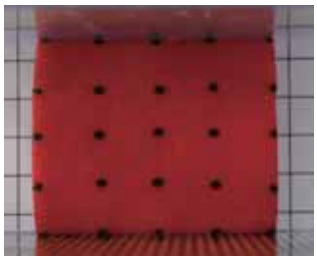

(b)

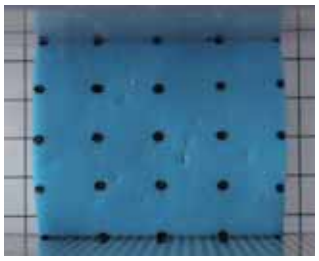

(c)

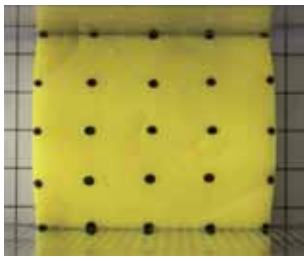

(d)

図 1.37: Commercial available clay product (a) and flat-squared objects used in experiments made of different colors: (b) red, (c) blue, and (d) yellow.

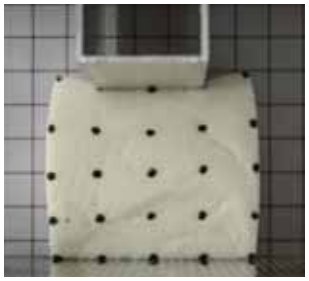

(a) v=0.1mm/s

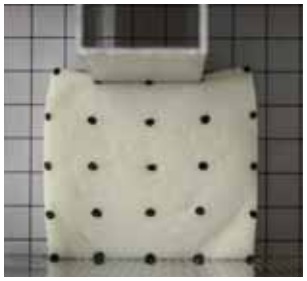

(b) v=0.2mm/s

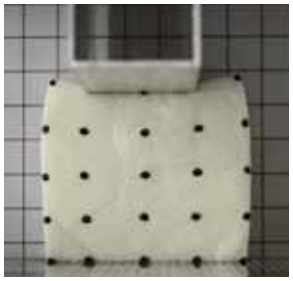

(c) v=0.5mm/s

図 1.38: Flat-squared objects made of white colored clay were compressed from the center part of top surfaces with different pushing velocities.

in Fig. 1.37a). The clay is made of flour, salt, and water mixed with a special ratio. Several different colors are available and were used to distinguish different pushing velocities in our experiments. Several flat-squared objects made by different colored

表 1.3: Detailed information of compression experiments with commercial clay

Object color	Object weight (g)	Object size W (mm)	Object size H (mm)	Object size T (mm)	Push velo. (mm/s)	Push disp. (mm)	Pushing time t_p (s)	Pushing time t_h (s)
red-06	37.75	52.0	52.5	12.0		6	12.07	303.78
red-08	43.36	60.5	60.0	10.5	0.5	8	16.10	304.78
red-10	45.01	58.0	61.0	10.5		10	20.12	311.82
blue-06	43.98	60.5	59.0	10.0		6	30.17	311.83
blue-08	45.04	61.0	59.5	10.0	0.2	8	40.24	321.88
blue-10	43.80	60.5	59.5	10.0		10	49.29	342.00
yellow-06	46.19	59.0	59.0	11.0		6	58.34	502.94
yellow-08	44.72	59.5	59.0	10.0	0.1	8	79.46	500.94
yellow-10	45.14	57.5	56.5	11.5		10	98.58	609.57
white-05	46.43	58.0	57.0	12.0	0.5		16.09	369.16
white-02	46.23	60.0	60.5	10.5	0.2	8	40.24	400.34
white-01	44.08	59.5	58.0	10.0	0.1		79.46	601.52

clays were prepared for compressive testing, as shown in Fig. 1.37b, 1.37c, and 1.37d. Some markers were drawn on the object surfaces for convenient capturing of internal deformation. During testing, the entire top surfaces of these objects were compressed downward with constant velocities. Different colors denote different velocities, *e.g.*, red color corresponding to the velocity of 0.5 mm/s, blue is 0.2 mm/s, and yellow is 0.1 mm/s. For each color, three objects were prepared and compressed with different displacements of 6 mm, 8 mm, and 10 mm, respectively. Measurements of these 9 objects were then used to estimate the physical parameters. In order to evaluate the estimated parameters, three white colored objects were prepared and compressed from the center part of top surfaces with different pushing velocities but same displacement, as shown in Fig. 1.38. Detailed information about these experiments with commercial clay was given in Table 1.3. Experimental trials with different pushing velocities (0.1, 0.2, and 0.5 mm/s) and different pushing displacements (6, 8, 10 mm) were performed to investigate how the pushing velocity and displacement affect the parameter estimation results.

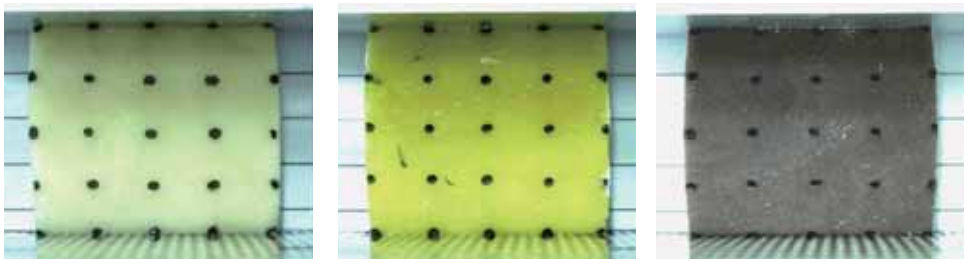

(a) material 1 (b) material 2 (c) material 3

図 1.39: Flat-squared objects made by different Japanese sweets materials.

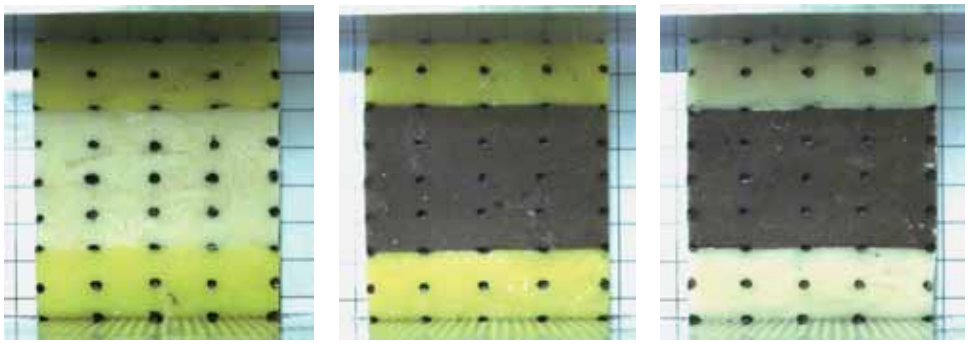

(a-1) material 1+2 (a-2) material 2+3 (a-3) material 1+3

(a) layered objects compressed from the top surface

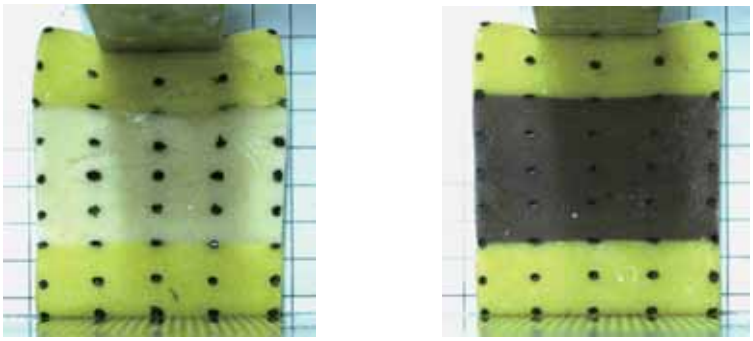

(b-1) material 1+2 (b-2) material 2+3

(b) layered objects compressed from the center of top surface

図 1.40: Non-uniform layered objects compressed over the entire or at the center of the top surfaces.

和菓子の材料

Three kinds of Japanese sweets materials were provided by OIMATU, a sweets company in Kyoto. Each was made of flour, water, and bean powder mixed at spe-

表 1.4: Detailed information of compression experiments with Japanese sweets materials

Material	Object weight (g)	Object size W (mm)	H (mm)	T (mm)	Push type	Push velo. (mm/s)	Push disp. (mm)	Time t_p (s)	t_h (s)
Mat. 1	52.43	58.0	59.5	12.0				28.87	182.06
Mat. 2	32.97	50.0	50.0	11.0	top	0.2	6	29.68	181.26
Mat. 3	34.99	50.0	50.0	11.0				29.97	181.46
Mat. 1+2	66.99	60.0	80.0	11.0				49.29	181.76
Mat. 2+3	69.12	60.0	80.0	11.0	top	0.2	10	49.49	181.47
Mat. 1+3	68.52	60.0	80.0	11.0				49.49	181.97
Mat. 1+2	66.99	60.0	80.0	11.0	center	0.2	10	49.69	181.86
Mat. 2+3	69.12	60.0	80.0	11.0			8	39.13	182.07

cific ratios. Three flat-squared objects, each composed of one material, were prepared for the compression tests, as shown in Fig. 1.39. The entire top surfaces of these objects were compressed at a constant velocity of 0.2 mm/s and with a displacement of 6 mm. Several markers were drawn on the surfaces and force responses and deformed images were recorded. These measurements were used to estimate the rheological parameters of these sweets materials. In addition, to validate the FE model and the estimated parameters, several non-uniform layered objects(each made of three layers with two alternating materials) were compressed over their entire or at the center of their top surfaces, as shown in 1.40a and 1.40b, respectively. Detailed experimental information using Japanese sweets materials is given in Table 1.4. Note that the pushing time t_p was quite different between uniform object (about 30 s) and layered objects (about 40 or 50 s) because they were compressed with the same velocity (0.2 mm/s) but different displacements (6, 8, and 10 mm). The holding time t_h, however, was quite similar (around 3 minutes, as shown in the last column of Table 1.4) among these experimental trials. During the experiments, we manually controlled the time t_h and concluded that 3 minutes was sufficient to obtain adequate information on force relaxation behaviors. In addition, the compressing displacements were chosen to be 6, 8, and 10 mm (see the eighth column of Table 1.4) based on the small-deformation assumption of generalized Hooke's law. We used the same

compressing displacement (10 mm) for the three trials (middle three rows of Table 1.4) with layered objects compressed over their entire top surfaces to investigate the performance of our model with different material combinations. Additionally, two further trials (the last two rows of Table 1.4) with layered objects compressed at the centers of their top surfaces were performed to validate our FE model and estimated parameters with different operations and different compressive displacements (8 and 10 mm).

1.6.3 パラメータ推定の結果

Generally, the material property of an object will not differ even though the object is subjected to different operations or it has different shape or size. This feature allows us to use regular shaped objects with simple pushing operations to estimate their physical parameters. Then, the estimated parameters should be able to simulate arbitrary shaped objects with any operations. In our experiments, we used flat-squared objects pushed on the entire top surfaces with constant velocities to estimate the parameters. As an example of our step-by-step estimation method, we show the case of the object made by red colored clay pushed with a displacement of 8 mm, denoted by red-08 in Table 1.3. A parallel five-element model was employed to model the rheological behaviors of this object. According to the discussions presented in the previous section, parameter c_3 in the parallel five-element model was mainly responsible for eliminating the vibration from the simulation. Based on our experience, a small value of c_3 comparing with c_1 and c_2 is enough to remove the vibration and without significant effect on simulation results of force and deformation. Usually, parameter c_1 and c_2 of real materials have a magnitude about 10^5 or 10^6 Pa·s. We have therefore set a value of 100 Pa·s to parameter c_3 in advance. Now, we have 5 unknown parameters to be estimated, *i.e.*, Poisson's ratio γ, Young's moduli E_1, E_2, and viscous moduli c_1, and c_2.

ポワソン比の推定

In the first step, we estimated the Poisson's ratio γ by minimizing the differences of held-shapes. Since other parameters do not affect held-shape, we therefore assigned some arbitrary values to the other parameters. Three trials were performed and the arbitrary values for other parameters are listed Table 1.5. The optimization for

表 1.5: Arbitrary values of E_1, E_2, c_1, c_2, and c_3 for estimating γ

Case no.	E_1 (Pa)	E_2 (Pa)	c_1 (Pa·s)	c_2 (Pa·s)	c_3 (Pa·s)
trial 1	5×10^2	1×10^3	2×10^3	3×10^3	1×10^2
trial 2	5×10^3	1×10^4	2×10^4	3×10^4	1×10^2
trial 3	5×10^4	1×10^5	2×10^5	3×10^5	1×10^2

表 1.6: Estimation results for Poisson's ratio γ

Case number	Initial value x_0	Final value x^*	$E(\gamma)$ ($\times 10^{-6}\,\mathrm{m}^2$)	Iteration count	Cost (hr)
trial 1	0.15	0.29023634	3.7546	4	0.26
	0.25	0.29023308	3.7546	3	0.20
	0.35	0.29023665	3.7546	4	0.25
trial 2	0.15	0.29024458	3.7546	4	0.37
	0.25	0.29022518	3.7546	3	0.32
	0.35	0.29021075	3.7546	4	0.42
trial 3	0.15	0.29023707	3.7546	4	1.55
	0.25	0.29023282	3.7546	3	1.25
	0.35	0.29023569	3.7546	4	1.63

minimizing the differences of held-shapes were then performed, as discussed in the previsou section. Table 1.6 shows the estimated Poisson's ratios γ at different cases and different initial values. We find that parameter γ quickly (only 3 or 4 iterations) converge to a global minimum of about $\gamma = 0.2902$. This value will be used in the following calculation of $\sum_{i=1}^{3} c_i$ and force optimization.

粘性率の総和の計算

Using Eq. 1.97, we can easily calculate the value of summation $\sum_{i=1}^{3} c_i$ based on experimental data on force and residual deformation. In this case, we found that $\sum_{i=1}^{3} c_i = 9.6961 \times 10^6$Pa·s. Note that the value of $\sum_{i=1}^{3} c_i$ can guarantee a good reproduction of final deformed shape since the residual deformation has been considered during the calculation.

表 1.7: Estimation results of E_1, E_2, and c_1 using simulation-based optimization

Trial number	Parameter	Initial value x_0	Final value x^*	$F(\mathbf{\Theta})$ (N^2)	Iteration count	Cost (hr.)
trial 1	E_1 (Pa)	4×10^4	2.4722×10^4	90.519	36	4.47
	E_2 (Pa)	6×10^4	5.0771×10^4			
	c_1 (Pa·s)	8×10^6	8.1142×10^6			
trial 2	E_1 (Pa)	8×10^4	5.5790×10^4	27.383	43	5.77
	E_2 (Pa)	6×10^4	3.8065×10^4			
	c_1 (Pa·s)	4×10^6	4.5349×10^5			
trial 3	E_1 (Pa)	3×10^4	3.7607×10^4	24.536	33	4.79
	E_2 (Pa)	8×10^4	7.6996×10^4			
	c_1 (Pa·s)	9×10^6	9.1985×10^6			

パラメータの推定

After estimating Poisson's ratio γ and the value of $\sum_{i=1}^{3} c_i$, the other parameters can be then estimated by minimizing the difference of rheological forces with a constraint of summation $\sum_{i=1}^{3} c_i$. However, depending on the way obtaining virtual force data, the estimation of other parameters can be divided into two categories: simulation- and calculation-based methods, as discussed in the previous sections.

Estimation Results of Simulation-Based Optimization In simulation-based optimization, the FE simulations were iterated with updated parameters until the differences between simulation results and experiment measurements becomes minimal. Three optimization trials were performed with different initial conditions. The estimation results associated with computation costs were given in Table 1.7. We can see that the optimal solutions are quite sensitive with the initial setting of parameter values. The optimization curves (solution evolution) of these three trials were shown in Fig. 1.41. We are not able to obtain a global solutions in this optimization problem. We only can pick one local minimum by comparing the values of objective function $F(\mathbf{\Theta})$. In this case, we pick the third trial as a solution. We also can see that the simulation-based optimization took several hours to reach a local minimum even with a very close setting of initial values (the third trial). Usually, it is quite hard to find the close settings of initial values and we may have to perform a plenty of trials to finally reach an acceptable solution. This method is time-consuming but

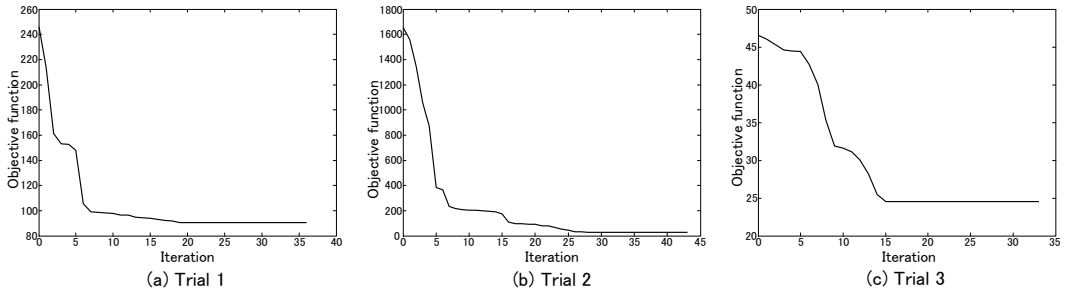

図 1.41: Optimization curves of three trials given in Table 1.7.

quite robust and widely applicable. It can be used in any model to estimate the parameters as long as the simulation can be done.

Estimation Results of Calculation-Based Optimization In calculation-based optimization, the force results were calculated using Eqs. 1.99 and 1.100 instead of running FE simulations. The calculated force results were then used in optimization to minimize the force differences. Totally, five optimization trials were performed for this case. The fist three trials used the same initial conditions with simulation-based optimization (Table 1.7) for the convenience of comparison. The last two trials were with other arbitrary initial values. The estimation results associated with computation costs are given in Table 1.8. We can see that all trials converged to the same solution and it seems like we can find the global minimum by using this method. The optimization curves of the first three trials were shown in Fig. 1.42. Comparing Figs. 1.41 and 1.42, we found that the values of objective function from both simulation- and calculation-based optimization were start from the same value (because the initial parameter setting are the same) but converged to the different minimal values in the end of optimization. Figure 1.41 shows that the curves in simulation-based optimization have more ladder-shaped regions which make the optimization easy to be trapped into a local minimum. On the other hand, the curves from calculation-based optimization are appears more smooth. Smaller tolerance used to terminate the optimization can yield better solutions, especially for simulation-based optimization method. However, it will take much more computation time. From the estimation results given in Tables 1.7 and 1.8, we can see that both optimization methods converge to the very similar solutions, as shown in trial 3 of Table 1.7 and all trials of Table 1.8. Note that the first and second layer Maxwell element are exchangeable in a parallel five-element model. Therefore, the values of E_1 and E_2, c_1 and c_2 are also

表 1.8: Estimation results of E_1, E_2, and c_1 using calculation-based optimization

Trial number	Parameter	Initial value x_0	Final value x^*	$F(\mathbf{\Theta})$ (N^2)	Iteration count	Cost (s)
trial 1	E_1 (Pa)	4×10^4	3.7730×10^4	24.514	15	0.17
	E_2 (Pa)	6×10^4	8.0916×10^4			
	c_1 (Pa·s)	8×10^6	9.2022×10^6			
trial 2	E_1 (Pa)	8×10^4	8.0914×10^4	24.514	20	0.20
	E_2 (Pa)	6×10^4	3.7730×10^4			
	c_1 (Pa·s)	4×10^6	4.9375×10^5			
trial 3	E_1 (Pa)	3×10^4	3.7730×10^4	24.514	14	0.19
	E_2 (Pa)	8×10^4	8.0917×10^4			
	c_1 (Pa·s)	9×10^6	9.2023×10^6			
trial 4	E_1 (Pa)	2×10^3	8.0952×10^4	24.514	23	0.23
	E_2 (Pa)	3×10^4	3.7731×10^4			
	c_1 (Pa·s)	4×10^5	4.9381×10^5			
trial 5	E_1 (Pa)	6×10^5	8.0917×10^4	24.514	16	0.18
	E_2 (Pa)	4×10^5	3.7730×10^4			
	c_1 (Pa·s)	2×10^5	4.9375×10^5			

exchangeable, which makes the solutions of trials 1, 3, and trials 2, 4, 5 of Table 1.8 actually very similar. In addition, the computation costs in the calculation-based optimization were extremely short (less than 1 second in all trials listed in Table 1.8) since there is no FE simulations involved during optimization. However, the disadvantage is that this method only can be used in parallel models which provide the analytical expressions of forces.

粘性率の総和を用いない推定

The value of $\sum_{i=1}^{3} c_i$ calculated separately before force optimization will guarantee a good reproduction of final deformed shape. In the last subsection, this value was used as a constraint during the force optimization. Since this constraint makes the optimization problem losing one independent variable, the result of force optimization will be suffered. We have to compromise the accuracy between the reproductions of final-shapes and force behaviors. Note that the held-shape is affected only by Poisson's ratio γ. Therefore, we do not have to do the same compromise for held-shapes.

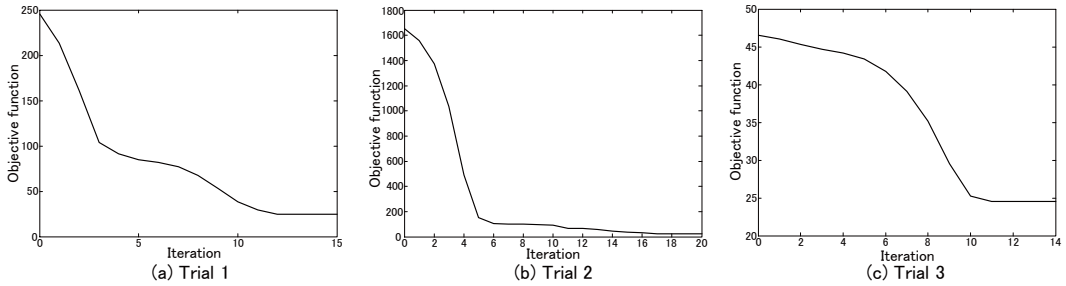

図 1.42: Optimization curves of three trials given in Table 1.8.

表 1.9: Estimation results of E_1, E_2, c_1 and c_2 using simulation-based optimization

Trial number	Parameter	Initial value x_0	Final value x^*	$F(\mathbf{\Theta})$ (N^2)	Iteration count	Cost (hr.)
trial 1	E_1 (Pa)	4×10^4	3.1736×10^4	4.0351	24	24.9
	E_2 (Pa)	7×10^4	7.1867×10^4			
	c_1 (Pa·s)	9×10^6	1.3298×10^7			
	c_2 (Pa·s)	6×10^5	6.9787×10^5			
trial 2	E_1 (Pa)	3×10^4	3.1735×10^4	4.0351	39	39.8
	E_2 (Pa)	8×10^4	7.1884×10^4			
	c_1 (Pa·s)	9×10^6	1.3298×10^7			
	c_2 (Pa·s)	7×10^5	6.9787×10^5			
trial 3	E_1 (Pa)	2×10^3	7.1851×10^4	4.0351	26	26.7
	E_2 (Pa)	3×10^4	3.1732×10^4			
	c_1 (Pa·s)	4×10^5	6.9809×10^5			
	c_2 (Pa·s)	5×10^6	1.3300×10^7			

In some situations, such as deformable objects handled by robotic hand, we may care about the force response and the held-shape much more than the final-shape. In such situations, we can just ignore the calculation of $\sum_{i=1}^{3} c_i$ during the parameter estimation procedure. Instead, we use all four parameters: E_1, E_2, c_1, and c_2 as unknown variables to perform the force optimization. This should give us better results of force reproduction. In the following subsections, the estimation results of these four parameters using both simulation- and calculation-based methods will be presented. Note that $\gamma = 0.2902$ and $c_3 = 100$Pa·s are still used in the following discussions.

表 1.10: Estimation results of E_1, E_2, c_1 and c_2 using calculation-based optimization

Trial number	Parameter	Initial value x_0	Final value x^*	$F(\mathbf{\Theta})$ (N^2)	Iteration count	Cost (s)
trial 1	E_1 (Pa)	4×10^4	3.1752×10^4	4.0766	25	0.3108
	E_2 (Pa)	7×10^4	7.2145×10^4			
	c_1 (Pa·s)	9×10^6	1.3291×10^7			
	c_2 (Pa·s)	6×10^5	6.9733×10^5			
trial 2	E_1 (Pa)	3×10^4	3.1753×10^4	4.0766	24	0.3205
	E_2 (Pa)	8×10^4	7.2147×10^4			
	c_1 (Pa·s)	9×10^6	1.3291×10^7			
	c_2 (Pa·s)	7×10^5	6.9731×10^5			
trial 3	E_1 (Pa)	2×10^3	7.2131×10^4	4.0766	26	0.3554
	E_2 (Pa)	3×10^4	3.1750×10^4			
	c_1 (Pa·s)	4×10^5	6.9745×10^5			
	c_2 (Pa·s)	5×10^6	1.3292×10^7			

Estimation Results with Simulation-Based Optimization Three optimization trials with different initial conditions were performed and the estimation results were given in Table 1.9. The optimization curves are shown in Fig. 1.43. In this case, we are able to find a global minimum and the solution is much better than the ones shown in Tables 1.7 and 1.8 (by comparing the values of objective function $F(\mathbf{\Theta})$).

Estimation Results with Calculation-Based Optimization Estimation results using calculation-based optimization method were given in Table 1.10 and op-

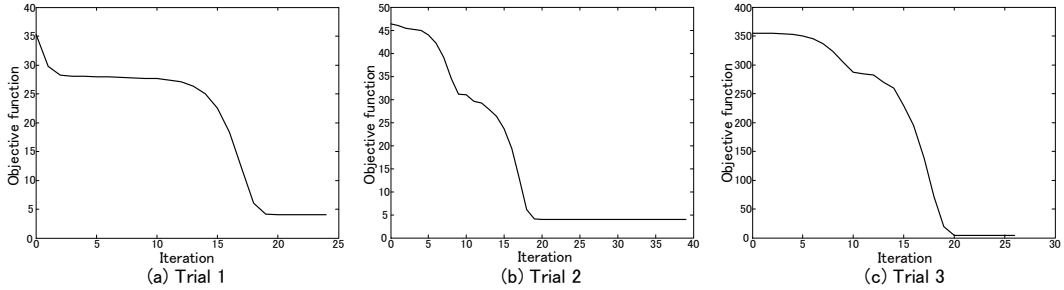

図 1.43: Optimization curves of three trials given in Table 1.9.

表 1.11: Estimation results with the constraint of $\sum_{i=1}^{3} c_i$ for all objects made by clay materials

Trial name	γ	E_1 (Pa)	E_2 (Pa)	c_1 (Pa·s)	$\sum_{i=1}^{3} c_i$ (Pa·s)	$E(\mathbf{\Theta})$ (N^2)
red-06	0.2672	3.1706×10^4	6.4702×10^4	7.4606×10^6	7.9035×10^6	6.3658
red-08	0.2902	3.7730×10^4	8.0916×10^4	9.2022×10^6	9.6961×10^6	24.514
red-10	0.2367	2.7237×10^4	7.5406×10^4	5.4256×10^6	5.9092×10^6	31.5945
blue-06	0.2537	2.0182×10^4	4.4243×10^4	4.4555×10^6	4.9014×10^6	3.1863
blue-08	0.2292	2.6344×10^4	6.4348×10^4	6.9430×10^6	7.6884×10^6	5.5283
blue-10	0.2602	3.0593×10^4	7.5570×10^4	5.7866×10^6	6.5596×10^6	50.4884
yellow-06	0.2593	2.0820×10^4	3.9699×10^4	7.9776×10^6	8.5615×10^6	2.4562
yellow-08	0.2479	2.9216×10^4	4.6662×10^4	1.1663×10^7	1.2385×10^7	28.5041
yellow-10	0.2494	2.1480×10^4	4.1776×10^4	8.0970×10^6	8.9095×10^6	32.8334
average	0.2549	2.7256×10^4	5.9258×10^4	7.4457×10^6	8.0571×10^6	—

timization curves are shown in Fig. 1.44. Comparing with simulation-based method, very similar results were obtained using calculation-based optimization but the computation costs are significantly reduced. Figures 1.43 and 1.44 also show very similar curves of solution evolution.

粘土

By following the same estimation procedures presented above, we can estimate the physical parameters for all experimental objects made of clay materials. Note that $c_3 = 100$Pa·s and the calculation-based optimization method were used in all trials. Estimation results for clay objects with and without the constraint of $\sum_{i=1}^{3} c_i$ are given in Tables 1.11 and 1.12, respectively. Note that the estimated parameters

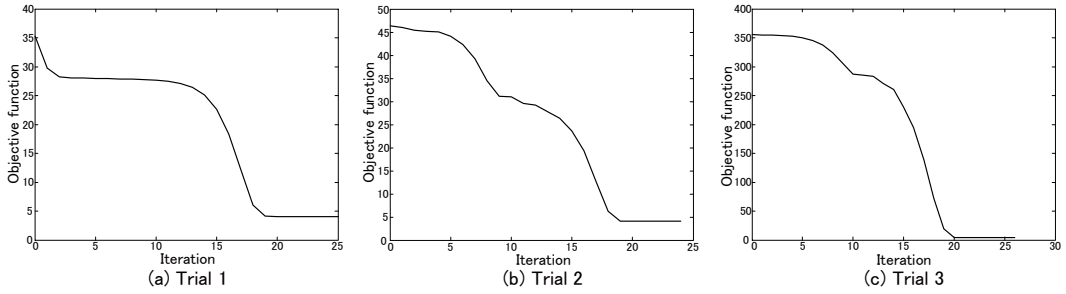

図 1.44: Optimization curves of three trials given in Table 1.10.

表 1.12: Estimation results without the constraint of $\sum_{i=1}^{3} c_i$ for all objects made by clay materials

Trial name	γ	E_1 (Pa)	E_2 (Pa)	c_1 (Pa·s)	c_2 (Pa·s)	$E(\mathbf{\Theta})$ (N^2)
red-06	0.2672	2.8650×10^4	6.0364×10^4	8.8323×10^6	5.4820×10^5	3.1418
red-08	0.2902	3.1753×10^4	7.2147×10^4	1.3291×10^7	6.9731×10^5	4.0766
red-10	0.2367	2.1954×10^4	6.7528×10^4	8.4719×10^6	6.8294×10^5	4.2865
blue-06	0.2537	1.6582×10^4	4.2801×10^4	6.0304×10^6	6.1032×10^5	0.3573
blue-08	0.2292	2.2164×10^4	6.0319×10^4	8.7880×10^6	9.6051×10^5	1.2468
blue-10	0.2602	2.2424×10^4	7.1494×10^4	9.3098×10^6	1.2391×10^6	1.8716
yellow-06	0.2593	1.7273×10^4	3.6229×10^4	1.0636×10^7	8.4945×10^5	0.2495
yellow-08	0.2479	2.1804×10^4	4.2930×10^4	1.9429×10^7	1.3657×10^6	0.6176
yellow-10	0.2494	1.5206×10^4	4.1475×10^4	1.4602×10^7	1.4882×10^6	0.5583

listed in Table 1.11 yield good reproductions of final-shapes while parameters in Table 1.12 result in good approximation of force responses. We can see that both sets of parameters of some clay objects are quite close and the optimal values of objective function (given in the last column of both tables) are also not very different. This means that it is possible for those objects (*e.g.*, red-06, blue-06) to use one set of parameters to accurately reproduce both deformation and force behaviors. However for most objects, the differences of parameters and objective function values are significant, especially the values of $\sum_{i=1}^{3} c_i$ which dominate both final-shape and force amplitude as discussed in Section 1.2. For these objects, one set of parameters is not enough to reproduce both rheological deformation and force simultaneously.

和菓子の材料

The same parameter estimation procedures were also performed for objects made by three kinds of Japanese sweets materials. Experimental information was given in Table 1.4. Estimation results for these three objects with and without the constraint of $\sum_{i=1}^{3} c_i$ are given in Tables 1.13 and 1.14, respectively. Comparing with results of clay materials, two sets of parameters of sweets objects are very different with each other. The values of $\sum_{i=1}^{3} c_i$ from Table 1.14 (not given directly but can be easily calculated) are around 10 times larger than those given in Table 1.13. The optimal values of objective function are even hundreds times different. This means it is impossible for objects made by sweets materials to accurately reproduce both rheological deformation and forces simultaneously. This problem comes from the

表 1.13: Estimation results with the constraint of $\sum_{i=1}^{3} c_i$ for three objects made by Japanese sweets materials

Trial name	γ	E_1 (Pa)	E_2 (Pa)	c_1 (Pa·s)	$\sum_{i=1}^{3} c_i$ (Pa·s)	$E(\mathbf{\Theta})$ (N^2)
material 1	0.3746	8.1002×10^3	9.7210×10^3	1.0804×10^6	2.3761×10^6	326.01
material 2	0.3353	1.0662×10^4	3.7979×10^3	1.2423×10^6	1.6849×10^6	186.48
material 3	0.3267	5.8791×10^3	7.3308×10^3	8.6015×10^5	1.9319×10^6	76.41

表 1.14: Estimation results without the constraint of $\sum_{i=1}^{3} c_i$ for three objects made by Japanese sweets materials

Trial name	γ	E_1 (Pa)	E_2 (Pa)	c_1 (Pa·s)	c_2 (Pa·s)	$E(\mathbf{\Theta})$ (N^2)
material 1	0.3746	1.3468×10^4	2.4695×10^4	2.9631×10^7	7.2381×10^4	0.9152
material 2	0.3353	1.0553×10^4	3.7276×10^4	1.3213×10^7	1.1593×10^5	0.8385
material 3	0.3267	9.1565×10^3	5.0802×10^4	8.1809×10^6	1.3427×10^5	0.7208

physical model (*e.g.*, parallel five-element model) itself and it cannot be resolved by adding more basic elements to the physical model or changing the configuration of the model. Further validation of this phenomenon with simulation results comparing with experimental ones will be presented in the later of this chapter.

多重粘性要素を用いたモデルにおける推定

For some materials, such as clay materials discussed above, one set of parameters seems enough to capture both rheological forces and deformation behaviors. However for most rheological objects, such as Japanese sweets products, it is impossible to use only one set of parameters to cover both force and deformation simultaneously. We have therefore introduced FE model with dual-moduli viscous elements (Section 1.3) to solve this problem. Here, we suppose that the FE model was formulated using parallel five-element model with two dual-moduli viscous elements (Fig. 1.12b) and we preassigned a value of 100 Pa·s to parameter c_3. By following the estimation procedure presented in the previous section, we can determine those parameters for FE model with dual-moduli viscous elements and listed them in Table 1.15. Note that the Poisson's ratios are not listed in this table and they take the same values as given in Table 1.14.

表 1.15: Estimation results of FE model with dual-moduli viscous elements for simulating the objects made of Japanese sweets materials

Trial name	E_1 (Pa)	E_2 (Pa)	c_1 (Pa·s)	c_2 (Pa·s)	α_1 (Pa·s)	α_2 (Pa·s)
mat.1	1.3468×10^4	2.4695×10^4	1.4820×10^7	5.3855×10^4	1.4811×10^7	1.8527×10^4
mat.2	1.0553×10^4	3.7276×10^4	6.6096×10^6	7.8271×10^4	6.6034×10^6	3.7659×10^4
mat.3	9.1565×10^3	5.0802×10^4	4.0958×10^6	8.2198×10^4	4.0851×10^6	5.2072×10^4

1.6.4 検証結果

In the above sections, the experimental information was introduced and the physical parameters for clay and Japanese sweets materials were estimated using different methods. In this section, the simulation results using the estimated parameters will be compared with experimental measurements to show the performance of our FE model and parameter estimation methods. Note that the physical parameters were estimated by using measured data of the uniform objects (for both clay and sweets materials) with compressing operations from the entire top surfaces. The measurements of uniform objects compressed from the center-top surfaces (white colored clay objects) and non-uniform sweets objects compressed from top and center-top surfaces were used to evaluate the estimated parameters.

粘土

At first, the estimated parameters listed in Tables 1.11 and 1.12 were used to simulate the corresponding clay objects to show performance of our optimization-based estimation methods and also to demonstrate the difference between these two methods with or without the constraint of $\sum_{i=1}^{3} c_i$. Simulation results compared with experimental measurements for three trials (denote by red-08, blue-06, and yellow-08 in Tables 1.11 and 1.12) were shown in Figs. 1.45, 1.46, and 1.47, respectively. From these figures we can see that estimated parameters with the constraint of $\sum_{i=1}^{3} c_i$ yield better results of final-shapes. On the other hand, estimated parameters without this constraint result in better results in force approximation. This is coincide with our theoretical analysis, *i.e.*, the summation $\sum_{i=1}^{3} c_i$ dominates the residual deformation. We can also see that the estimated parameters with the constraint always under-approximated the force amplitudes, especially in the end of the holding phases. On the other hand, the estimated parameters without the constraint

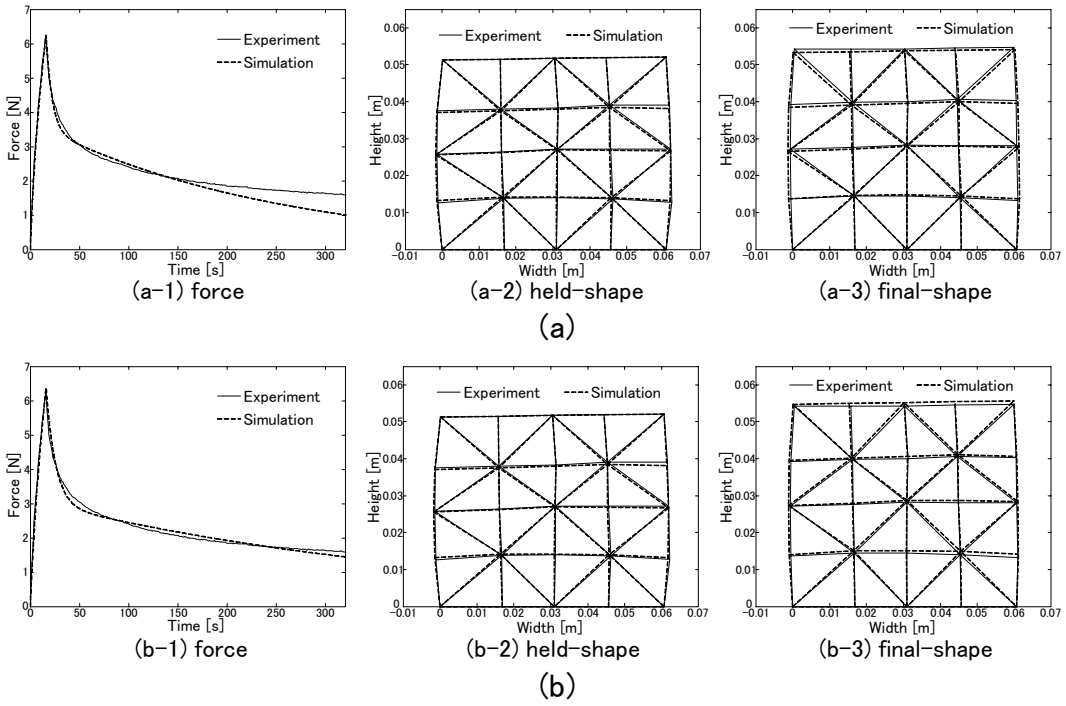

図 1.45: Validation results for object red-08 (a) with and (b) without the constraint of $\sum_{i=1}^{3} c_i$.

always over-approximated the final-shapes, especially for object yellow-08 shown in Fig. 1.47. It can be explained that accurate approximation of final-shape requires relative smaller values of $\sum_{i=1}^{3} c_i$ while accurate approximation of force behaviors requires relative larger values. If we look at Tables 1.11 and 1.12, we find that the values of $\sum_{i=1}^{3} c_i$ in Table 1.12 are always larger than those in Table 1.11. The object yellow-08 has the largest difference (about 1.8 times) between two sets of parameters among these three objects. This is why the differences in both force and deformation behaviors shown in Fig. 1.47 are larger than those in Figs. 1.45 and 1.46. However, we can obtain good reproductions of both rheological forces and deformation behaviors for objects red-08 and blue-06 within a relative short time (within 200 seconds) using the estimated parameters with the constraint of $\sum_{i=1}^{3} c_i$. Actually in most applications, the holding time may not be very long. In such cases, the parameters listed in Table 1.11 are good enough to reproduce both rheological forces and deformation behaviors simultaneously.

The simulation results shown in Figs. 1.45, 1.46, and 1.47 were performed using their own estimated parameters. In other words, these validation results only showed

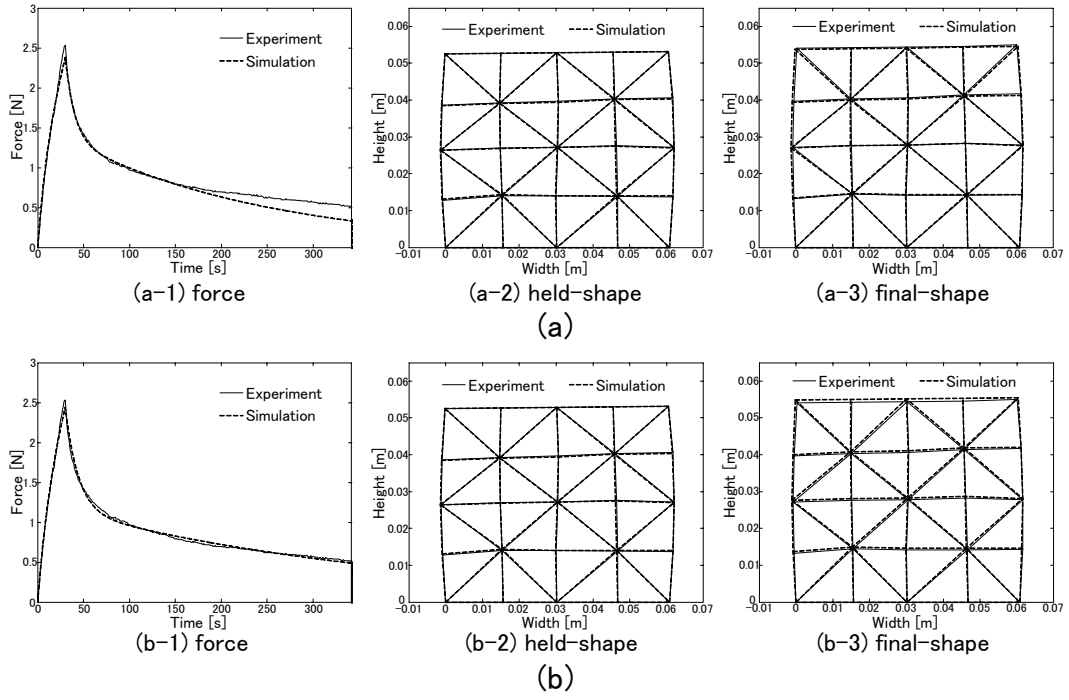

図 1.46: Validation results for object blue-06 (a) with and (b) without the constraint of $\sum_{i=1}^{3} c_i$.

how well the force and shape optimizations were performed. These validation results are thus quite insufficient. We therefore conducted three other experiments with objects made by white colored clay materials. In order to investigate how the estimated parameters can handle different operations, we compressed these three objects from the center area of the top surfaces instead of the entire top surfaces and also with different compressing velocities of 0.5 m/s, 0.2 m/s, and 0.1 m/s, respectively. Detailed experimental information of these three trials can be found in Table 1.3. Note that different colored clay materials actually denote different materials and they may have different properties. However, since they were sold in the same pack and manufactured at the same time, the difference in properties among them was supposed to be negligible. Therefore, the average values of estimated parameters listed in the last row of Table 1.11 were used to reproduce the rheological behaviors of these three objects. The simulation results compared with experimental measurements were shown in Fig. 1.48. Because the deformation behaviors are more complicated (especially in the contact corners) than compressing from the entire top surfaces, we have used a 16×16 triangular mesh instead of a 4×4 mesh to simulate the

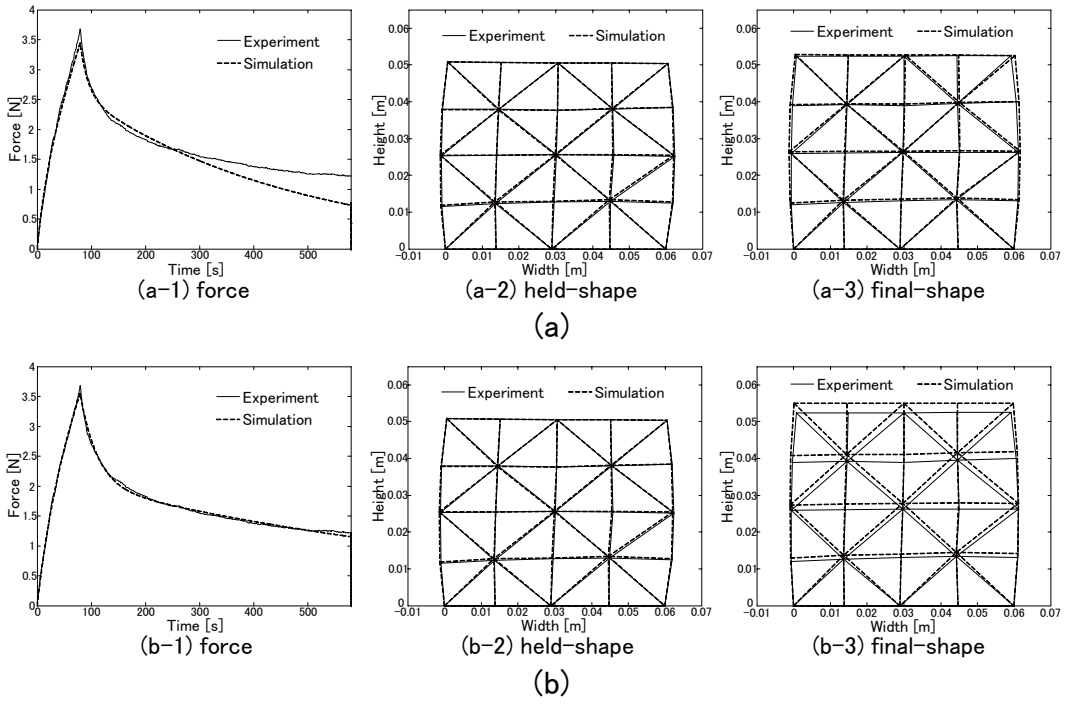

図 1.47: Validation results for object yellow-08 (a) with and (b) without the constraint of $\sum_{i=1}^{3} c_i$.

behaviors of these white colored objects. In order to clearly show the deformation comparisons between simulation and experiments, only 8×8 lattice mesh was shown in Fig. 1.48. We find that both held-shapes and final-shapes are pretty well matched between simulation results and experimental measurements and we can achieve good reproductions of force behaviors in a short term (within about 200 seconds). We can therefore say that we can obtain acceptable reproduction results of both rheological force and deformation for clay objects by using our FE model and the estimated parameters listed in Table 1.11.

和菓子の材料

The estimated parameters listed in Tables 1.13 and 1.14 were used to simulate these three objects to see what happen for sweets materials with two estimation methods with or without the constraint of $\sum_{i=1}^{3} c_i$. Simulation results compared with experimental measurements for these three trials are shown in Figs. 1.49, 1.50, and 1.51, respectively. We can see that estimated parameters with the constraint of

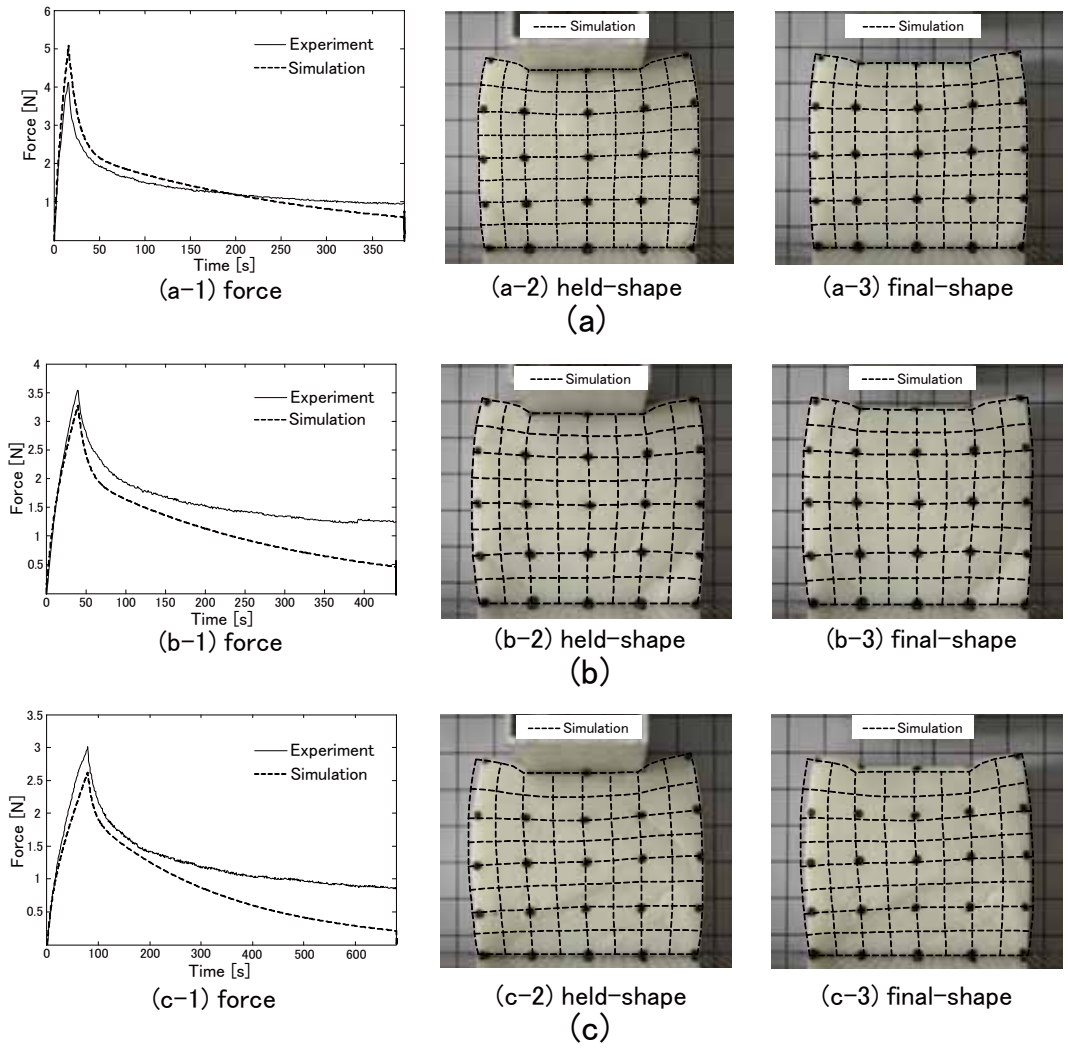

図 1.48: Validation results for white colored objects with a compressing velocity of (a) 0.5 m/s, (b) 0.2 m/s, and (c) 0.1 m/s.

$\sum_{i=1}^{3} c_i$ yield good results of final-shapes but bad results of forces. On the contrary, estimated parameters without this constraint result in good results in force but bad in final-shapes. This again proved our theoretical discussions of $\sum_{i=1}^{3} c_i$ dominating both force amplitude and residual deformation. The values of $\sum_{i=1}^{3} c_i$ in Tables 1.13 and 1.14 are very different with each other. The ratios between these two set of values $\sum_{i=1}^{3} c_i$ are 12.5, 7.91, and 4.3 (values in Table 1.14 divided by values in Table 1.13) for sweets materials 1, 2, and 3, respectively. We can see that material 1 has the largest ratio and also the largest difference of the objective function values (listed

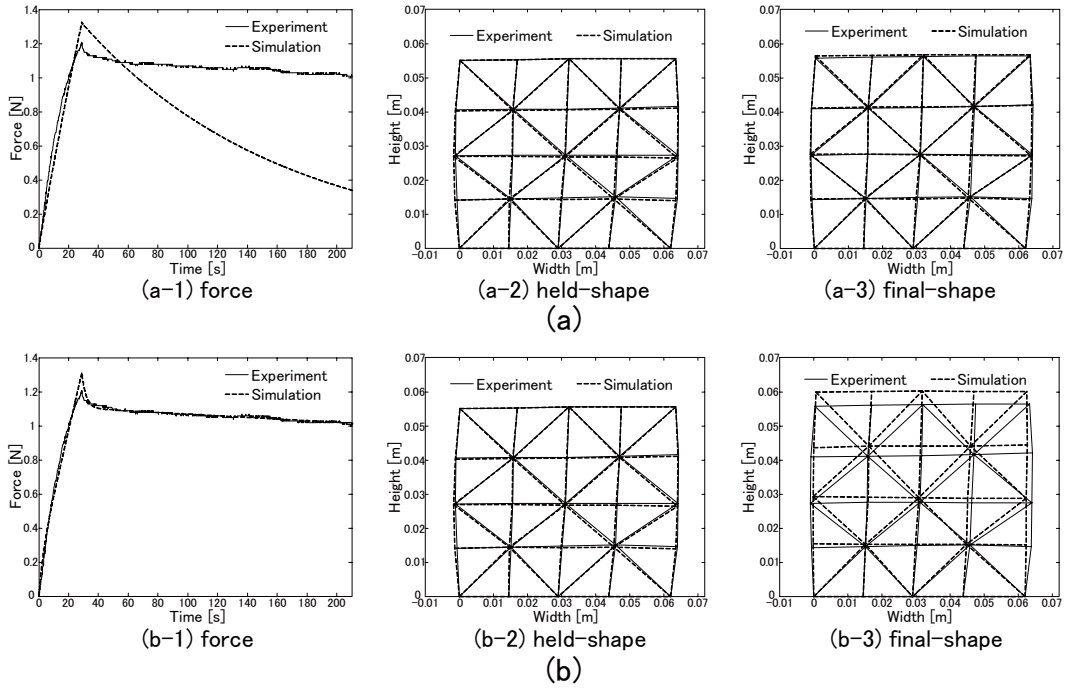

図 1.49: Validation results for sweets material 1 (a) with and (b) without the constraint of $\sum_{i=1}^{3} c_i$.

in the right most column in Tables 1.13 and 1.14). We are not able to accurately reproduce both forces and deformation behaviors simultaneously for sweets objects by using only one set of parameters. Using one set of parameters, we can reproduce either rheological forces or deformation behaviors alone. It is impossible to cover both in the same time. If we use only one set of parameters, we always have to compromise between the reproductions of force and deformation behaviors. We believe the reason of this phenomenon arises from the nonlinearity of material properties. Our FE model is based on linear Hooke's law, which provided a proportional relationship between stress and strain (force and displacement in 2D case). Most real materials include nonlinear, rate-, and time-dependent properties. Therefore, it is hard to use a linear model to approximate such nonlinear behaviors. We can introduce nonlinear modeling, such as the model with Green strain tensor as presented in Section 1.3, to cope with this problem. Such nonlinear models suffer from high computational cost because of the complicated constitutive equations and the intensive calculation for updating the stiffness matrices. Analytical expressions of force are usually not available for such nonlinear models, which makes the parameter estimation more

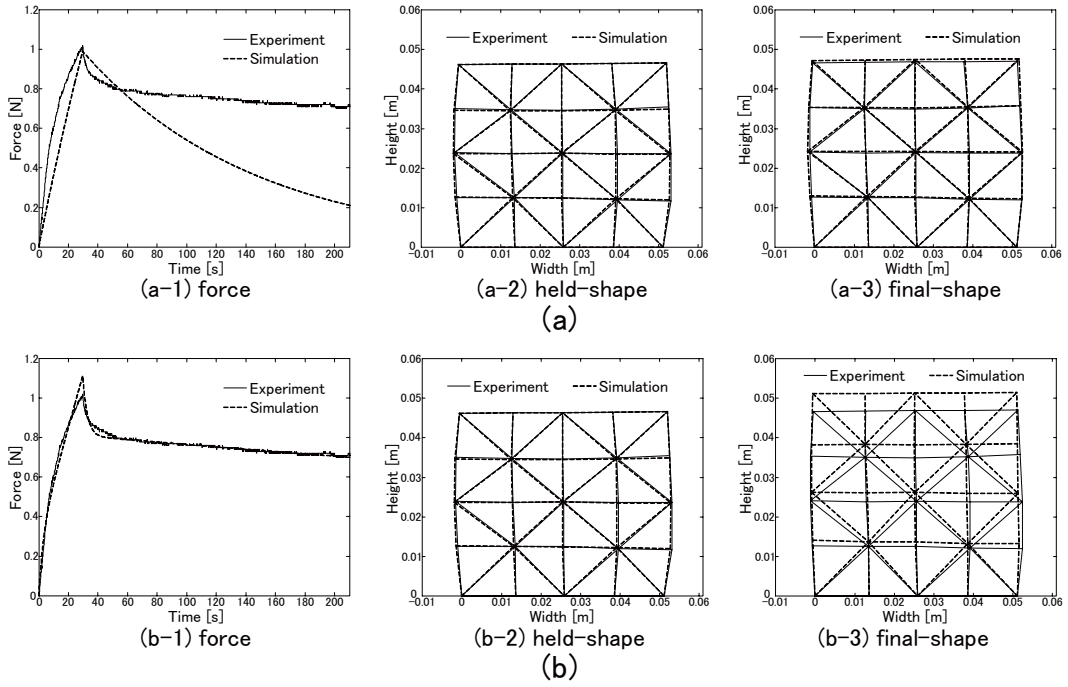

図 1.50: Validation results for sweets material 2 (a) with and (b) without the constraint of $\sum_{i=1}^{3} c_i$.

difficult and sometimes inapplicable. We have therefore introduced dual-moduli viscous elements into our FE model to deal with this problem and next section will demonstrate validation results of this model.

多重粘性 FE モデルの検証

The dual-moduli viscous element has an ability to switch two parameters from one to the other during simulation. The FE model is still linear model and only some parameters (c_1 and c_2 in the case of parallel 5-element model) change values before and after the switching moment. This model can yield accurate reproductions of both rheological forces and deformation behaviors simultaneously with the same computation cost as a linear model with one set of parameters.

Validation Results for Corresponding Uniform Objects At first, we have used the estimated parameters listed in Table 1.15 to simulate the corresponding objects made by three sweets materials. The simulation results compared with ex-

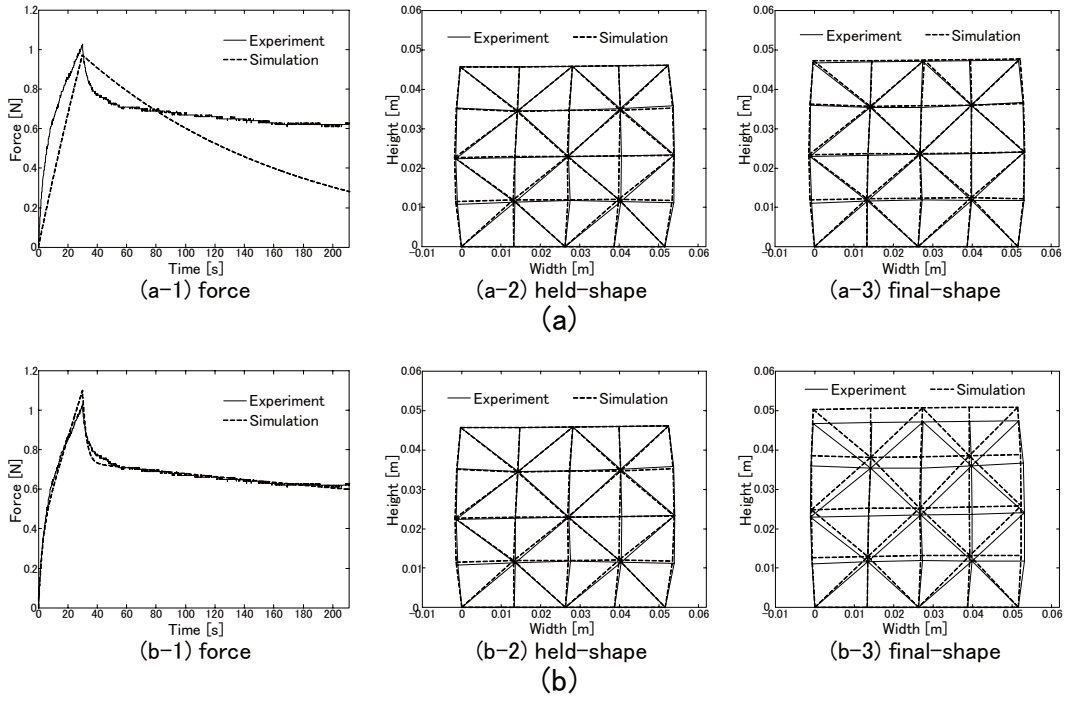

図 1.51: Validation results for sweets material 3 (a) with and (b) without the constraint of $\sum_{i=1}^{3} c_i$.

perimental measurements are shown in Fig. 1.52, where the solid line denotes the results from experimental measurements and dashed line (may be hard to distinguish) denotes the results from simulation. We can see that this model successfully captured both rheological forces and deformation behaviors simultaneously.

Validation Results for Non-Uniform Layered Objects Made by Sweets Materials Again, the simulation results shown in Fig. 1.52 were performed using their own estimated parameters. These validation results therefore only demonstrate how well the parameter estimation procedures were conducted. In order to further evaluate the estimated parameters, several other experimental trials with layered objects, as shown in Fig. 1.40, were performed. Each object consists of three layers and two different materials, with the materials of the top and bottom layers being identical. These types of layered structures are often encountered in food products, such as sandwich and sushi. Different combinations of two materials were tested, *e.g.*, in Fig. 1.40a-1, the object was made of Materials 1 and 2 with Material 1 in the middle. The objects were compressed over their entire top surfaces (Fig.

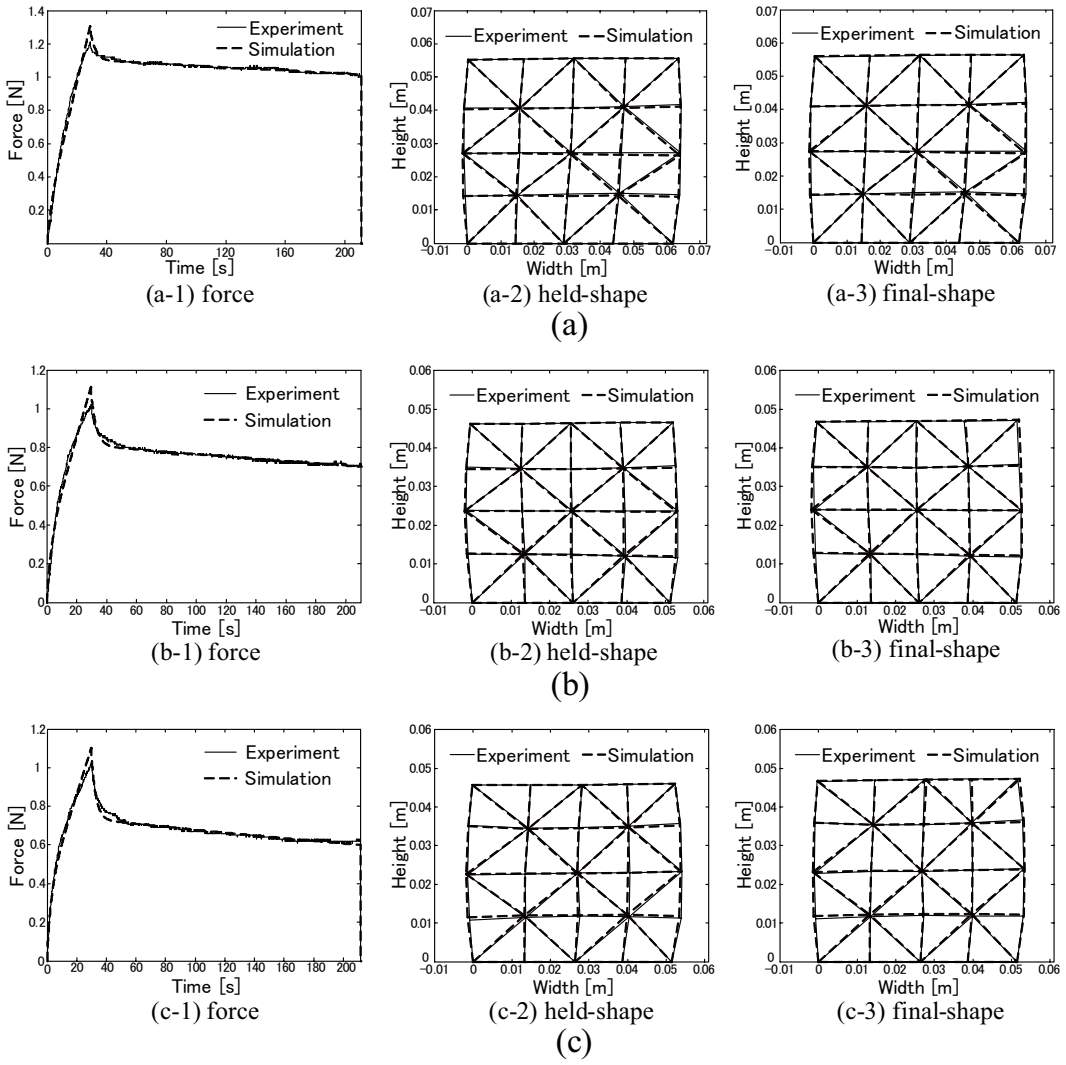

図 1.52: Validation results of FE model with dual-moduli viscous elements for objects made by Japanese sweets material 1 (a), 2 (b), and 3 (c).

1.40a) or at the center (Fig. 1.40b) of the top surfaces with a constant velocity of 0.2 mm/s. Detailed experimental information can be found in Table 1.4. The estimated parameters listed in Table 1.15 were then used to simulate these layered objects. Comparisons of the simulation results and experimental measurements are shown in Figs. 1.53 and 1.54. In Fig. 1.54, the object images are from experiments and the blue and red lines are obtained from simulations. Because the objects compressed over their entire top surfaces showed simple deformation behaviors, 4×8

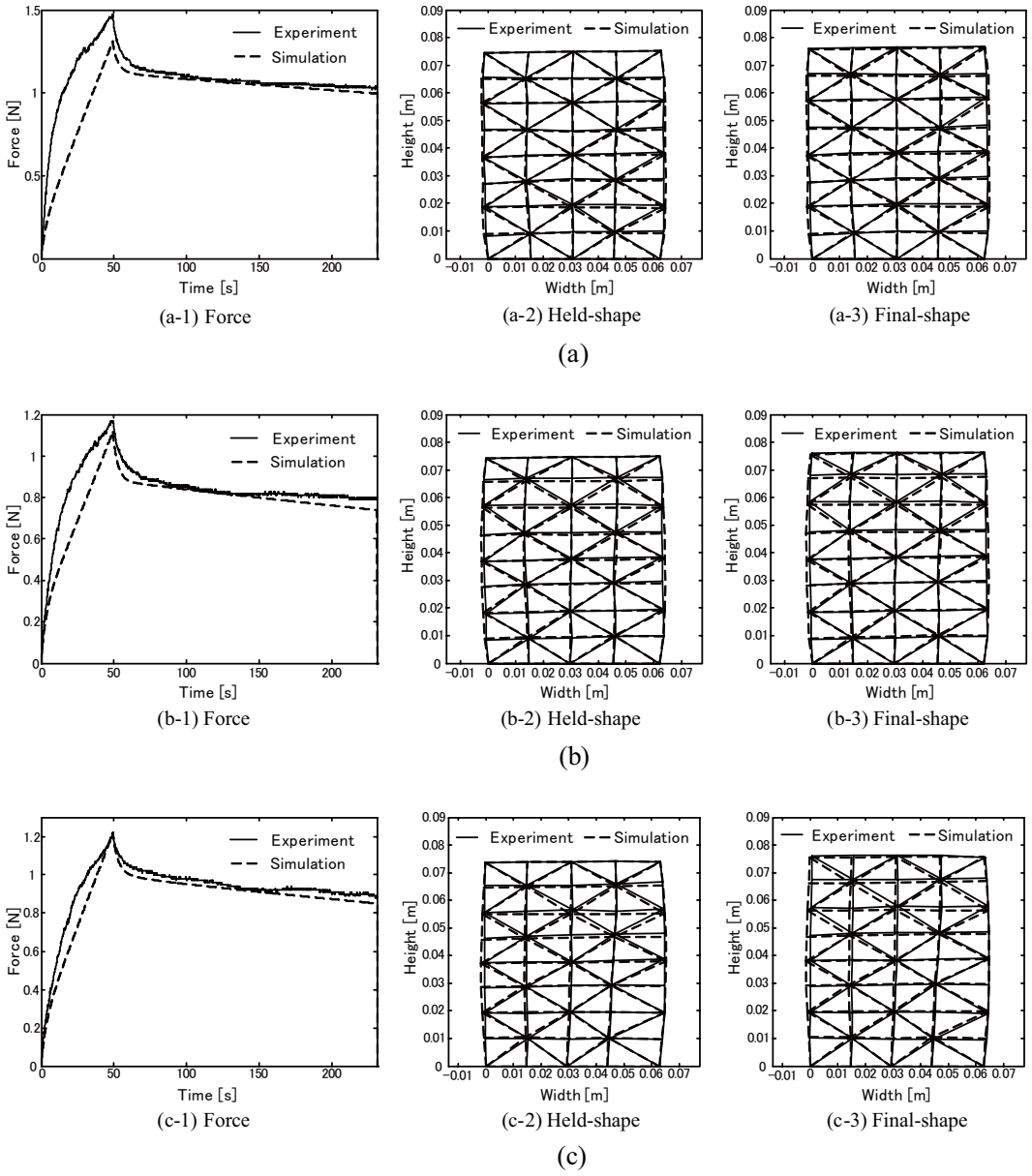

図 1.53: Validation results of layered objects compressed over the entire top surfaces. The layered objects made by materials 1+2 (a), 2+3 (b), and 1+3 (c), respectively.

triangular meshes are sufficient for their simulations, as shown in Fig. 1.53. On the other hand, the objects compressed at the center of top surfaces demonstrate more complicated deformations around the contact corners. We therefore use triangular meshes with finer resolution (16×32) to reproduce these deformation behaviors. In

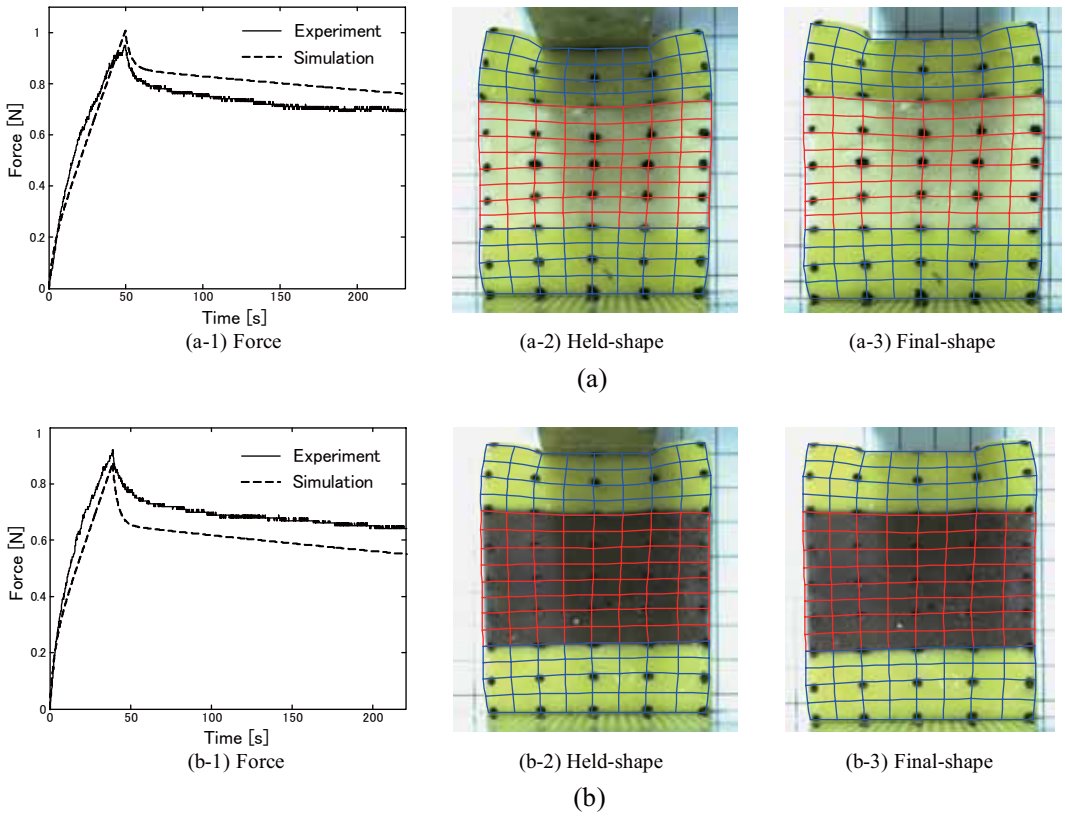

図 1.54: Validation results of layered objects compressed at the center of the entire top surfaces. The layered objects made by materials 1+2 (a) and 2+3 (b), respectively.

Fig. 1.54, only 8×16 lattice meshes are given for the convenience of comparisons with the experimental images. The validation results in Figs. 1.53 and 1.54 show the successful reproductions of both deformation behaviors and force responses for these layered objects. But the simulations results shown in Fig. 1.54 exhibited larger errors than those in Fig. 1.53, especially the force behaviors. This suggests that better validation results might be obtained if the operation conditions used in parameter estimation and application are identical. Even though the force reproductions in Fig. 1.54 suffer from some errors, the errors are still in acceptable range for most applications.

1.6.5 まとめ

In this section, experimental setup and compressing tests were demonstrated and simulation results were compared with experimental measurements to validate our FE models and parameter estimation methods. Two kinds of rheological materials, commercial available clay and Japanese sweets materials, were employed in our experiments. Flat-squared objects made by these two materials were compressed using a linear stage with a pushing-holding-releasing operations. The force data and static images were recorded for estimating the physical parameters. The estimation methods presented in the previous chapter were used to estimate the physical parameters for these objects. Two sets of parameters with or without the constraint of $\sum_{i=1}^{3} c_i$ were given to compare the differences. The simulations were then performed using the estimated parameters and comparisons between simulation results and experimental measurements were done to validate the proposed FE models and parameter estimation methods. We found that the estimated parameters with the constraint of $\sum_{i=1}^{3} c_i$ yield better reproduction of final-shapes while parameters without $\sum_{i=1}^{3} c_i$ result in better force reproductions. For some objects made by clay materials, good reproductions of both rheological forces and deformation behaviors can be achieved simultaneously by using only one set of parameters. However for other objects, this is impossible and the reason caused the failure is the linearity of the physically-based models. Fortunately, after introducing the dual-moduli viscous elements into our FE models, we have finally solved this problem and successfully reproduced both rheological forces and deformation behaviors simultaneously. The estimated parameters from uniform objects can also be used in simulating non-uniform layered objects even with different compressing operations.

Note that the measurement requirements for our estimation methods included three static images of the object: the initial shape, the held-shape, and the final-shape, and the force responses during the experiments. In addition, we have used regular shaped objects with some markers drawn on the surfaces throughout our experiments. However, our estimation method is not limited by the shape of the object and can be applied to arbitrary object as long as the deformation field of some feature points is available. Besides, the loading position is also not limited to the top surface but may be anywhere, even at just one point convenient for force measurements.

1.7 結言

1.7.1 結論

Modeling and simulation of deformable objects has been playing an important role in many applications, such as surgical simulation, robotic manipulation, food engineering, and so on. Many modeling methods have been proposed, such as MSD, FEM, and particle-based methods, *etc*. They all have their own advantages and disadvantages. There are even many commercial softwares available for simulating deformable objects, such as ANSYS and ABAQUS. However, the modeling and simulation of deformable objects is still a unmature and hot research field. This is not only because the development of computation technology makes more methods applicable, but also because the diversity of deformation behaviors demonstrated in real world objects.

The work presented in this dissertation is focusing on modeling and reproducing the behaviors of rheological objects, which include both elastic and plastic properties and always yield residual deformation after loading-unloading operations. The difficult part of this subject is how to accurately reproduce both rheological forces and deformation, especially residual deformation behaviors simultaneously. The main contributions of our current work are as follows:

1. We have summarized the physically-based models which can be used to simulate rheological behaviors. We categorized such physical models into serial and parallel models and proposed a criterion to choose an appropriate one for certain application. We have derived the generalized constitutive laws for both models and found a corresponding relation between the two models. We then derived the analytical expressions of rheological forces and residual deformation for generalized parallel models. Through a series of analysis, we found that there is contradiction between accurate reproductions of rheological forces and residual deformation. In order to cope with this contradiction, we have proposed a dual-moduli viscous element and integrated it with our physically-based models.

2. We have developed 2D and 3D FE dynamic models for simulating rheological behaviors based on the physically-based models and linear Cauchy strain tensor. In order to simulate large deformation and deformation with rotation motion, the nonlinear Green strain tensor has also been introduced into our FE formulations. The FE dynamic model with dual-moduli viscous elements was also derived. We

have then extended our FE model to deal with non-uniform layered objects and contact interaction between rheological objects and external instruments. We found that the losing contact moment can serve as a perfect criterion for dual-moduli viscous element to switch the parameters.

3. We have proposed several methods for estimating the physical parameters of rheological objects. The basic idea is to minimize the difference between simulation results and experimental measurements with updated physical parameters. In order to capture both rheological forces and deformation behaviors, we proposed a three-step method with a separate estimation of Poisson's ratio γ and calculation of summation $\sum_{i=1}^{n} c_i$. Both simulation- and calculation-based optimization methods were investigated and compared. The simulation-based method is robust but time-consuming, while the calculation-based method is very efficient but limited to only parallel models. we found that the three-step method works well for some rheological objects but failed to others. We have therefore estimated the parameters of FE model with dual-moduli viscous elements. We employed the calculation-based optimization method to minimize the force difference and simulation-based method to optimize the difference of final-shapes.

4. A series of compressing tests were performed using objects made by commercial available clay and Japanese sweets materials. Experimental measurements of uniform objects with compressing from the top surfaces were used to estimate the physical parameters. The estimated parameters were then employed to simulate uniform objects with compressing operation from the top-center surfaces and even non-uniform layered objects. Through various validations, we proved the contradiction between the reproductions of rheological forces and residual deformation. For several clay objects, this contradiction phenomenon is not obvious and we could obtain acceptable results for both force and deformation using only one set of parameters. For other objects, however, this contradiction phenomenon is very strong and it is impossible to use one set of parameters to cover both rheological forces and deformation behaviors. This coincides with our theoretical discussions. The FE model with dual-moduli viscous elements and estimated parameters were then employed to solve this problem and finally we successfully reproduced both rheological forces and deformation behaviors simultaneously.

Even though our current work concentrated on reproductions of rheological behaviors, most of our discussions and methods can be easily applied to elastic, visco-

elastic, and plastic models as long as the physically-based models were used. Since our attention is focusing on the reproduction accuracy of both forces and deformation, we have to sacrifice the computation costs and real-time performance is not of concern in the current situation.

1.7.2 今後の課題

According to our current works, we have done a systematic analysis of modeling for simulating rheological behaviors and we have established efficient methods for estimating physical parameters of rheological objects. In the future, we plan to make our efforts on the following directions:

1. 3D validation of our FE model and estimated parameters. 3D FE formulation has been presented in this dissertation. But we did not perform any simulation validation for real objects with estimated parameters. The physical parameters were mainly estimated by using 2D FE model and they are supposed to be applicable in 3D simulation. Thus, we need experimental validations of this issue. If the proposed methods are not applicable, new parameter estimation methods with 3D model have to be investigated. This is theoretically feasible but practically difficult because the computation costs.

2. Therefore, the second future target is to speed up our FE simulation. We plan to use the new computing architecture called GPGPU (General Purpose Graphic Processing Unit) to achieve this target.

3. In the current experiments, only two kinds of materials were tested. This is quite limited. We will perform more experiments with other rheological objects, such as Japanese tofu and various kinds of sushi. There might be some interesting behaviors which have not been discovered.

4. We are now working on particle-based model, such as Smoothed Particle hydrodynamics (SPH). This could be another option for simulating rheological objects. Comparing with FE model, SPH model has advantages of low computation costs and convenient implement for complex operations, such as cutting and reforming. The SPH model also need parameter estimation when dealing with real materials. The parameter estimation ideas presented in this dissertation can serve as a good reference.

第2章　人指の内部変位計測と変形シミュレーション

2.1　緒言

人は，意識していなくても手を使い物体を把持したり，操作することができる．このような人の巧みな操作を解明，実現するために，様々な分野で人の巧みな動作を解明する試みが行われている．従来より，人の軟組織が物体の安定な把持，操作に貢献していることは指摘されていたが，指先の面接触による摩擦の増加や指先への衝撃力の緩和などの簡単な議論しかされてこなかった．そこで，ロボティクスの分野では，軟組織を含む系を力学的に解析することで，軟組織が人の巧みな動作にどのように貢献しているかを解明する努力がなされている．その結果，軟組織がポテンシャルエネルギー場を形成することで，物体の安定な把持や操作に貢献していることが明らかになりつつある．しかし，このような解析を行う場合，指の軟組織の部分には半球体の単純な系の柔軟指が用いられることが多い．ゆえに，実際に人が指先で物体を把持や操作している場合に同じ理論が使用できるかは分かっていない．また，実際に人の巧みな動作を行う人間型のロボットハンドの研究や開発もなされている．しかし，このようなロボットハンドの指先には金属やプラスティック樹脂などの剛体指が使用されることが一般的である．たとえ，指先に柔軟な素材が使われていたとしても，物体の把持，操作の際に使われる制御則は剛体指と同様の制御則が用いられることがほとんどである．ゆえに，柔軟指の特徴が考慮されておらず，制御則としては適しているものであるとは言い難い．

著者らはこれまでに，人の巧みな動作における軟組織の役割の解明を試みた．その結果，柔軟指における物体の安定的な把持，操作には指先の弾性ポテンシャルエネルギーが大きな役割を果たしていることを解明することができた[45]．これは，硬い板と半球体の柔軟物からなる指先において，弾性ポテンシャルエネルギーは柔軟物の凹み量だけでなく，指と物体の姿勢にも依存し，物体の安定な把持，操作にはポテンシャル場の極小により力学的に説明できるというものである．また，MRI 等の内部イメージング技術を用い，柔軟物内部の変形計測の研究がなされている [46]．この研究では，FE モデルを用いたシミュレーションで，生体組織などの非一様な変

形特性を持つ物体の力学パラメータの同定方法を確立することを目的としている．

本章では，三次元での人指の変形シミュレーションの作成とその評価を研究の目的とする．まず，MR 装置を用いて得られた画像から人指の内部変位を三次元的に計測する．そして，人指の変形シミュレーションを作成し，計測結果と比較し，その評価を行う．

2.2 指の変形シミュレーション

本節では，指の物体の接触判定法および指の変形シミュレーションについて述べる．

2.2.1 物体同士の接触判定

二次元での接触判定

物体の変形シミュレーションを行う場合，物体同士の接触を判定する必要がある．図 2.1 に二次元での物体同士の接触モデルを示す．板状物体は一定速度で図の下方向に移動し，変形物体は固定されている．接触判定には，板状物体に含まれる三角形要素 $\triangle \mathrm{P}_i\mathrm{P}_j\mathrm{P}_k$ と物体の一つの節点 Q を使用する．今，節点 Q と $\triangle \mathrm{P}_i\mathrm{P}_j\mathrm{P}_k$ で構成される三角形は，$\triangle \mathrm{QP}_j\mathrm{P}_k$，$\triangle \mathrm{P}_i\mathrm{QP}_k$，$\triangle \mathrm{P}_i\mathrm{P}_j\mathrm{Q}$ の 3 個である．これら 3 個の三角形要素の面積は，図 2.2-(a) のように，節点 Q が $\triangle \mathrm{P}_i\mathrm{P}_j\mathrm{P}_k$ 内側にあるとき以下の条件が成り立つ．

$$\triangle \mathrm{QP}_j\mathrm{P}_k > 0, \quad \triangle \mathrm{P}_i\mathrm{QP}_k > 0, \quad \triangle \mathrm{P}_i\mathrm{P}_j\mathrm{Q} > 0. \tag{2.1}$$

このように，三角形要素の面積は全て正の値になる．しかし，図 2.2-(b) のように物体の節点 Q が外部にあるときは，3 個の三角形要素の面積は，

$$\triangle \mathrm{QP}_j\mathrm{P}_k > 0, \quad \triangle \mathrm{P}_i\mathrm{QP}_k > 0, \quad \triangle \mathrm{P}_i\mathrm{P}_j\mathrm{Q} < 0 \tag{2.2}$$

となり，$\triangle \mathrm{P}_i\mathrm{P}_j\mathrm{Q}$ が負の値となる．この性質を利用することで，物体の接触判定を行うことが可能となる．つまり，物体に含まれる全ての節点と $\triangle \mathrm{P}_i\mathrm{P}_j\mathrm{P}_k$ で構成される 3 個の三角形の面積を計算することで，物体同士の接触判定を行うことができる．

三次元での接触判定

図 2.3 に三次元での接触モデルを示す．図のように硬い板状物体と節点 Q があるとする．板状物体は一定の速度で図中の下方向に移動し，節点 Q と接触する．板状物体に含まれる四面体要素 $\Diamond \mathrm{P}_i\mathrm{P}_j\mathrm{P}_k\mathrm{P}_l$ を図のように設定したとき，節点 Q と $\Diamond \mathrm{P}_i\mathrm{P}_j\mathrm{P}_k\mathrm{P}_l$

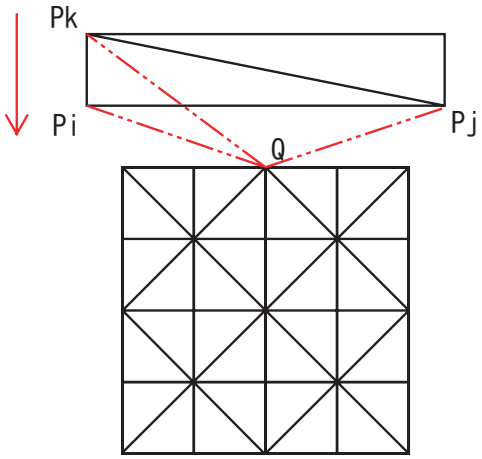

図 2.1: 二次元での接触モデル

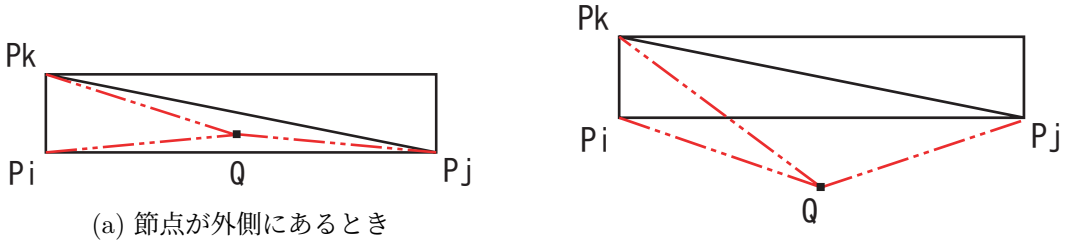

(a) 節点が外側にあるとき

(b) 節点が内部にあるとき

図 2.2: 二次元の節点の位置

で構成される四面体要素は，$\Diamond \mathrm{QP}_j\mathrm{P}_k\mathrm{P}_l$，$\Diamond \mathrm{P}_i\mathrm{QP}_k\mathrm{P}_l$，$\Diamond \mathrm{P}_i\mathrm{P}_j\mathrm{QP}_l$，$\Diamond \mathrm{P}_i\mathrm{P}_j\mathrm{P}_k\mathrm{Q}$ の 4 個である．今，図 2.4-(a) のように節点 Q が $\Diamond \mathrm{P}_i\mathrm{P}_j\mathrm{P}_k\mathrm{P}_l$ の内側にあるとき，これら 4 個の四面体要素は以下の条件を満たす．

$$\Diamond \mathrm{QP}_j\mathrm{P}_k\mathrm{P}_l > 0, \quad \Diamond \mathrm{P}_i\mathrm{QP}_k\mathrm{P}_l > 0, \quad \Diamond \mathrm{P}_i\mathrm{P}_j\mathrm{QP}_l > 0, \quad \Diamond \mathrm{P}_i\mathrm{P}_j\mathrm{P}_k\mathrm{Q} > 0. \tag{2.3}$$

つまり，全ての四面体要素の体積は 0 より大きくなる．しかし，図 2.4-(b) のように点 Q が $\Diamond \mathrm{P}_i\mathrm{P}_j\mathrm{P}_k\mathrm{P}_l$ の外側にあるときは，

$$\Diamond \mathrm{QP}_j\mathrm{P}_k\mathrm{P}_l > 0, \quad \Diamond \mathrm{P}_i\mathrm{QP}_k\mathrm{P}_l > 0, \quad \Diamond \mathrm{P}_i\mathrm{P}_j\mathrm{QP}_l < 0, \quad \Diamond \mathrm{P}_i\mathrm{P}_j\mathrm{P}_k\mathrm{Q} > 0 \tag{2.4}$$

となる．したがって，物体同士の接触判定は板状物体に含まれる四面体要素と物体の節点から生成される四つの四面体の体積を計算すればよい．ここで注意することは，二次元では接触判定には下側一つの三角形要素のみに注目していれば良かったが，三次元では節点が板状物体のどの部分の四面体要素に接触するかはわからない．そのため，板状物体に含まれる 5 つの四面体要素それぞれについて体積計算を行わ

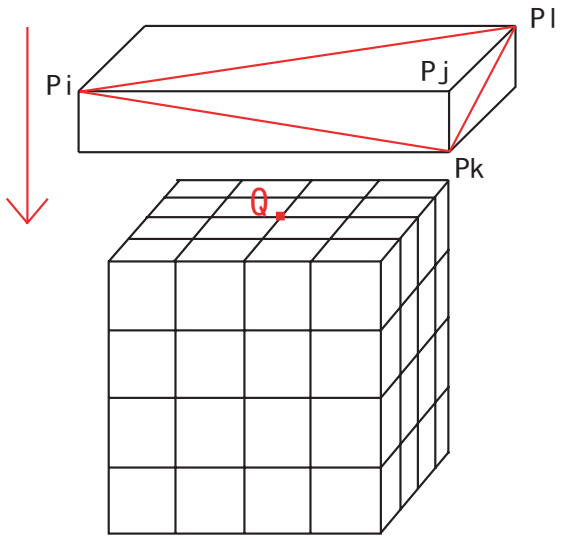

図 2.3: 三次元での接触モデル

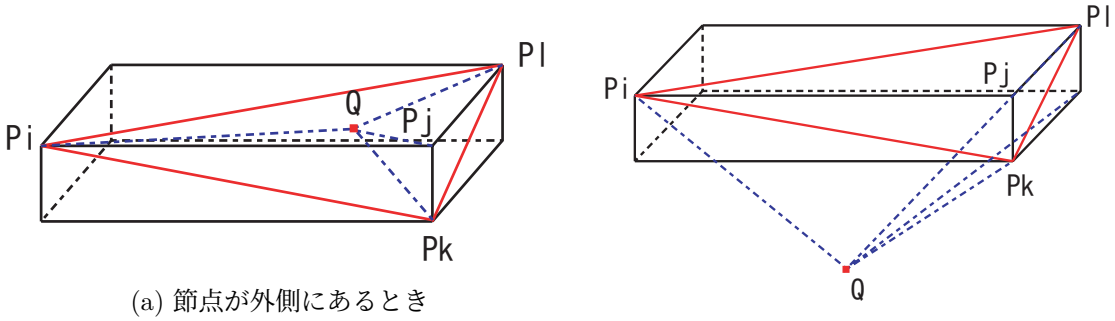

(a) 節点が外側にあるとき

(b) 節点が内部にあるとき

図 2.4: 三次元の節点の位置

なければならない．また，接触した節点は，制約安定化法によって板表面に固定され，板と同じ速度で移動する．

2.2.2 指のモデル

本節では変形シミュレーションで使用した指のモデルについて述べる．今回，シミュレーションで使用した指のモデルは AIM@SHAPE[47] で公開されている Olivier hand(図 2.5) を使用している．この Web サイトから入手できるのは，モデルのポイントの座標データおよび表面を覆う三角形要素のデータである．このモデルから，人差し指の第一関節以降の座標データおよび三角要素を抽出して使用している．しか

図 2.5: ハンドモデル

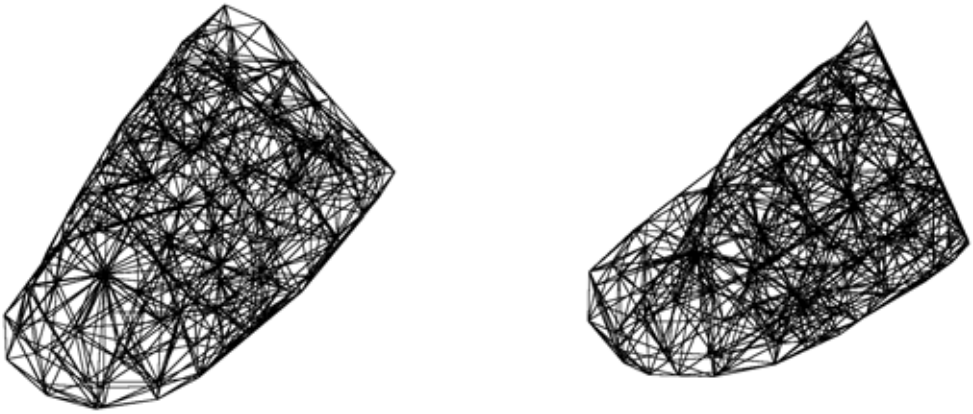

(a) 斜め上からの図　　(b) 横からの図

図 2.6: 指モデル

し，三次元で指の変形シミュレーションを行う場合，指表面を三角形要素で覆うだけではなく，指全体を四面体要素の集合でモデリングしなければならない．そこで，TetGen [48] で公開されているプログラムを使用し，四面体要素を作成する．このプログラムは，座標データと三角形要素のデータから Deraunay Triangulation によってモデルを四面体要素の集合に変換する．図 2.6 は，図 2.5 の人差し指の第一関節以降を抽出し，再構成した指のモデルである．

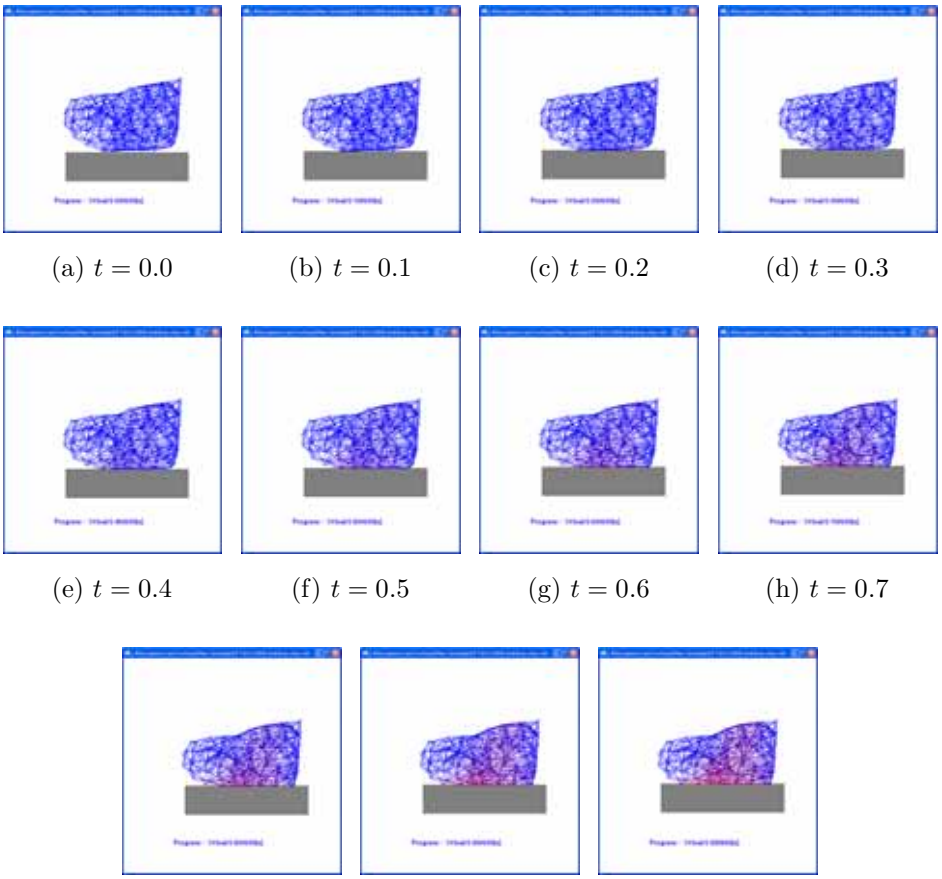

(a) $t = 0.0$ (b) $t = 0.1$ (c) $t = 0.2$ (d) $t = 0.3$

(e) $t = 0.4$ (f) $t = 0.5$ (g) $t = 0.6$ (h) $t = 0.7$

(i) $t = 0.8$ (j) $t = 0.9$ (k) $t = 1.0$

図 2.7: 横から見る指変形のシミュレーション結果

2.2.3 シミュレーション結果

前節で示したモデルを使用して指の変形シミュレーションを作成した．本シミュレーションでは，指を一応な物体としてシミュレーションを行った．また，制約安定化法により指の付け根の部分と爪の部分を動かないように固定してある．シミュレーションで用いたパラメータの値は，$E = 2$，$C = 400$，$\omega = 1000$，$\nu_p = 0.35$，である．サンプリング時間は $1\,\mu$s，シミュレーション時間は 1 s である．

図 2.7 および図 2.8 に指変形シミュレーションの結果を示す．図 2.8 のシミュレーションの結果より，指と板状物体が接触した後，指の節点が板状物体と同じ速度で動いていることがわかる．このことから，三次元での指の接触判定モデルは機能していることがわかる．本シミュレーションでは，指の節点の変位量が大きくなるにつれ，色が青から赤に変わるように表示してある．シミュレーションの結果を見ると，

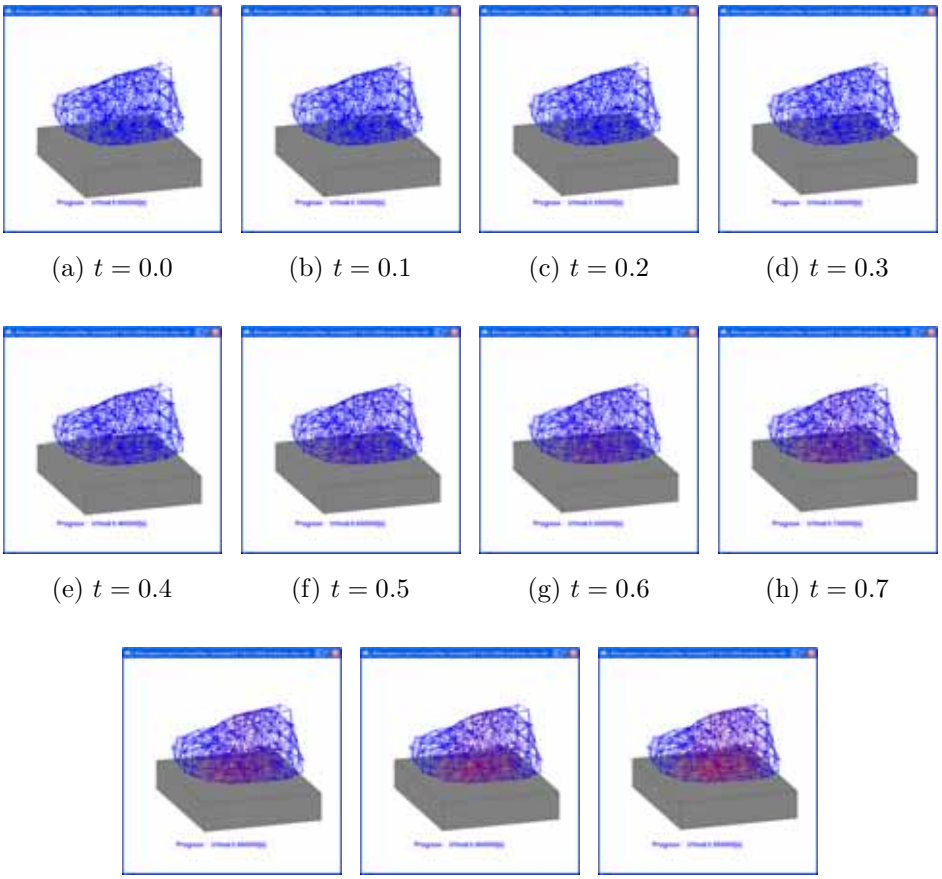

(a) $t = 0.0$ (b) $t = 0.1$ (c) $t = 0.2$ (d) $t = 0.3$

(e) $t = 0.4$ (f) $t = 0.5$ (g) $t = 0.6$ (h) $t = 0.7$

(i) $t = 0.8$ (j) $t = 0.9$ (k) $t = 1.0$

図 2.8: 斜め上から見る指変形のシミュレーション結果

板状物体に押されている部分やその周辺の節点の変位量が大きいだけでなく，指の爪側まで変位が出ていることがわかる．しかし，指の変形計測では押されている部分が変位が大きく，その他の部分では変位が出ていない．これは，指を一様な物体としたために起こってしまったと考えられる．そのため，より正確なシミュレーションを行うためには指モデルを一様な物体とせず，複数の領域に分けてシミュレーションを行う必要性がある．

2.2.4 まとめ

本節では，三次元での指の接触判定法と指変形のシミュレーションを示した．指と物体の接触判定については，シミュレーションの結果より，板状物体と指の節点が接触したときに，接触した節点が板状物体と同じ速度で移動していることからも

正確に機能していることがわかる．指の変形シミュレーションでは，指が板状物体に押されることで指の変形が外部変形だけでなく，指内部の変形も起こっていることが確認できた．本シミュレーヨンでは，指は一様な物体としている．しかし，実際の指は骨や皮膚といったパラメータの違う様々な体組織が存在する．そのため，正確なシミュレーションを行うためにはそれら体組織を考慮し，指の四面体要素によってパラメータを変える必要性がある．

2.3 人指の変形の計測

本章では，人指の MR 装置による撮影条件，内部変位の計測について述べる．また，Snake 法による指の輪郭検出および指表面の変位計測について述べる．

2.3.1 計測手法

MRI による指の撮影

本計測では，人指の内部変位を計測する．人指内部の変形の撮影には，核磁気共鳴画像法 (Magnetic Resonance Imaging：MRI) を使用した．MRI は，核磁気共鳴現象を利用して生体内部の情報を画像化する方法である．MRI は，超伝導電磁石を使用することで強磁場を発生させる．これにより，本来ばらばらの方向である原子核スピンの向きを揃え，磁場をかけた向きに巨視的磁場を発生させる．この核磁化に特定の周波数のラジオ波を照射し，静磁場方向から傾けると，核磁化は静磁場方向を軸として歳差運動を行う．MRI では，このパルス照射を止め，定常状態に戻るまでの過程の違いをパルスシーケンスのパラメータにより画像化する．

本計測では，滋賀医科大学に設置してある診察用の 3 T の MRI を使用している．MRI の環境下では，強磁場を発生しているため，金属物質を使用することができない．そのため，図 2.9 に示すように木片に指を押し当て撮影を行った．指を木片にわずかに触れる程度の指表面の変形が無い状態を初期状態とし，指をしっかり押し当て，指の輪郭がしっかり変形した状態を変形状態としている．撮影の注意点として，指の断面の位置を変形前と変形後で一致させるために，指先の撮影開始位置が変化しないように撮影を行う必要がある．また，診断用の MR 装置では体などの比較的大きな物体を対象としている．そのため，指という小さな対象物を撮影するためには撮影時間が長くかかってしまう．撮影中は指の位置がずれないように注意を払う必要性がある．画像サイズは 512 × 512 pixel，FOV は 120 × 120 mm である．

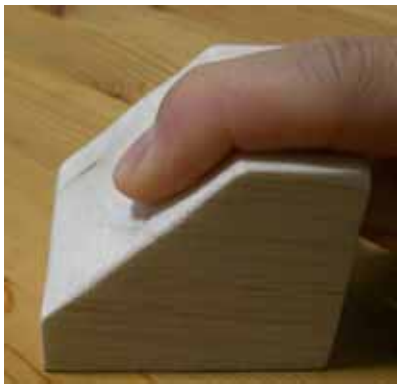

図 2.9: 木片に押し当てている指先

スライス間隔は 0.6 mm でスライス枚数はいずれも 64 枚である．スライス枚数 64 枚のうち指断面が実際に写っているのは 49 枚である．

図 2.10 は指の変形前と変形後の同一スライスの画像である．図 2.10-(a) および図 2.10-(b) は指の先端の MR 画像で，図 2.10-(c) および図 2.10-(d) は爪の中腹付近の MR 画像である．また，図 2.10-(e) および図 2.10-(f) は第一関節付近の MR 画像である．そして，図 2.11 は得られた 64 枚の MR 画像を構築し，指の初期状態と変形状態を三次元イメージとして示したものである．

図 2.10-(a) および図 2.10-(b) より，指先端が現れるスライスが同じであることや形状に大きな差異が見られないことから初期状態と変形状態でスライス間のずれはほぼ起きていないと思われる．また，画像がぼやけず鮮明に写っているため，撮影中に指が動くといったことは起こっていないといえる．医療診断用の MR 装置では，主に水素原子のスピンを計測している．そのため，指の皮膚や神経，血管などといった水分を多く含む部分が画像に写っていることがわかる．しかし，爪や骨，木片などどいった水分を含まないであろう体組織や物体については，画像に一切写っていないことがわかる．

指内部の説明を図 2.12 に示す．指の皮下組織の部分には，神経や血管といった体組織が写っている．指の内部変位量は，これら図中の皮下組織の移動量より求めている．

指の変位量の計測

MRI によって得られた画像から，指の内部変位量を三次元的に計測した．指の変位量計測は，張が作成したプログラム [49] を用いて行った．内部変位計測は SIFT を用いて特徴点を抽出し，それらの移動量を三次元的に計測することで変位量を求め

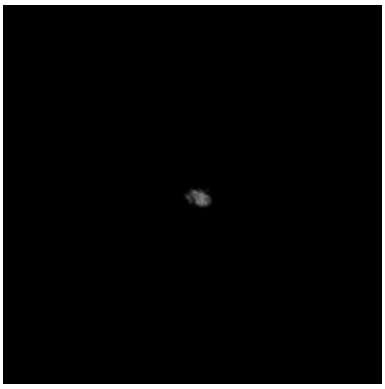

(a) 初期状態の指先端の MR 画像

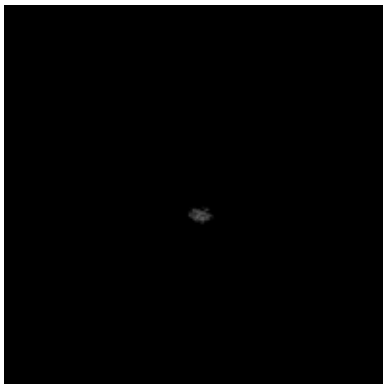

(b) 変形状態の指先端の MR 画像

(c) 初期状態の爪付近の指の MR 画像

(d) 変形状態の爪付近の指の MR 画像

(e) 初期状態の第一関節付近の指の MR 画像

(f) 変形状態の第一関節付近の指の MR 画像

図 2.10: MR 装置による指の断面画像

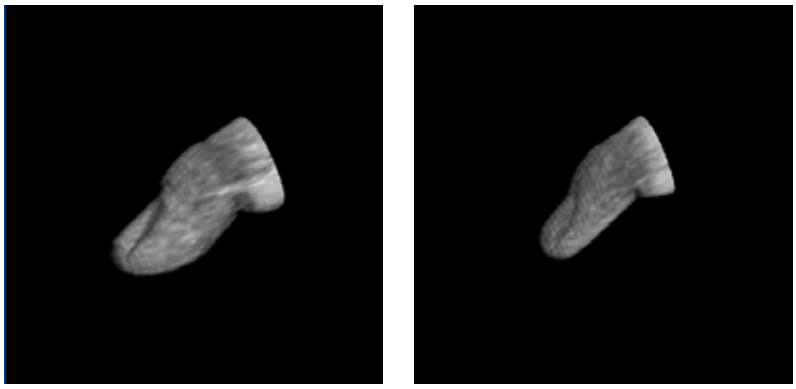

(a) 初期状態の三次元 MR 画像　　(b) 変形状態の三次元 MR 画像

図 2.11: 指の三次元 MR 画像

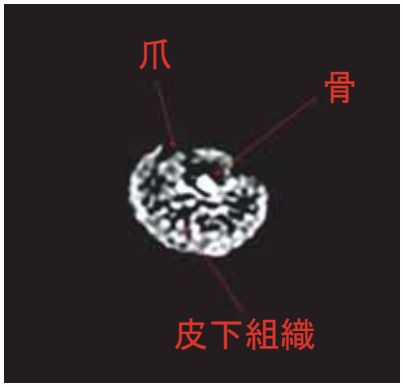

図 2.12: 指の MR 画像

ている．内部変位計測の手順としては，まず，MR 画像に写っているノイズを削除し，指の断面図の部分のみを残す．そして，指の変形前と変形後の指の位置や姿勢を一致させる．その後，それぞれの断面画像からボリュームデータを作成する．得られたボリュームデータを用い，特徴点を検索する範囲を指定し，変位量を求めている．特徴点の検索範囲は，同一スライス内のみではなく，前後のスライス間でも検索する．

以下に内部変位計測の結果を示す．それぞれの結果の画像は，変形後の指の形であり，変位量が大きくなるにつれ色が緑から黄色に変化していく．図 2.13 は指の腹側の変位状態である．また，図 2.14，図 2.15 はそれぞれ，指の背中側，指の腹側から見た変位状態である．図 2.13 より，指の押された部分が変形していることがわかる．しかし，指の背中側では変位があまり出ていない．これは，爪などの硬い組織の影響によるものと思われる．これらの計測は，指内部の変位に注目している．そ

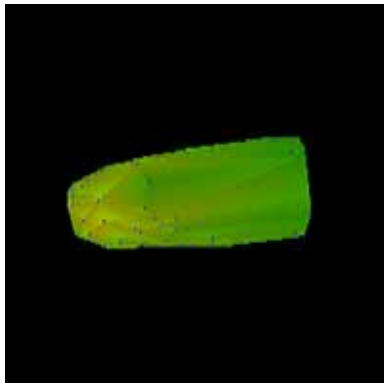

図 2.13: 指の腹側の内部変位

図 2.14: 横側から見た指の内部変位

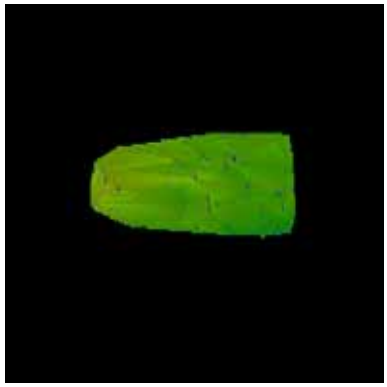

図 2.15: 爪側から見た指の内部変位

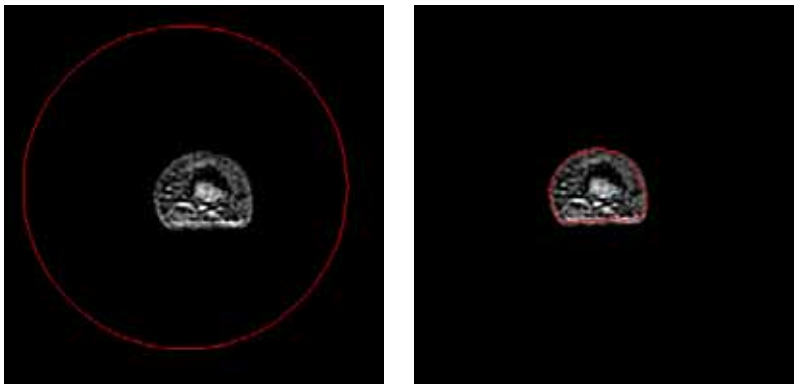

(a) Snake 法の初期状態　　(b) Snake 法の最終状態

図 2.16: 指の三次元 MR 画像

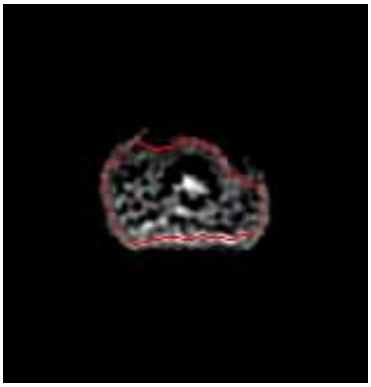

図 2.17: 指の爪付近の輪郭抽出

のため，指の形状ははっきりとはでていない．

2.3.2　Snake 法による輪郭抽出

Snake 法について

指表面の変位を計測するため，Snake 法による輪郭抽出を行った．Snake 法とは，閉曲線が形を変えることで物体の輪郭をとらえる動的輪郭検出法の一種である．輪郭検出方法として，色の濃度や閉曲線の形を評価関数として扱い，輪郭線上に閉曲線がのったときに評価関数の値が一番小さくなるように設定することで輪郭検出を行う．Snake 法の閉曲線は，正確には点と点を結んだものである．そのため，抽出したい輪郭のサイズによって点の数を調整しなければ，点が同じ場所で重なるなどし，

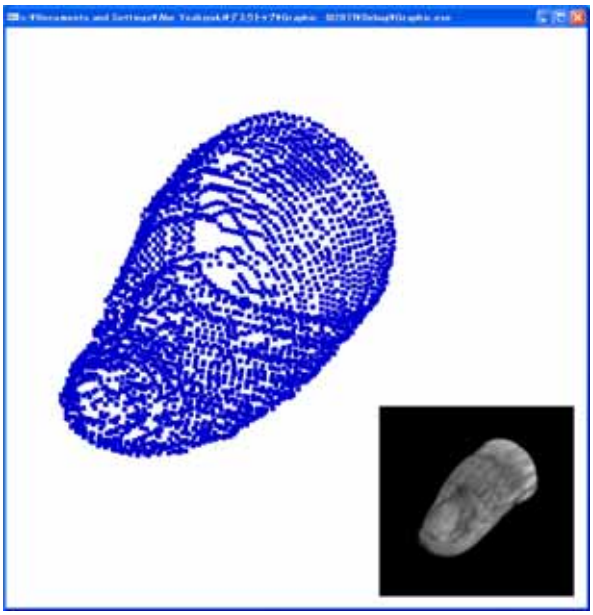

図 2.18: 上から見た Snake 法による輪郭抽出の結果

輪郭の検出が不正確になってしまう．

図 2.16-(a) および図 2.16-(b) は，指の第一関節付近の輪郭抽出の初期状態の画像と輪郭検出が終了した最終状態の画像である．これらの画像から，MR 画像に写る指の輪郭は正確に抽出できている．また，図 2.17 に示すように，指の爪付近のように輪郭が複雑な場合でも検出が可能である．

Snake 法による輪郭抽出結果

図 2.18 および図 2.19 に Snake 法による変形状態の指の輪郭抽出の結果を示す．図 2.19 は斜め下から見た状態である．図 2.18 より，爪部分などの複雑な形状であってもその形状をよくとらえていることがわかる．また，図 2.19 より，指の腹の部分が押さえつけられ，輪郭が大きく変形していることがわかる．

2.3.3 まとめ

MR 装置を用い指の断面の撮影を行った．また，得られた MR 画像から指の変位量を計測した．内部変位計測では，指を押し当てた部分の変位量が大きく，その他の部分の変位はあまり見られないという結果が出た．これは，骨などの硬い生体組織が皮下組織の変形に影響しているためだと思われる．

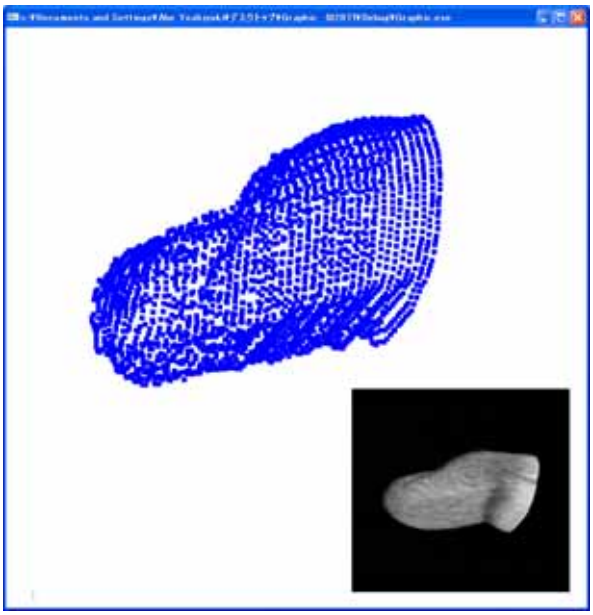

図 2.19: 下から見た Snake 法による輪郭抽出の結果

2.4　計測結果を用いた指モデルの変形シミュレーション

本章では，前章で得られた指の計測データを用いて指モデルを作成する．そして，そのモデルを用いて指の変形シミュレーションを行う．

2.4.1　シミュレーションで用いた指モデル

図 2.20 に変形シミュレーションで用いた指のモデルを示す．本章の指モデルでは前章の計測で得られた指の輪郭データを使用している．ここで，指の変形シミュレーションには有限要素法を用いるため，計測で得られた節点全てを用いるとシミュレーション時間が長くなってしまう．そのため，シミュレーション時間短縮のために指の形状がわかる程度に節点を削減している．

MR 装置から得られた 64 スライスの画像から，4 スライス間隔に 16 スライス使用する．そして，Snake 法で得られた指の輪郭から 10 点使用した．その表面を三角形要素で覆い，TetGen を使用して四面体要素の集合に変換した．

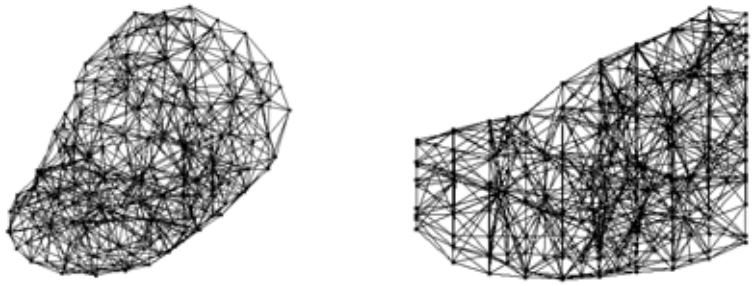

(a) 斜め上からの図　　(b) 横からの図

図 2.20: 計測データを用いた指のモデル

2.4.2　シミュレーション手法

指は一様な物体と仮定し，制約安定化法により指の付け根の部分と爪の部分を固定する．シミュレーションで用いたパラメータの値は，$E = 2$，$C = 400$，$\omega = 1000$，$\nu_p = 0.35$，である．サンプリング時間は $1\,\mu$s，シミュレーション時間は $0.5\,$s である．

2.4.3　シミュレーション結果

図 2.21 に横から見たシミュレーション結果を，図 2.22 に斜め上から見たシミュレーション結果を示す．本シミュレーション結果では，指モデルの押されている部分が大きく変形しているが，その他の部分では変位が見られないことがわかる．この結果は，指の内部変位計測の結果と似ている．

2.4.4　まとめ

本章では，MR 画像から得られた計測データを使用して指モデルを作成した．また，そのモデルを用いて指の変形シミュレーションを行った．指モデルの作成では，計測したデータ全てを用いず，節点を減らして使用している．この理由として，FE モデルでシミュレーションする場合，節点の数が多いとシミュレーション時間が長くなるという問題があるためである．また，表面や内部のメッシュ分割を行うことが困難になるという問題もあったためである．

指の変形シミュレーションでは，指と板状物体の接触している部分以外ではほとんど変形が見られなかった．これは，前章の指変位の計測結果と比較しても妥当な

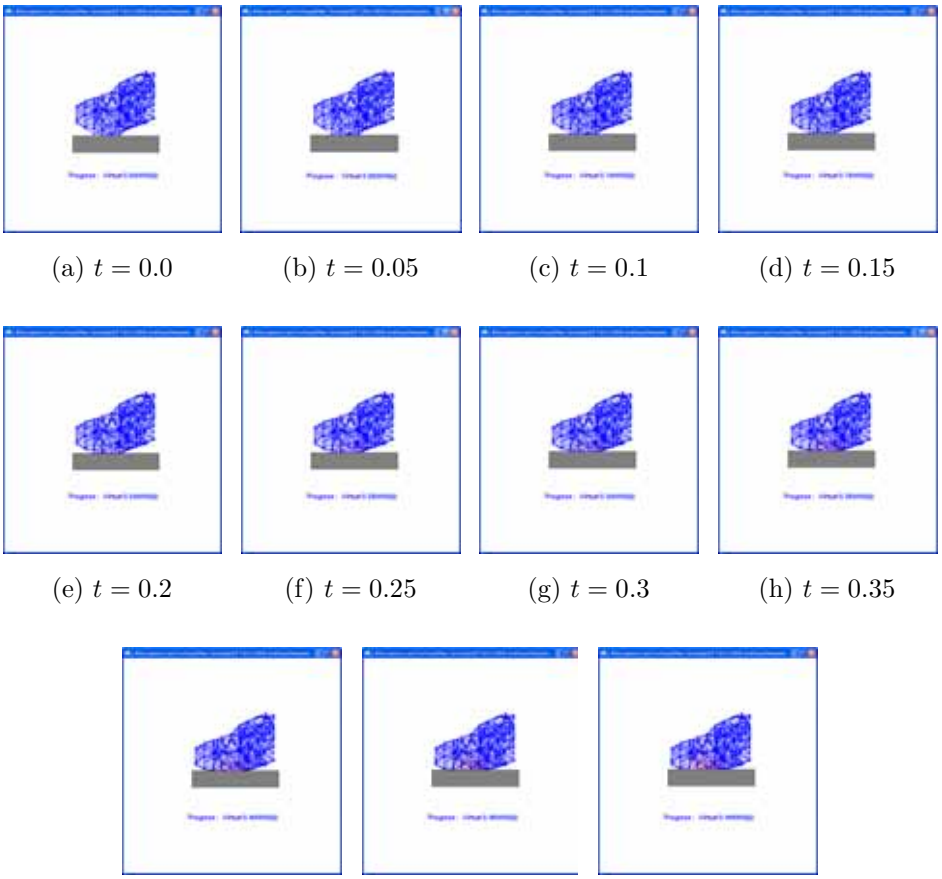

(a) $t = 0.0$ (b) $t = 0.05$ (c) $t = 0.1$ (d) $t = 0.15$

(e) $t = 0.2$ (f) $t = 0.25$ (g) $t = 0.3$ (h) $t = 0.35$

(i) $t = 0.4$ (j) $t = 0.45$ (k) $t = 0.5$

図 2.21: 横から見る指変形のシミュレーション結果

ものであるといえる．しかし，より正確に行うためには体組織を考慮した複数のパラメータ設定が必要となる．

2.5 結論

本章では，人指のモデルを作成した．そして，三次元空間での接触判定法を提案し，変形シミュレーションを行った．また，MR 装置を用いて人指を撮影し，得られた画像から人指の内部変位量および表面変位量を計測した．人指の変形シミュレーションでは，三次元での物体同士の接触判定を提案し，変形のシミュレーションを行った．その結果，三次元空間でも物体同士の接触を行えることを示した．また，指の変形シミュレーションでは接触部分から遠ざかるにつれ変位量が小さくなるという結果を得ることができ，実際の変形に近い結果を得ることができた．しかし，指

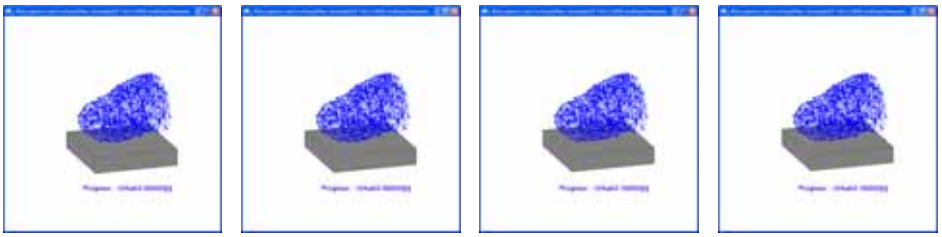

(a) $t = 0.0$ (b) $t = 0.05$ (c) $t = 0.1$ (d) $t = 0.15$

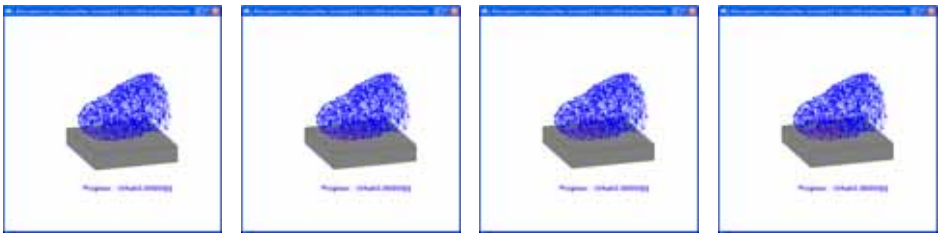

(e) $t = 0.2$ (f) $t = 0.25$ (g) $t = 0.3$ (h) $t = 0.35$

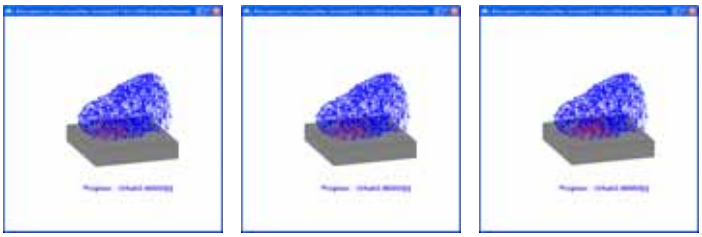

(i) $t = 0.4$ (j) $t = 0.45$ (k) $t = 0.5$

図 2.22: 斜め上から見る指変形のシミュレーション結果

を均一な物体と仮定しており，内部変位は全体的に押し上げられるように変形している．このため，より正確な変形シミュレーションを行う場合，骨などの体組織を考慮したパラメータ分割が必要になってくる．人指の変位量計測では，MR 画像から骨や皮下組織などの体組織を画像処理を使用して抽出し，それらのマッチングを行うことで三次元的に内部変位量を計測できることを示した．また，Snake 法を用いることで指表面の輪郭を抽出し，それによって得られたデータから指表面の形状を計測した．最後に，MR 画像から得られた計測データを用いて指のモデルを作成し，変形シミュレーションを行った．指の変形シミュレーションでは有限要素法を用いているため，節点が多いとシミュレーションに膨大な時間がかかってしまう．そのため，指モデルを作成する際には指の形状がわかる程度に節点を削減している．また，指の変形シミュレーションでは指の接触している部分が変位量が大きく，その他の部分では変位があまり見られなかった．これは，内部変位の計測結果と比較し

ても妥当なものであるといえる．しかし，より正確に行うためには体組織を考慮したパラメータ分割が必要になると思われる．

第3章　MR画像からの内部変形場の計算

3.1　緒言

本章では，軟組織のMR画像から内部変形を計算する手法を述べる．変形前と変形後のMR画像を撮影し，これらを比較することにより内部変形を計算する．変形場の計算においては，画像のアフィン変換に加えて画像の変形に対処する必要がある．また，軟組織のMR画像は，解像度が少なく輪郭が明瞭でない場合が多い．このようなMR画像に対して，ロバストに画像間の対応点を求め，変形場を計算するアルゴリズムが求められる．本章では，局所不変特徴量を用いた変形場の計算手法と，SACとTPSを用いた変形場の計算手法について述べる．

3.2　局所不変特徴量を用いた変形場の計算

本節では，局所的に不変な特徴量を用いて画像間の対応点を計算し，変形場を求める手法について述べる．

Proceedings of the 2010 IEEE
International Conference on Robotics and Biomimetics
December 14-18, 2010, Tianjin, China

A Local Geometric Preserving Approach For Interior Deformation Fields Measurement From MR Volumetric Images of Human Tissues

Penglin Zhang and Shinichi Hirai

Abstract— **While a variety of different features matching algorithms have been reported in rigid areas, few features matching algorithm used in non-rigid area have been reported. This work is concerned about interior deformation fields measurement of non-rigid, non-uniform human tissue or organs from 3D magnetic resonance volumetric images. In this paper, a local geometric preserving approach was proposed to find homologous features from a given features in MR volume obtained at the initial state. Three dimension invariant moment and geometric preserving property of a local 3D region have been used to design the function which was used to measure the strength of match of the candidate feature pair. Interior density deformation fields is then inferred to use a linear approximate approach in an irregular tetrahedra finite element model. To test the validity of the proposed approach, it is applied to actual MR volumetric images obtained from a volunteer's finger. The primary result is consistent with the fact.**

I. INTRODUCTION

Because magnetic resonance imaging (MRI) affords superb anatomic images with excellent spatial resolution and contrasts among soft tissues, it is widely used in computer-assisted medical applications, such as clinical diagnosis, surgery simulation, operation planning, and evaluation of physical characteristics of biological tissues. Therefore, as basic techniques, interior deformation fields or motion measurement of biological tissues from magnetic resonance (MR) volumetric images are becoming the focused research branch in medical image processing. Moreover, interior deformation fields or motion estimation are also the foundation of medical virtual reality and medical virtual simulation.

Generally, the approach for estimation of deformation from MR volumetric images can be classified into three types: elastic deformation models based methods, tagging methods and feature matching based methods.

The elastic deformation models based method can be classified into either parametric or geometric active models [3]. In order to obtain the deformation information of object, the parametric active contours, also called snakes, tries to minimise a defined cost function so that it deforms a given initial contour toward the boundary of the object. it was first introduced by Kass et al. in 1987 [4], and subsequently developed and used by Lang et al. [5], Cho et al. [2] and Matuszewski et al. [1] to estimate deformation motion of non-rigid objects. In the geometric active model [3], [6], [7], [8], the curve and surface of object was first to be detected, then the deformation propagation of curve and surface are used to track the motion. However, no matter what elastic deformation models are, disadvantages exist in deformation estimation. Such as, the parametric active model cannot handle changes in the topology of the evolving contours when implementations of deformation are performed directly, and specially, often heuristic, topology handling procedures must be used [8]. In the geometric active model, when contrast is poor and boundaries are not clear or continuous in the images, the contours tend to leak through the boundary [9]. The tagged images must have a regular grid pattern in the imaging plane, and if the number of tagged points is low,the accuracy of the measurements will be poor. More important than the former two aspects, no matter what elastic deformation models are, they can only handle the deformation on the boundary of non-rigid object, not the interior deformation.

The MRI tagging method was proposed by Zerhouni [10], and has been subsequently developed. Amini et al. [11] introduced a coupled B-snake grids and constrained thin-plate splines to analyze 2D tissue deformations; Wang et al. [13] proposed to use subspace approximation techniques to compute motion fields and introduced a spline technique to reconstruct dense displacement fields; Chen et al.[14] introduced an approach for tracking the tags; and Huang et al.[12] introduced an environment to fit and track volumetric tagged MRI data by a 4D deformable B-spline model. In all these MRI tagging methods, a set of radio-frequency (RF) pulses are used to make trackable tags in thin slices which are perpendicular to the imaging plane [11].

Different from the former two types methods, in our previous work [17], [18], our method presents a feature matching combine with interpolation approach for measurement interior deformation fields of non-rigid object using MR images. Its primary idea is to obtain local deformation fields based on homologous feature pairs inner images, then, the deformation fields of each pixel or voxel will be interpolated to use the local deformation fields of adjacent homologous feature pairs.Obviously, the key problem of the approach is to find enough homologous feature pairs in the MR volumetric images obtained at initial situation (initial volume) and MR volumetric images obtained at deformed situation (deformed volume), respectively. Therefore, to further improve the proposed feature matching based approach, this paper proposes a local geometric preserved approach. In the Section 2, we will describe the approach and give examples and preliminary experimental results in Section 3. In the final section, we

This work was supported by the freedom research plan of Wuhan University (6081008)

P.L. Zhang is with School of Remote Sensing and Information Engineering, Wuhan University, 430079 Wuhan, China zplcy@263.net

H. Shinichi is with Faculty of Science and Engineering, Ritsumeikan University, Kusatsu, 525-8577, Japan hirai@se.ritsumei.ac.jp

978-1-4244-9317-3/10/$26.00 © 2010 IEEE

will present a discussion and conclusions.

II. METHOD

In general, our approach is consists of four steps: Features extraction, Affine transformation, Feature matching and Deformation fields measurement. Here, to find enough homologous feature pairs, it is necessary to extract enough features from the initial and deformed volumes. In this study, high curvature 3D points as features are pre-extracted from MR volumetric images. In this case, we extend 2D Harris operator [24] to a 3D operator for extracting features from MR volumetric images [15].

In addition, because the initial volume and deformed volume are acquired at different time, conditions and MRI device without any calibration, they only have local coordinate systems, respectively. Thus, to make them into a global uniform coordinate system to ensure result correctly, in this case, we choose a set of corresponding features around bone which can be regarded as rigid as control points. Then, affine transformation operation is applied to the initial and deformed volumes using affine registration approach defined in [17] and [21].

In the next subsections, we will present feature matching method and interior deformation fields measurement method in succession, which are key part of this work.

A. Local Geometric Preserving Feature Matching Algorithm

Finding enough robust homologous feature pairs, also called feature matching, is the central work of the proposed approach. On the global view, because of the non-uniform characteristic of human tissues or organs, when force is applied on them, the magnitude and orientation of deformation in different location must be different. However, for a local region,the difference of deformation we take note is slight. Thus, we can suppose that deformation fields in a local region are consistent. Based on this hypothesis, a local geometric preserved feature matching algorithm has been developed as following. The performance process of algorithm is iterative.

1) Invariant Moment of Local Region: Three dimension (3D) moment can characterize the surfaces of objects effectively and each of size, position and orientation [20]. Thus, it is widely used in the area of computer vision, the recognition and understanding of 3D objects [19], [20]. In this case, for a given region in initial volume , 3D moment invariants is used to recognise its corresponding region in deformed volume. We suppose that $g(x, y, z)$ represents the intensity function of a region in 3D MR volumetric image, so that its 3D moment of order $i + j + k$ can be defined as [20]:

$$M_{ijk} = \int\int\int x^i y^j z^k g(x, y, z) dxdydz \tag{1}$$

writing in discrete form, we yield:

$$M_{ijk} = \sum\sum\sum x^i y^j z^k g(x, y, z) \tag{2}$$

Then, we assume that $f(x, y, z)$ is the intensity function of a 3D region around feature point P in the initial volume, let I_i be the i-th order moment. literature [19] and [20] show that 1st, 2nd and 3rd order moment can be given as follow:

$$I_1 = M_{200} + M_{020} + M_{002}, \tag{3}$$

$$I_2 = M_{200}M_{020} + M_{020}M_{002} + M_{002}M_{200} - \\ -M_{011}^2 - M_{101}^2 - M_{110}^2, \tag{4}$$

$$I_3 = M_{200}M_{020}M_{002} + 2M_{011}M_{101}M_{110} - \\ -M_{011}^2 M_{200} - M_{101}^2 M_{020} - M_{110}^2 M_{002}. \tag{5}$$

In the same way, the 1st, 2nd and 3rd order moment of the intensity function $f'(x, y, z)$ which is a region around feature point P' in deformed volume can be obtained as follows:

$$I'_1 = M'_{200} + M'_{020} + M'_{002}, \tag{6}$$

$$I'_2 = M'_{200}M'_{020} + M'_{020}M'_{002} + M'_{002}M'_{200} - \\ -M'^2_{011} - M'^2_{101} - M'^2_{110}, \tag{7}$$

$$I'_3 = M'_{200}M'_{020}M'_{002} + 2M'_{011}M'_{101}M'_{110} - \\ -M'^2_{011}M'_{200} - M'^2_{101}M'_{020} - M'^2_{110}M'_{002} \tag{8}$$

where I'_1, I'_2 and I'_1 represent the 1st, 2nd and 3rd order moment of the intensity function $f'(x, y, z)$, respectively.

For non-uniform, non-rigid objects, though the deformation is different in different location, the deformation in a small local region can be thought as rigid deformation approximately. Moreover, literature [19] and [20] have proved that the 1st, 2nd and 3rd order 3D moment are absolute moment invariants undering rigid transformation. Therefore, if $P1_1$ in deformed volume is the corresponding feature of $P2_1$ in initial volume, then, the Euclid distance between the 3D invariant moment of the 3D region around them must be the least. Namely,

$$\mathbf{D}_I(P1_1, P2_1) < \mathbf{D}_I(P1_1, P2_i \mid i = 0, 2, 3, \cdots, n), \tag{9}$$

where $\mathbf{D}_I(P1_i, P2_j)$ represents the Euclid distance between 3D regions which around $P1_i$ and $P2_j$, it is defined as:

$$\mathbf{D}_I(P1_i, P2_j) = \sqrt{\sum (I_i - I'_j)^2}, i, j = 1, 2, 3, \cdots, n. \tag{10}$$

2) Strength of Match: Intensity correlation between two local image regions around match features is the most widely approach to measure the strength of match (SOM). However, for a non-rigid object, the deformation greatly changes the intensity in MR volume. Obviously, intensity correlation is inadequate in features match of MR volumes from non-rigid object. In this case, a type of geometric correlation has been introduced to improve the reliability of match. Such as Fig.1, let c_1 and c_2 be moment center of point set from initial volume (PTS1) and its projection in point set from deformed volume (PTS2), $P1_i$ and $P2_j$ be the i-th and j-th point in PTS1 and PTS2, respectively.

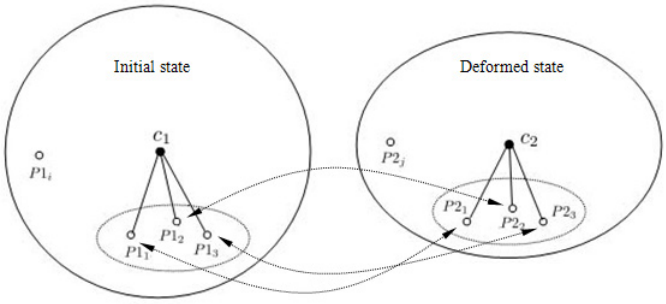

Fig. 1. Local geometric preserve consistency

We suppose that $P1_1$, $P1_2$, and $P1_3$ are lay in a local region, and $P2_1$, $P2_2$, $P2_3$ are their corresponding features respectively, we yield:

$$\frac{\mathbf{d}(P1_1, c_1)}{\mathbf{d}(P2_1, c_2)} \simeq \frac{\mathbf{d}(P1_2, c_1)}{\mathbf{d}(P2_2, c_2)} \simeq \frac{\mathbf{d}(P1_3, c_1)}{\mathbf{d}(P2_3, c_2)} = \mu \tag{11}$$

where $\mathbf{d}(P1_i, c_1)$ represents distance between $P1_i$ and c_1, $\mathbf{d}(P2_j, c_2)$ represents Euclid distance between $P2_j$ and c_2, μ represents the Euclid distance ratio. Eq.11 shows the magnitude of deformation in a local region preserves consistency approximately. Thus, we conclude that if a pair of features are potential match (PM) each other, then, each pairs in potential match set (PMS) of a local region around PM must be formed a strong correlation PMS. Here, correlated score is used to describe the correlation of PMS. In detail, let $\mathbf{P}_{d_1}$ = $\{\mathbf{d}_{1_i}$=$\mathbf{d}(P1_i, c_1) \mid$ i=1,2,3,$\cdots$,n$\}$ be the distance which consists of $\mathbf{d}(P1_i, c_1)$, and $\mathbf{P}_{d_2}$ = $\{\mathbf{d}_{2_j}$=$\mathbf{d}(P2_j, c_2) \mid$ j=1,2,3,$\cdots$,n$\}$ be the distance which consists of $\mathbf{d}(P2_j, c_1)$, E_{d_1} and E_{d_2} be expectation of $\mathbf{P}_{d_1}$ and $\mathbf{P}_{d_2}$, respectively, then, the geometric correlation score $gCor(\mathbf{P}_{d_1}, \mathbf{P}_{d_2})$ between $\mathbf{P}_{d_1}$ and $\mathbf{P}_{d_2}$ is given by:

$$gCor(\mathbf{P}_{d_1}, \mathbf{P}_{d_2}) = \frac{\sum \omega_{ij}(\mathbf{d}_{1_i} - E_{d_1})(\mathbf{d}_{2_j} - E_{d_2})}{\sqrt{(\sum (\mathbf{d}_{1_i} - E_{d_1})^2 \sum (\mathbf{d}_{2_j} - E_{d_2})^2}} \tag{12}$$

where ω_{ij} is the weight, which defines the contribution of a match pair in local region for geometric correlation score. If ω_{ij} is large, it shows that the pair may be strong pair, thus, its contribution must be large too. Let η be the ration of E_{d_1} and E_{d_2} (see Eq.13), and the ω_{ij} is defined as Eq.14.

$$\eta = \frac{E_{d_1}}{E_{d_2}} \tag{13}$$

$$\omega_{ij} = \frac{1.0}{1.0 + |\mu - \eta|} \tag{14}$$

Because the value of $gCor(\mathbf{P}_{d_1}, \mathbf{P}_{d_2})$ lies in [-1,1], normalize Eq.12 yields:

$$NgCor(\mathbf{P}_{d_1}, \mathbf{P}_{d_2}) = \frac{gCor(\mathbf{P}_{d_1}, \mathbf{P}_{d_2}) + 1}{2} \tag{15}$$

So far, we have already defined the invariant moment and geometric correlation between two local regions. To integrate these two approaches, a robust SOM can be defined as:

$$SOM(\mathbf{P_1}_i, \mathbf{P_2}_j) = \frac{NgCor(\mathbf{P}_{d_1}, \mathbf{P}_{d_2}) + IoM(\mathbf{P}_{d_1}, \mathbf{P}_{d_2})}{2.0} \tag{16}$$

3) Cost Function: To eliminate false match and increase the reliability of successful match as soon as possible, in this case, relaxation technique is used in the process of feature match. The relaxation technique is first proposed by Rosenfel et al. [22], who uses iterated local context updates to achieve a global consistent result [23]. As an iterative process, relaxation technique requires a cost function to ensure it works well. In this paper, the cost function is defined as the average of SOM of all candidate matches, as follows:

$$\varepsilon = \frac{1}{N} \sum_{i,j=1}^{N} SOM(\mathbf{P_1}_i, \mathbf{P_2}_j) \tag{17}$$

where N represents the total numbers of matched pairs in PMS at time t.

The matches can be disambiguated by maximizing the energy function ε, using an iterative procedure. Here, we note that if the PMS varies dynamically, the SOM (16) also varies. Therefore, potential matches can be constantly updated in iteration, and this process will be stopped when the value of cost function ε began to decrease. Here, matches in PMS consist of a robust potential matches set (RPMS), which is the final match result.

B. Density Deformation Fields Computation

After obtaining a potential matches set by using methods mentioned above sections, next, we will describe the method used for obtaining the interior density deformation fields of objects. In this study, the methods proposed in our previous work [25] is used to obtain interior density deformation fields. In summary, the interior density deformation fields are interpolated by sparse deformation fields using finite element model (FEM). In detail, the magnitude of sparse deformation fields was first computed by corresponding pair in RPMS using Euclid distance. The start point and end point of field direction are defined by points of a corresponding pair. Next, non-rigid object was reconstructed by using tetrahedra, whose nodes are points in RPMS. Here, density deformation fields then can be interpolated by using following finite element method.

Let P be an arbitrary volume voxel at $\mathbf{x} = (x, y, z)$ within a tetrahedron $\diamondsuit P_i P_j P_k P_l$. Its displacement may be approximated by weighting the finite element's node displacements $\mathbf{u}_i$ by their shape function [25]

$$\mathbf{u}(\mathbf{x}) = \sum_{n=1}^{4} \mathbf{u}_n N_n \tag{18}$$

where N_n is the shape function of nodal $n = (i, j, k, l)$, which is given by

$$N_n = \frac{\diamondsuit P P_j P_k P_l}{\diamondsuit P_i P_j P_k P_l}. \tag{19}$$

Finally, approximation displacements of all voxels $\mathbf{x}_i$ in the volume can be obtained by using Eq.18.

III. EXPERIMENTS AND RESULTS

Some experiments are designed to demonstrate the capabilities of the proposed approach. All experiments are performed by using our own tool developed with Visual C++, which runs on Microsoft Windows XP. And all experimental results described below are obtained on a Lenovo Portable PC with a 2.20 GHz Intel(R) Core(TM) 2 Duo CPU T6600 and 4 GB of RAM.

Here, the initial MR volume and deformed MR volume are acquired from a volunteer's finger tip using an MR scanner under initial and deformed situations, respectively, refering to Fig.2. The size of initial MR volume and deformed MR volume are all $512 \times 512 \times 52$ voxels. Figure 3 illustrates some slices in initial and deformed MR volume are used in the experiments.

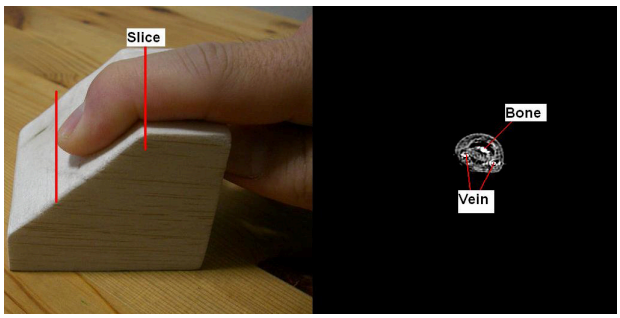

Fig. 2. The illustration of obtaining MR volume

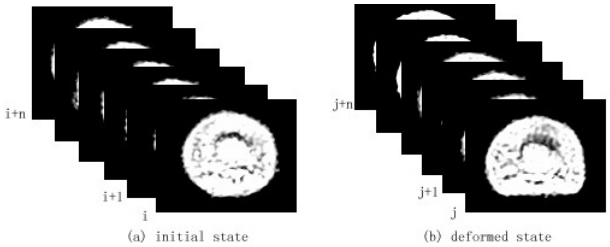

Fig. 3. Some slices used in experiment

First of all, 1000 features have been extracted from initial volume and deformed volume, respectively. Next, intensity correlation approach presented in [16], [17] is used as first match. The iterative match algorithm is applied on the result of first match resulted to an RPMS with 252 pairs. Doubtlessly, false matches must exist in RPMS, but, we note that most of them are robust,through checking it one by one artificially. This viewpoint will prove by the subsequent experiment too.

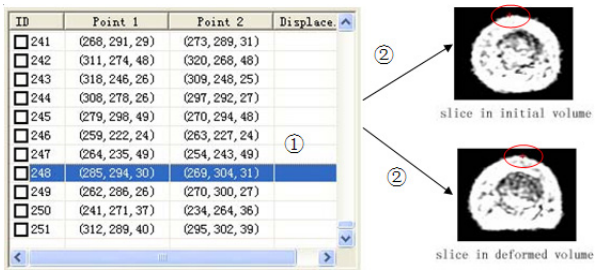

Fig. 4. The process of match result checking

Fig.4 is the process of feature match result checking. In the Fig.4, the red cross in the red ellipse represents location of the 248-th match pair in the RPMS.

Next, sparse deformation fields and density deformation fields are computed to use method mentioned in above subsections. Fig.5 shows the density fields model. From the figure, we note that the large deformation takes place in tip and bottom side of finger. this result is consistent with the fact.

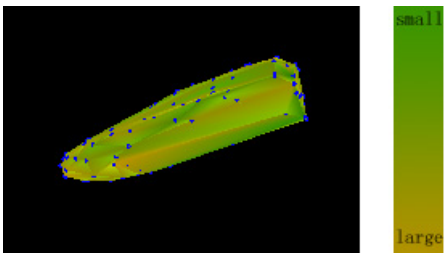

Fig. 5. The finger volume model with density deformation fields

IV. CONCLUSIONS AND FUTURE WORKS

A. Conclusions

We propose a local geometric preserved approach to find the homologous feature for feature in initial MR volume so that a robust PMS can be built. The PMS is used to compute sparse deformation fields of non-rigid object.Moreover, the deformation field of each voxels is interpolated by using deformation fields of the nodes of tetrahedron.The preliminary experiment reveals that result obtained from using the proposed approach is consistent with the fact. In summary, advantages of the proposed approach include:

1). The proposed approach takes full advantage of the local geometric properties of non-rigid object. Compared to the traditional intensity based approaches, the geometric based approach is not sensitive to the noise in image.

2). The feature matching based approach for deformation measurement does not need the initial contour of an object. This is independent shape of the initial contour.

3). The proposed approach provide an option for feature match in MR volume of non-rigid, non-uniform objects.

B. Future Works

1). The concave on the surface of object could not be effectivelly handled when the volume of object are reconstructed. This will lead that the volume model is inconsistent with the actual situation. An effective method for reconstructing the volume model need to be developed so that the density deformation fields can be correctlly and intuitionisticaly visualized.

2). False matches existing in the PMS will lead the low precision result of interior deformation fields. Therefore, a effective method for eliminating the false matches need to be developed in future work.

V. ACKNOWLEDGMENTS

This work is partially supported by Associate Prof. Xubin Zhang in Ritsumeikan University, Japan. Moreover, the author acknowledges Master Yoshiyuki Abe in Ritsumeikan University provide the experiment MR volumetric images. The author also gratefully acknowledges the helpful comments and suggestions of the reviewers, which have improved the presentation.

REFERENCES

[1] B.J. Matuszewski, Jian-Kun Shen, Lik-Kwan Shark and Moore C., "Estimation of Internal Body Deformations Using an Elastic Registration Technique," *Proceedings of the International Conference on Medical Information Visualisation-BioMedical Visualisation.* Jul. 2006, pp.15-20.

[2] J. Cho and P.J. Benkeser, "Elastically deformable model-based motion-tracking of left ventricle," *Proceedings of the 26th Annual International Conference of the IEEE EMBS*. Vol. 1, No. 3, Sept. 2004, pp.1925-1928.

[3] Y. Chenoune, E. Delechelle, E. Petit, T. Goissen, J. Garot and A. Rahmouni, "Segmentation of cardiac cine-MR images and myocardial deformation assessment using level set methods," *Computerized Medical Imaging and Graphics*. Vol. 29, No. 8, Dec. 2005, pp.607-616.

[4] M. Kass, A. Witkin and D. Terzopoulos, "Snakes: active contours models," *International Journal of Computer Vision*. Vol. 1, No. 4, Jan. 1987, pp.321-331.

[5] J. Lang, D.K. Pai and R.J.Woodham, "Robotic acquisition of deformable models," *IEEE International Conference on Robotics and Automation, 2002. Proceedings. ICRA '02*. Vol. 1, 2002, pp.933- 938.

[6] C. Vicent, C. Francine, C. Tomeu and D. Francoise, "A geometric model for active contours in image processing," *Numerische Mathematik*. Vol.66, No.1, Dec. 1993, pp.1-31.

[7] R. Malladi, J.A. Sethian and B.C. Vemuri, "Shape modeling with front propagation: a level set approach," *IEEE Transactions on Pattern Analysis and Machine Intelligence*. Vol.17, No.2, Feb. 1995, pp.158-175.

[8] C. Vicent, "Geometric models for active contours," *International Conference on Image Processing, Proceedings*. Vol. 3, Oct. 1995, pp.19-12.

[9] F. Huang and J. Su, "Face Contour Detection Using Geometric Active Contours," *Proceedings of the 4th World Congress on Intelligent Control and Automation. Shanghai*, Vol.3, 2002, pp.2090- 2093.

[10] E. Zerhouni, D. Parish, W. Rogers, A. Yang, and E. Shapiro, "Human heart: Tagging with MR imaging-A method for noninvasive assessment of myocardial motion," *Radiology*. Vol.169, 1988, pp.59-63.

[11] A.A. Amini, Y. Chen, R.W. Curwen, V. Mani and J. Sun, "Coupled B-snake grids and constrained thin-plate splines foranalysis of 2-D tissue deformations from tagged MRI," *IEEE Transactions on Medical Imaging*. Vol. 17, No. 3, Jun 1998, pp.344-356.

[12] J. Huang, D. Abendschein , G.Victor Dávila-Román and A.A. Amini, "Spatio-Temporal Tracking of Myocardial Deformations with a 4-D B-Spline Model from Tagged MRI," *IEEE Transactions on Medical Imaging*.Vol.18, No.10, Oct. 1999 , pp. 957-971.

[13] Y.P. Wang and A.A. Amini, "Fast computation of tagged MRI motion fields with subspace approximation techniques," *IEEE Workshop on Mathematical Methods in Biomedical Image Analysis, 2000. Proceedings*. June 2000 , pp. 119-126.

[14] Y. Chen and A.A. Amini, "A MAP framework for tag line detection in SPAMM data using Markov random fields on the B-spline solid," *IEEE Workshop on Mathematical Methods in Biomedical Image Analysis, 2001. MMBIA.2001*. June 2000 , pp.131-138 .

[15] P.L. Zhang, S. Hirai and K. Endo, "A Feature Tracking-based Approach for Local Deformation Fields Measurement of Biological Tissue from MR Volumes", "*The Third Joint Workshop on Machine Perception and Robotics, 2007. Proceedings*. Dec. 2007.

[16] Z.Y. Zhang, R. Deriche, O. FAUGERAS and Q.T. LUONG, "A robust technique for matching two uncalibrated images through the recovery of the unknown epipolar geometry," *Special volume on computer vision*. Vol.78, October 1995, pp. 87 - 119.

[17] P.L. Zhang, S. Hirai, K. Endo and S. Morikawa, "Local Deformation Measurementof Biological Tissues Based on Feature Tracking of 3D MR Volumetric Images," *IEEE/ICME International Conference on Complex Medical Engineering, 2007. Beijin*, May 2007, pp. 711-716.

[18] P.L. Zhang, S. Hirai and K. Endo, "A Feature Matching-based Approach to Deformation Fields Measurement From MR Images of Non-rigid Object," *International Journal of Innovative Computing, Information and Control*, Volume 4, Number 7, July 2008 pp. 1607-1615.

[19] F.A. SADJADI, and E.L. HALL, "Three-Dimensional Moment Invariants," *IEEE Transactions on Pattern Analysis and Machine Intelligence,*, Vol. PAMI-2, No. 2, March 1980, pp. 127-136.

[20] X. Guo, "Three-Dimensional Moment Invariants under Rigid Transformation," *Lecture Notes in Computer Science*. Volume 719, 1993, pp. 518-522.

[21] B.K.P. Horn, "Closed Form Solution of Absolute Orientation using Unit Quaternions," *Optical Society of America A: Optics, Image Science, and Vision*. Vol.4, No.4, April 1987 , pp. 629-642.

[22] A. Rosenfeld, R. A. Hummel and S. W. Zucker, "Scene Labeling by Relaxation Operations," *IEEE Transactions on Systems, Man, and Cybemetics*. 1976, pp. 420-433.

[23] Y. Zheng, D. Doermann, "Scene Labeling by Relaxation Operations," *IEEE Transactions on Pattern Analysis and Machine Intelligence*. Vol. 28, No. 4, April 2006, pp. 643-649.

[24] C. Harris and M.J. Stephens, "A combined corner and edge detector," *Proceedings of The Fourth Alvey Vision Conference.* 1988, pp. 147-151.

[25] P.L. Zhang, S. Hirai and K. Endo, "A Method for Non-rigid 3D Deformation Fields Measurement: Application to Human Calf MR Volumetric Images," *Proceedings of Workshop at IEEE/RSJ International Conference on Intelligent Robots and Systems.* 2007, pp. 8-13.

3.3 SAC と TPS を用いた変形場の計算

本節では，Spatial Association Correspondence (SAC) と Thin Plate Spline (TPS) を用いて，局所的な対応点探索と大域的なモデル更新を交互に実行することで，変形場を計算する手法を述べる．

Feature Points Matching of Nonrigid Tissues Based on SURF, Spatial Association Correspondence and Clustering: Application to MR 2-D Slice Deformation Measurement

Xubing Zhang [1,2], Shinichi Hirai [1], Penglin Zhang[3]
[1]Dept. of Robotics, Faculty of Science and Engineering, Ritsumeikan University, Kusatsu, Shiga 525-8577, Japan
[2]School of Computer Science, Wuhan Textile University, Wuhan 430073, China
[3]School of Remote Sensing and Information Engineering, Wuhan University, Wuhan 430079,China

***Abstract*-Due to the nonlinear and nonuniform local deformation of the nonrigid tissues, it is difficult whereas important to extract and correctly match a considerable number of feature points from the MR images for deformation measurement. Current approaches are dissatisfying towards this issue. In this paper, firstly the authors use SURF algorithm to extract the feature points in the initial MR image, and take every point in the deformed MR image as the feature point. Then the SURF descriptors and Spatial Association Correspondence (SAC) of the neighborhood pixels is adopted to match the corresponding feature points between the initial and deformed MR images. Finally, by clustering the coordinate differences between the deformed points matched by SURF-SAC with the corresponding points calculated by affine transformation, most of wrong match points are eliminated. The experimental results prove that the proposed method can extract and match more correct corresponding feature point pairs than SURF and SIFT methods.**

***Key words*—SURF, Spatial Association Correspondence, Clustering, Feature point, Matching, Deformation**

I. INTRODUCTION

Deformation field measurement of nonrigid biological tissues from MR (Magnetic Resonance) images is often required for clinical diagnosis, surgery simulation, operation planning, and evaluation of physical characteristics of biological tissues [1-4]. Usually we need to measure the local irregular deformations accurately between the two MR images obtained at different rotation, displacement, and soft tissue deformations. In our opinions, current nonrigid medical image registration and deformation measurement methods can be classified into four categories, transformation model estimation [5-7], physical model method [8-12], mutual information [13-14], and feature points combined with TIN (Triangular Irregular Network) [1-2].

The space transformation model such as low degree polynomial [5], thin plate splines (TPS) [6], and B-splines [7] can be applied to measure the nonlinear deformation of images. According to such approaches, the interpolation and matching of images is based on many feature points. Actually, it is difficult to extract and correctly matched a considerable number of feature points between the deformed images.

The typical methods of physical model include elastic deformation model [8-9], viscous fluid [10], optical flow [11], and finite element [12]. In elastic deformation models, popular parametric deformation model cannot handle topological changes [8], and geometric active model cannot measure the interior deformation and tends to leak through the weak boundary [9]. The viscous fluid method tends to wrong matching when there are some different tissue fabrics with similar pixel intensity distribution. When the gradient information is weak, the optical flow method cannot behave well in the deformation image estimation. The deformation measurement accuracy of finite element model depends on the matching boundary of image fabric, which is difficult to obtain.

The maximal mutual information method is originally applied in the rigid image registration. Now it is widely adopted to match the nonrigid deformed images when combined with the other methods, such as thin-plate splines, B-splines, optical model and so on. In these cases, the mutual information method mainly acts as a global estimate of the image registration accuracy, so that it cannot avoid the limitation of the other combined methods.

Zhang presented a deformation field measurement method based on the feature point tracking and Delaunay TIN. Considering the irregular local deformation of nonrigid and nonuniform tissues, Zhang extracts and matches a considerable number of feature points in MR images by means of Harris algorithm and relaxation labeling method, and then the Delaunay TIN is constructed based on feature points to measure the deformation fields. While in this method, the initial rough match is based on the points around the rigid bone, and actually, a certain number of wrong matched points which have negative effect on measurement accuracy cannot be eliminated automatically [1], [2].

According to above discussion, we can see that the extraction and correct matching of a considerable number of feature points is very important to the deformation measurement of nonrigid biological tissues, also it is a key difficult to be solved.

Extraction and matching of the feature points, which should be robust against the change in illumination, scaling, rotation, and noise or slight distortion, is one of the most important methods used to detect the correspondences between the images. A wide variety key point detectors and descriptors have already been proposed in the literature [15-18]. The most widely used detector probably is the Harris corner detector [19], based on the eigenvalues of the second-moment matrix. However, Harris corners are not scale-invariant. Lindeberg introduced the concept of automatic scale selection, which detects interest points with their own characteristic scale [15]. Mikolajczyk and Schmid created robust and scale-invariant feature detectors with high repeatability, called Harris-Laplace and Hessian-Laplace [20].

Lowe presented the Scale Invariant Feature Transform (SIFT) approach, which approximated the Laplacian of Gaussian (LoG) by a Difference of Gaussians (DoG) filter [16], and can bring speed at a low cost in terms of lost accuracy [21], [22]. Shown in the literature [22], SIFT outperforms the other feature descriptors like Gaussian derivatives [23], moment invariants [24], complex features [25], phase-based local features. Various refinements on the SIFT scheme have been proposed, the PCA-SIFT and the GLOH methods are known well in them [18], [22].

Bay Herbert presented SURF (Speeded-UP Robust Feature) in 2006 [26], it is invariant to scaling, rotating, illumination change, affine transformation, and is robust to noise and detection errors. By using the 'Fast-Hessian' to approximate the Laplacian, describing a distribution of Haar-wavelet responses within the interest point neighborhood, reducing the descriptor to 64 dimensions, and exploiting integral images, the SURF is more repeatable, distinctive, robust, and furthermore the computing velocity is three times more than SIFT. In the experimental results, Bay also proved that, SURF outperformed the other methods such as GLOH and PCA-SIFT [22], [26], [27].

Unfortunately, when we attempted to evaluate the deformation measurement by SURF, the experimental results were not inspiring. The amount of the matched points was too few and not enough to construct the TIN which was very important to the accurate deformation measurement.

In order to obtain more correct matched points, the authors combined the SURF with the analysis of spatial association correspondence to extract and match the feature points between the initial and deformed MR images. Secondly, in order to eliminate the wrong matched point pairs, we apply clustering to analyze the coordinate differences between the deformed corresponding points matched by our method and the theoretic corresponding points calculated by the affine transformation. The points which are not included in the range of the maximum clustering are regarded as the wrong matching points.

In our experiments, the SIFT, SURF, and the method combined SURF, SAC and clustering are compared, and the results showed that SURF-SAC can obtain more correct corresponding points, furthermore, most of wrong matching feature points can be eliminated by adopting coordinate difference clustering algorithm.

II. SURF

The interest point detector of SURF is based on the Hessian matrix. It relies on integral images to reduce the computation time and called 'Fast-Hessian' detector [20]. On the other hand, the descriptor of interest point describes a distribution of Haar-wavelet responses within the interest point neighbourhood.

A. Fast-Hessian Detector

Rather than using a different measure for selecting the location and the scale as the Hessian-Laplace detector [20], SURF relies on the determinant of Hessian for both. Given a point $p = (x, y)$ in an image *I*, the Hessian matrix $\mathrm{H}(p,\sigma)$ in *P* at scale σ is defined as follows

$$H(p,\sigma) = \begin{bmatrix} L_{x,x}(p,\sigma) & L_{x,y}(p,\sigma) \\ L_{x,y}(p,\sigma) & L_{y,y}(p,\sigma) \end{bmatrix}, \qquad (1)$$

where σ is the scale factor, $L_{x,x}(p, \sigma)$ is the convolution of Gaussian second order derivative $(\partial^2 / \partial x^2) g(\sigma)$ with the image *I* in point *p*, and similarly for $L_{x,y}(p, \sigma)$ and $L_{y,y}(p, \sigma)$.

As Gaussian filters are nonideal in any case, and given Lowe's success with LoG approximations, Bay further applied the box filters to approximate the second order Gaussian derivatives. The other hand, the integral images is applied to accelerate the process of interested point detection and descriptor estimation, independently of the image size. The 9×9 box filters $D_{x,x}$, $D_{x,y}$ and $D_{y,y}$ in Fig. 1 approximate Gaussian second order derivatives with the lowest scale σ = 1.2, and the grey regions in the figures equal to zero.

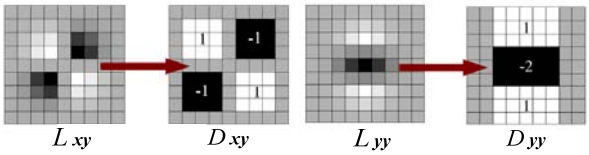

Figure 1. The box filters Dx,y and Dy,y used to approximate Gaussian second order partial derivatives in xy-direction and yy-direction

The weights, 1 in black regions while –1 in white regions, applied to the rectangular regions are kept simple for computational efficiency. Bay proposes the following formula as an accurate approximation for the Hessian determinant using the approximated Gaussians:

$$\det(H_{approx}) = D_{xx}D_{yy} - (0.9D_{xy})^2 \qquad (2)$$

In SURF, the scale space can be created by applying kernels of increasing size to the original image. This allows multiple layers of the scale space pyramid to be processed

simultaneously. The scale-space is divided into a number of octaves, where an octave refers to a series of response map layers covering a doubling of scale. In SURF the output of the above 9×9 filter is considered as the lowest level of scale space, which correspond to a real valued Gaussian with σ = 1.2. The scales of subsequent layers can be evaluated by the following formula

$$\sigma_{approx} = CurrentFilterSize \cdot (1.2/9). \quad (3)$$

In the lowest octave, the filter size of the first layer is 9×9, and the filter size increases by 6 between the two neighboring layers. For each new octave, the filter size increases double.

B. Descriptor

The SURF descriptor describes how the pixel intensities are distributed within a scale dependent neighbourhood of each interest point detected by the Fast-Hessian. This approach is similar to that of SIFT but integral images used in conjunction with filters known as Haar wavelets are used in order to increase robustness and decrease computation time. The first step consists of fixing a reproducible orientation based on information from a circular region around the interest point. Then describing the interest point by calculating the Haar wavelet responses over the square region aligned to the selected orientation.

1) Orientation Assignment: Assigning the interest point a reproducible orientation is to achieve invariance to image rotation. To determine the orientation, Haar wavelet responses of size 4σ are calculated for a set of pixels around the detected point with a radius of 6σ, where σ refers to scale at which the point was detected.

Once the wavelet responses are weighted with a Gaussian (2.5σ) centered at the interest point, they are represented as vectors in space with the horizontal response strength along the abscissa and the vertical response strength along the ordinate. The dominant orientation is estimated by calculating the sum of all responses within a sliding orientation window covering an angle of $\pi/3$. The longest responses vector lends its orientation to the interest point.

2) Descriptor Components: The first step in extracting the SURF descriptor is to construct a square window around the interest point. This window contains the pixels which will form entries in the descriptor vector and is of size 20σ, where σ also refers to the detected scale. Furthermore the window is oriented along the dominant orientation such that all subsequent calculations are relative to this direction.

As shown in Fig. 2 the descriptor window is divided into 4 ×4 regular subregions. Within each subregion Haar wavelets of size 2σ are calculated for 25 regularly distributed sample points. If we refer to the *x* and *y* wavelet responses by *dx* and *dy* respectively, then for these 25 sample points (i.e. each subregion) we collect,

$$v_{subregion} = \left[\sum dx, \sum dy, \sum |dx|, \sum |dy|\right]. \quad (4)$$

Therefore each subregion contributes four values to the descriptor vector leading to an overall vector of length 4×4 × 4 = 64. The resulting SURF descriptor is invariant to rotation, scale, brightness and, after reduction to unit length, contrast.

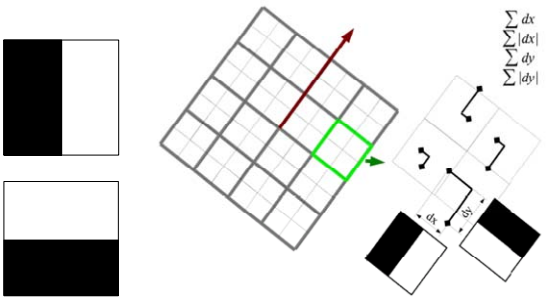

Figure 2. Left: Haar wavelet types for SURF (top the x-direction and bottom the y-direction). Right: SURF descriptor component. The brown arrow directs the dominant orientation, and the green rectangle refers to one of the descriptor subregion.

III. Spatial Association Correspondence

Although SURF is outstanding to extract the invariant interest points in an image, the number of correctly matched point pairs is too few to measure the tissue deformation accurately. Actually, many interest points that SURF extracts between the initial and deformed images are not really corresponding because of the nonuniform elastic deformation of the nonrigid tissues. In this paper the Spatial Association Corresponding method is proposed to obtain more correctly matched point pairs.

A. Spatial Association Correspondence

The Spatial Association Correspondence method is based on the supposition that the neighboring pixels in the initial MR image would also be most probably neighboring in the deformed MR image although the elastic deformation.

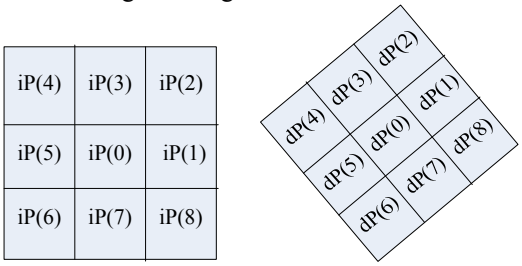

Figure 3. A pair of corresponding pixel neighbourhood regions between initial and deformed MR images. Left: neighbourhood in initial image, Right: corresponding neighbourhood in deformed image.

As shown in Fig. 3, there is a pixel neighbourhood region in initial and deformed image respectively. Because the pixel neighborhood has only 9 pixels and is very small, we only need consider the rotation and translation. We can suppose that if the initial point *iP(0)* is corresponding to the deformed point *dP(0)*, the initial neighboring pixel *iP(1)* would be corresponding to the deformed neighborhood pixel *dP(1)*.

Pixels *iP(2)* through *iP(8)* also correspond to the *dP(2)* though *dP(8)*.

B. *Feature Point Matching*

How to match the interest points between the images is based on the method as follows:

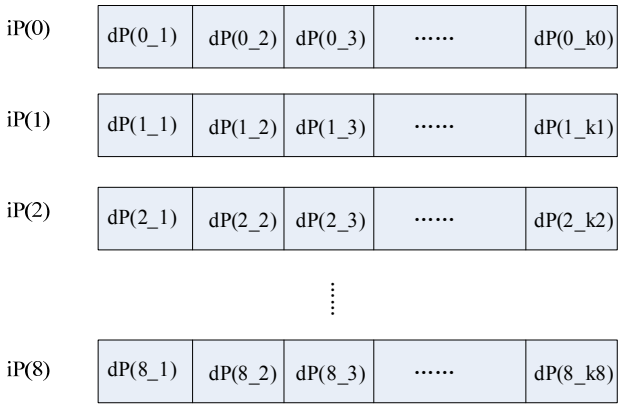

Figure 4. Candidate corresponding points of the the neighbourhood of *iP(0)*.

1) Corresponding Candidates Searching: We extract and match several correctly corresponding point pairs between the two images by means of SURF and the ratio of the nearest and the second nearest neighbor (NN/SCN) matching method. Then approximate affine transformation model of deformed image is calculated with the several matching pairs.

For the interest point *iP(0)* extracted, we only need to search a region in the deformed image. This region centered with the corresponding point of *iP(0)* calculated by the approximate affine transformation model, and the range of the corresponding region reflects a pre-estimation of maximum deformation. The SURF descriptors distances between *iP(0)* and all of the pixels in the corresponding region are compared. Usually, the point with the least descriptor distance to *iP(0)* may not be the real corresponding point. So we can set a threshold which is a little bigger than the least descriptor distance to *iP(0)*, the deformed pixels whose SURF descriptor distances to *iP(0)* are smaller than the threshold will be taken as the corresponding candidates such as *dP(0_1)* through *dP(0_k0)*. For the other pixels in the 3×3 neighborhood of pixel *iP(0)*, the corresponding candidates would be detected by the same process. For every point of *iP(0)* through *iP(8)* there are several corresponding candidates in the deformed image as shown in Fig. 4.

2) Corresponding Point Detection: In this step, we need to detect the corresponding point of *iP(0)* from the corresponding candidates by using Spatial Association Corresponding as shown in Fig. 5.

Firstly, we create a chain set *C*, which consists of the corresponding candidates of *iP(0)*, those are *dP(0_1)* through *dP(0_k0)*, as shown in the Fig. 5-a) are the red circles. Secondly, if every corresponding candidate of *iP(1)*, which refers to the green circle, is adjacent to any corresponding candidates of *iP(0)*, the two candidates are composed as a new binary chain element of the chain set *C*. Then check the set *C*, and eliminate the elements which consist of only one point, Such as the {*dP(0_4)*} and {*dP(0_6)*} in Fig. 5-b). Thirdly, if every corresponding candidate of *iP(2)*, which refers to the blue circle, is adjacent with both of the corresponding candidates of *iP(0)* and *iP(1)* in one of the binary chain elements of *C*, and the spatial position relationship between the three candidates is the same as *iP(0)*, *iP(1)* and *iP(2)* except the rotation, it is combined with the binary chain as a ternary chain element of *C*. Similarly eliminate the elements which consist of only two point, such as the {*dP(0_5)*, *dP(1_5)*} in Fig. 5-c).

Step by step, we check the corresponding candidate points of the other neighboring points *iP(3)* through *iP(8)* as the same process shown above. When only one element left in the chain set, we regard the first point of the element as the corresponding point of the pixel *iP(0)*.

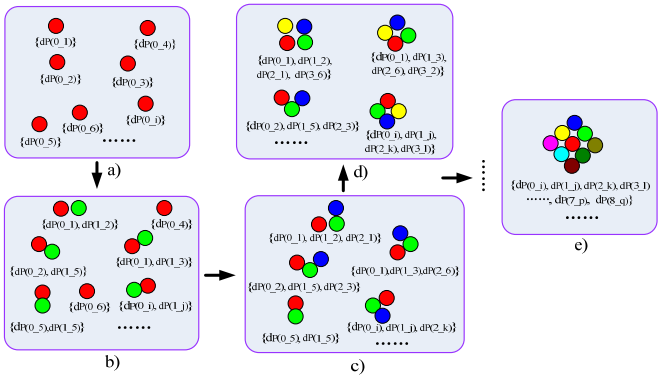

Figure 5. Corresponding point detection process of *iP(0)*.

IV. CLUSTERING

Actually, although matching the points between the initial and deformed images by means of the SURF and Spatial Association Correspondence, many feature points are incorrectly matched because of the deformation, blurry, noise, or other complex influence factors of the MR images. In order to eliminate the wrong matching points, the authors adopt the affine transformation and the clustering of the coordinate differences between the corresponding points matched by our method and the corresponding points calculated by the affine transformation method.

A. *Affine Transformation*

Given a point *P* in the initial image, the corresponding point *P'* in the deformed image matched by the affine transformation is as follows

$$p' = p \cdot T_{affine}, \tag{5}$$

where T_{affine} is the affine transformation matrix, which can be calculate by

$$T_{afine} = T_{scale} \times T_{rotate} \times T_{trans}, \quad (6)$$

where T_{scale}, T_{rotate} and T_{trans} are respectively scaling matrix, rotate matrix and translation motion matrix, given as follows:

$$T_{scale} = \begin{bmatrix} u & 0 & 0 \\ 0 & v & 0 \\ 0 & 0 & 0 \end{bmatrix}, \quad (7)$$

$$T_{rotate} = \begin{bmatrix} \cos\theta & \sin\theta & 0 \\ -\sin\theta & \cos\theta & 0 \\ 0 & 0 & 1 \end{bmatrix}, \quad (8)$$

$$T_{trans} = \begin{bmatrix} 1 & 0 & \Delta x \\ 0 & 0 & \Delta y \\ 0 & 0 & 1 \end{bmatrix}. \quad (9)$$

There are five variables in the three matrices; the scaling parameter u and v are along x-direction and y-direction respectively, θ is the rotation angle, Δx and Δy are the displacement along x-direction and y-direction.

B. Difference Clustering

In this paper, several correct matched pairs of points are detected by SURF, and the affine transformation was evaluated based on the least square method. Then, the difference cluster method is adopted to judge a pair of matching points is correctly corresponding or not.

The difference clustering is as follows. Suppose that $P(x, y)$ refers to a feature point in the initial image, $P'(x', y')$ is the corresponding point in the deformed image calculated by the affine transformation T_{affine}, and $P''(x'', y'')$ is the corresponding point in the deformed image matched by SURF-SAC. The difference between P' and P'' refers to difference point $dP(d_x, d_y)$ is as follows

$$dp(d_x, d_y) = (p'' - p') = \begin{bmatrix} x'' \\ y'' \end{bmatrix} - \begin{bmatrix} x' \\ y' \end{bmatrix}. \quad (10)$$

Difference clustering method is based on the supposition that if the point pairs are matched correctly the values of their difference points maybe most probably near to each other. Because the main tendencies of the biological deformation in the correct matched points are probably similar to each other, although the deformation displacements of them are not uniform. The other hand, the wrong matched point elimination is based on our method SURF-SAC, and the affine transformation can evaluate the great deformation such as scaling, rotation, and translation.

Given R refers to the cluster radius, $C(i)$ refers to a cluster centered with the difference point $dP(i)$, and $C(i)$ consists of the difference points whose distance with $dP(i)$ is less than R. In this paper, every difference point is taken as the cluster center, and the cluster which includes the most difference points are considered as consisting of correctly matched feature points.

V. Experiment Results Analysis

In our experiments, SIFT, SURF, and the proposed SURF-SAC are compared. An initial MR 2-D slice image and a deformed MR 2-D slice image of the volunteer's calf are tested. For SIFT and SURF method, the image pyramid consists of 3 octaves, every octave have 4 layers with the different scales (more octaves and more layers are not better to this experiments), and after the feature points are extracted, the method of NN/SCN is adopted to match the feature points between MR images. The procedure of SURF-SAC is as follows. 1) Extract the feature points in the initial MR image by SURF; 2) Take all the points in the deformed MR image as the feature points, and match the feature points between the two images based on SURF-SAC; 3) Eliminate the wrong matched pairs by coordinate difference clustering. We showed the experiments results from Fig. 6 to Fig.10.

The experiment results of SIFT were shown in Fig. 6. We can see that only 9 pairs of points are matched, which were signed in Fig. 6-b). Furthermore, the pairs 7 and 9 are matched incorrectly obviously.

The experiment results of SURF were shown as Fig. 7. The parameter T is defined as the threshold value of the determinant of the Fast-Hessian, the point whose fast-Hessian determinant is smaller than T would not be extracted. We set T equal to 0.0004. In SURF experiments, among many feature points extracted by SURF, there are 41 pairs of points are matched, even though the ratio of NN/SCN is assigned to 0.9 to obtain more matched pairs. Furthermore only 11 pairs of points are matched correctly, and the matching correct rate is 26.83%.

The experiment results of SIFT and SURF showed that the correct matched points was few, which are not enough to used to measure the deformation field of nonrigid nonuniform biological tissues. Actually in SIFT and SURF methods, many interest points of initial image could not obtain the really corresponding points among the interest points in the deformed image, when the MR images are blurry and especially with nonuniform elastic deformation in the tissues. On the other hand, the match method such as the ratio of NN/SCN behaved not well in this case.

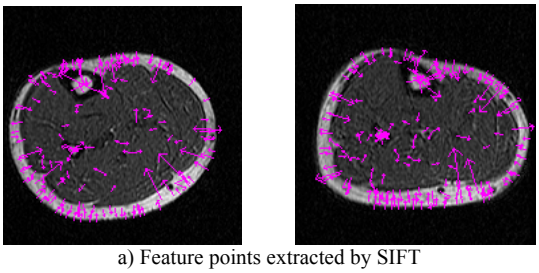

a) Feature points extracted by SIFT

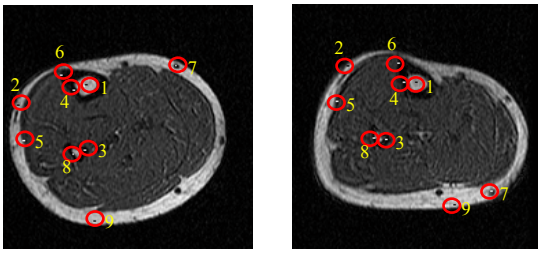

b) Matched points between initial and deformed MR image

Figure 6. The results of SIFT. Left: initial slice, Right: deformed slice.

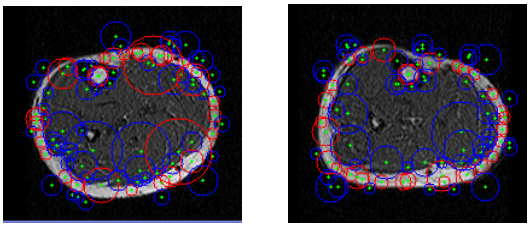

a) Feature points extracted by SURT

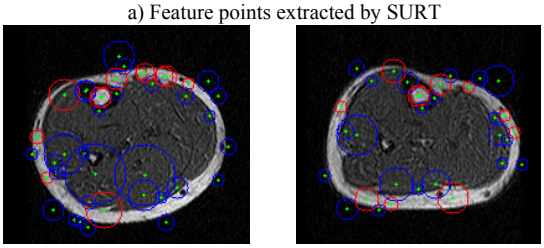

b) Matched points between initial and deformed MR image (41 pairs)

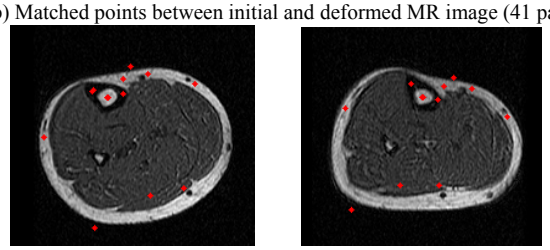

c) Correctly matched points (11 pairs)

Figure 7. The results of SURF

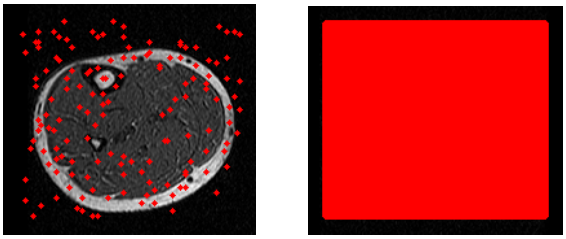

a) Feature points extracted by SURT

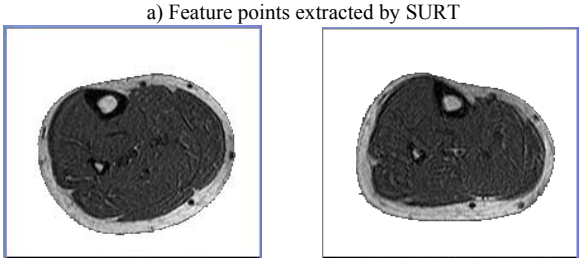

b) The results of background segmentation

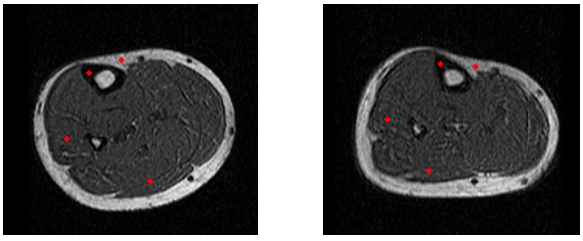

c) The matched points used for affine transformation evaluation

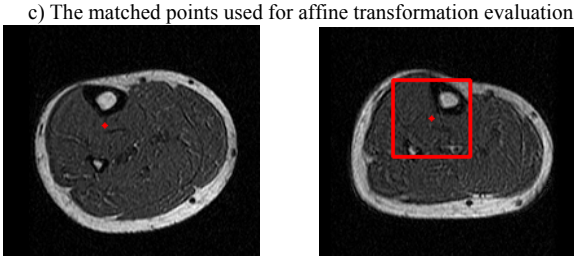

d) Searching region evaluated by affine transformation (radius = 30)

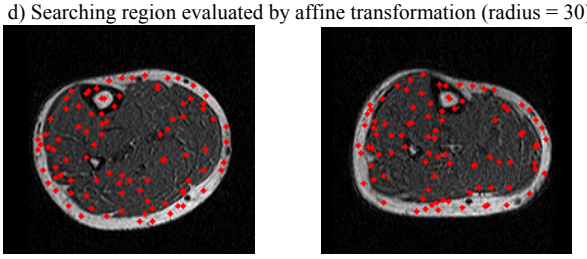

e) Matched points between initial and deformed MR image (93 pairs)

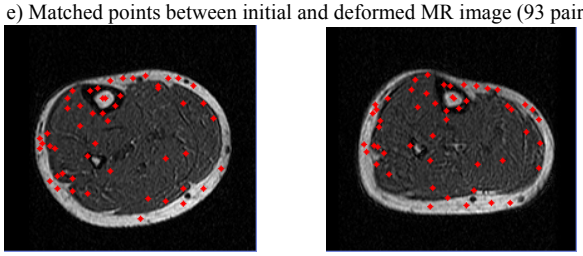

f) Correctly matched points (52 pairs)

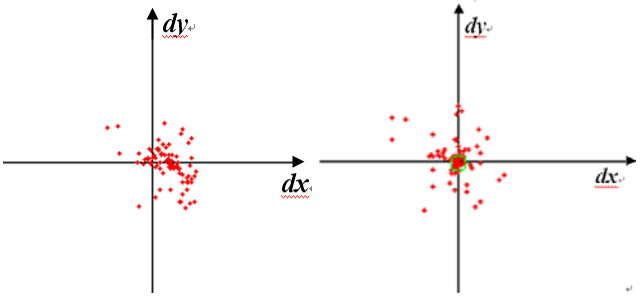

g) Coordinate difference points distribution h) The results of the clustering

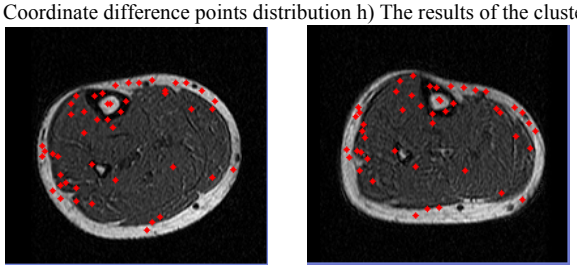

i) The matching points after clustering (48 pairs)

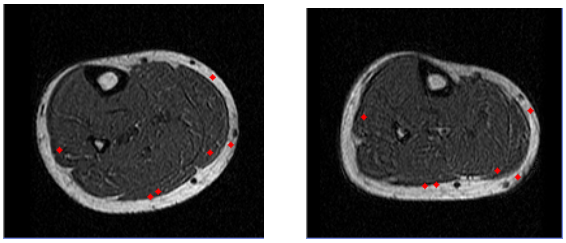

j) The wrong matched points are not eliminated by clustering (6 pairs)

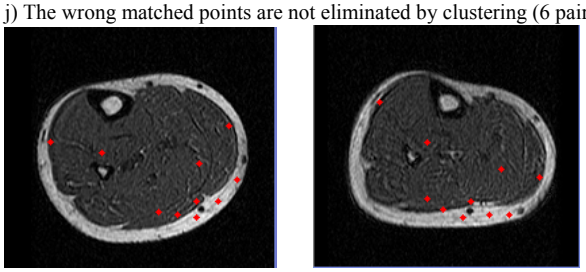

k) The correct matched points missed by clustering (10 pairs)

Figure 8. The results of SURF-SAC and Clustering

The experiment results are shown in Fig. 8. We used SURF-SAC to extract and match the feature points from the two MR images. In SAC method, we adopted spatial association corresponding relationship of two points in the neighbourhood of feature point, because when the number of the point increase the correct matched pairs decrease although the correctly match rate increase in this experiment. The matched points extracted by SURF-SAC are shown in Fig. 8-a). Fig. 8-b) showed the results of background segmentation, we used seed fill algorithm to segment the background, which avoided estimating the feature point in the background.

The evaluation of the affine transformation is based on the 4 pairs of matched points extracted by SURF (parameter T = 0.0004) and matched by NN/SCN with the ratio is of 0.65, which is shown in Fig. 8-c). The parameters of the affine transformation are $\theta = -14.19$, u = 13.869, v = 0.8974, $\Delta x = 44.73$, and $\Delta x = -13.68$. Given a feature point in the initial image, we only need to search the region centered with the corresponding point of affine transformation in the deformed image. The radius of the rectangle region equal to 30, and it reflects a pre-estimation of maximum deformation. Fig. 8-d) shows this step. By means of SURF-SAC, we obtained 93 pairs of matched points, and 52 pairs of points were correctly matched as shown in Fig. 8-e) and 10-f). The number of the correctly matched points was much more than that of SURF (or SIFT).

After this, for all initial points of the 93 matched pairs by SURF-SAC, we calculated the coordinate differences between the deformed points estimated by SURF-SAC with the corresponding points of affine transformation. Then we adopted clustering of the differences to eliminate the wrong matched points. The initial affine transformation model is estimated by the 4 points obtained by SURF, which is shown in Fig. 8-c). We set radius of the cluster circle equal to 5, and the difference points located in the cluster circle are used to calculate the affine transformation model again. Then the second affine transformation model is adopted to estimate the coordinate clustering. This process is repeated, and it can reduce the error introduced by the initial transformation model, which only adopted 4 points. In this experiment we set the iterative time equal to 10, more times are proved no much use to the results. The distribution of coordinate difference points is shown in Fig. 8-g), and results of clustering after 10 times iterative process is showed in Fig. 8-h), where the red points in the green circle denote to the correctly matched pairs.

There are 48 pairs of points are left after clustering, as shown in Fig. 8-i), and 6 wrong pairs are not eliminated by clustering as shown in Fig. 8-j). The correct rate reaches to 87.5%, especially in Fig. 8-j), the initial points and the wrong matched deformed points seem very likely to corresponding to each other although they are not the really corresponding pairs actually. Furthermore, there 10 correct pairs are missed by this means as shown in Fig. 8-k).

From the results of the experiments by our method, we can see that, SURF-SAC method can obtain more correctly matched point pairs between the initial and deformed MR images of the elastically deformed biological tissues than SURF (or SIFT) combined NN/SCN method. Furthermore, the coordinate difference clustering method can eliminate a large number of the wrong matched pairs.

VI. Conclusion

Current methods such as the transformation model estimation, physical model method, mutual information, and feature points combined with TIN cannot measure the nonrigid and nonuniform biological tissues deformation accurately. The extraction and matching of considerable number of feature points and elimination of the wrong matching pairs are the key issues of accurate elastic deformation field measurement.

SURF maybe the most outstanding method of feature point extraction, while unfortunately, when used in the deformation field measurement with the MR images of the nonrigid nonuniform biological tissues, the correctly matched points detected by SURF is too few to measure the local elastic deformation accurately.

In order to detecting more correct matching points between the initial and deformed MR images, the authors present Spatial Association Correspondence method combined SURF (SURF-SAC) to extract and match the feature points. SAC is based on the supposition that the neighboring pixels in the initial MR image would be probably neighboring in the deformed MR image. Further, clustering of the coordinate difference method is adopted to eliminate the wrong matched point pairs.

In the experiments, SIFT, SURF, and SURF-SAC are compared in the feature points extraction and matching of the MR images of the volunteer's calf. The experiment results show that SURF-SAC can detect more correctly matched points. For the elastic local deformation of nonrigid

nonuniform tissues, the accurate deformation is better to be measured by getting more correctly matched features. The other hand, the clustering of the difference between the deformed points matched by SURF-SAC with the corresponding points calculated by affine transformation can eliminate most of the wrong matched pairs.

While there are some limitations about our method, such as the computation cost is more than that of SIFT and SURF, and there are still some wrong matched pairs are not eliminated by clustering method also some correctly matched pairs are missed.

ACKNOWLEDGMENT

This work is partially supported by Prof. Shigerhiro Morikawa in Shiga University of Medical Science, Japan. The authors also gratefully acknowledge the helpful comments and the MR image data obtained.

REFERENCES

[1] P. L. Zhang, S. Hirai, K. Endo, and S. Morikawa, "Local deformation measurement of biological tissues based on feature tracking of 3D MR volumetric images," *IEEE/ICME International Conference on Complex Medical Engineering*, p. 711, 1982.

[2] P. L. Zhang, S. Hirai, and K. Endo, K., "A feature matching-based approach to deformation fields measurement from MR images of non-rigid object," *International Journal of Innovative Computing, Information and Control*, vol.4, pp. 1607–1625, 2008.

[3] Z. K. Wang, K. Namima, and S. Hirai, "Physical Parameter Identification of Uniform Rheological Deformation Based on FE Simulation," *Trans. Japanese Society for Medical and Biological Engineering*, Vol.47, No.1, pp. 1-6, Feb. 2009.

[4] Z. K. Wang, K. Namima, and S. Hirai, "Physical Parameter Identification of Rheological Object Based on Measurement of Deformation and Force," *IEEE International Conference on Robotics and Automation (ICRA 2009)*, *Kobe*, p. 1238, May. 2009.

[5] P. Kotsas, S. Malasiotis, M. G. Strintzis, et al. "A Fast and Accurate Method for Registration of MR Images of the Head", *International Journal on Medical Informatics*, vol. 52 (1-3), pp. 167-182, 1998.

[6] F. L. Bookstein. "Principal warps: thin-plate splines and decomposition of deformations", *IEEE Trans on Pattern Analysis and Machine Intelligence*, vol. 11(6), pp. 567-585, 1989.

[7] D. Rueckert, L. I. Sonoda, C. Hayes, et al. "Non-rigid registration using free-form deformations: Application to breast MR images", *IEEE Transactions on Medical Imaging*, vol. 18(8), pp. 712-721, 1999.

[8] M. Kass, A. Witkin, and D. TerzoPoulos, "Snake: active contour models," *International Journal of Computer Vision*, vol.1, pp. 321–331, 1987.

[9] V. Caselles, F. Catte, T. Coll, and F. Dibos, "A geometric model for active contours in image processing," *Numer. Math*., vol. 66, pp.1–31, 1993.

[10] Christensen G E, Rabbitt R D, Miller, et al. "Deformable templates using large deformation kinematics," IEEE Trans Image Process, 1996, 5: 1435-1447.

[11] J. P. Thirion. "Image matching as a diffusion process: an analogy with Maxwell's Demons", *Medical Image Analysis*, vol. 2, pp. 243-260, 1998.

[12] M. Ferrant. "Registration of 3-D intraoperative MRI images of the brain using a finite-element biomechanical model", *IEEE Trans. on Medical Imaging*, vol. 20(12), pp. 1384-1397, 2001.

[13] B. Likar, F. Pernus. "A Hierarchical Approach to Elastic Registration Based on Mutual Information", *Image and Vision Computing*, vol. 19(1-2), pp. 33-44, 2001.

[14] M. B. Skouson, Q. Guo, Z. P. Liang, "A Bound on Mutual Information for Image Registration", *IEEE Transactions on Medical Imaging*, vol. 20(8), pp. 843-846, 2001.

[15] T. Lindeberg, "Feature detection with automatic scale selection," *International Journal of Computer Vision*, vol. 30(2), pp. 79–116, 1998.

[16] D. Lowe, "Distinctive image features from scale-invariant keypoints, " *International Journal of Computer Vision*, vol. 60, pp. 91–110, 2004.

[17] K. Mikolajczyk, C. Schmid, "An affine invariant interest point detector," *The 7th European Conference on Computer Vision-Part I*, p.128, 2002.

[18] Y. Ke, and R. Sukthankar, "PCA-SIFT: A more distinctive representation for local image descriptors," *Computer Vision and Pattern Recognition*, vol. 2, pp. 506–513, 2004.

[19] C. Harris, and M. Stephens, "A combined corner and edge detector," *in Proceedings of the Alvey Vision Conference*, p.147, 1988.

[20] K. Mikolajczyk, and C. Schmid, "Indexing based on scale invariant interest points," *Proceedings of the 8th International Conference on Computer Vision, Vancouver, Canada*, p. 525. 2001.

[21] K. Mikolajczyk, and C. Schmid, "Scale and affine invariant interest point detectors." *International Journal of Computer Vision*, vol. 60, pp.63–86, 2004.

[22] K. Mikolajczyk, and C. Schmid, "A performance evaluation of local descriptors." *IEEE Transactions on Pattern Analysis and Machine Intelligence,* vol. 27, pp.1615–1630, 2005.

[23] L. M. J. Florack, Haar, B. M. t. Romeny, J. J. Koenderink, and M. A. Viergever, "General intensity transformations and differential invariants," *Journal of Mathematical Imaging and Vision*, vol. 4, pp. 171–187, 1994.

[24] F. Mindru, T. Tuytelaars, Gool, L.Van, and T. Moons, "Moment invariants for recognition under changing viewpoint and illumination," *Computer Vision and Image Understanding*, vol. 94, pp. 3–27, 2004.

[25] A. Baumberg, "Reliable feature matching across widely separated views," *IEEE Conference on Computer Vision and Pattern Recognition, Hilton Head Island, South Carolina, USA*, p. 774, 2000.

[26] H. Bay, T. Tuytelaars, and L. V. Gool, "SURF：Speeded Up Robust Features," *9th European Conference on Computer Vision, ECCV, Graz, Austria*, p.404, 2006.

[27] H. Bay, A. Ess, T. Tuytelaars, and L. V. Gool, "Speeded-up Robust Features (SURF)," *Computer Vision and Image Understanding*, vol. 110, pp. 346-359, March, 2008.

Proceedings of the 2010 IEEE
International Conference on Robotics and Biomimetics
December 14-18, 2010, Tianjin, China

SURF and Spatial Association Correspondence Applied in Extraction and Matching of Feature Points from MR Images of Deformed Tissues

Xubing Zhang [1,2], Shinichi Hirai [1], Penglin Zhang[3]
[1]Dept. of Robotics, Faculty of Science and Engineering, Ritsumeikan University, Kusatsu, Shiga 525-8577, Japan
[2]School of Computer Science, Wuhan Textile University, Wuhan 430073, China
[3]School of Remote Sensing and Information Engineering, Wuhan University, Wuhan 430079,China
E-mail: zxbwf001@163.com; hirai@se.ritsumei.ac.jp

***Abstract*—The extraction and matching of feature points is very important for measuring deformation fields of MR images. Current methods cannot extract and match enough feature points correctly when non-rigid soft biological tissues are deformed in MR images. The authors have therefore used SURF to extract feature points from initial MR images, utilizing every point in deformed MR images as feature points. Subsequently, SURF descriptors and Spatial Association Correspondence (SAC) of neighboring pixels are utilized to match the corresponding feature points of the initial and deformed MR images. Finally, by clustering the differences between deformed points matched by SURF-SAC with the corresponding points calculated by affine transformation, most incorrect match points can be eliminated. Our experimental results show that the proposed method can extract and match more correct corresponding feature point pairs than SURF and SIFT methods.**

***Key words*—SURF, Spatial Association Correspondence, Feature point, Extraction, Matching, Deformed**

I. INTRODUCTION

MATCHING the correspondence between two images is an important aspect of computer vision applications. Many actual problems depend on correspondences matching, including the detection of differences between images obtained at different times and under different conditions, the calculation of information on three dimensional objects from images obtained when the scene is changed or the imaging system is transformed, motion tracking, pattern identification and object recognition.

Extraction and matching of the feature points, which should be robust against the change in illumination, scaling, rotation, and some noise or slight distortion, is one of the most important methods used to detect the correspondences between the images. Many key point detectors and descriptors have already been described [1] – [4]. The most widely used detector is likely the Harris corner detector [5], based on eigenvalues of the second-moment matrix. Harris corners, however, are not scale-invariant. Other important methods include automatic scale selection, which detects points of interest at their own characteristic scale [1] and robust, scale-invariant feature detectors with high reproducibility, called Harris-Laplace and Hessian-Laplace detectors [6].

The Scale Invariant Feature Transform (SIFT) approach approximates the Laplacian of Gaussian (LoG) by using a Difference of Gaussians (DoG) filter [2], resulting in greater speed with reduced loss of accuracy [7], [8]. SIFT has been shown to outperform other feature descriptors, including Gaussian derivatives [9], moment invariants [10], complex features [11], phase-based local features, and the descriptors representing the distribution of smaller-scale features within the area of the point of interest [12].

SURF (Speeded-UP Robust Feature), first presented in 2006 [13], uses the 'Fast-Hessian' to approximate the Laplacian, describing a distribution of Haar-wavelet responses within the area of the point of interest. By reducing the descriptor to 64 dimensions and exploiting integral images, the SURF is more reproducible, distinctive, and robust, with a computing velocity 3 times greater than that of SIFT. Experimentally, SURF outperformed other methods, such as GLOH and PCA-SIFT [8], [13], [14].

Deformation field measurements of non-uniform and non-rigid biological tissues from magnetic resonance (MR) images are often required for clinical diagnosis, simulation and planning of surgery, and evaluation of the physical characteristics of biological tissues. Usually, there is a need to accurately measure local, non-regular deformations between initial and deformed images. When used to evaluate deformation fields, popular parametric deformation models cannot handle topological changes, whereas geometric active models cannot measure interior deformations [15], [16]. A deformation field measurement method, based on feature point tracking, has been found to overcome the disadvantages of deformation model methods. Using this method, there are a certain amount of wrong matched points which have negative effect on the measurement accuracy [17], [18].

Using SURF, we attempted to evaluate deformation measurements, but our experimental results were not encouraging. Too few points could be matched or used to construct the triangle mesh necessary for accurate measurements of deformation. To obtain more correctly matched points, we combined SURF with Spatial Association Correspondence (SAC) to extract and match featured points in the initial and deformed MR images. We also analyzed differences between the deformed points matched by SURF-SAC and those calculated by affine transformation, using difference clustering methods to automatically eliminate incorrectly matched points.

Experimentally, we compared the method combining SURF and Spatial Association Correspondence (SURF-SAC) methods with the SIFT and SURF. We found that SURF-SAC can result in more correctly corresponding

points, and most incorrectly matched feature points can be eliminated by the difference clustering algorithm.

II. SURF

The interest point detector of SURF is based on the Fast-Hessian matrix, and the descriptor of each interest point describes a distribution of Haar-wavelet responses within the area of that point of interest.

A. Fast-Hessian Detector

In contrast to the Hessian-Laplace detector [6], which uses different measures to select the location and the scale , SURF relies on the Hessian determinant for both. At a point $p=(x,y)$ in an image *I*, the Hessian matrix $\mathrm{H}(p,\sigma)$ in *P* at scale σ is defined as

$$H(p,\sigma)=\begin{bmatrix} L_{x,x}(p,\sigma) & L_{x,y}(p,\sigma) \\ L_{x,y}(p,\sigma) & L_{y,y}(p,\sigma) \end{bmatrix} \quad (1)$$

where σ is the scale factor, $L_{x,x}(p,\sigma)$ is the convolution of the Gaussian second order derivative $(\partial^2/\partial x^2)g(\sigma)$ with the image *I* at point *p*, and similarly for $L_{x,y}(p,\sigma)$ and $L_{y,y}(p,\sigma)$.

Application of box filters to approximate the second order Gaussian derivatives results in very rapid evaluations using integral images, independent of size. The 9×9 box filters $D_{x,x}$, $D_{x,y}$ and $D_{y,y}$ in Fig. 1 approximate Gaussian second order derivatives with the lowest scale $\sigma=1.2$, and the grey regions in the figures equal to zero.

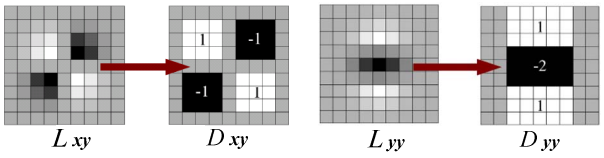

Fig. 1. The box filters $D_{x,y}$ and $D_{y,y}$ used to approximate Gaussian second order partial derivatives in the xy- and yy-directions.

The following formula has been proposed as an accurate approximation for the Hessian determinant using the approximated Gaussians:

$$\det(H_{approx})=D_{xx}D_{yy}-(0.9D_{xy})^2 \quad (2)$$

In SURF, the scale space can be created by applying kernels of increasing size to the original image. This allows for multiple layers of the scale space pyramid to be processed simultaneously [13].

B. Descriptor

The SURF descriptor describes how pixel intensities are distributed within a scale dependent on the area surrounding each point of interest, as detected by the Fast-Hessian.

1) Assignment of Orientation: To determine the orientation, Haar wavelet responses of size 4σ are calculated for a set of pixels at a radius of 6σ around the point of interest, with σ referring to the scale at which the point was detected.

Once the wavelet responses are weighted with a Gaussian (2.5σ) centered at the interest point, they can be represented as vectors in space, with the horizontal response strength along the abscissa and the vertical response strength along the ordinate. The dominant orientation can be estimated by calculating the sum of all responses within a sliding orientation window covering an angle of $\pi/3$. The longest responses vector lends its orientation to the interest point.

2) Descriptor Components: The first step in extracting the SURF descriptor is to construct a square window around the point of interest. This window contains the pixels that will form entries in the descriptor vector and is of size 20σ, where σ also refers to the detected scale. Furthermore the window is oriented along the dominant orientation, such that all subsequent calculations are relative to this direction.

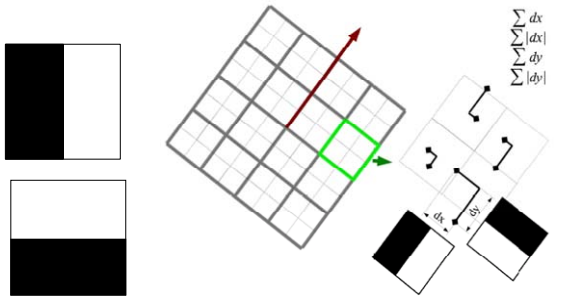

Fig. 2. Left: Haar wavelet types for SURF (top, x-direction; bottom, y-direction). Right: SURF descriptor component. The brown arrow shows the dominant orientation, and the green rectangle refers to one of the descriptor subregions.

As shown in Fig. 2 the descriptor window can be divided into regular 4×4 subregions. Within each subregion, Haar wavelets of size 2σ are calculated for 25 regularly distributed sample points. At *x* and *y* wavelet responses of *dx* and *dy* respectively, 25 sample points (i.e. each subregion) can be described as

$$v_{subregion}=\left[\sum dx,\sum dy,\sum|dx|,\sum|dy|\right] \quad (4)$$

Therefore each subregion contributes four values to the descriptor vector leading to an overall vector of length $4\times4\times4=64$.

III. Spatial Association Correspondence

Although SURF is outstanding in its ability to extract the invariant interest points in an image, the number of the correct corresponding point pairs is too few to measure the tissue deformation accurately. Many points of interest extracted by SURF in the initial and deformed images do not correspond because of the non-uniform elastic deformation and blurriness of the MR images. In our opinions, only considering the distance between the SURF descriptor is not suitable, the other useful information can be used to match the feature points, such as the spatial association between the neighboring pixels is very useful to the interest point matching.

A. Spatial Association Correspondence

To obtain more correctly matched pairs of points, we developed the Spatial Association Correspondence method, which is based on the hypothesis, that neighboring pixels in the initial MR image would likely also be neighboring pixels in the deformed MR image, despite elastic deformation.

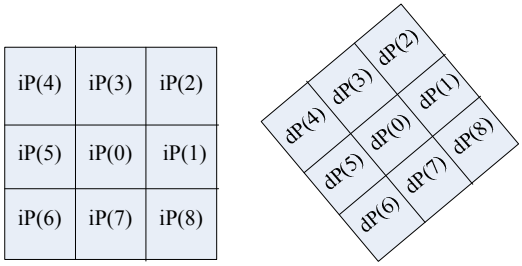

Fig. 3. A pair of corresponding pixel neighborhood regions in initial (left) and deformed (right) MR images.

For example, Figure 3 shows a pixel neighborhood region in initial and deformed images. Because this pixel neighborhood, which consists of only 9 pixels, is very small, we need to consider only its rotation and translation. Thus, if the initial point *iP(0)* corresponds to the deformed point *dP(0)*, the initial neighboring pixel *iP(1)* would correspond to the deformed neighboring pixel *dP(1)*. Similarly, pixels *iP(2)* through *iP(8)* would correspond to pixels *dP(2)* though *dP(8)*.

B. Feature Point Matching

The method of matching the points of interest in the initial and the deformed images is based on Spatial Association Correspondence:

dP(0_1)	dP(0_2)	dP(0_3)	……	dP(0_k0)
dP(1_1)	dP(1_2)	dP(1_3)	……	dP(1_k1)
dP(2_1)	dP(2_2)	dP(2_3)	……	dP(2_k2)
⋮				
dP(8_1)	dP(8_2)	dP(8_3)	……	dP(8_k8)

Fig. 4. Candidate points corresponding to the points neighboring *iP(0)*.

1) Searching for Corresponding Candidates: For point *iP(0)*, extracted by SURF from the initial image, all of the pixels in the deformed image are regarded as interest points, and the distances between their SURF descriptor vectors and that of *iP(0)* are compared. Usually, the point with the least descriptor distance to *iP(0)* may not be the real corresponding point. Therefore, we can determine a threshold slightly larger than the least descriptor distance to *iP(0)*. Thus, the deformed pixels whose SURF descriptor distances to *iP(0)* are smaller than the threshold would be regarded as the corresponding candidates; e.g., *dP(0_1)* through *dP(0_k0)*. For the other pixels in the 3×3 neighborhood of pixel *iP(0)*, the corresponding candidates would be detected by the same process. Every point, from *iP(0)* through *iP(8)*, would therefore have several corresponding candidates in the deformed image (Fig. 4).

2) Detection of Corresponding Points: The next step is to use Spatial Association Corresponding to identify the point corresponding to *iP(0)* from the corresponding candidates (Fig. 5).

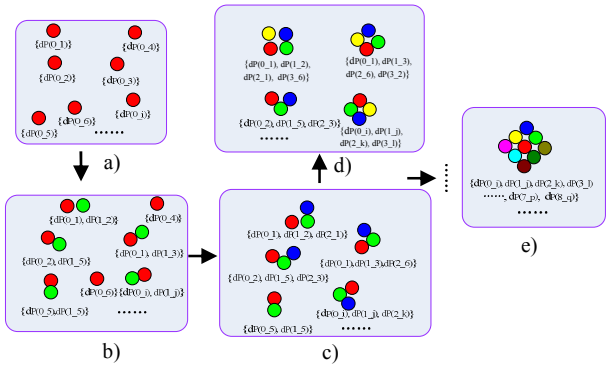

Fig. 5. Processing of detecting points corresponding to *iP(0)*.

The first step is to create a chain set *C*, which consists of the candidates corresponding to *iP(0)*; this set, *dP(0_1)* through *dP(0_k0)* consists of the red circles in Fig. 5-a). Second, if any candidate corresponding to *iP(1)*, designated by the green circles, is adjacent to any candidate corresponding to *iP(0)*, the two candidates are used to compose a new binary chain element of the chain set *C*. By examining set *C*, any elements consisting of a single point can be eliminated (e.g., {*dP(0_4)*} and {*dP(0_6)*} in Fig. 5-b). Third, if every candidate corresponding to *iP(2)*, indicated by the blue circles, is adjacent to both the candidates corresponding to *iP(0)* and *iP(1)* in one of the binary chain elements of *C*, and the spatial position relationship among the three candidates is the same as that *iP(0)*, *iP(1)* and *iP(2)*, except for rotation, it is combined with the binary chain to form a ternary chain element of *C*. This is followed by the elimination of elements consisting of only two points, e.g. {*dP(0_5)*, *dP(1_5)*} in Fig. 5-c).

Using this same process, we can determine the candidates corresponding to the points of interest of the other neighboring points, *iP(3)* through *iP(8)*. When only one element is left in the chain set, the first point of the element is regarded as the point corresponding to pixel *iP(0)*.

IV. Elimination of Wrong Matching Points

Actually, although matching the points by means of the SURF and Spatial Association Correspondence, many wrong matching feature points still existed because of the deformation, blurry, noise, or other complex influence factors of the MR images. To eliminate incorrectly matched points, we utilized clustering of differences between deformed points matched by our method and those calculated by affine transformation.

A. Affine Transformation

For each point *P* in the initial image, the corresponding point *P'* in the deformed image matched by the affine transformation may be described as

$$p' = p \cdot T_{affine} \tag{5}$$

where T_{affine} is the affine transformation matrix, which can be calculated as

$$T_{afine} = T_{scale} \times T_{rotate} \times T_{trans} \tag{6}$$

where T_{scale}, T_{rotate} and T_{trans} are the scaling, rotating and translation motion matrices, respectively, which can be described as:

$$T_{scale} = \begin{bmatrix} u & 0 & 0 \\ 0 & v & 0 \\ 0 & 0 & 0 \end{bmatrix} \tag{7}$$

$$T_{rotate} = \begin{bmatrix} \cos\theta & \sin\theta & 0 \\ -\sin\theta & \cos\theta & 0 \\ 0 & 0 & 1 \end{bmatrix} \tag{8}$$

$$T_{trans} = \begin{bmatrix} 1 & 0 & \Delta x \\ 0 & 0 & \Delta y \\ 0 & 0 & 1 \end{bmatrix} \tag{9}$$

There are five variables in the three matrices: the scaling parameters u and v along the x- and y-directions, respectively, the rotation angle θ, and the displacements along the x- and y-directions, Δx and Δy, respectively.

B. Difference Clustering

In this paper, we choose several correctly matched pairs of points to calculate the approximate affine transformation between the two images based on the least square method. This was followed by application of the difference cluster method, which was utilized to determine whether or not a pair of matching points corresponds correctly.

Difference clustering was determined as follows: If $p(x, y)$ refers to a feature point in the initial image, then $P'(x', y')$ would be the corresponding point in the deformed image, calculated by the affine transformation T_{affine}, and $P''(x'', y'')$ would be the corresponding point in the deformed image matched by SURF-SAC. The difference between P' and P'' refers to the difference point $dP(d_x, d_y)$, calculated as

$$dp(d_x, d_y) = (p'' - p') = \begin{bmatrix} x'' \\ y'' \end{bmatrix} - \begin{bmatrix} x' \\ y' \end{bmatrix} \tag{10}$$

The difference clustering method is based on the supposition that, if the two pairs are matched correctly, the values of their difference points would most probably be near to each other. Why we can draw the supposition is because of that although the deformation displacements of them are not uniform, the main tendencies of the biological deformation in the correct matched points are probably similar to each other. Furthermore, the wrong matched point elimination is based on our method SURF-SAC, and the affine transformation can evaluate the great deformation such as scaling, rotation, and translation.

If R refers to the cluster radius and $C(i)$ refers to a cluster centered at the difference point $dP(i)$, then $C(i)$ consists of the difference in points whose distance with $dP(i)$ is less than R. In this paper, we regarded every difference point as the cluster center, with the cluster that included the most difference points considered as consisting of correctly matched feature points.

V. Analysis of Experimental Results

In our experiments, SIFT, SURF, and the proposed SURF-SAC calculations were compared, using initial and deformed MR images of a volunteer's calf. For the SIFT and SURF methods, the image pyramid consisted of 3 octaves, each having 4 layers with different scales (increases in octaves and layers did not yield better results). Following extraction of the feature points, the NN/SCN method was used to match the feature points in the initial and deformed MR images. The procedure for SURF-SAC consisted of 3 steps: 1) SURF extraction of the feature points in the initial MR image; 2) Taking all the points in the deformed MR image as the feature points, followed by matching the feature points between the two images based on SURF-SAC; 3) Elimination of wrongly matched pairs by evaluating affine transformation and difference clustering. Experimental results are shown in Fig. 6-12.

The experimental results of SIFT are shown in Fig. 6. Only 9 pairs of points were matched, with pairs 7 and 9 being matched incorrectly.

The experimental results of SURF are shown in Fig. 7 and 8. These two experiments utilized different values for the parameter T, defined as the threshold value of the determinant of the Fast-Hessian; thus, any point whose fast-Hessian determinant was smaller than T would not be extracted. Usually, the stabilities of the points of interest increase as the threshold T increases. Table I shows the relationship between the value of T and the number of feature points. Many feature points were extracted by SURF, with more extracted in Fig. 8 than in Fig. 7. Although 41 and 48 pairs of points were matched in Figs 8 and 9, respectively, only 11 pairs were correctly matched in both, making the rates of correct matching 26.83% and 28.92%, respectively.

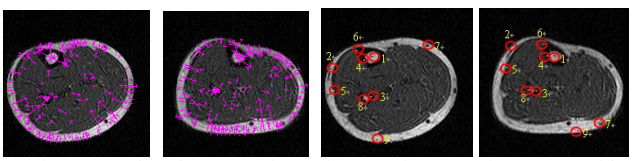

Fig. 6. Results of SIFT. Left two images: feature points extracted by SIFT. Right two images: matched points between two images

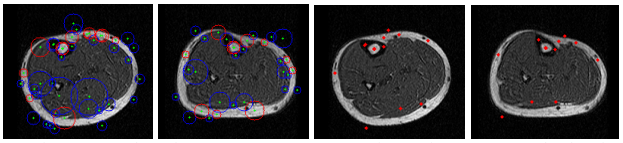

Fig. 7. Results of SURF, T = 0.0004, Left two images: matched points (41). Right two images: correctly matched points (11).

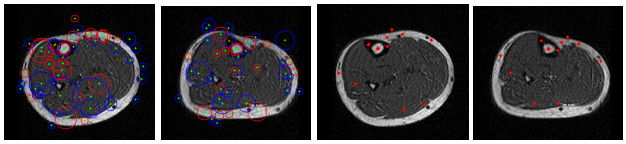

Fig. 8. Results of SURF, T = 0.00001. Left two images: matched points (48). Right two images: correctly matched points (11).

TABLE I
RELATIONSHIP BETWEEN VALUES OF T AND PN (NUMBER OF FEATURE POINTS)

T	0.0000001	0.000001	0.00001	0.0001	0.001	0.01	0.1
PN	150	148	123	102	65	3	0

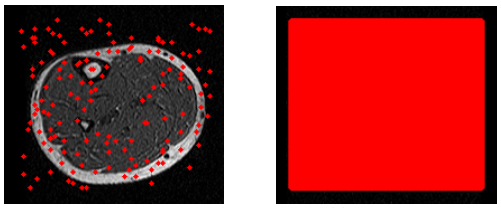

a) Feature points extracted by SURT

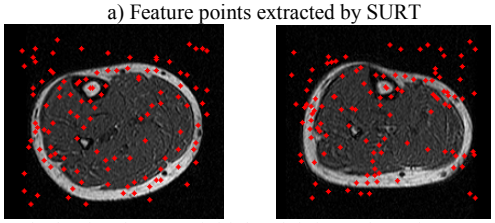

b) Matched points between initial and deformed MR image (116 pairs)

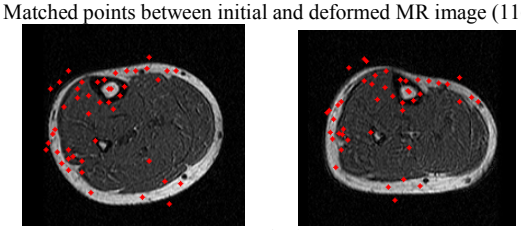

c) Correctly matched points (46 pairs)

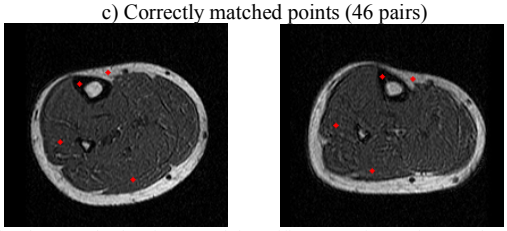

d) The matched points used for affine transformation evaluation

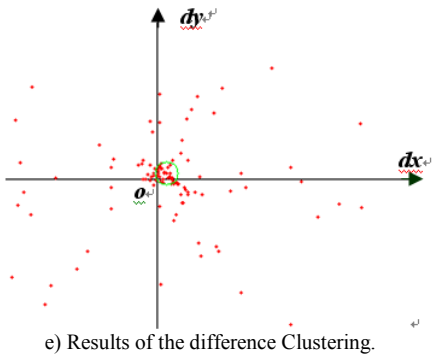

e) Results of the difference Clustering.

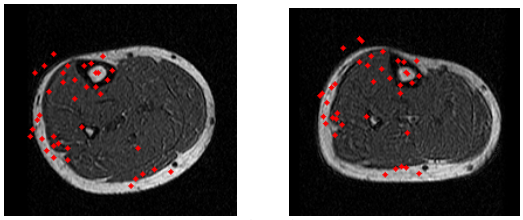

f) Matched points after clustering (38 pairs)

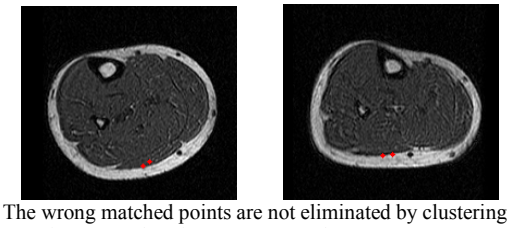

g) The wrong matched points are not eliminated by clustering (2 pairs)

Fig. 9. Results of SURF-SAC and SURF: T = 0.00001.

Experimental results are shown in Fig. 9. We used SURF-SAC to extract and match the feature points from the two MR images. T equaled 0.00001, small enough to determine many feature points. In this case, 123 feature points were extracted (Table I). Although some of these feature points were not very stable, that had no effect on our experimental results. The feature points extracted from the initial MR image are shown in Fig. 9-a), the matched points extracted by SURF-SAC shown in Fig. 9-b), and the 46 pairs of correctly matched points are shown in Fig. 9-c), which are much more than the correctly matched pairs extracted by using SURF (or SIFT) and NN/SCN.

The evaluation of the affine transformation was based on the 4 pairs of points correctly matched by SURF (Fig. 9-d)). The parameters of the affine transformation were $\theta = -14.19^{\circ}$, $u = 1.3869$, $v = 0.8974$, $\Delta x = 44.73$, and $\Delta y = -13.68$. Subsequently, for all initial points of the pairs matched by SURF-SAC, we calculated the differences between the deformed points matched by SURF-SAC with the corresponding points evaluated by affine transformation. We then clustered the differences to eliminate incorrectly matched points.

TABLE Ⅱ
RELATIONSHIP BETWEEN DIFFERENCE CLUSTERING RADII AND ELIMINATION OF INCORRECTLY MATCHED PAIRS (T = 0.00001)

Radius	8	9	10	11	12
NP	32	37	41	43	47
NCP	30	35	37	39	40
NWP	2	2	4	4	7
NMP	16	9	9	7	6

The radius of the clustering had a significant effect on the elimination of incorrectly matched points. In Table Ⅱ, NP (the number of the points in the biggest cluster), NCP (the number of correctly matched points in the biggest cluster), NWP (the number of wrongly matched points in the biggest cluster) and NMP (the number of correctly matched points missed by clustering) were compared. We can see that a clustering radius equal to 9 pixels gave the best results.

The red points in the green circles in Fig. 9-e) denote correctly matched pairs decided by clustering. We found that 38 pairs of points were included in the biggest difference cluster (Fig. 9-f)), with only 2 wrongly matched pairs not eliminated by clustering (Fig. 9-g)). The rate of correctly matched pairs was as high as 94.74%, especially in Fig. 9-g), the wrongly matched points likely corresponding to each other although they are not really corresponding pairs. Furthermore, this method missed 9 correct pairs.

Another experimental comparison of our method with SIF and SURF also show that our method was much better (Figs. 10-12). We found that our SURF-SAC method could result in more correctly matched pairs of points in the initial and deformed MR images of elastically deformed biological tissues than the SURF (or SIFT) combined NN/SCN method. Furthermore, the difference clustering method could eliminate most of the incorrectly matched pairs.

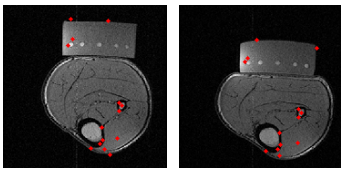

Fig. 10. Matching results of SIFT, showing that 10 of 14 pairs were matched correctly.

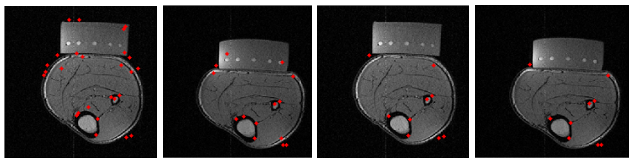

Fig. 11. Matching results of SURF. Left two images: matched points (26 pairs); Right two images: correctly matched points (9 pairs).

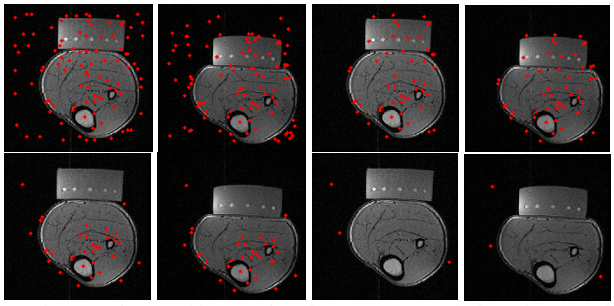

Fig. 12. The matching results of SURF-SAC and clustering. Top left two images: matched pairs (96 pairs). Top right two images: correctly matched pairs (50 pairs). Bottom left two images: clustering results (33 pairs). Bottom right two images: wrongly matched points were not eliminated by clustering (3 pairs).

VI. Conclusion

Feature points are important for image registration, pattern identification, motion tracking, and tumor detection. Although SURF may be a superior method of feature point extraction, when used in deformation field measurements of MR images of non-rigid, non-uniform biological tissues, this method yields too few correctly matched points to accurately measure local elastic deformation.

Our SURF-SAC method was able to detect more correctly matched points for accurate measurement of deformation, by extracting and matching feature points. Further, we used affine transformation and the clustering method to eliminate wrongly matched pairs of points.

In the experiments, SIFT, SURF, and SURF-SAC are compared in the feature points extraction and matching of the MR images of the volunteer's calf. The experiment results show that SURF-SAC could detect more correctly matched points, which is very important to the deformation field measurement. For elastic local deformation of non-rigid non-uniform tissues, accurate deformation is better measured by obtaining more correctly matched features. Furthermore, the clustering of differences between deformed points matched by SURF-SAC with the corresponding points calculated by affine transformation can eliminate most incorrectly matched pairs.

These two improvements may be very useful in measuring the deformation field of non-rigid non-uniform biological tissues, similar to other applications, such as image registration and motion tracking.

Our method had some limitations, including a higher computation cost than SIFT and SURF. These limitations must be addressed in future research.

References

[1] T. Lindeberg, "Feature detection with automatic scale selection," *IJCV* 30(2), 1998, pp. 79– 116

[2] D. Lowe, "Distinctive image features from scale-invariant keypoints, " *International Journal of Computer Vision,* vol. 60, pp. 91– 110, 2004.

[3] K. Mikolajczyk and C. Schmid, "An affine invariant interest point detector," in *Proc. The 7th European Conference on Computer Vision-Part I*, 2002, pp.128–142

[4] Y. Ke, and R. Sukthankar, "PCA-SIFT: A more distinctive representation for local image descriptors," *Computer Vision and Pattern Recognition*, vol. 2, pp. 506–513, 2004.

[5] C. Harris and M. Stephens, "A combined corner and edge detector," in *Proceedings of the Alvey Vision Conference*, 1988, pp.147–151

[6] K., Mikolajczyk and C. Schmid, "Indexing based on scale invariant interest points," in Proc. *Proceedings of the 8th International Conference on Computer Vision*, Vancouver, Canada, 2001, pp. 525–531.

[7] K. Mikolajczyk and C. Schmid, "Scale and affine invariant interest point detectors." *International Journal of Computer Vision*, vol. 60, pp.63–86, 2004.

[8] K. Mikolajczyk and C. Schmid, "A performance evaluation of local descriptors." *IEEE Transactions on Pattern Analysis and Machine Intelligence*, vol. 27, pp.1615–1630, 2005.

[9] L. M. J. Florack, Haar, B. M. t. Romeny, J. J. Koenderink, and M. A. Viergever, "General intensity transformations and differential invariants," *Journal of Mathematical Imaging and Vision*, vol. 4, pp. 171–187, 1994.

[10] F. Mindru, T. Tuytelaars, Gool, L.Van, and T. Moons, "Moment invariants for recognition under changing viewpoint and illumination," *Computer Vision and Image Understanding*, vol. 94, pp. 3–27, 2004.

[11] A. Baumberg, "Reliable feature matching across widely separated views," *in Proc. IEEE Conference on Computer Vision and Pattern Recognition*, Hilton Head Island, South Carolina, USA, 2000, pp. 774–781.

[12] W. T. Freeman and E.H. Adelson, "The design and use of steerable filters," *IEEE Transactions on Pattern Analysis and Machine Intelligence*, vol. 13, pp.891–906, 1991.

[13] H. Bay, T. Tuytelaars, and L. V. Gool, "SURF：Speeded Up Robust Features," in *Proc. 9th European Conference on Computer Vision, ECCV*, Graz, Austria, 2006, pp.404–417.

[14] H. Bay, A. Ess, T. Tuytelaars, and L. V. Gool, "Speeded-up Robust Features (SURF)," *Computer Vision and Image Understanding*, vol. 110, pp. 346-359, March, 2008.

[15] M. Kass, A. Witkin, and D. TerzoPoulos, "Snake: active contour models," *International Journal of Computer Vision*, vol.1, pp. 321–331, 1987.

[16] V. Caselles, F. Catte, T. Coll, and F. Dibos, "A geometric model for active contours in image processing," *Numer. Math*., vol. 66, pp.1–31, 1993.

[17] P. L. Zhang, S. Hirai, K. Endo, and S. Morikawa, "Local deformation measurement of biological tissues based on feature tracking of 3D MR volumetric images," in *Proc. IEEE/ICME International Conference on Complex Medical Engineering*, 2007, pp.711–716.

[18] P. L. Zhang, S. Hirai, and K. Endo, K., "A feature matching-based approach to deformation fields measurement from MR images of non-rigid object," *International Journal of Innovative Computing, Information and Control*, vol.4, pp. 1607–1625, 2008.

3.4 結言

本章では，軟組織の MR 画像から内部変形場を計算する二つの手法，局所不変特徴量を用いた変形場の計算手法と SAC と TPS を用いた変形場の計算手法について述べた．双方ともに，軟組織の変形にロバストな特徴量を用いており，軟組織の内部変形場を計算することが可能になった．現在の手法は，二次元画像間における変形場を計算することが可能である．変形前と変形後の MR 画像の撮影において，変形が主に撮像面内で生じる場合には，現在の手法で変形場を計算することができる．しかしながら，変形前と変形後の MR 画像の撮影において，軟組織の姿勢のずれが無視できない，あるいは MR のスライス間で変形が生じる場合には，ボリューム画像から三次元の内部変形場を計算することが必要になる．MR ボリューム画像から三次元の内部変形場を計算する手法は，今後の課題としたい．

第4章　柔軟指操作の三次元力学モデル

4.1　緒言

It is well known that we can grasp and manipulate objects with outstanding dexterity thanks to our highly developed brain, binocular vision, and abundance of motor and sensory nerves in our hands and fingers. Human structure of fingertips may contribute such dexterity in grasping and manipulation. It is well known that, not only the anatomy of our hands, but also that of our fingers are well designed for grasping and manipulating objects. In addition to allowing us to pick up small objects, the fingernails are essential for the high level sensitivity and as a buttress for the pad. Because our fingers are so good at grasping and manipulating, much research in the field of robotics has focused on soft-fingered grasping and manipulation. However, little research has considered the shape and function of our fingernails. Recently, it has been reported that such structure consisting soft fingertips and hard fingernail behind contributes to stable grasping and manipulation [45, 50]. A mechanical model of fingertips has been proposed and grasping and manipulation process has been analyzed based on the proposed model. Unfortunately, the model and the analysis were two-dimensional; three-dimensional grasping and manipulation have not been formulated.

This paper focuses on three-dimensional grasping and manipulation by robotic fingers with softtips. As shown above, we have proposed two-dimensional *parallel-distributed model* of a soft fingertip to describe the dependency of its potential energy to the relative orientation between the fingertip and the object. Here we extend the previous two-dimensional model to three-dimensional model, incorporating the rotation in three-dimensional space. We formulate the elastic potential energy stored in a soft fingertip due to the contact with the planar surface in three-dimensional space. We sketch the Lagrangian of the system consisting of a rigid prism grasped by three fingers with soft fingertips.

Related work

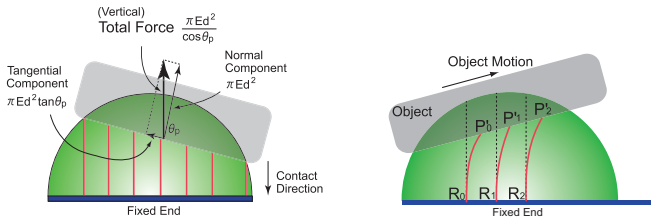

(a) normal deformation (b) tangential deformation

図 4.1: Parallel distributed model

Finite element (FE) analysis is often used when studying the deformation of objects, and can be used to describe deformation of a hemispherical soft fingertip exactly [51, 52, 53]. However, though FE analysis can be used to simulate grasping and manipulation numerically but cannot be applied to theoretical analysis of grasping and manipulation due to its complex formulation. The Hertzian contact model provides a simple closed-form description of the contact between two quadratic surfaces of elastic objects [54], but because the surfaces are assumed to be open-ended, it cannot be applied to a hemispherical elastic fingertip with a rigid back plate. Arimoto *et al.* formulated dynamics of pinching by a pair of soft fingertips [55], and used a *radially distributed deformation model* to analyze the mechanics of a soft fingertip [56]. Based on the concept of *stability on a manifold*, they showed theoretically that a 2-DOF finger and a 1-DOF finger can together realize secure grasping and posture control [57, 58].

Rolling contact in three-dimensional space yields nonholonomic Pfaffian constraints. Rolling contact between rigid bodies has been formulated in [59] and rolling contact between a soft fingertip and a rigid body has been formulated in [60, 61].

4.2 二次元平行分布モデル

We have proposed *parallel distributed model* of soft fingertips to formulate the dynamics of planar soft-fingered grasping and manipulation [45, 50]. Figure 4.1-(b) shows the parallel distributed model. Let a be the radius of a hemispherical fingertip in its natural shape and E be Young's modulus of the material of the fingertip. When the soft fingertips contact the planar surface of the rigid object, they deform, thereby applying elastic forces. Let d be the maximum displacement of the soft fingertip and $\theta_{\rm p}$ be the relative orientation between the fingertip and the

object. In the parallel-distributed model, the contact force given by

$$F_{\mathrm{perp}} = \frac{\pi E d^2}{\cos\theta_{\mathrm{p}}}. \tag{4.1}$$

The force is perpendicular to the planar surface behind the fingertip, as illustrated in the figure. Note that the force magnitude depends on both the maximum displacement d and the relative orientation θ_{p}. This dependency is due to the hemispherical shape of the soft fingertip subtended by a fixed rigid end, which is similar to a human finger consisting of a soft fingertip and a hard fingernail. The parallel distributed model reflects this structure consisting of a soft fingertip and a hard fingernail. The potential energy of the fingertip is described as follows:

$$U_{\mathrm{perp}}(d, \theta_{\mathrm{p}}) = \frac{\pi E d^3}{3\cos^2\theta_{\mathrm{p}}}. \tag{4.2}$$

Note that the energy depends on the maximum displacement d and the relative orientation θ_{p}.

In addition, tangential deformation should be introduced into the parallel distributed model so that a pinched object can rotate on a plane when an external force is applied, which happens in actual grasping and manipulation. Let us introduce the tangential displacement of a fingertip shown in Figure 4.1-(b). Letting d_{t} be the tangential displacement, the total potential energy caused by the tangential deformation is as follows:

$$U_{\mathrm{tangent}}(d, d_{\mathrm{t}}, \theta_{\mathrm{p}}) = \pi E\{d^2 d_{\mathrm{t}} \tan\theta_{\mathrm{p}} + d d_{\mathrm{t}}^2\}. \tag{4.3}$$

As the perpendicular and tangential displacements are not orthogonal, the above equation shows the coupling between them. Consequently, the total potential energy of a hemispherical soft fingertip in the parallel distributed model can be formulated as follows:

$$U_{\mathrm{parallel}}(d, d_{\mathrm{t}}, \theta_{\mathrm{p}}) \;=\; U_{\mathrm{perp}}(d, \theta_{\mathrm{p}}) + U_{\mathrm{tangent}}(d, d_{\mathrm{t}}, \theta_{\mathrm{p}}). \tag{4.4}$$

Note that this potential energy is dependent on the maximum displacement d, tangential displacement d_{t}, and relative angle θ_{p}.

4.3 一自由度三指による三次元操作の観察

It has been reported that a pair of 1-DOF fingers with soft fingertips can regulate both grasping force and the orientation of a grasped object along 2D vertical space

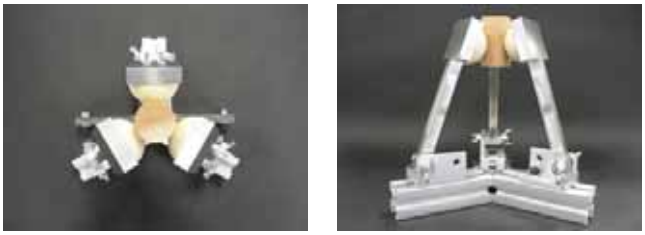

(a) 71°, 71°, 71°

(b) 67°, 71°, 74°

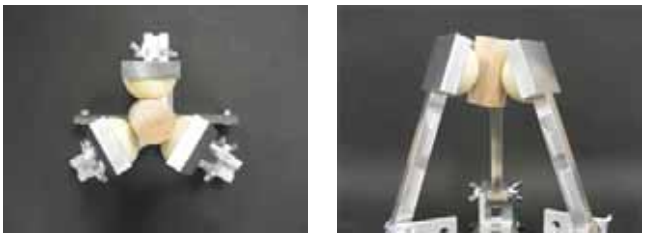

(c) 71°, 71°, 69°

図 4.2: Grasping by three 1-DOF fingers with soft fingertips

[45, 50]. Let us observe the grasping and manipulation of a rigid object by three fingers with soft fingertips. Figure 4.2 shows the grasping of a rigid cylindrical object by three 1-DOF fingers with hemispherical soft fingertips. Figure 4.2-(a) shows the initial location where joint angles at the base of three fingers are constantly equal to 71°. The object is perpendicular to the planar surface. Figure 4.2-(b) shows one location where three joint angles are 67°, 71°, and 74°. The cylindrical object grasped by the three fingers is inclined. Figure 4.2-(c) shows one location where three joint angles are 71°, 71°, and 69°. The object inclines toward the finger with its joint angle 69°. Through such experiments, we found that both the grasping force and the direction of the cylindrical object can be regulated by the joint angles of the three fingers. Noting that the direction of the cylindrical object is described by two parameters, this implies that this spatial hand system consisting of three fingers can regulate three variables; one for the grasping force and two for the object direction.

4.4 三次元操作における指と物体の幾何制約

4.4.1 法線方向の制約

This section formulates normal and tangential constraints between a soft fingertip and a rigid object in 3D space, based on rolling contact kinematics in [59] and rolling contact between a soft fingertip and a rigid body in [60, 61]. A hemispherical soft fingertip of radius a is in contact with a planar surface S of a rigid object, as shown in Figure 4.3. Let $\Sigma^{\rm obj}$ be a coordinate system attached to the object, $\Sigma^{\rm fin}$ be a coordinate system attached to the finger, and $\Sigma^{\rm spc}$ be a system fixed to space. Let O be the origin of $\Sigma^{\rm spc}$ and G be the origin of $\Sigma^{\rm obj}$. The position of the object is given by position vector $\boldsymbol{x}_{\rm obj}$ and its orientation is described by rotation matrix $R_{\rm obj}$. Let us describe rotation matrix $R_{\rm obj}$ by quaternions q_0 through q_3:

$$R_{\rm obj} = \begin{bmatrix} 2(q_0^2+q_1^2)-1 & 2(q_1q_2+q_0q_3) & 2(q_1q_3-q_0q_2) \\ 2(q_1q_2-q_0q_3) & 2(q_0^2+q_2^2)-1 & 2(q_2q_3+q_0q_1) \\ 2(q_1q_3+q_0q_2) & 2(q_2q_3-q_0q_1) & 2(q_0^2+q_3^2)-1 \end{bmatrix}.$$

Let $\boldsymbol{n}^{\rm obj}$ be the outward normal vector of plane S described in the object coordinate system. The outward normal vector is then described in spacial coordinate system as $\boldsymbol{n} = R_{\rm obj}\,\boldsymbol{n}^{\rm obj}$. Let $\boldsymbol{u}^{\rm obj}$ and $\boldsymbol{v}^{\rm obj}$ be tangential vectors along the surface described in the object coordinate system. Assume that $\boldsymbol{n}^{\rm obj}$, $\boldsymbol{u}^{\rm obj}$, and $\boldsymbol{v}^{\rm obj}$ form a right-handed

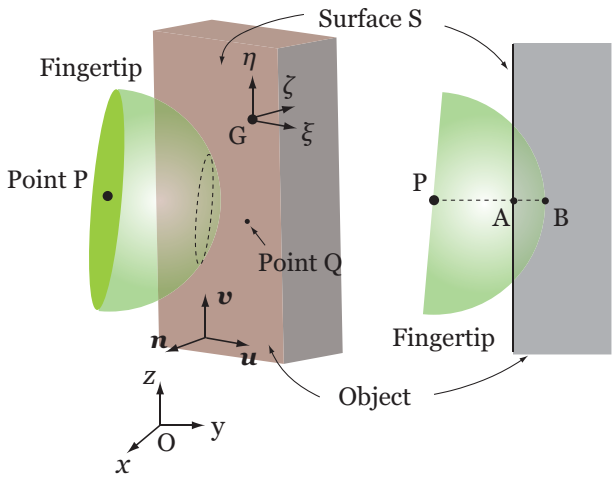

図 4.3: Contact between fingertip and planar surface in 3D space

coordinate system. Namely, $\boldsymbol{n}^{\mathrm{obj}}$, $\boldsymbol{u}^{\mathrm{obj}}$, and $\boldsymbol{v}^{\mathrm{obj}}$ are unit vectors orthogonal one another. The tangential vectors are then described in spacial coordinate system as $\boldsymbol{u} = R_{\mathrm{obj}}\,\boldsymbol{u}^{\mathrm{obj}}$ and $\boldsymbol{v} = R_{\mathrm{obj}}\,\boldsymbol{v}^{\mathrm{obj}}$. Let Q be a point on planar surface S and $\boldsymbol{\xi}_{\mathrm{Q}}$ be its position in the object coordinate system. The spacial position of point Q is given by $\boldsymbol{x}_{\mathrm{Q}} = R_{\mathrm{obj}}\,\boldsymbol{\xi}_{\mathrm{Q}} + \boldsymbol{x}_{\mathrm{obj}}$. Any point on the planar surface then must satisfy the following equation:

$$\boldsymbol{n}^{\mathrm{T}}(\boldsymbol{x} - \boldsymbol{x}_{\mathrm{Q}}) = 0.$$

Let P be the center of the hemispherical fingertip and A be its foot of perpendicular on surface S. Let $\boldsymbol{x}_{\mathrm{fin}}$ be the position of point P. Let d_{n} be the maximum normal displacement of the hemispherical soft fingertip. The positional vector of point A is then given by $\boldsymbol{x}_{\mathrm{fin}} + (a - d_{\mathrm{n}})(-\boldsymbol{n})$. Since this point is on surface S, we have the following equation:

$$\boldsymbol{n}^{\mathrm{T}}\{\boldsymbol{x}_{\mathrm{fin}} + (a - d_{\mathrm{n}})(-\boldsymbol{n}) - (R_{\mathrm{obj}}\,\boldsymbol{\xi}_{\mathrm{Q}} + \boldsymbol{x}_{\mathrm{obj}})\} = 0.$$

This equation yields a normal constraint between a fingertip and an object:

$$C_{\mathrm{n}} \triangleq \boldsymbol{n}^{\mathrm{T}}(\boldsymbol{x}_{\mathrm{obj}} - \boldsymbol{x}_{\mathrm{fin}}) - d_{\mathrm{n}} + a + (\boldsymbol{n}^{\mathrm{obj}})^{\mathrm{T}}\boldsymbol{\xi}_{\mathrm{Q}} = 0. \tag{4.5}$$

This constraint is holonomic. Note that the fourth term $(\boldsymbol{n}^{\mathrm{obj}})^{\mathrm{T}}\boldsymbol{\xi}_{\mathrm{Q}}$ is a constant denoting a signed distance between the origin of Σ^{obj} and surface S.

4.4.2 接線方向の制約

Assume that the deformation of a fingertip is at the maximum at point B. The position of point B is given by $\boldsymbol{x}_{\rm fin} - a\boldsymbol{n}$. Let $\boldsymbol{V}_{\rm obj}^{\rm tip}$ be the velocity of point B on the object. Since the orientation of the object is given by rotation matrix $R_{\rm obj}$, angular velocity $\boldsymbol{\omega}_{\rm obj}$ of the object is determined by

$$\left[\begin{array}{c} \boldsymbol{\omega}_{\rm obj} \times \end{array} \right] = \dot{R}_{\rm obj}\, R_{\rm obj}^{\rm T}.$$

Noting that $\overrightarrow{GB} = (\boldsymbol{x}_{\rm fin} - a\boldsymbol{n}) - \boldsymbol{x}_{\rm obj}$, velocity $\boldsymbol{V}_{\rm obj}^{\rm tip}$ is described as follows:

$$\boldsymbol{V}_{\rm obj}^{\rm tip} = \left[\begin{array}{c} \boldsymbol{\omega}_{\rm obj} \times \end{array} \right] \{(\boldsymbol{x}_{\rm fin} - a\boldsymbol{n}) - \boldsymbol{x}_{\rm obj}\} + \dot{\boldsymbol{x}}_{\rm obj} \tag{4.6}$$

where $\dot{\boldsymbol{x}}_{\rm obj}$ denotes the translational velocity of the rigid object. The tangential velocity of $\boldsymbol{V}_{\rm obj}^{\rm tip}$ along surface S is described by its projection on the surface. Since the projection matrix on surface S is given by $\boldsymbol{u}\boldsymbol{u}^{\rm T} + \boldsymbol{v}\boldsymbol{v}^{\rm T}$, the tangential velocity is described as

$$(\boldsymbol{u}\boldsymbol{u}^{\rm T} + \boldsymbol{v}\boldsymbol{v}^{\rm T})\, \boldsymbol{V}_{\rm obj}^{\rm tip} = (\boldsymbol{u}^{\rm T}\boldsymbol{V}_{\rm obj}^{\rm tip})\, \boldsymbol{u} + (\boldsymbol{v}^{\rm T}\boldsymbol{V}_{\rm obj}^{\rm tip})\, \boldsymbol{v},$$

implying that velocity components along $\boldsymbol{u}$ and $\boldsymbol{v}$ are $\boldsymbol{u}^{\rm T}\boldsymbol{V}_{\rm obj}^{\rm tip}$ and $\boldsymbol{v}^{\rm T}\boldsymbol{V}_{\rm obj}^{\rm tip}$, respectively. Let us describe the orientation of a fingertip by rotation matrix $R_{\rm fin}$. Let $\boldsymbol{V}_{\rm fin}^{\rm tip}$ be the velocity of point B on the fingertip. Since the orientation of the finger is given by rotation matrix $R_{\rm fin}$, angular velocity $\boldsymbol{\omega}_{\rm fin}$ of the finger is determined by

$$\left[\begin{array}{c} \boldsymbol{\omega}_{\rm fin} \times \end{array} \right] = \dot{R}_{\rm fin}\, R_{\rm fin}^{\rm T}.$$

Noting that $\overrightarrow{PB} = -a\boldsymbol{n}$, velocity $\boldsymbol{V}_{\rm fin}^{\rm tip}$ is described as follows:

$$\boldsymbol{V}_{\rm fin}^{\rm tip} = \left[\begin{array}{c} \boldsymbol{\omega}_{\rm fin} \times \end{array} \right] (-a\boldsymbol{n}) + \dot{\boldsymbol{x}}_{\rm fin} \tag{4.7}$$

where $\dot{\boldsymbol{x}}_{\rm fin}$ denotes the translational velocity of the fingertip. The tangential velocity of $\boldsymbol{V}_{\rm fin}^{\rm tip}$ along surface S is described by its projection on the surface, which is described as

$$(\boldsymbol{u}\boldsymbol{u}^{\rm T} + \boldsymbol{v}\boldsymbol{v}^{\rm T})\, \boldsymbol{V}_{\rm fin}^{\rm tip} = (\boldsymbol{u}^{\rm T}\boldsymbol{V}_{\rm fin}^{\rm tip})\, \boldsymbol{u} + (\boldsymbol{v}^{\rm T}\boldsymbol{V}_{\rm fin}^{\rm tip})\, \boldsymbol{v},$$

implying that velocity components along $\boldsymbol{u}$ and $\boldsymbol{v}$ are $\boldsymbol{u}^{\rm T}\boldsymbol{V}_{\rm fin}^{\rm tip}$ and $\boldsymbol{v}^{\rm T}\boldsymbol{V}_{\rm fin}^{\rm tip}$, respectively. Let $d_{\rm u}$ and $d_{\rm v}$ be tangential deformations along $\boldsymbol{u}$ and $\boldsymbol{v}$. From the above

discussion, we find that the time rate of the tangential deformations are described by

$$\dot{d}_{\rm u} = \boldsymbol{u}^{\rm T}\boldsymbol{\Delta}^{\rm tip}, \qquad \dot{d}_{\rm v} = \boldsymbol{v}^{\rm T}\boldsymbol{\Delta}^{\rm tip}$$

where

$$\begin{aligned}\boldsymbol{\Delta}^{\rm tip} &\triangleq \boldsymbol{V}_{\rm obj}^{\rm tip} - \boldsymbol{V}_{\rm fin}^{\rm tip} \\ &= \left[\begin{array}{c} \boldsymbol{\omega}_{\rm obj}\times \end{array}\right](\boldsymbol{x}_{\rm fin} - \boldsymbol{x}_{\rm obj} - a\boldsymbol{n}) + \left[\begin{array}{c} \boldsymbol{\omega}_{\rm fin}\times \end{array}\right] a\boldsymbol{n} + \dot{\boldsymbol{x}}_{\rm obj} - \dot{\boldsymbol{x}}_{\rm fin}\end{aligned}$$

denotes the relative velocity at point B. Note that when $\dot{d}_{\rm u} = 0$ and $\dot{d}_{\rm v} = 0$, we have no tangential deformations. The above equations yield the tangential constraints between a fingertip and an object given by

$$\dot{C}_{\rm u} \triangleq \boldsymbol{u}^{\rm T}\boldsymbol{\Delta}^{\rm tip} - \dot{d}_{\rm u} = 0, \tag{4.8}$$

$$\dot{C}_{\rm v} \triangleq \boldsymbol{v}^{\rm T}\boldsymbol{\Delta}^{\rm tip} - \dot{d}_{\rm v} = 0. \tag{4.9}$$

The above two are nonholonomic Pfaffian constraints.

4.5 三次元操作における指のポテンシャルエネルギー

Let us formulate elastic potential energy stored in a hemispherical soft fingertip due to the contact with a planar surface of a rigid body. Recall that the surface can slide along $\boldsymbol{u}$ and $\boldsymbol{v}$ with constant $d_{\rm n}$ keeping. Let $d_{\rm t}$ is the displacement along the direction of inclination and $d_{\rm s}$ is the displacement perpendicular to the inclination. Displacement $d_{\rm n}$ is described in Eq. (4.5). Let us formulate $d_{\rm t}$, $d_{\rm s}$, and $\theta_{\rm p}$ in three-dimensional grasping and manipulation.

Let us first derive derive the relative angle $\theta_{\rm p}$ between a fingertip and a planar surface. Let $\boldsymbol{b}^{\rm fin}$ be the unit normal vector of the plate behind a fingertip described in the finger coordinate system. The unit normal vector is then described in spacial coordinate system as $\boldsymbol{b} = R_{\rm fin}\boldsymbol{b}^{\rm fin}$. The relative angle $\theta_{\rm p}$ is given by the angle between two unit vector, $\boldsymbol{n}$ and $\boldsymbol{b}$. Thus, the relative angle is formulated as follows:

$$\cos\theta_{\rm p} = \boldsymbol{n}^{\rm T}\boldsymbol{b} = (R_{\rm obj}\boldsymbol{n}^{\rm obj})^{\rm T}(R_{\rm fin}\boldsymbol{b}^{\rm fin}), \tag{4.10}$$

$$\sin\theta_{\rm p} = \sqrt{1-\cos^2\theta_{\rm p}}. \tag{4.11}$$

Any non-zero $\theta_{\rm p}$ shows that the object surface inclines to one direction with respect to the back plate of a fingertip. The direction of inclination is given by the projection of

$\boldsymbol{b}$ on planar surface composed of $\boldsymbol{u}$ and $\boldsymbol{v}$. The tangential deformation takes positive values in the negative direction of the projection. Consequently, the direction of tangential deformation is described as

$$(\boldsymbol{u}\boldsymbol{u}^{\mathrm{T}} + \boldsymbol{v}\boldsymbol{v}^{\mathrm{T}})(-\boldsymbol{b}) = (-\boldsymbol{u}^{\mathrm{T}}\boldsymbol{b})\boldsymbol{u} + (-\boldsymbol{v}^{\mathrm{T}}\boldsymbol{b})\boldsymbol{v},$$

implying that components of the direction vector along $\boldsymbol{u}$ and $\boldsymbol{v}$ are given by $(-\boldsymbol{u}^{\mathrm{T}}\boldsymbol{b})$ and $(-\boldsymbol{v}^{\mathrm{T}}\boldsymbol{b})$. Letting ϕ_{t} be the angle between $\boldsymbol{u}$ and the direction vector, we have

$$\cos\phi_{\mathrm{t}} = \frac{-\boldsymbol{u}^{\mathrm{T}}\boldsymbol{b}}{\{(\boldsymbol{u}^{\mathrm{T}}\boldsymbol{b})^2 + (\boldsymbol{v}^{\mathrm{T}}\boldsymbol{b})^2\}^{1/2}}, \tag{4.12}$$

$$\sin\phi_{\mathrm{t}} = \frac{-\boldsymbol{v}^{\mathrm{T}}\boldsymbol{b}}{\{(\boldsymbol{u}^{\mathrm{T}}\boldsymbol{b})^2 + (\boldsymbol{v}^{\mathrm{T}}\boldsymbol{b})^2\}^{1/2}}. \tag{4.13}$$

Displacements d_{u} and d_{v} are converted into d_{t} and d_{s} as follows:

$$\begin{bmatrix} d_{\mathrm{t}} \\ d_{\mathrm{s}} \end{bmatrix} = \begin{bmatrix} \cos\phi_{\mathrm{t}} & \sin\phi_{\mathrm{t}} \\ -\sin\phi_{\mathrm{t}} & \cos\phi_{\mathrm{t}} \end{bmatrix} \begin{bmatrix} d_{\mathrm{u}} \\ d_{\mathrm{v}} \end{bmatrix}. \tag{4.14}$$

Potential energy is then described by

$$U = \frac{1}{2}\int_{ell} k\left\{(PQ + d_{\mathrm{t}}\sin\theta_{\mathrm{p}})^2 + (d_{\mathrm{t}}\cos\theta_{\mathrm{p}})^2 + (d_{\mathrm{s}})^2\right\}. \tag{4.15}$$

Computing the above equation, we have

$$U = U_{\mathrm{normal}} + U_{\mathrm{tangent}} + U_{\mathrm{side}} \tag{4.16}$$

where

$$U_{\mathrm{normal}}(d_{\mathrm{n}}, \theta_{\mathrm{p}}) = \frac{\pi E d_{\mathrm{n}}^3}{3\cos^2\theta_{\mathrm{p}}},$$
$$U_{\mathrm{tangent}}(d_{\mathrm{n}}, d_{\mathrm{t}}, \theta_{\mathrm{p}}) = \pi E\{d_{\mathrm{n}}^2 d_{\mathrm{t}}\tan\theta_{\mathrm{p}} + d_{\mathrm{n}} d_{\mathrm{t}}^2\},$$
$$U_{\mathrm{side}}(d_{\mathrm{n}}, d_{\mathrm{s}}) = \pi E d_{\mathrm{n}} d_{\mathrm{s}}^2.$$

Potential energy U_{normal} is caused by normal displacement d_{t}. Potential energies U_{tangent} and U_{side} are caused by tangential displacements d_{t} and d_{s}, respectively. Note that letting $d_{\mathrm{s}} = 0$, the above equation coincide with two-dimensional model Eq. (4.4).

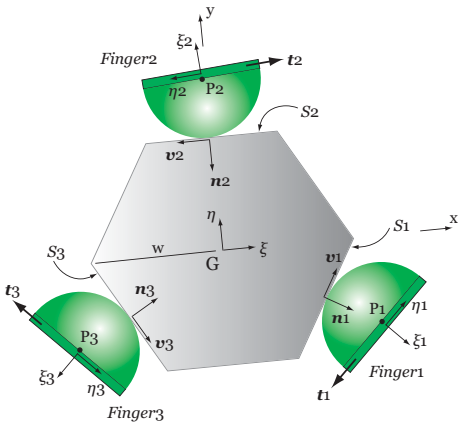

(a) top view

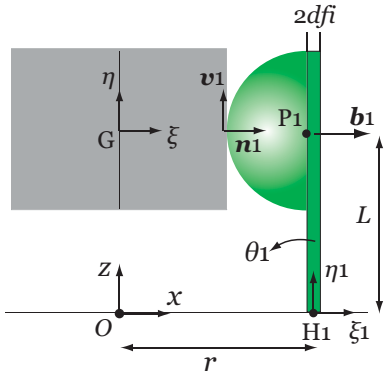

(b) side view

図 4.4: Three 1-DOF fingers grasping rigid hexagonal prism

4.6 三次元操作の定式化

Assume that three 1-DOF fingers with hemispherical soft fingertips grasp a rigid hexagonal prism, as shown in Figure 4.4. The hexagonal prism is inscribed to a cylinder of radius w. The radius of each fingertip is given by a Fingertip 1 is in contact with side face S_1, fingertip 2 is in contact with side face S_2, and fingertip 3 is in contact with side face S_3 of the hexagonal prism. Let $\mathrm{O}-xyz$ be the coordinate system attached to space. Let $\mathrm{G}-\xi\eta\zeta$ be the coordinate system attached to the prism. Let $\boldsymbol{x}_{\mathrm{obj}} = [\, x_{\mathrm{obj}},\, y_{\mathrm{obj}},\, z_{\mathrm{obj}} \,]^{\mathrm{T}}$ be the position of the prism and $\boldsymbol{q}_{\mathrm{obj}} = [\, q_0,\, q_1,\, q_2,\, q_3 \,]^{\mathrm{T}}$ be quaternions describing the orientation of the prism. Let $\boldsymbol{\omega}_{\mathrm{obj}} = [\, \omega_\xi,\, \omega_\eta,\, \omega_\zeta \,]^{\mathrm{T}}$ be the angular velocity of the prism. Let θ_k be the rotation angle of the k-th finger and R_k be the rotation matrix from spacial coordinate system $\mathrm{O}-xyz$ to the k-th finger coordinate system $\mathrm{F}_k - \xi_k\eta_k\zeta_k$. Let $d_{\mathrm{n}k}$ be the normal displacement of the k-th fingertip and $d_{\mathrm{u}k}$ and $d_{\mathrm{v}k}$ are its tangential displacements.

Let us derive the Lagrange equations of motion in grasping by three 1-DOF fingers. Generalized coordinates are $\boldsymbol{x}_{\mathrm{obj}}$, $\boldsymbol{q}_{\mathrm{obj}}$, $\boldsymbol{\theta}_{\mathrm{fin}} = [\, \theta_1,\, \theta_2,\, \theta_3 \,]^{\mathrm{T}}$, $\boldsymbol{d}_{\mathrm{n}} = [\, d_{\mathrm{n}1},\, d_{\mathrm{n}2},\, d_{\mathrm{n}3} \,]^{\mathrm{T}}$, $\boldsymbol{d}_{\mathrm{u}} = [\, d_{\mathrm{u}1},\, d_{\mathrm{u}2},\, d_{\mathrm{u}3} \,]^{\mathrm{T}}$, and $\boldsymbol{d}_{\mathrm{v}} = [\, d_{\mathrm{v}1},\, d_{\mathrm{v}2},\, d_{\mathrm{v}3} \,]^{\mathrm{T}}$. Kinetic energy is described as follows:

$$\begin{aligned} T &= \frac{1}{2}\, m_{\mathrm{obj}}\, \dot{\boldsymbol{x}}_{\mathrm{obj}}^{\mathrm{T}} \dot{\boldsymbol{x}}_{\mathrm{obj}} + \frac{1}{2} \boldsymbol{\omega}_{\mathrm{obj}}^{\mathrm{T}}\, I_{\mathrm{obj}}\, \boldsymbol{\omega}_{\mathrm{obj}} + \sum_{k=1}^{3} \frac{1}{2} I_{\mathrm{fin}} \dot{\theta}_k^2 \\ &+ \sum_{k=1}^{3} \frac{1}{2} m_{\mathrm{n}} \dot{d}_{\mathrm{n}k}^2 + \sum_{k=1}^{3} \frac{1}{2} m_{\mathrm{u}} \dot{d}_{\mathrm{u}k}^2 + \sum_{k=1}^{3} \frac{1}{2} m_{\mathrm{v}} \dot{d}_{\mathrm{v}k}^2. \end{aligned} \tag{4.17}$$

Potential energy is formulated as

$$U = U_1 + U_2 + U_3 \tag{4.18}$$

where

$$\begin{aligned} U_k &= U_{\mathrm{normal}}(d_{\mathrm{n}k}, \theta_{\mathrm{p}k}) + U_{\mathrm{tangent}}(d_{\mathrm{n}k}, d_{\mathrm{t}k}, \theta_{\mathrm{p}k}) + U_{\mathrm{side}}(d_{\mathrm{n}k}, d_{\mathrm{s}k}) \\ &= \frac{\pi E d_{\mathrm{n}k}^3}{3\cos^2\theta_{\mathrm{p}k}} + \pi E \left\{ d_{\mathrm{n}k}^2 d_{\mathrm{t}k} \frac{\sin\theta_{\mathrm{p}k}}{\cos\theta_{\mathrm{p}k}} + d_{\mathrm{n}k} d_{tk}^2 + d_{\mathrm{n}k} d_{\mathrm{s}k}^2 \right\}, \qquad (k = 1, 2, 3). \end{aligned}$$

Let τ_k be the torque to drive the joint of the k-th finger. Work done by external torques is given by

$$W = \tau_1\theta_1 + \tau_2\theta_2 + \tau_3\theta_3. \tag{4.19}$$

Since the distance between origin G and the three side faces is constantly equal to $(\sqrt{3}/2)w$, the normal constraint at the k-th fingertip is described as follows:

$$C_{\mathrm{n}k} = (R_{\mathrm{obj}}\,\boldsymbol{n}_k^{\mathrm{obj}})^{\mathrm{T}}(\boldsymbol{x}_{\mathrm{obj}} - R_k\,\boldsymbol{x}_k^{\mathrm{fin}} - \boldsymbol{r}_k) - d_{\mathrm{n}k} + a + (\sqrt{3}/2)w = 0. \quad (4.20)$$

Two tangential constraints at the k-th fingertip are described as follows

$$\dot{C}_{\mathrm{u}k} = (R_{\mathrm{obj}}\boldsymbol{u}_k^{\mathrm{obj}})^{\mathrm{T}}\boldsymbol{\Delta}_k^{\mathrm{tip}} - d_{\mathrm{u}k} = 0, \quad (4.21)$$

$$\dot{C}_{\mathrm{v}k} = (R_{\mathrm{obj}}\boldsymbol{v}_k^{\mathrm{obj}})^{\mathrm{T}}\boldsymbol{\Delta}_k^{\mathrm{tip}} - d_{\mathrm{v}k} = 0, \quad (4.22)$$

where

$$\boldsymbol{\Delta}_k^{\mathrm{tip}} = \left[\ \boldsymbol{\omega}_{\mathrm{obj}}\times\ \right](\boldsymbol{x}_k - \boldsymbol{x}_{\mathrm{obj}} - a\boldsymbol{n}_k) + \left[\ \boldsymbol{\omega}_k\times\ \right]a\boldsymbol{n}_k + \dot{\boldsymbol{x}}_{\mathrm{obj}} - \dot{\boldsymbol{x}}_k. \quad (4.23)$$

Summing holonomic constraints with Lagrange multipliers yields

$$C_{\mathrm{H}} = \lambda_{\mathrm{Q}}Q + \lambda_{\mathrm{n}1}C_{\mathrm{n}1} + \lambda_{\mathrm{n}2}C_{\mathrm{n}2} + \lambda_{\mathrm{n}3}C_{\mathrm{n}3}. \quad (4.24)$$

Summing Pfaffian constrains with Lagrange multipliers yields

$$\dot{C}_{\mathrm{P}} = \mu_{\mathrm{u}1}\dot{C}_{\mathrm{u}1} + \mu_{\mathrm{u}2}\dot{C}_{\mathrm{u}2} + \mu_{\mathrm{u}3}\dot{C}_{\mathrm{u}3} + \mu_{\mathrm{v}1}\dot{C}_{\mathrm{v}1} + \mu_{\mathrm{v}2}\dot{C}_{\mathrm{v}2} + \mu_{\mathrm{v}3}\dot{C}_{\mathrm{v}3}. \quad (4.25)$$

Let us introduce collective vectors consisting of Lagrange multipliers: $\boldsymbol{\lambda}_{\mathrm{n}} = [\,\lambda_{\mathrm{n}1},\ \lambda_{\mathrm{n}2},\ \lambda_{\mathrm{n}3},\,]^{\mathrm{T}}$, $\boldsymbol{\mu}_{\mathrm{u}} = [\,\mu_{\mathrm{u}1},\ \mu_{\mathrm{u}2},\ \mu_{\mathrm{u}3},\,]^{\mathrm{T}}$, and $\boldsymbol{\mu}_{\mathrm{v}} = [\,\mu_{\mathrm{v}1},\ \mu_{\mathrm{v}2},\ \mu_{\mathrm{v}3},\,]^{\mathrm{T}}$. Lagrangian of the system is then given as follows:

$$\mathcal{L} = T - U + W + C_{\mathrm{H}}. \quad (4.26)$$

Note that partial derivatives of the Lagrangian with respect to generalized coordinates and their time derivatives are shown in the previous sections. Consequently, applying the Lagrange equations of motion to the above Lagrangian, we can derive dynamic equations of motion of the object and the three fingers with soft fingertips. Nonholonomic Pfaffian constraints are imposed to the equations of motion with Lagrange multipliers [62].

4.7 シミュレーション

Let us simulate the spatial grasping and manipulation of a hexagonal prism via three 1-DOF fingers with soft fingertips. The radius of the circumcircle of the

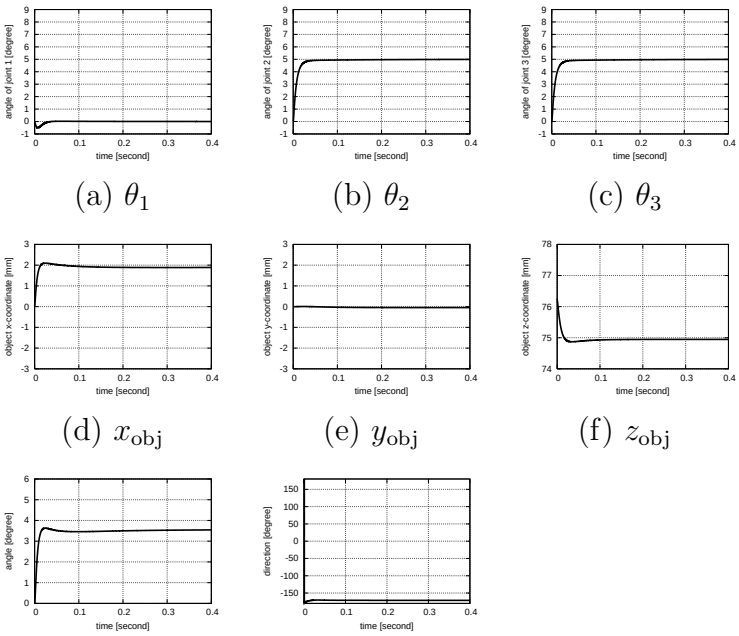

(a) θ_1 (b) θ_2 (c) θ_3

(d) x_{obj} (e) y_{obj} (f) z_{obj}

(g) incl. (h) dir.

図 4.5: Simulation result of three-fingered grasping ($\theta_1^* = 0°$, $\theta_2^* = 5°$, $\theta_3^* = 5°$).

hexagon is 25 mm and the height of the prism is 80 mm. Let the density of the prism be $6.88 \times 10^2\,\mathrm{kg/m^3}$, implying that its inertial properties are $m_{\mathrm{obj}} = 8.94 \times 10^{-2}\,\mathrm{kg}$, $I^{\xi}_{\mathrm{obj}} = I^{\eta}_{\mathrm{obj}} = 5.93 \times 10^{-5}\,\mathrm{kg{\cdot}m^2}$, and $I^{\zeta}_{\mathrm{obj}} = 2.33 \times 10^{-5}\,\mathrm{kg{\cdot}m^2}$. The inertial properties of each finger are given by $m_{\mathrm{fin}} = 100\,\mathrm{g}$ and $I_{\mathrm{fin}} = 582\,\mathrm{kg{\cdot}mm^2}$. In this simulation, we have assumed that the gravitational effect is negligible during grasping and manipulation. We have applied a simple PID law to control individual finger joints to observe the motion of the grasped object during the control of three fingers. Letting $\Delta\theta_k = \theta_k - \theta_k^*$, control input $\boldsymbol{\tau}_k$ for the k-th finger joint is expressed as

$$\tau_k = -K_{\mathrm{P}}\Delta\theta_k - K_{\mathrm{D}}\dot{\theta}_k - K_{\mathrm{I}}\int_0^t \Delta\theta_k(\tau)\,\mathrm{d}\tau, \tag{4.27}$$

where K_{P}, K_{D}, and K_{I} denote the proportional, differential, and integral gains, respectively. Let us apply the same gain values of $K_{\mathrm{P}} = 300\,\mathrm{Nm}$, $K_{\mathrm{D}} = 1\,\mathrm{Nm{\cdot}s}$, and $K_{\mathrm{I}} = 0.2\,\mathrm{Nm/s}$ to the three fingers.

Figures 4.5 through 4.7 show the simulation results when the desired angles of the three finger joints are given at time 0 s. The desired angles are $\theta_1^* = 0°$, $\theta_2^* = 5°$, and $\theta_3^* = 5°$ in Figure 4.5. As shown in Figures 4.5-(a) through (c), the joint angles converge to their desired values within 0.05 s. Figures 4.5-(d) through (f) denote

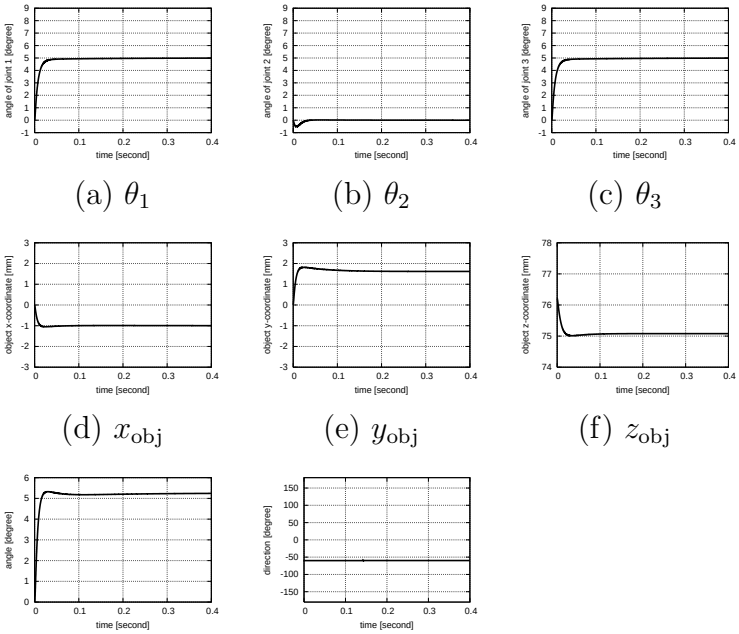

(a) θ_1 (b) θ_2 (c) θ_3

(d) x_{obj} (e) y_{obj} (f) z_{obj}

(g) incl. (h) dir.

図 4.6: Simulation result of three-fingered grasping ($\theta_1^* = 5°$, $\theta_2^* = 0°$, $\theta_3^* = 5°$).

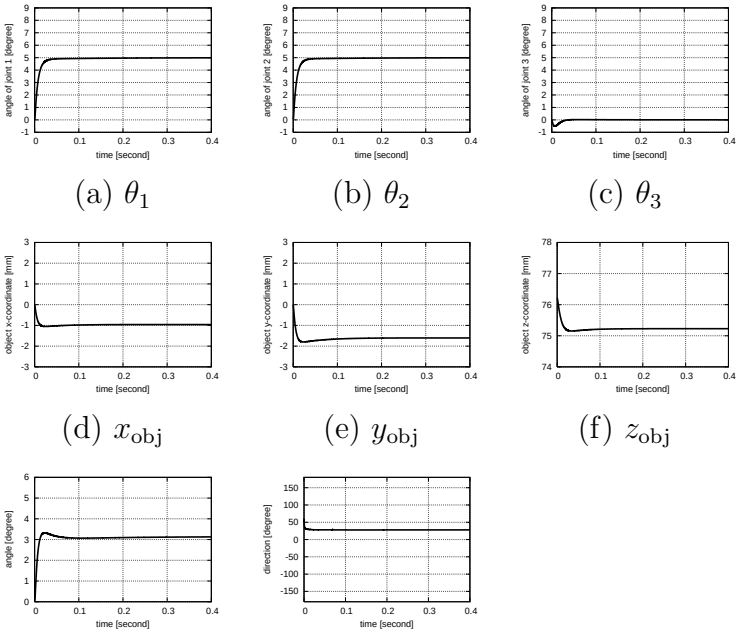

(a) θ_1 (b) θ_2 (c) θ_3

(d) x_{obj} (e) y_{obj} (f) z_{obj}

(g) incl. (h) dir.

図 4.7: Simulation result of three-fingered grasping ($\theta_1^* = 5°$, $\theta_2^* = 5°$, $\theta_3^* = 0°$).

the coordinates of the grasped object. The coordinates converge, implying that the object is stable with respect to the motion of three fingers. Let us investigate the direction of the central axis of the hexagonal prism. The unit vector along ζ-axis, which specifies the central axis, is described as $[\,2(q_1q_3 - q_0q_2),\ 2(q_2q_3 + q_0q_1),\ 2(q_0^2 + q_3^2) - 1\,]^{\mathrm{T}}$. Note that this vector coincides with the third column of the rotation matrix. Figure 4.5-(g) denotes the angle between the ζ-axis and the z-axis, which is given by $\cos^{-1}(2(q_0^2 + q_3^2) - 1)$. This angle represents the inclination of the prism. Figure 4.5-(h) denotes the direction of the projection of the ζ-axis on the $x - y$ plane, which is given by $\mathrm{atan2}\,(2(q_2q_3 + q_0q_1), 2(q_1q_3 - q_0q_2))$. This angle represents the direction of the inclined prism. The desired angles are $\theta_1^* = 5°$, $\theta_2^* = 0°$, and $\theta_3^* = 5°$ in Figure 4.6. The desired angles are $\theta_1^* = 5°$, $\theta_2^* = 5°$, and $\theta_3^* = 0°$ in Figure 4.5. Figures 4.5-(g), 4.6-(g), and 4.7-(g) suggest that the three fingers can incline the prism toward any direction, implying that a set of three 1-DOF fingers with soft fingertips can regulate the inclination and the direction of the grasped object.

4.8 結言

This chapter focused on the formulation of grasping and manipulation via soft-fingered hand in 3D space. First, we have formulated geometric constraints between a hemispherical soft fingertip and an object planar surface. Second, we have formulated the elastic potential energy stored in a soft fingertip due to the contact with the planar surface. We proposed to decompose the energy into three terms: U_{normal}, U_{tangent}, and U_{side}. Finally, we have sketched the Lagrangian of the system consisting of a rigid prism and three fingers with soft fingertips.

We have formulated soft-fingered grasping and manipulation in 3D space but not performed its experimental verification yet. We are measuring the object posture manipulated by three fingers with soft fingertips. We will compare the simulation result and experimental result to validate the formulation in this chapter.

第5章　柔軟指による視覚情報遅れ下における物体操作

5.1　緒言

画像処理を施した物体情報をシステムにフィードバックし所望のタスクを実現しようとする従来のマシンビジョンシステムにおける制御手法では，画像取得間隔（フレームレート：fps or Hz）やカメラ画素数に相当するメモリへのアクセス時間（画像処理時間）が，制御系の性能を大きく左右することになる．このような性能劣化を防ぐためにより高速な制御周期が要求され，その要求をハード面から満たし得るVGAで1kHzを超える高速度カメラがシステムに導入される研究事例が近年数多く見受けられ[63, 64, 65]，そのような方向性が確立しつつある．このような流れとは逆に，人の運動制御メカニズムはロボット制御に比して，遅れの多いシステムであると言える[66, 67]．体性感覚の物理的な伝達遅れが複合的に潜在する動的システムにもかかわらず，人は適応的な制御を実現している．この”遅れ”は，人の運動制御におけるα運動ニューロンの伝達速度に起因する．その値は筋の種類によって異なるが，最大でも100 m/sであり神経軸索上を神経パルスとして伝達される．筋張力が大きく瞬発力のある大腿四頭筋の場合，神経パルスの発生から筋活動までに約30∼40 msかかると言われている[68]．また，ひとつの神経軸索が終端する筋線維数が少ない動眼神経では約80 msの時間を要する反面[68]，眼球運動はより細かく制御されることになる．また，視覚情報を処理する視神経に至ってはさらなる遅れが生じる．

以上のように，視覚情報処理という観点から考えると，ロボットの制御と人の運動制御との間には，その進むべき方向性に隔たりがあると言える．このような観察を下に，従来のマシンビジョンにおけるビデオフレームレート[69, 70]より遅いサンプリングタイムでのビジュアルフィードバックシステムの検証を試みる．具体的には，ロボットビジョンでの画像取得と画像処理を故意に遅らせ，両者を含めた画像更新間隔を最大100 msに設定する．生体運動に内在する大幅な信号伝達遅れを模擬することで，本稿では10 Hz (100 ms)の遅い視覚更新レートにおけるビジュアルフィードバックシステムがロボットの制御に有効であることをシミュレーションと実験を通して明らかにする．ここで例示するタスクは，対向構造の柔軟指を持つ2指

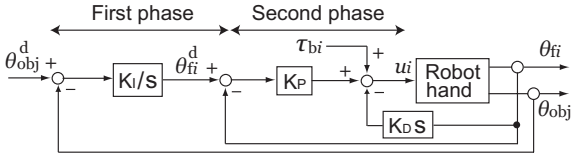

図 5.1: A block diagram of the proposed control method.

1 自由度対ロボットハンドによる物体操りであり，把持物体の姿勢制御を行う．指の物理的柔軟性が視覚遅れを伴った制御系において重要な役割を果たすことを示す．

5.2 柔軟指システムの運動方程式と制御則

柔軟指操作をモデル化しダイナミクスを表現する場合，指先の弾性モデルは欠かせない．人指と共通する弾性材料の柔軟性に着目しモデル化を行った結果，指先弾性力曲線に極小が存在することが明らかになっている [45, 71]．この知見は，指の柔軟特性をうまく利用すれば柔軟指による物体操作が，脳機能や体性感覚による複雑な制御や感覚フィードバックを介さなくても安定な把持と操りが実現可能であることを示唆する．柔軟指の平行分布モデルを含んだ 2 指ハンドシステム全体での運動方程式を以下に示す [72, 71].

$$\boldsymbol{M}\ddot{\boldsymbol{q}} + \boldsymbol{C}(\boldsymbol{q}, \dot{\boldsymbol{q}}) + \boldsymbol{D}\dot{\boldsymbol{q}} + \boldsymbol{f}_{\mathrm{p}} - \boldsymbol{\Phi}^{\mathrm{T}}\boldsymbol{\lambda} = \boldsymbol{f}_{\mathrm{ext}} + \boldsymbol{u}. \tag{5.1}$$

ここで，$\boldsymbol{M}$ は慣性行列，$\boldsymbol{C}$ は遠心力・コリオリ力項・非線形項，$\boldsymbol{D}$ は指先の粘性係数行列，$\boldsymbol{f}_{\mathrm{p}}$ は指先弾性力と重力を含んだ一般化ポテンシャル力，$\boldsymbol{\Phi}$ は本システムに存在する幾何拘束と速度拘束をまとめた拘束行列，$\boldsymbol{\lambda}$ は拘束に伴う拘束力，$\boldsymbol{f}_{\mathrm{ext}}$ は一般化外力，$\boldsymbol{u}$ は指関節への制御入力を意味する．次に，本稿で与える把持物体姿勢制御タスクを実現する制御則（直列連動 2 段階制御則）を以下に示す [71].

$$\theta_{\mathrm{f}i}^{*} = -(-1)^{i} K_{\mathrm{I}} \int_{0}^{T} (\theta_{\mathrm{obj}} - \theta_{\mathrm{obj}}^{*})\,\mathrm{dt}, \tag{5.2}$$

$$u_i = -K_{\mathrm{P}}(\theta_{\mathrm{f}i} - \theta_{\mathrm{f}i}^{*}) - K_{\mathrm{D}}\dot{\theta}_{\mathrm{f}i} + \tau_{\mathrm{b}i}. \tag{5.3}$$

本制御手法のブロック線図を図 5.1 に示す．式 (5.2) の 1 段目積分器で物体姿勢を偏差なくロバストに制御し，その過程で動的に生成される関節角目標を式 (5.3) の 2 段目 PD 制御器に代入することで安定な操り動作を実現している．また，2 段目 PD 制御器が負のトルクを生成しないように，定数バイアストルクを加えている．

5.3　視覚情報の遅れとロボット制御周期との関係

ロボット制御に関わらず視覚情報取得を前提としたマシンビジョンシステムでは従来，カメラによる画像取得と計算機内での画像処理時間の制御系に与える影響はほとんど議論されてこなかった．一方のシミュレーションにおいては，動的システムの挙動を解くルンゲクッタ法による for ループ内で，時間遅れのないカメラ取得と画像処理が前提となっている．つまり，制御ループのある時点で瞬時に画像を取得し処理を行っていることになる．これは,「カメラによる撮像時間と計算処理時間をゼロに仮定する」ことと等価である．しかし，これが理想的な条件であり実現不可能であることは容易に理解されよう．一方で人の視覚情報処理過程においては，網膜に結像した像が視神経路を介して神経パルス信号として一次視覚野（V1）に到達し，その後，頭頂連合野や側頭葉下部においてパターン認識や空間認識が行われ視知覚として処理されている [73]．各受容野からの視覚ニューロンは電気信号であるため，5.1 章で述べた神経軸索上の信号伝播速度を考慮すると，網膜に照射された像が運動制御に役立つ情報として脳から取り出せるまでに，数十 ms 程度の遅れを生じることが知られている [74]．さらに，手指による物体把持操りタスクにおいては指関節の角度制御が必要になるため，遠心性神経路を介した脳や脊髄からの神経系伝達遅れを生じる．このようなことから，本稿ではまず，人の運動制御とロボットの実制御とを比較して，マシンビジョンシステムの「情報伝達の遅れ」を以下のように厳密に分類し定義する．

I　処理遅れ（時間）Processing delay, T_{p}：撮像，画像転送，ならびに画像処理に費やされる時間の合算であると定義する．これは同一のカメラ，コンピュータ，画像処理アルゴリズムを利用している限り不変である．ただし，画像をロボット制御におけるフィードバック情報として用いない場合，画像をカメラからメモリ上に取り込む必要がないため画像転送時間と画像処理時間が共にゼロとなり，処理遅れ時間＝撮像時間となる．また，画像処理時間は撮像時間や画像転送時間に比べて一般的に長い．

II　伝達遅れ（時間）Transmission delay, T_{t}：計算し得られた視覚情報によって発射された筋活動指令が神経路を通って末梢神経に伝播するということは，それに掛かった時間分過去の視覚情報が伝わり，それに基づいて手指の運動制御が行われていることを意味する．この遅れ時間をロボット制御において模擬するために，人為的に取得画像の更新を遅らせる．この時間を伝達遅れと定義する．

A　撮像時間, T_{cp}：撮像時間の長短はカメラ（CCD や CMOS）の光学素子の構造やスペック，画素数に依存する．受光した撮像面の光電変換と走査によってピクセル毎の電気信号（アナログ）を取り出す．

B　画像転送時間, T_{tf}：キャプチャプログラム内の指定された画像キャプチャ関数に

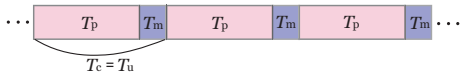

(a) continuous updating of a camera image

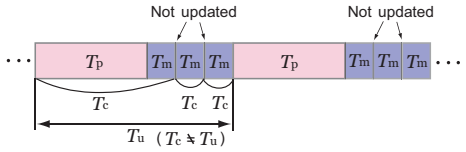

(b) irregular updating of a camera image

図 5.2: A conceptual diagram of the time-delayed robotic system in visual feedback control.

よって 1 フレームの画像情報をコンピュータメモリ（もしくは画像キャプチャカード上のメモリ）に転送する時間．本稿で利用するカメラは VGA サイズで 200 fps であるため，$T_{\rm cp} + T_{\rm tf} = 5$ ms である．

C 画像処理時間, $T_{\rm cm}$：メモリ上にプールしたフレーム毎の画像データから種々の画像処理アルゴリズムを用いて，当該システムに必要な情報（2 値画像処理，パターン検出，特徴抽出等）を計算し求める時間．

以上の定義を制御ループを想定した時系列で考えた場合の，ビジュアルフィードバックループを有するロボットの制御周期の概念を図 5.2 のようにパターン分けすることができる．図内において，$T_{\rm m}$ はモータの動作指令にかかる時間であり，$T_{\rm c}$ はロボットの制御時間（周期）でありプログラム内では for ループの周期に相当する．また，画像の更新周期を $T_{\rm u}$ とし，伝達遅れを伴った場合は図 5.2-(b) のように，制御周期 $T_{\rm c}$ と一致しない．結局図 5.2-(b) の例では，$2T_{\rm m}$ 分画像情報の伝達が遅れていることになり，$T_{\rm t} = 2T_{\rm m}$ の関係を満たす．また，$T_{\rm m}$ はおよそ数十 μs 以下であり，一般的にカメラ画像の取得や処理に費やす時間に比して極端に短い．以上のように本章では，遠心性神経路での信号伝達遅れを画像の更新遅れで模擬し，その更新周期を 4 通りに変更させ最大で $T_{\rm p}$ のおよそ 4 倍の更新遅れを有するロボットビジョンシステムの把持操り動作解析を行う．

5.4 ビジョンシステムのパラメータ同定実験

前章で述べた処理遅れ（時間）$T_{\rm p}$ は当該システムで利用されるカメラやコンピュータの性能に大きく依存する．したがって，本稿で用いるビジュアルフィードバックロボットシステムの $T_{\rm p}$ と $T_{\rm m}$ を基礎実験により同定する．本稿で取り扱うロボットハンドシステムを図 5.3-(a) に示し，各機器の仕様を表 5.1 に示す．本同定実験では，

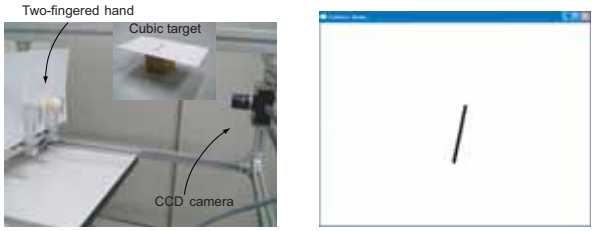

(a) total view (b) a binarized image

図 5.3: A robotic hand system with a monochrome camera.

表 5.1: Specifications in the verification test

Camera model	Point Gray Research, Dragonfly Express
Interface	IEEE 1394b (FireWire)
Imaging sensor	Progressive scan CCD
Resolution	VGA Grayscale image
Frame Rates	200 fps (Format 7 mode)
PC spec.	Pentium 4 1.9 GHz
FSB & Cache	400 MHz, 256 KB
Memory	512 MB DDR 400 MHz × 1
OS	Vine Linux 3.2 (kernel 2.4.31) Non-RT

黒色マーカを貼り付けた 50mm 四方の木片立方体をカメラの直下に置き（図 5.3-(a) の上側），画像キャプチャを開始する．ここで得られる 2 値化画像を図 5.3-(b) に示す．したがって，画像処理時間 $T_{\rm cm}$ は画像データを得るためのメモリへのアクセスから 2 値化までに要する時間と言える．

まず，システム固有の処理遅れ時間 $T_{\rm p}$ を求めるために，人為的遅れのない図 5.2-(a) のような設定でキャプチャと画像処理を開始する．よって，キャプチャプログラム内の for ループでは，$T_{\rm cp}$，$T_{\rm t}$，$T_{\rm cm}$，$T_{\rm m}$ の合計 $T_{\rm p}+T_{\rm m}$ が計測される．この結果を図 5.4-(a) に示す．ここで，$T_{\rm p}+T_{\rm m}$ は 1 ループの所要時間であるため制御周期 $T_{\rm c}$ に等しい．結果から分かるように，画像取得と処理計算がおよそ 25 ms の定周期で実行されている．次に，図 5.2-(b) の条件に準じて人為的に画像の更新を遅らせる．ここでは，50 ms 毎に一度だけ更新を行った結果を図 5.4-(b) に示す．この実験では制御周期が一定ではなく二分されていることが分かる．制御周期が人為的に変えられているために多少のばらつきはあるが，25 ms と 17〜19 μs の制御周期とに分かれる．以上から，$T_{\rm p}\approx 25$ ms，$T_{\rm m}\approx 18$ μs の同定結果を得る．なお，$T_{\rm cp}+T_{\rm tf}=5$ ms

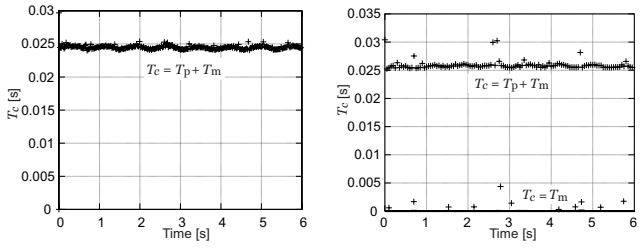

(a) $T_u = T_c$ (b) $T_u = 50$ ms

図 5.4: A wide gap in the control period, T_c, of a loop between the conditions of $T_c = T_p + T_m$ (図 5.2-(a)) and $T_c = T_m$ (図 5.2-(b)).

表 5.2: Four patterns of control period

updating period (T_u)	control period (T_c)	time interval
continuous (25 ms)	25 ms	constant
50 ms	25 ms (long period)	0〜25 ms
	18μs (short period)	25〜50 ms
75 ms	25 ms	0〜25 ms
	18μs	25〜75 ms
100 ms	25 ms	0〜25 ms
	18μs	25〜100 ms

であることから $T_{cm} \approx 20$ ms であることが分かる．他に，$T_u = 25$ ms と $T_u = 100$ ms の同定実験を行っている．それらと共にまとめると表 5.2 を得る．表から分かるように，画像更新遅れのある下側 3 つのパターンにおいて，画像取得を行っていない制御ループで制御周期が 18 μs のように極端に短くなっていることが確認できる．これは，画像取得と処理に費やす時間が省略されているため，結果的にモータ制御に限定した制御ループになっていることに因る．したがって，画像更新遅れが大きくなればなるほど，高速な制御周期でロボットを動作させる時間が必然的に長くなる．このように，画像更新遅れがある場合，可変な制御周期となっていることが分かる．次章以降では，以上のような制御パターンに基づいて，操りシミュレーションと実験を行う．

表 5.3: Simulation parameters

Parameters	Values	Parameters	Values
K_{P}	50 Nm	a	20 mm
K_{D}	1 Nm·sec	W_{obj}	50 mm
K_{I}	variable	M_{obj}	86 g
τ_{b}	3 Nm	M_i	88 g
L	76.2 mm	I_{obj}	12 kg·mm^2
$2W_{fi}$	98 mm	$I_{\mathrm{f}i}$	171 kg·mm^2

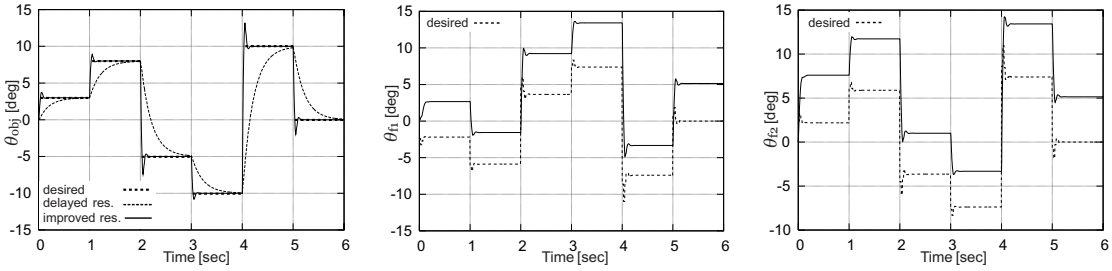

a) θ_{obj} (b) θ_{f1} and θ^*_{f1} (c) θ_{f2} and θ^*_{f2}

図 5.5: Orientation trajectory of a grasped object when $T_{\mathrm{u}} = T_{\mathrm{p}} + T_{\mathrm{m}}$.

5.5 操りシミュレーション

本章では，画像更新間隔を $T_{\mathrm{u}} = T_{\mathrm{p}} + T_{\mathrm{m}}$，$T_{\mathrm{u}} = 50$ ms，$T_{\mathrm{u}} = 75$ ms，$T_{\mathrm{u}} = 100$ ms の 4 通りに変化させたときの把持操りタスクの検証を行う．シミュレーションで用いる 2 指ロボットハンドのモデルには先行研究 [72, 75] で導出したモデルを用いる．2 指関節ベース間距離 $2W_{fi}$，指長 L，立方把持物体の一辺長さ W_{obj}，指先半径 a，物体重量 M_{obj}，物体慣性 I_{obj}，指重量 M_i，指慣性 $I_{\mathrm{f}i}$ をそれぞれ定義しそれらの値を表 5.3 に記す．また，操りタスクに適用される式 (5.2) と式 (5.3) で表される 2 段階制御則における各ゲイン K_{P}，K_{D} を同時に示している．ロボットに与えた操りタスクは把持物体の姿勢制御であり，1 sec 毎ステップ状に初期平行把持状態からカメラ側から見て反時計周りに 3°，8°，-5°，-10°，10°，0° の順で切り換えた．本タスクでは図 5.1 と式 (5.2)，式 (5.3) のようなセンサベーストの閉ループ制御則を施し，把持物体の姿勢をビジョンシステムによって精度良く計算可能であると仮定している．したがって，本制御手法において指先位置を求めるためのセンシングや運動学的手法による計算は行っていない．また，本タスクでは画像更新が行われていない間，物

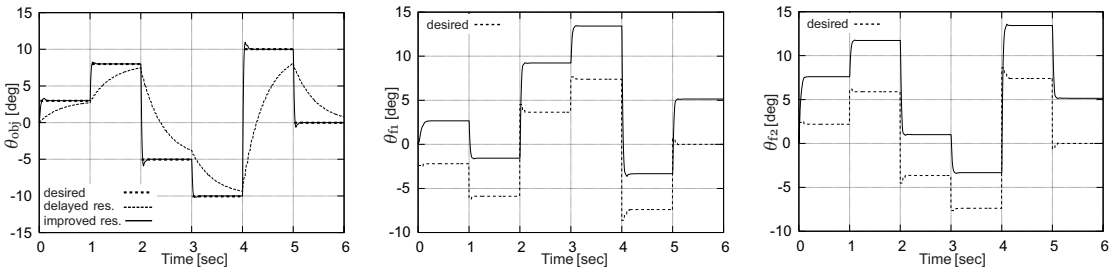

(a) $\theta_{\rm obj}$ (b) $\theta_{\rm f1}$ and $\theta^*_{\rm f1}$ (c) $\theta_{\rm f2}$ and $\theta^*_{\rm f2}$

図 5.6: Orientation trajectory of a grasped object when $T_{\rm u} = 50$ ms.

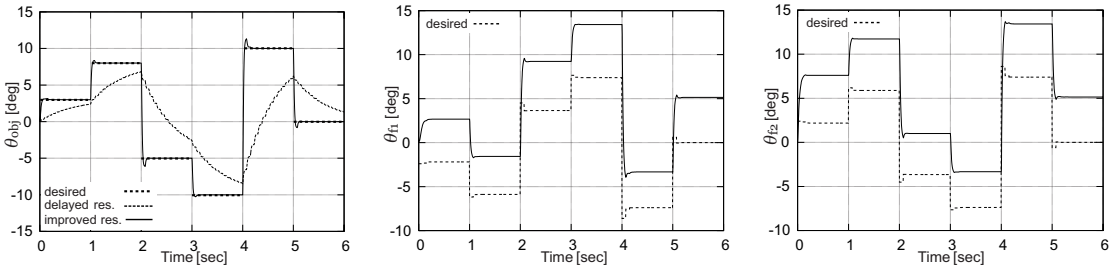

(a) $\theta_{\rm obj}$ (b) $\theta_{\rm f1}$ and $\theta^*_{\rm f1}$ (c) $\theta_{\rm f2}$ and $\theta^*_{\rm f2}$

図 5.7: Orientation trajectory of a grasped object when $T_{\rm u} = 75$ ms.

体姿勢も同様に更新されずに一定値となることに注意する．例えば，$T_{\rm u} = 100$ ms の場合，その 100 ms 間は常に直前で得られた物体姿勢がフィードバックされ目標値と比較される．つまり，最大で 100 ms 古い姿勢情報が目標値に返される．よって，その誤差に基づいて式 (5.2) の第 1 段制御器が動作することになる．

まず，伝達遅れのない例（$T_{\rm u} = T_{\rm p} + T_{\rm m}$）を図 5.5 に示す．図 5.5-(a) には与えたステップ状目標軌道（太い点線）と，ケーススタディとして試行錯誤的に選んだ $K_{\rm I} = 0.08$ の場合の改善前の例（細い点線），ならびに，その 10 倍である $K_{\rm I} = 0.8$ の場合の改善応答例（実線）を図示している．ここで，結果から，応答の改善に寄与したパラメータは積分ゲインのみであることが理解できる．第 1 段制御器（式 (5.2)）の積分ゲインのみを 10 倍することで，500 ms から 900 ms 要していた各時間ステップでの立ち上がり時間が劇的に改善されていることが分かる．この結果は，視覚情報処理を考慮したロボットシステムにおいて，その視覚情報を用いたフィードバック系を構築する場合，ゲインチューニングが容易であることを示唆する．次に，図 5.5-(b), (c) は，第 2 段目制御器（式 (5.3)） での両指関節角の偏差を示しており，図 5.5-(a) における改善例に対応するデータである．対象物姿勢が所望値に収束しているにもかかわらず，大きな定常偏差を残している．つまり，1 段目でターゲットとしている

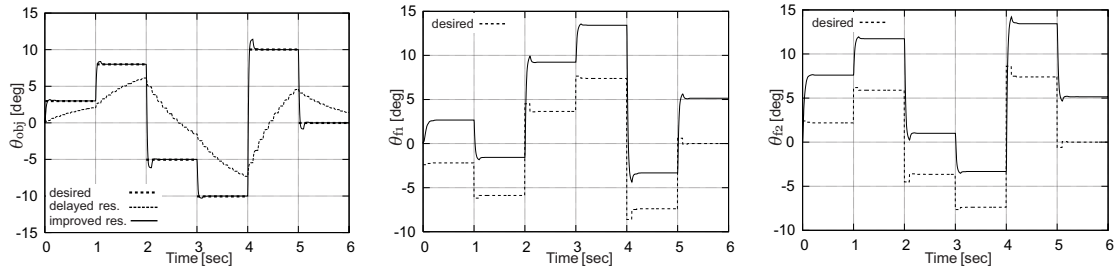

(a) $\theta_{\rm obj}$ (b) $\theta_{\rm f1}$ and $\theta^*_{\rm f1}$ (c) $\theta_{\rm f2}$ and $\theta^*_{\rm f2}$

図 5.8: Orientation trajectory of a grasped object when $T_{\rm u} = 100$ ms.

物体姿勢さえ収束させることができれば，両指の角度偏差は許容され得るものであると言える．したがって，2 段目制御器の役割は，把持物体の落下に直接結びつく負の把持トルクを発生させないことであり，PD 制御器で生じる可能性のある負のトルクを相殺するために定数バイアストルク $\tau_{\rm b}$ を印加している．次に，図 5.6 は $T_{\rm u}$ を 50 ms に設定した場合の結果である．なお，本稿のシミュレーションにおいては（図 5.5 〜図 5.8），積分ゲインに改善例として $K_{\rm I} = 0.8$ を，改善前の例として $K_{\rm I} = 0.08$ を一貫して利用している．図 5.6-(a) から分かるように，画像更新が 50 ms 遅れると，改善前の例では物体姿勢が 1 s 以降で目標値に達していない．さらに，4 s 〜 5 s では物体姿勢の目標軌道を− 10 °から＋ 10 °まで大きく変化させているため大きな定常偏差を残している．加えて改善例では，図 5.5 と同様に積分ゲインのみを 10 倍することで，著しく応答性能が向上している．また，第 1 段制御器で動的に生成される仮想的な目標関節角と実関節角を比較した図 5.6-(b), (c) においても同様に，”安定的な”定常偏差が顕著に現れている．さらには，画像更新時間を 75 ms まで遅らせた例（図 5.7）では，0 s 〜 1 s で示されている初期操り動作においても，目標値に到達できず偏差が生じている．また，改善前の例では更新遅れの増大に伴って階段状の不連続応答になっていることが見て取れる．さらに，改善例では図 5.5 や図 5.6 と比較すると，ステップ状目標軌道を与えているにもかかわらず，急峻な動きが徐々に目立たなくなっている．これは，更新遅れが 100 ms まで拡張された図 5.8-(a) の改善例において顕著である．これらの現象は両指関節角の挙動においても見受けられる．つまり，視覚情報の更新遅れが制御系に振動的振る舞いをもたらすのではなく，与えられたタスクにおいてむしろ”コンプライアントな”立ち上がり性能を実現しているのである．これらの結果には，解析モデルに用いられている柔軟指による対象物との面接触が寄与していると考えられる [45]．また，図 5.8 においては，積分ゲインが低いままの状態では応答曲線が階段状となりさらに悪化している．しかし，図 5.5〜図 5.7 の場合と同様に，積分ゲインのみを単純増加させることで応答を改善

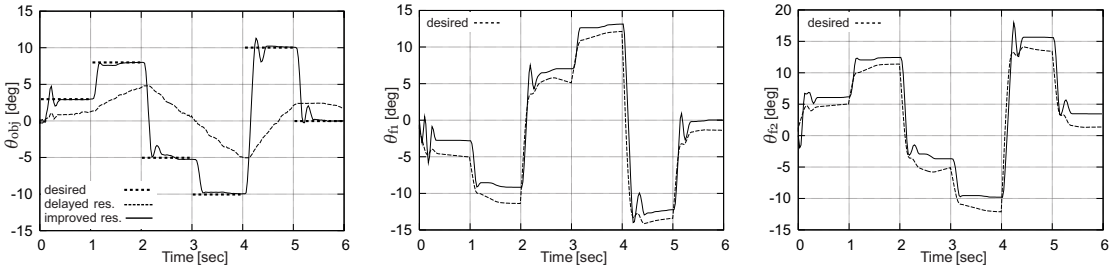

(a) θ_{obj} (b) θ_{f1} and θ^*_{f1} (c) θ_{f2} and θ^*_{f2}

図 5.9: Experimental results of orientation trajectory of a grasped object when $T_{\mathrm{u}} = T_{\mathrm{p}} + T_{\mathrm{m}}$, $K_{\mathrm{P}} = 40$, $K_{\mathrm{D}} = 0.001$. K_{I} is set at 12 in success and 1.2 in failure.

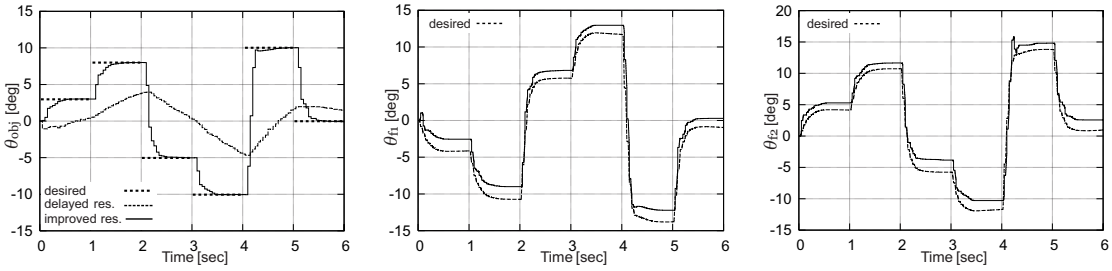

(a) θ_{obj} (b) θ_{f1} and θ^*_{f1} (c) θ_{f2} and θ^*_{f2}

図 5.10: Experimental results of orientation trajectory of a grasped object when $T_{\mathrm{u}} = 50$ ms, $K_{\mathrm{P}} = 60$, $K_{\mathrm{D}} = 0.001$. K_{I} is set at 0.02 in success and 0.002 in failure.

できている．以上のように，視覚情報遅れが存在するマシンビジョンシステムにおいてその遅れはもはや致命的ではなく，応答特性を”滑らかに鈍化”させ得るという意味で利点を持つと言える．これらの知見を検証するために，次章では柔軟指を配した 1 自由度対ロボットハンドを用いた操り実験を行う．

5.6 操り実験

5.6.1 ステップ入力に対する応答

本実験で利用する 2 指 1 自由度対ロボットハンドを図 5.3-(a) に示す．与えたタスクはシミュレーションと同様である．図 5.9 で与えた積分ゲインは，シミュレーションと同様にケーススタディとして成功例において $K_{\mathrm{I}} = 12$，改善前の例においては $K_{\mathrm{I}} = 1.2$ である．また，バイアストルクはすべての結果において $\tau_{\mathrm{b}} = 0.55$ Nm である．結果から分かるように，積分ゲインを 10 倍にすることで大きな定常偏差を含ん

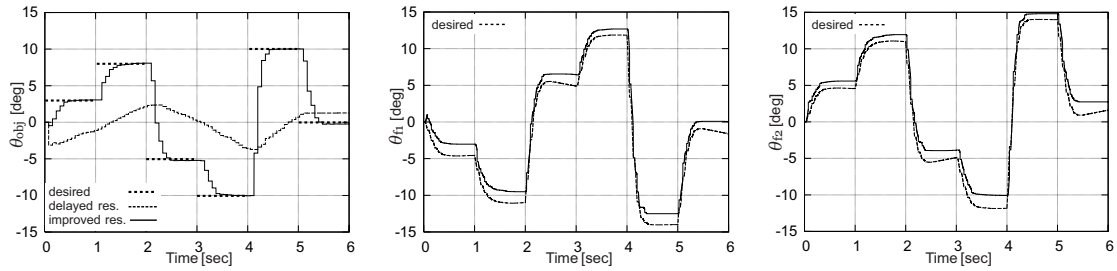

(a) θ_{obj} (b) θ_{f1} and θ^*_{f1} (c) θ_{f2} and θ^*_{f2}

図 5.11: Experimental results of orientation trajectory of a grasped object when $T_{\mathrm{u}} = 75$ ms, $K_{\mathrm{P}} = 60$, $K_{\mathrm{D}} = 0.001$. K_{I} is set at 0.01 in success and 0.001 in failure.

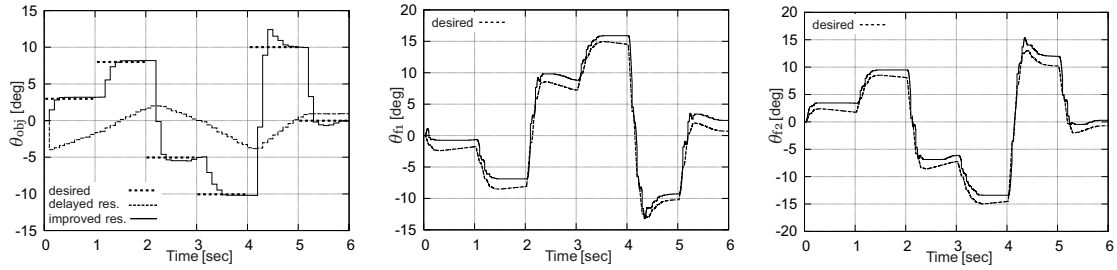

(a) θ_{obj} (b) θ_{f1} and θ^*_{f1} (c) θ_{f2} and θ^*_{f2}

図 5.12: Experimental results of orientation trajectory of a grasped object when $T_{\mathrm{u}} = 100$ ms, $K_{\mathrm{P}} = 60$, $K_{\mathrm{D}} = 0.001$. K_{I} is set at 0.008 in success and 0.0008 in failure.

だ応答を劇的に改善し，300 ms 以下の立ち上がり時間を達成している．また，更新周期が 25 ms から 100 ms のように著しく大きいために，図 5.9-(a) から図 5.12-(a) を概観すると成功例において徐々に反応が遅れ階段状の応答軌道が現れている．しかし，各ステップでの更新回数が明らかに少ないにもかかわらず，積分ゲインのみを増大させることによって目標値にロバストに追従していることが分かる．また，各タイムステップの初期に目標のステップ入力に対して，反応が他点より著しく遅れて出力されていることが分かる．データを観察するとすべての結果（図 5.9-(a)〜図 5.12-(a)）において，更新間隔の倍の時間分遅れて立ち上がりの開始が見られる．つまり，図 5.12-(a) では各ステップの初期に 200 ms 遅れて立ち上がっているように見える．シミュレーションではこの現象は見られない．この原因は，カメラによる画像取得と処理には T_{p} の実時間を要するが，その間プログラム内ではメモリへのアクセス処理を実行しているため，モータ制御信号を変化させることができないためである．図 5.12-(a) を例に挙げると，ある時刻で目標ステップが立ち上がり画像取得

と処理を終了した後にモータ制御コマンドが発生する．その直後に次ループでの画像取得と処理が始まるために，直前のモータ制御コマンドと画像取得開始との時間間隔がT_{m}となり，モータ駆動電圧の微小変化によって生じる物体位置姿勢の変化を画像として捉えることができない．その結果として，更新遅れ（$T_{\mathrm{u}} = 100$ ms）の倍の時間遅れることになる．次に，操り動作中の両指関節角の軌道を観察する．図 5.9〜図 5.12 の (b), (c) を見ると，シミュレーション結果と同様に，物体姿勢の収束性に関与しない”安定的な定常偏差”が現れている．これは，1 段目制御器と 2 段目制御器とが仮想的な関節角目標を介して動的に連動していることに起因する．つまり，ターゲットである物体姿勢が収束したときに初めて，最終的な関節角目標を決定するというアルゴリズムに起因する．結果的に，ビジュアルフィードバックに関わる 1 段目制御器の積分ゲインのみを単純に増加させることによって，視覚情報に関連する大幅な時間遅れが存在するシステムにおいて，把持物体の応答が著しく改善できることを示した．

5.6.2 正弦波入力に対する応答

次に，連続的な動的タスクに対する提案制御手法の効果を検証するために，周期 2 秒の正弦波を目標入力として印加する．そのときの実験結果を図 5.13-(b)，(d)，(f) に示し，比較のために図 5.13-(a)，(c)，(e) にシミュレーション結果を図示している．また，画像更新遅れT_{u}はすべて 25 ms で統一している．なお，それぞれのキャプションに積分ゲインを示している．

結果から分かるように，どちらの結果においても積分ゲインを単純増加させることで応答軌道が改善しており，速応性のみならず振幅に対する誤差が著しく改善している．このようなことから，本稿での 2 段階制御則における積分ゲインの調整（増加）が，ロボットハンドによる動的タスクにおいても制御性能を大きく向上させる主因であることが理解できる．他方，実験結果を観察すると，タスク開始時に比較的大きな振動的挙動が見受けられる．この原因は，タスク初期においては静止状態からの目標軌道入力になるため，それによって生じる静止摩擦による不感帯であると考えられる．実際，本稿で利用しているロボットシステムのギヤ減速比が 100 対 1 であることに起因する．以上のような観察を基に積分ゲインを増加させると図 5.13-(f) のように，急峻な振動が抑制され追従性が向上していることが分かる．また，実験において見受けられる階段状の応答は，前記した高減速比によるクーロン摩擦やモータの比線形特性によって引き起こされていると推察される．

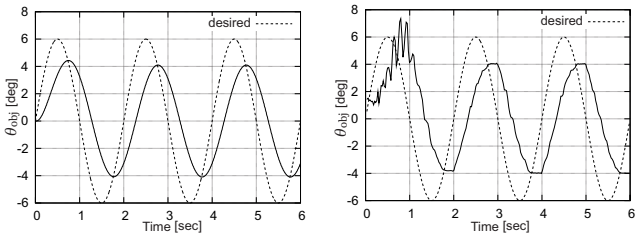

(a) $K_{\rm I} = 0.07$ (b) $K_{\rm I} = 0.4$

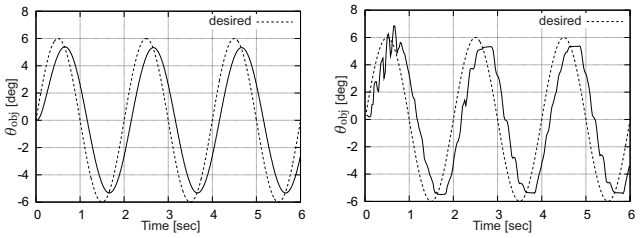

(c) $K_{\rm I} = 0.14$ (d) $K_{\rm I} = 0.8$

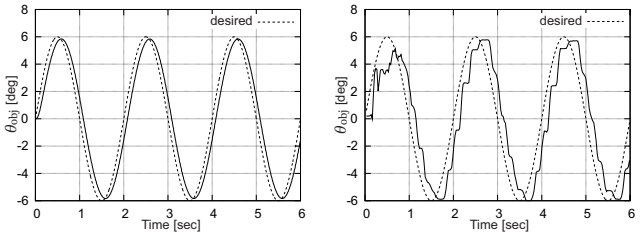

(e) $K_{\rm I} = 0.28$ (f) $K_{\rm I} = 1.2$

図 5.13: Simulations and experimental results of the response of object orientation in sinusoidal wave input.

5.6.3 考察

本節では，本稿で採用している 2 段階制御則の積分ゲインの増加が把持物体の軌道を劇的に改善する理由について，定性的な考察を加える．

まず，式 (5.2) と式 (5.3) をひとつにまとめると次式となる．

$$u_i \;=\; -(-1)^i K_{\rm P} K_{\rm I} \int_0^T (\theta_{\rm obj} - \theta^*_{\rm obj})\,{\rm dt} - K_{\rm P}\theta_{{\rm f}i} - K_{\rm D}\dot{\theta}_{{\rm f}i} + \tau_{{\rm b}i}. \qquad (5.4)$$

上式から分かることは，ロボットへの入力トルクが物体姿勢積分制御に起因するトルクと，関節角 PD 制御によるトルク，バイアストルクの 3 つの要素の線形和によって構成されていることである．以下ではまず，上式右辺の各トルクの役割について詳述する．

右辺第 1 項は 1 段目制御器に比例ゲイン K_{P} を掛けることで生成されるトルクである．この積分制御器は，”対向型ハンド”という把持形態の特徴を上手く利用している．例えば，把持物体を時計回りに回転させる場合，指先上での転がりを上手く利用すると，両指を同調して左回転するだけで良い．物体を反時計回りに回転させる場合は，その逆手順を採れば良い．このような簡単な操りアルゴリズムに基づいて，1 段目制御器が設計されている．したがって，式 (5.4) の第 1 項はどちらかの指で負値になり得る．最終的なロボットへの制御トルクが定常状態で $u_i > 0$ を満たさなければ把持は失敗するため，関節角比例制御器によるトルク（第 2 項）とバイアストルク（第 4 項）によって定常的に $u_i > 0$ を維持しなければならない．逆言すれば，上記条件を満たすように $K_{\mathrm{P}}, \tau_{\mathrm{b}i}$ を決定した上で，積分ゲイン K_{I} を調節（増加）することで姿勢追従性能の向上を図ることが可能になる．また，姿勢制御が積分器のみで構成されていることから，K_{I} の調節が速応性に直接的に寄与することになる．さらには，積分制御の制御工学的特徴を考慮すると，速応性のみならず定常偏差を解消する機能も併せ持つことになる．したがって，図 5.5 から図 5.12 までのすべての結果における改善前の例（安定把持はできるが操り動作の速応性が悪い）になるような K_{I} が存在する限り，その K_{I} を増加させることで，偏差のない姿勢追従が可能である．

以上のことから，続いて「柔軟指ハンドリングでの把持接触を保持する」という観点から制御則を観察する．柔軟指による把持操りタスクでは指先が容易にかつ大きく変形し得るため，指先と物体間で 2 次元的なマス・バネ・ダンパ系として考えることができ，指先と物体が柔軟接触を保っている限り安定的な把持が実現される．柔軟指が変形可能な分，剛体指によるハンドリングに比して，ゲインチューニングが容易であり安定把持を保つ指関節角の取り得る範囲が広い．その範囲内に指関節を維持することが，柔軟指による安定把持と操り動作には重要であることが分かる．当然，指先変形の増減はいわゆる把持力の強弱に相当することになる．ここで，制御則を再見する．式 (5.4) での関節角 PD 制御部分は見かけ上，局所的に 0 deg を目標値とした閉ループに相当する．一方で，式 (5.2) と式 (5.3) を見ると，1 段目で生成された目標関節角への動的な関節角追従制御であることが分かる．このように，目標値に関して相違なる 2 通りの解釈ができる場合考えるべきことは，従来の”目標値に収束させる”のではなく，”誤差を許容する”ことであると言える．つまり，関節角の定常偏差を残すように K_{P} を決定すれば良いことが理解できる．結局，前述したように，関節角度偏差が残ったとしても単純把持を成し得る範囲内に各関節角が入っていさえすれば良いことになる．単純把持の実現をバイアストルクと関節角制御器が担い，物体姿勢制御を 1 段目積分制御器が担うという独立的な制御構造になっていると結論付けることができる．他方，各種ゲインや制御パラメータの決定は，本

システムの閉ループダイナミクスにおける入出力間の受動性を検証することで行うことができる．

また，本研究で用いている柔軟指が視覚情報遅れの存在する制御系の安定性に大きな役割を果たす．柔軟指の受動的変形特性が指先と物体間の接触を滑らかにし，指関節やロボット全体の振動を抑制する（タスクスペースに伝えない）一種のローパスフィルタの役割を果たしている．しかも，柔軟指の形状に起因するエネルギー曲線（極小）が存在することが先行研究 [45, 72, 71] において明確になっており，両特性が視覚情報遅れのあるタスクを可能にしていると考えられる．

5.7 結言

本稿では，ヒトの視覚系情報伝達遅れを模擬したマシンビジョンシステムと柔軟指ロボットハンドシステムを組み合わせ，伝達遅れを仮定した画像更新周期が最大 100 ms 遅れた制御系において，タスクターゲットとしている把持物体の姿勢制御器のゲインパラメータを唯一増大させることで，著しく遅れた応答を容易にかつ劇的に改善できることを明らかにした．大幅な視覚系情報伝達遅れがある系におけるタスクの実現は，柔軟指の「柔らかさ」に起因するものであり，柔軟指は制御系設計を容易にする効果がある．100 ms という大幅な制御遅れを許容できると，カメラに起因する処理遅れ（T_{p}）を除いた 75 ms 間に他の様々なセンシング処理を実行でき，触知覚等の求心性神経路を模した別制御ループを画像取得ループとシリアルに接続できるメリットがある．今後は，上記したような視触覚融合ロボットシステムの小型化の具体的検討を行いたい．また，本研究で一貫して用いている柔軟指の力学特性が視覚情報遅れによる制御系にどのような影響を与えるのかをシミュレーションと実験両面から検証する予定である．さらには，本稿での 1 自由度対ハンドでは物体を操る範囲が狭いことから，より実用的なアプリケーションを想定した 2 指 5 自由度ハンドを開発し，提案制御則の検証を行う予定である．

2010 IEEE/ASME International Conference on
Advanced Intelligent Mechatronics
Montréal, Canada, July 6-9, 2010

Robotic Manipulation with Large Time Delay on Visual Feedback Systems

Takahiro Inoue and Shinichi Hirai

***Abstract*— A difference between the human and robots from the viewpoint of motor control is a sampling time in everyday movements. That is, the sampling time for controlling conventional robot systems is required to become approximately 1 ms. On the other hand, the motor control based on human nervous system permits considerably large time-delay due to the transmission latency on afferent/efferent pathways of the central nervous system. To date, it has been difficult for the robot to acquire dexterous tasks and precise movements as long as the robot system has an unexpected large delay in terms of sensory informations. Based on the above observation, this paper provides a new control strategy to accomplish precise orientation control of a target object grasped by a robotic hand consisting of two degrees-of-freedom (DOFs). The controller, named as *serial two-phased (STP)* controller, proposed in this study can realize secure grasping and manipulation in the case that a large visual feedback delay induced by the low specification of a camera is hiding in the control loop. Finally, through several simulations, we indicate that the closed loop dynamics designed by integrating the STP controller and a soft-fingertip structure is robust even in at most 100 ms-delay relating to the updating of camera images.**

I. Introduction

Generally, most robots show high performance and enormously high-speed motion than everyday movements of the human. For instance, present automation technology is able to accomplish 1 ms-periodic loop control because of high performance of the computer. On the other hand, if intrinsic neurophysiological latency that is expressed as a sum of central motor conduction time (CMCT) and neuromuscular transmission delay is applied to a controller designed for the robot, it is clear that certain fatal disadvantages occur in the robot control system. Fig. 1 shows a summary of the neurophysiological latency that stems from central nervous system (CNS) [1]. Based on these investigations, this paper proposes a novel and simple control law and demonstrates that stable and dexterous two soft-fingered manipulation can be achieved even under at most 100 ms-delay relating to the updating of camera images that are utilized for the visual feedback of the robot.

This work was supported in part by KAKENHI(20246049, 20860066, 22760191).

T.Inoue is with Faculty of Department of Systems Engineering for Sports, Computer Science and Systems Engineering, Okayama Prefectural University, 111 Kuboki, Soja, Okayama, 719-1197, Japan inoue@ss.oka-pu.ac.jp

S.Hirai is with the Laboratory for Integrated Machine Intelligence, and Faculty of Department of Robotics, Ritsumeikan University, Japan hirai@se.ritsumei.ac.jp

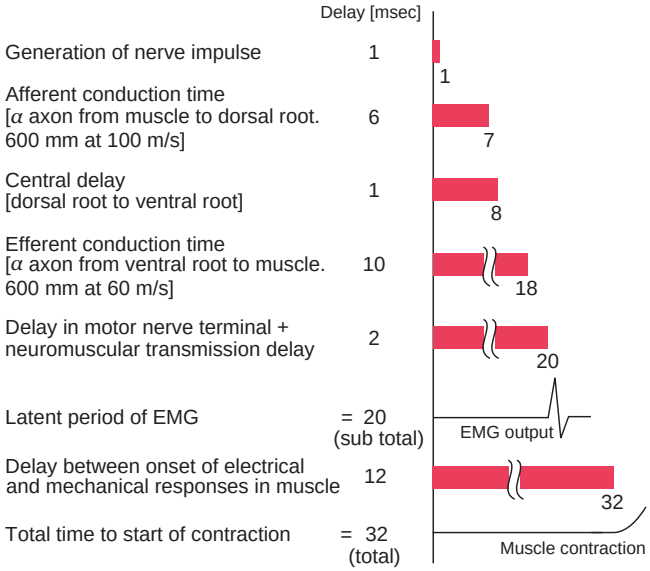

Fig. 1. The delay in latency from the stimulation to the onset of the CMAP is summarized with the exception of the optic [1]. This neurophysiological latency of human motor control is due to the sum of the nerve propagation delay, the neuromuscular transmission delay, and the muscle fiber propagation delay [2].

II. Equations of Motion of a Two-fingered Hand with Soft Fingers

Recalling a simple two degrees-of-freedom (2-DOFs) robotic hand structure (Fig. 2) from our previous studies [3], [4], Lagrangian of the hand can be rewritten as (Fig. 2)

$$\mathscr{L} = K - P + \sum_{i=1}^{2} \lambda_{\mathrm{n}i} C_{\mathrm{n}i}, \tag{1}$$

where K and P be the kinetic energy of the total system and be the potential energy including not only gravitational potential but also elastic energy induced by deformation of the soft fingertip, as shown in Fig. 2. Therefore, K and P can be finally described as [3]

$$P = P_1(d_{\mathrm{n}1}, d_{\mathrm{t}1}, \theta_{\mathrm{o}}, \theta_1) + P_2(d_{\mathrm{n}2}, d_{\mathrm{t}2}, \theta_{\mathrm{o}}, \theta_2) + M_{\mathrm{o}} g y_{\mathrm{o}} + \sum_{i=1}^{2} M_i g L \cos\theta_i, \tag{2}$$

$$K = \frac{1}{2} M_{\mathrm{o}} (\dot{x}_{\mathrm{o}}^2 + \dot{y}_{\mathrm{o}}^2) + \frac{1}{2} I_{\mathrm{o}} \dot{\theta}_{\mathrm{o}}^2 + \frac{1}{2} \sum_{i=1}^{2} I_i \dot{\theta}_i^2 + \frac{1}{2} m \sum_{i=1}^{2} \dot{d}_{\mathrm{n}i}^2 + \frac{1}{2} m \sum_{i=1}^{2} \dot{d}_{\mathrm{t}i}^2. \tag{3}$$

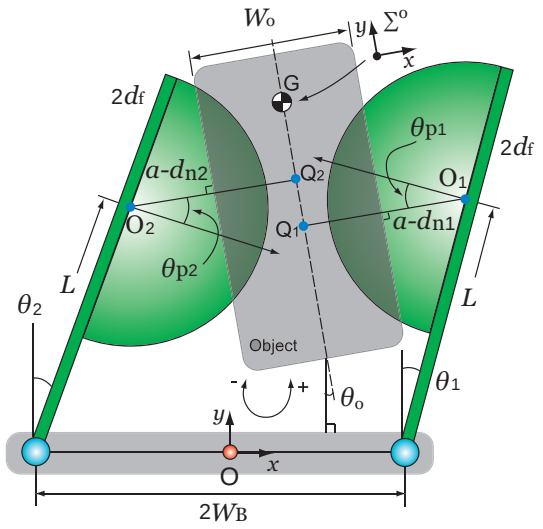

Fig. 2. Soft-fingered manipulation by a pair of 1-DOF rotational joints.

TABLE I

DEFINITIONS OF PARAMETERS.

parameter	definition
$2W_B$	base width of the hand
a	fingertip radius
L	length of each finger
d_f	thickness of the finger
W_o	width of object
M_o	mass of object
M_i	mass of i-th finger
m	mass of fingertip
θ_i	joint angle of i-th finger
θ_o	orientation angle of object
θ_{pi}	$(\theta_i+(-1)^i\theta_o)$
d_{ni}	maximum displacement of i-th fingertip
d_{ti}	tangential displacement of i-th fingertip
x_o, y_o	position of object
I_o	inertia of object
I_i	inertia of the finger

where parameters of the system are defined in Table I. In addition, the last term of the right-hand side of Eq. (1) corresponds to energy due to constraint forces, λ_{ni}, which appear on the contact between object and soft fingertips. Differentiating geometric constraints, C_{ni}, with respect to system variables, the direction of λ_{ni} that is dynamically changed during the manipulation motion can be clarified. As a result, the equations of motion of whole system are described as

$$\frac{\mathrm{d}}{\mathrm{d}t}\frac{\partial \mathscr{L}}{\partial \dot{\boldsymbol{q}}} - \frac{\partial \mathscr{L}}{\partial \boldsymbol{q}} = \sum_{i=1}^{2} \lambda_{ti}\frac{\partial \dot{C}_{ti}}{\partial \dot{\boldsymbol{q}}} + \boldsymbol{f}_{\mathrm{ext}} + \boldsymbol{u}, \tag{4}$$

where external force vector and control input vector are newly added. Note that the input, $\boldsymbol{u}$, corresponds to input torque applied to the joint angle of the finger. The first term on the right-hand side of Eq. (4) denotes constraint forces tangential to the grasped object.

III. CONTROL STRATEGY

First, we introduce a very simple controller for achieving precise object manipulation, which is named *serial two-phased (STP)* controller in this paper [5], and recall

$$\theta_i^{\mathrm{d}} = -(-1)^i K_{\mathrm{I}} \int_0^t (\theta_{\mathrm{o}} - \theta_{\mathrm{o}}^{\mathrm{d}})\mathrm{d}\tau, \tag{5}$$

$$u_i = -K_{\mathrm{P}}(\theta_i - \theta_i^{\mathrm{d}}) - K_{\mathrm{D}}\dot{\theta}_i + \tau_{\mathrm{b}}, \tag{6}$$

where K_{P}, K_{D}, and K_{I} denote proportional, differential, and integral gain respectively. This controller can perform precise position and orientation control of grasped object even when the robotic hand has minimal degrees-of-freedom shown in Fig. 2 [3]. The block diagram of the STP controller can be simplified as Fig. 3. In addition, the biased torque, τ_{b}, has a positive constant value and acts to prevent that the motor torque u_i produced in Eq. (6) remains negative.

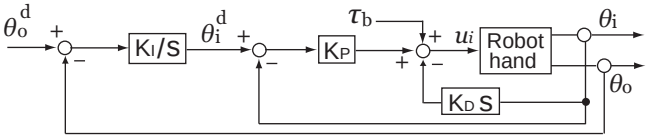

Fig. 3. It shows a block diagram of *serial two-phased (STP)* controller capable of achieving robust convergence of object orientation, which is grasped by two soft fingertips. Characteristic of this controller is that desired trajectory of the joint angle in second stage (Eq. (6)) is serially coupled and remains constant when the object orientation goes to convergence.

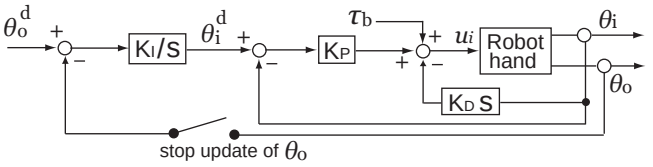

Fig. 4. It shows a block diagram of STP controller, in which the updating delay of information that results from image processing computation contains.

Through this research, we have consistently carried out object-orientation control in two-fingered robotic hand. Especially, in simulation studies, the real-time trajectory of the grasped object, θ_o in Eq. (5), has been computed on the basis of assuming minimal periodic time defined in the numerical computation. That is, the orientation trajectory to be used in the feedback loop could be updated according to the periodic time of Runge-Kutta method, i.e., 0.1 ms. Hence, this paper introduces true time-delay induced by the image processing in the visual feedback robotic system.

IV. SIMULATIONS

In this paper, we verify a case that the updating delay of information obtained by image processing exists on visual feedback control system, as shown in Fig. 4. Usually, conventional machine vision systems have inevitable time-delay such as 33 ms as video frame rate. In this simulation, we show successful results of object orientation control under the case that the time-delay increases up to 99 ms.

In our previous studies, we had demonstrated that the serial two-phased (STP) controller (Fig. 3) works well so as to make the grasped object converge to a desired trajectory, and obtained a successful result shown in Fig. 5. This simulation

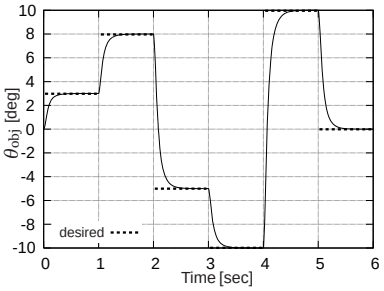

Fig. 5. This simulation result shows a successful convergence of the object-orientation trajectory, where the periodic time of image updating is 0.1 ms because of the numerical computation with Runge-Kutta method.

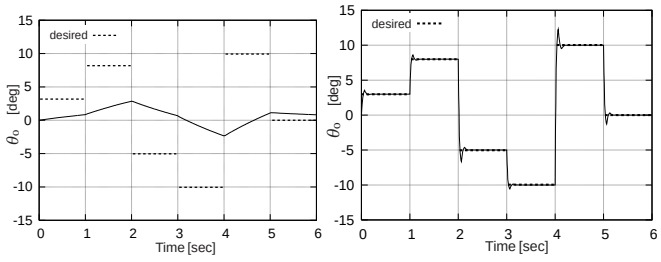

(a) before improvement (b) after improvement

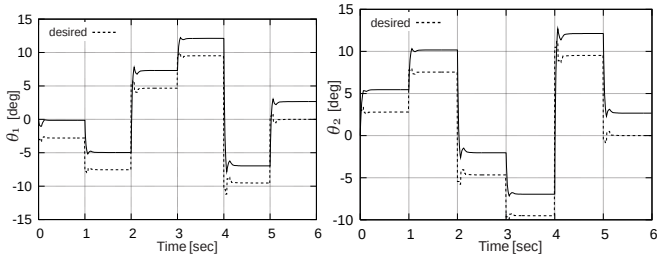

(c) θ_1 vs. $\theta_1^{\rm d}$ (d) θ_2 vs. $\theta_2^{\rm d}$

Fig. 6. This result shows an improved trajectory of the object orientation, in which the periodic time of image updating is assumed to be 33 ms. In this result, we set the integral gain to be $K_{\rm I} = 0.01$ in the case of failure (a), and to be $K_{\rm I} = 1$ in the successful result (b). In addition, it implies that the joint angle does not converge to each desired trajectory produced in Eq. (5). That is, the desired angle, $\theta_i^{\rm d}$, corresponds to virtual desired trajectory. Note that mechanical parameters and values for the controller is expressed in Table II.

result indicates robust and fast convergence in terms of the object orientation. However, the periodic time of the control loop complies with the condition of numerical computation, which corresponds to the step size of Runge-Kutta method, i.e., 0.1 ms. Obviously, there does not exist such an extremely fast periodic control combined with image processing.

On the other hand, we show another successful result shown in Fig. 6, in which the periodic time of image updating is assumed to be 33 ms. In fact, this improved trajectory was obtained by only changing the integral gain from 0.01 to 1. Thus, we can verify a very simple gain-tuning method such as the STP controller for object manipulation. In addition, we show another result obtained when the updating delay be 99 ms, in which the dynamic response of the object orientation was drastically improved by only modifying the integral gain from $K_{\rm I} = 0.01$ to $K_{\rm I} = 1$. This successful result

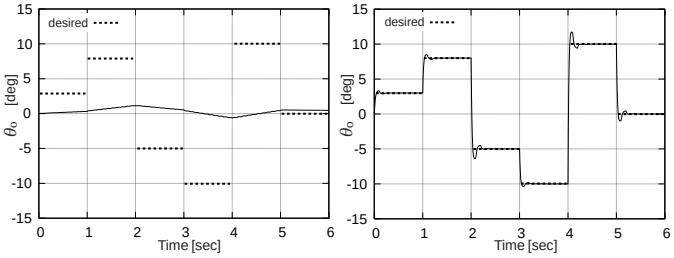

(a) before improved (b) after improved

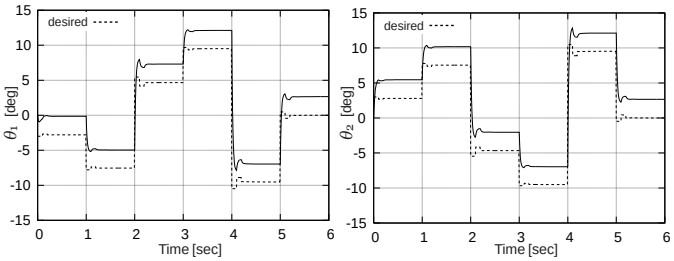

(c) θ_1 vs. $\theta_1^{\rm d}$ (d) θ_2 vs. $\theta_2^{\rm d}$

Fig. 7. This result shows an improved trajectory of the object orientation, in which the periodic time of image updating is assumed to be 99 ms. In this result, we set the integral gain to be $K_{\rm I} = 0.01$ in the case of failure (a), and to be $K_{\rm I} = 1$ in the successful result (b).

TABLE II

MECHANICAL AND SIMULATION PARAMETERS.

parameter	value
$W_{\rm B}$	98 mm
a	20 mm
L	76.2 mm
$d_{\rm f}$	4 mm
$W_{\rm o}$	50 mm
$M_{\rm o}$	86 g
M_i	88 g

parameter	value
$I_{\rm o}$	12 kg·mm^2
I_i	171 kg·mm^2
$K_{\rm P}$	50
$K_{\rm D}$	1
$\tau_{\rm b}$	3 Nm
m,m	10 g

comes from the fact that passive deformation of the soft fingers contributes to stable rotation of the object grasped by them. Further explanations of the successful grasping are detailed in Sec.VI.

V. EXPERIMENTS

As well as the simulation, we give same task to the soft-fingered robotic hand that is designed as opposed structure by two fingers, as shown in Fig. 8-(a) and Fig. 2. In this experiment, we utilize a CCD camera capable of capturing a gray-scale image with keeping 200 fps (frame per second). Continuously, the image grabbed is processed to converse to a binary image and the object orientation can finally be computed as Fig. 8-(b). As a result, this algorithm can obtain object position and orientation at the interval of 5 ms. Therefore, we intentionally slow the update of the object information used for feedback control, that is, the update timing becomes once per twenty times to simulate 100-ms updating delay.

Fig. 9 shows an experimental result, in which the desired trajectory of the object orientation, the delayed response, and the improved response are depicted. It is obvious that the orientation trajectory of the grasped object is dramatically improved by only changing the integral gain. However, the

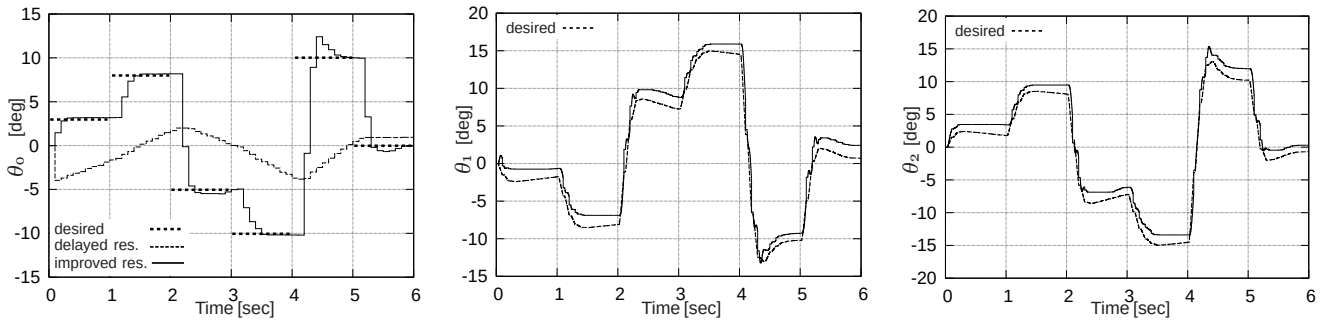

(a) θ_{o} (b) θ_1 and θ_1^{d} (c) θ_2 and θ_2^{d}

Fig. 9. It shows an experimental result of the orientation trajectory of the grasped object, where the updating delay is equivalent to 100 ms. Gain parameters were decided as $K_{\mathrm{P}} = 60$, $K_{\mathrm{D}} = 0.001$. As well as the simulation result, the orientation trajectory has been dramatically improved by only changing K_{I} from 0.0008 to 0.008.

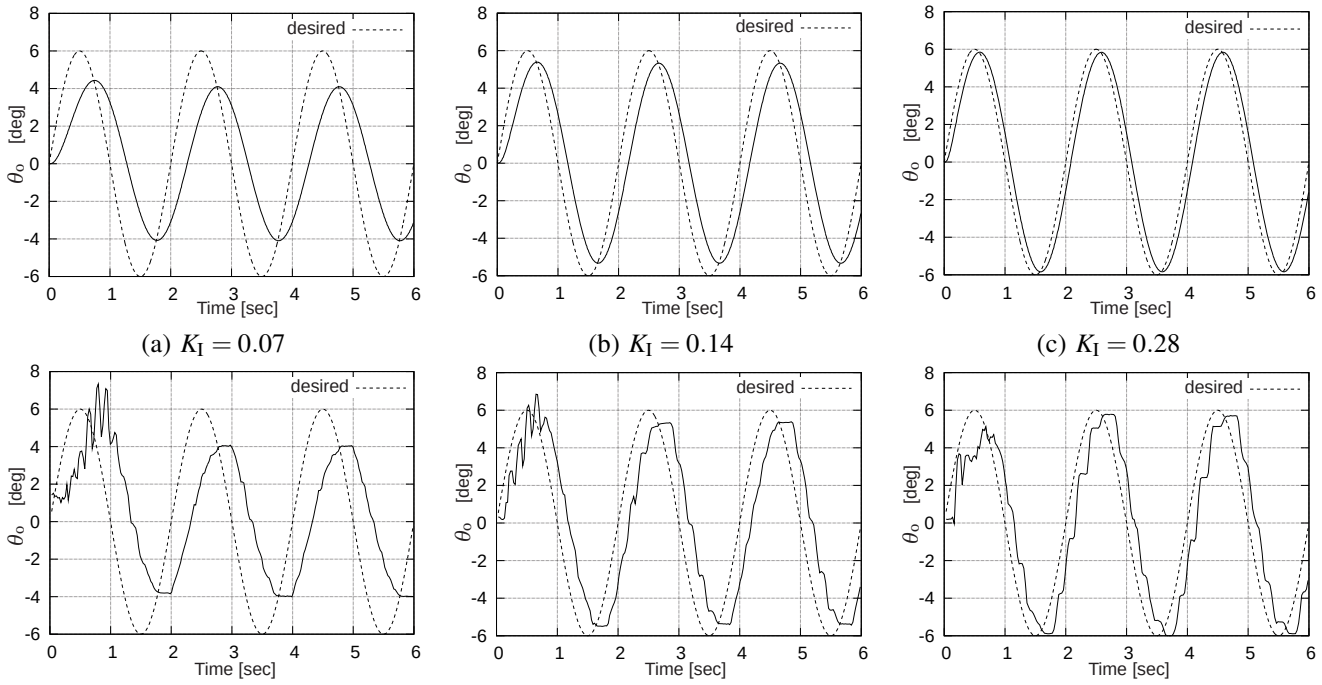

(a) $K_{\mathrm{I}} = 0.07$ (b) $K_{\mathrm{I}} = 0.14$ (c) $K_{\mathrm{I}} = 0.28$

(d) $K_{\mathrm{I}} = 0.4$ (e) $K_{\mathrm{I}} = 0.8$ (f) $K_{\mathrm{I}} = 1.2$

Fig. 10. Sinusoidal wave input for the desired object orientation, $\theta_{\mathrm{o}}^{\mathrm{d}}$, is given to the robotic system. In simulations (a)–(c), the performance of tracking control is gradually improved as the integral gain increases. Also in experiments (d)–(f), the same trend occurs, however the response in the initial state clearly indicates oscillatory appearance.

TABLE III

SPECIFICATIONS IN THE VERIFICATION TEST

Camera model	Point Gray Research, Dragonfly Express
Interface	IEEE 1394b (FireWire)
Imaging sensor	Progressive scan CCD
Resolution	VGA Gray-scale image
Frame Rates	200 fps (Format 7 mode)
PC spec.	Pentium 4 1.9 GHz
FSB & Cache	400 MHz, 256 KB
Memory	512 MB DDR 400 MHz × 1
OS	Vine Linux 3.2 (kernel 2.4.31) Non-RT

improved trajectory tends to become step-like response because of the large time delay. In addition, it is clearly clarified that the discrepancy of joint angles remains throughout the manipulation. In other words, this consistent error does not have to be eliminated as long as the object orientation converges to the desired trajectory, that is, θ_i^{d} corresponds to apparent desired trajectory in the STP controller.

Next, we show another simulation and experimental results shown in Fig. 10, where the sinusoidal desired input for the object orientation, $\theta_{\mathrm{o}}^{\mathrm{d}}$, is given in Eq. (5), and the updating delay is equivalent to 25 ms consistently. It is clearly indicated that the performance of tracking control is gradually improved as the integral gain increases in the both cases of simulation and experiment. In the experimental result, the step-like response starts to increase gradually. This result comes from the fact that nonlinearity due to Coulomb friction of the finger joint appears obviously when the joint torque increases according to the change of the integral gain.

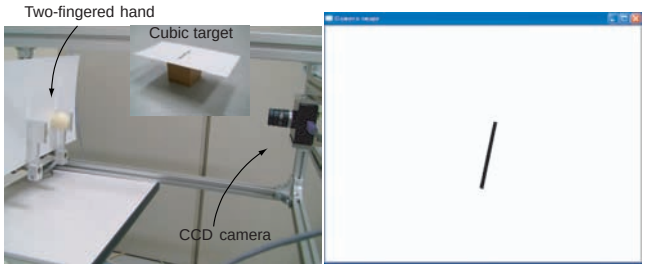

(a) total view (b) binary image

Fig. 8. It shows a two fingered robotic hand system with a CCD camera and binary image of the object orientation.

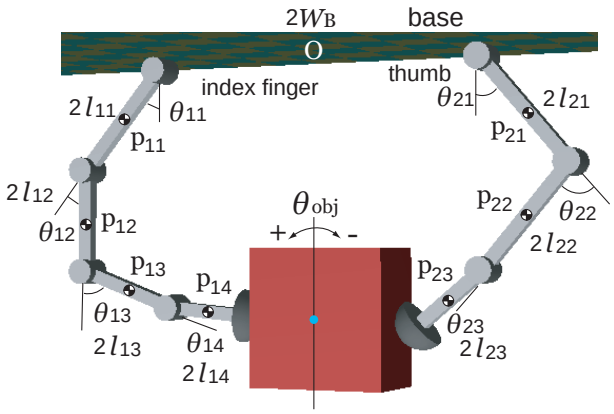

Fig. 11. It shows a five degrees-of-freedom robotic hand that consists of an index finger and a thumb. This system has also a pair of soft fingertips on the fore-end of each finger.

In addition, the response in the initial state of experimental results clearly indicates oscillatory appearance. This reason is that the response becomes to be particularly-susceptible to static friction when the angular velocity of the joint reduces.

VI. Discussions

The performance of robust trajectory tracking shown in all simulations and experiments results from passive flexibility of soft fingers and opposing structure of both fingers on two dimensional plane shown in Fig. 2. Soft fingers have such a superior mechanical characteristic that the grasped object comes to rest on a mechanically stable orientation during the manipulation. That is, the potential energy function has a minimal value with respect to the object orientation, θ_o, as expressed in Eq. (3) [4]. This mechanical feature has never been clarified, thereby, a relatively complicated control law had been proposed to date even though the soft finger was utilized in the robotic manipulation [6]. These control laws require a torque to prevent unexpected rotation of the grasped object. In contrast, the unstable rotation of the object never occurs in the soft-fingered manipulation because of the presence of the minimum of elastic potential energy.

In addition, the STP controller proposed contains no Jacobian matrix. Recently, we had obtained a similar result in a 5-DOFs robotic hand that consists of an index finger and a thumb, as shown in Fig. 11. In this case, in order to achieve the object orientation control, it is favorable that two links located at the side of the base of both fingers generate counter coupled movement. This corresponds to a kind of mechanical constraint, therefore, Jacobian matrix used in the case of individual joint control is not necessary. This contribution and its detail will be presented in the next paper.

VII. Concluding Remarks

This paper has proposed a simple object orientation controller that consists of two-phased controllers being serially connected each other, which is named STP controller expressed in Eqs. (5) and (6). The first stage acts as robust integral controller from which virtual desired trajectories of joint angles is generated. The actual joint angle is not necessary to converge to the virtually-generated joint angle as long as the object converges to a desired orientation of the first phase. This is why the desired joint angle is named *virtual trajectory*.

In addition, this paper has clarified that the STP controller with soft fingers works well in the case that large time delay exists within visual feedback robotic systems. It has also been shown that the method of gain tuning for improving delayed responses is very simple and useful in a lot of practical usage.

In future works, we are going to present theoretical verification associated with the stability of the STP controller by describing a Lyapunov function.

References

[1] O. Holmes, "Human Neurophysiology", *Unwin Hyman*, 1990.
[2] S.R. Devasahayam, "Signals and Systems in Biomedical Engineering", *Plenum Pub Corp*, 2000.
[3] T.Inoue and S.Hirai, "Mechanics and Control of Soft-fingered Manipulation", *Springer-Verlag, London*, 2008.
[4] T. Inoue and S. Hirai, "Elastic Model of Deformable Fingertip for Soft-Fingered Manipulation", *IEEE Trans. Robotics*, Vol.22, No.6, pp.1273–1279, 2006.
[5] T. Inoue and S. Hirai, "A Two-phased Object Orientation Controller on Soft Finger Operations", *Proc. of IEEE Int. Conf. Intelligent Robots and Systems*, pp.2528–2533, 2007.
[6] S. Arimoto, K. Tahara, M. Yamaguchi, P. Nguyen, and H. Y. Han, "Principle of superposition for controlling pinch motions by means of robot fingers with soft tips", *Robotica*, Vol.19, No.1, pp.21–28, 2001.

参考文献

[1] D. Terzopoulos, J. Platt, A. Barr, and K. Fleischer. Elastically deformable models. *Proc. 14th Annual Conference on Computer Graphics and Interactive Techniques (SIGGRAPH '87)*, pages 205–214, 1987.

[2] D. Terzopoulos and K. Fleischer. Modeling inelatic deformation: viscoelasticity, plasticity, fracture. *Proc. 15th Annual Conference on Computer Graphics and Interactive Techniques (SIGGRAPH '88)*, pages 269–278, 1988.

[3] K. Waters. A muscle model for animating three-dimensional facial expression. *Proc. 14th Annual Conference on Computer Graphics and Interactive Techniques (SIGGRAPH'87)*, 21:17–24, 1987.

[4] S. Cotin, H. Delingette, M. Bro-Nielsen, N. Ayache, J.M. Clément, V. Tassetti, and J. Marescaux. Geometric and physical representations for a simulator of hepatic surgery. *Proc. Medicine Meets Virtual Reality*, pages 139–151, 1996.

[5] D. Baraff and A. Witkin. Large steps in cloth simulation. *Proc. 25th Annual Conference on Computer Graphics and Interactive Techniques (SIGGRAPH'98)*, pages 43–54, 1998.

[6] K. Kähler, J. Haber, and H.-P. Seidel. Geometry-based muscle modeling for facial animation. *Proc. of Graphics Interface*, pages 37–46, 2001.

[7] B.A. Lioyd, G. Székely, and M. Harders. Identification of spring parameters for deformable object simulation. *IEEE Trans. Vis. Comput. Graph.*, pages 1081–1094, 2007.

[8] G. Bianchi, B. Solenthaler, G. Székely, and M. Harders. Simultaneous topology and stiffness identification for mass-spring models based on fem reference deformations. *Proc. 7th International Conference on Medical Image Computing and Computer-Assisted Intervention (MICCAI'04)*, pages 293–301, 2004.

[9] B. Ahn and J. Kim. Measurement and characterization of soft tissue behavior with surface deformation and force response under large deformations. *Med. Image Anal.*, 14:138–148, 2010.

[10] J.E. Bischoff, E.M. Arruda, and K. Grosh. Finite element modeling of human skin using an isotropic, nonlinear elastic constitutive model. *J. Biomech.*, 33:645–652, 2000.

[11] A. Nava, E. Mazza, M. Furrer, P. Villiger, and W.H. Reinhart. In vivo mechanical characterization of human liver. *Med. Image Anal.*, 12:203–216, 2008.

[12] M. Kauer, V. Vuskovic, J. Dual, G. Szekely, and M. Bajka. Inverse finite element characterization of soft tissues. *Med. Image Anal.*, 6:275–287, 2002.

[13] J.T. Hing, A.D. Brooks, and J.P. Desai. A biplanar fluoroscopic approach for the measurement, modeling, and simulation of needle and soft-tissue interaction. *Med. Image Anal.*, 11:62–78, 2007.

[14] C. Mendoza and C. Laugier. Simulating soft tissue cutting using finite element models. *Proc. the 2003 IEEE International Conference on Robotics and Automation (ICRA'03)*, pages 1109–1114, 2003.

[15] M. Bro-Nielsen and S. Cotin. Real-time volumetric deformable models for surgery simulation using finite element and condensation. *Computer Graphics Forum (EUROGRAPHICS'96)*, pages 57–66, 1996.

[16] M. Bro-Nielsen. Finite element modeling in surgery simulation. *Proc. IEEE*, 86:490–503, 1998.

[17] Z.A. Taylor, O. Comas, M. Cheng, J. Passenger, D.J. Hawkes, D. Atkinson, and S. Ourselin. On modelling of anisotropic viscoelasticity for soft tissue simulation: numerical solution and GPU execution. *Med. Image Anal.*, 13:234–244, 2009.

[18] R. Balaniuk and K. Salisbury. Soft-tissue simulation using the radial elements method. *Surgery simulation and soft tissue modeling*, pages 48–58, 2003.

[19] Y.-J. Lim and Suvranu De. Real time simulation of nonlinear tissue response in virtual surgery using the point collocation-based method of finite spheres. *Comput. Methods Appl. Mech. Engrg.*, 196:3011–3024, 2007.

[20] Z. Liu and M.G. Scanlon. Modelling indentation of bread crumb by finite element analysis. *Biosyst. Eng.*, 85:477–484, 2003.

[21] E. Purlis and V.O. Salvadori. Meat cooking simulation by finite elements. *2nd Mercosur Congress on Chemical Engineering and 4th Mercosur Congress on Process Systems Engineering*, pages 1–10, 2005.

[22] R.C. Martins. Simple finite volumes and finite elements procedures for food quality and safety simulations. *J. Food Eng.*, 73:327–338, 2006.

[23] M. Hrapko, J.A.W. van Dommelen, G.W.M. Peters, and J.S.H.M. Wismans. The mechanical behaviour of brain tissue: Large strain response and constitutive modelling. *Biorheology*, 43:623–636, 2006.

[24] P.Y. Chua, T. Ilschner, and D.G. Caldwell. Robotic manipulation of food products—a review. *Ind. Robot*, 30:345–354, 2003.

[25] I.H. Shames and F.A. Cozzareli. *Elastic and Inelastic Stress Analysis*. Englewood, New Jersey, 1992.

[26] E. Samur, M. Sedef, C. Basdogan, L. Avtan, and O. Duzgun. A robotic indenter for minimally invasive measurement and characterization of soft tissue response. *Med. Image Anal.*, 11:361–373, 2007.

[27] M. Tada, N. Nagai, and T. Maeno. Material properties estimation of layered soft tissue based on MR observation and iterative FE simulation. *Medical Image Computing and Computer-Assisted Intervention (MICCAI'05)*, 3750:633–640, 2005.

[28] K.F. Augenstein, B.R. Cowan, I.J. LeGrice, P.M.F. Nielsen, and A.A. Young. Method and apparatus for soft tissue material parameter estimation using tissue tagged magnetic resonance imaging. *J. Biomech. Eng.-Trans. ASME*, 127:148–157, 2005.

[29] T. Ikawa and H. Noborio. On the precision and efficiency of hierarchical rheology MSD model. *Proc. the 2007 IEEE/RSJ International Conference on Intelligent Robots and Systems (IROS'07)*, pages 376–383, 2007.

[30] T. Hoshi, Y. Kobayashi, K. Kawamura, and M.G. Fujie. Developing an intraoperative methodology using the finite element method and the extended kalman filter to identify the material parameters of an organ model. *Proc. the 29th Annual International Conference of the IEEE EMBS*, pages 469–474, 2007.

[31] M. Farshad, M. Barbezat, P. Flüeler, F. Schmidlin, P. Graber, and P. Niederer. Material characterization of the pig kidney in relation with beh biomechanical analysis of renal trauma. *J. Biomech.*, 32:417–425, 1999.

[32] N. Sakamoto, M. Higashimori, T. Tsuji, and M. Kaneko. An optimum disign of robotic hand for handling a visco-elastic object based on Maxwell model. *Proc. the 2007 IEEE International Conference on Robotics and Automation (ICRA'07)*, pages 1219–1225, 2007.

[33] C-H.D. Tsai, I. Kao, N. Sakamoto, M. Higashimori, and M. Kaneko. Applying viscoelastic contact modeling to grasping task: an experimental case study. *Proc. the 2008 IEEE/RSJ International Conference on Intelligent Robots and Systems (IROS'08)*, pages 1790–1795, 2008.

[34] H. Noborio, R. Enoki, S. Nishimoto, and T. Tanemura. On the calibration of deformation model of rheology object by a modified randomized algorithm. *Proc. IEEE International Conference on Robotics and Automation (ICRA'03)*, pages 3729–3736, 2003.

[35] R. Nogami, H. Noborio, F. Ujibe, and H. Fujii. Precise deformation of rheologic object under MSD models with many voxels and calibrating parameters. *Proc. IEEE International Conference on Robotics and Automation (ICRA'04)*, pages 1919–1926, 2004.

[36] H. Yoshida, Y. Murata, and H. Noborio. A smart rheologic MSD model pushed/calibrated/evaluated by experimental impulses. *Proc. IEEE/RSJ International Conference on Intelligent Robots and Systems (IROS'05)*, pages 269–276, 2005.

[37] R. Nogami, H. Noborio, S. Tomokuni, and S. Hirai. A comparative study of rheology MSD models whose structures are lattice and truss. *Proc. IEEE/RSJ International Conference on Intelligent Robots and Systems (IROS'04)*, pages 3809–3816, 2004.

[38] Y.-H. Chai, G.R. Luecke, and J.C. Edwards. Virtual clay modeling using the ISU exoskeleton. *Proc. IEEE Virtual Reality Annual International Symposium (VRAIS '98)*, pages 76–80, 1998.

[39] H. Yoshida, F. Ujibe, and H. Noborio. Force/shape reappearance of MSD rheology model calibrated by force/shape sequence. *17th International Conference on Artificial Reality and Telexistence 2007*, pages 121–128, 2007.

[40] H. Mirsaeedghazi, Z.E. Djomeh, and S.M.A. Mousavi. Rheometric measurement of dough rheological characteristics and factors affecting it. *Int. J. Agri. Biol.*, 10:112–119, 2008.

[41] H.P. Sivaramakrishnan, B. Senge, and P.K. Chattopadhyay. Rheological properties of rice dough for making rice bread. *J. Food Eng.*, 62:37–45, 2004.

[42] M. Wu, D. Li, L.J. Wang, N. Özkan, and Z.H. Mao. Rheological properties of extruded dispersions of flaxseed-maize blend. *J. Food Eng.*, 98:480–491, 2010.

[43] Z. Wang and S. Hirai. Modeling and parameter identification of rheological object based on fe method and nonlinear optimization. *Proc. IEEE/RSJ International Conference on Intelligent Robots and Systems (IROS '09)*, pages 1968–1973, 2009.

[44] J. Baumgarte. Stabilization of constraints and integrals of motion in dynamical systems. *Computer Methods in Applied Mechanics and Engineering*, pages 1–16, 1972.

[45] Takahiro Inoue and Shinichi Hirai. Elastic model of deformable fingertip for soft-fingered manipulation. *IEEE Transactions on Robotics*, 22(6):1273–1279, 2006.

[46] Kazumi Endo, Penglin Zhang, Shinichi Hirai, and Shinichi Tokumoto. Identification of nonuniform physical parameters through measurement of inner deformation. *3rd Joint Workshop on Machine Perception and Robotics (MPR2007)*, November 2007.

[47] AIM@SHAPE. http://shapes.aimatshape.net/.

[48] TetGen. http://tetgen.berlios.de/.

[49] Penglin Zhang, Shinichi Hirai, and Kazumi Endo. A feature tracking-based approach for local deformation fields measurement of biological tissue from mr volumes. *3rd Joint Workshop on Machine Perception and Robotics (MPR2007)*, November 2007.

[50] T. Inoue and S. Hirai. Experimental investigation of mechanics in soft-fingered grasping and manipulation. In O. Khatib, V. Kumar, and D. Rus, editors, *Experimental Robotics X*, Springer Tracts in Advanced Robotics 39, pages 13–22. Springer, 2008.

[51] N. Xydas and I. Kao. Modeling of contact mechanics and friction limit surfaces for soft fingers in robotics with experimental results. *Int. J. of Robotics Research*, 18(8):941–950, 1999.

[52] N. Xydas, M. Bhagavat, and I. Kao. Study of soft-finger contact mechanics using finite elements analysis and experiments. *Proc. IEEE Int. Conf. on Robotics and Automation*, pages 2179–2184, 2000.

[53] I. Kao and F. Yang. Stiffness and contact mechanics for soft fingers in grasping and manipulation. *IEEE Trans. on Robotics and Automation*, 20(1):132–135, 2004.

[54] K.L. Johnson. *Contact Mechanics*. Cambridge University Press, 1985.

[55] S. Arimoto, K. Tahara, M. Yamaguchi, P. Nguyen, and H.Y. Han. Principle of superposition for controlling pinch motions by means of robot fingers with soft tips. *Robotica*, 19:21–28, 2001.

[56] P. Nguyen and S. Arimoto. Performance of pinching motions of two multi-dof robotic fingers with soft-tips. *Proc. IEEE Int. Conf. on Robotics and Automation*, pages 2344–2349, 2001.

[57] Z. Doulgeri, J. Fasoulas, and S. Arimoto. Feedback control for object manipulation by a pair of soft tip fingers. *Robotica*, 20:1–11, 2002.

[58] J. Fasoulas and Z. Doulgeri. Equilibrium conditions of a rigid object grasped by elastic rolling contacts. *Proc. IEEE Int. Conf. on Robotics and Automation*, pages 789–794, 2004.

[59] R.M. Murray, Z. Li, and S.S. Sastry. *A Mathematical Introduction of Robotic Manipulation*. CRC Press, 1989.

[60] M. Yoshida, S. Arimoto, J.-H. Bae, and Y. Kishi. Modeling and computer simulation of 3d object grasping and manipulation by dual fingers under non-holonomic constraints. *2006 IEEE/RSJ Int. Conf. on Intelligent Robots and Systems*, pages 5675–5681, 2006.

[61] M. Yoshida, S. Arimoto, and Z.-W. Luo. Three-dimensional object manipulation by two robot fingers with soft tips and minimum d.o.f. *Proc. 2008 IEEE Int. Conf. on Robotics and Automation*, pages 4707–4714, 2008.

[62] H. Goldstein, C.P. Poole, and J.L. Safko. *Classical Mechanics, Third Edition*. Addison-Wesley, 2002.

[63] M. Higashimori, M. Kaneko, A. Namiki, and M. Ishikawa. Design of the 100g capturing robot based on dynamic preshaping. *Int. Journal of Robotics Research*, 24(9):743–753, 2005.

[64] A. Namiki, K. Hashimoto, and M. Ishikawa. Hierarchical control architecture for high-speed visual servoing. *Int. Journal of Robotics Research*, 22(10):873–888, 2003.

[65] Y. Watanabe, T. Komuro, S. Kagami, and M. Ishikawa. Parallel extraction architecture for information of numerous particles in real-time image measurement. *Journal of Robotics and Mechatronics*, (4):420–427, 2005.

[66] S.R. Devasahayam. *Signals and Systems in Biomedical Engineering*. Plenum Pub Corp, 2000.

[67] J. Hamill and K.M. Knutzen. *Biomechanical Basis of Human Movement 2nd Ed.* Lippincott Williams & Wilkins, 2003.

[68] R.E. Burke. Motor units: anatomy, physiology, and functional organization, in handbook of physiology. 2:345–422, 1981.

[69] 久野，細田，浅田. 視覚サーボと内力の制御の統合に基づく多指ハンドによる操り. **日本ロボット学会誌**, 19(5):104–109, 2001.

[70] 横小路，坂本，吉川. カメラ画像を併用した多指ハンドにより操られる物体の位置姿勢推定法. **日本ロボット学会誌**, 18(3):93–102, 2000.

[71] T. Inoue and S. Hirai. *Mechanics and Control of Soft-fingered Manipulation*. Springer-Verlag, London, 2008.

[72] 井上，平井. 柔軟指による物体把持と操作における力学の実験的解明. **日本ロボット学会誌**, 25(6):951–959, 2007.

[73] D.H. Hubel. *Eye, Brain, and Vision 2nd ed.* W. H. Freeman, 1995.

[74] D.A. Robinson. *Why visuomotor systems don't like negative feedback and how they avoid it.* 1990.

[75] 井上，平井. ソフトフィンガー型最小自由度ハンドを用いた把持・操り動作における安定把持効果. **計測自動制御学会論文集**, 43(2):135–144, 2007.